UNIVERSITY OF LIVERPOOL

Faculty of Science & Engineering
Department of Earth, Ocean & Ecological Sciences

Palaeomagnetic field behaviour in the Neoproterozoic: providing constraints on Inner Core Nucleation

Thesis submitted in accordance with the requirements of the University of Liverpool for the degree of Doctor of Philosophy

by

Simon James Lloyd

October 2021

“Patience is bitter, but its fruit is sweet”
Jean-Jacques Rousseau

UNIVERSITY OF LIVERPOOL

ABSTRACT

FACULTY OF SCIENCE & ENGINEERING
DEPARTMENT OF EARTH, OCEAN & ECOLOGICAL SCIENCES

Doctor of Philosophy

PALAEOMAGNETIC FIELD BEHAVIOUR IN THE NEOPROTEROZOIC; PROVIDING CONSTRAINTS ON INNER CORE NUCLEATION

Simon James Lloyd

The age of Earth's inner core is one of the fundamental unanswered questions in deep Earth science. The timing of inner core nucleation is a hugely significant event in Earth's evolution and has been the subject of intense debate. Some of the most recent theoretical estimates for the age of nucleation fall throughout the Neoproterozoic era; much younger than previously thought. A young inner core requires faster recent core cooling rates and a likely hotter early core; knowledge of its age would be invaluable in understanding Earth's thermal history and total energy budget. Predictions generated by numerical geodynamo models need to be tested against such data, but records are currently much too sparse to constrain the event sufficiently.

In this thesis, I present new palaeointensity data from three important time periods in the Proterozoic; 720 Ma Franklin Large Igneous Province dykes, 755 Ma Mundine Wells dykes and 1070 Ma Bangemall Sills. The rocks from these locations are associated with primary remanence and reliable palaeomagnetic directions determined from previous palaeomagnetic studies. Thermal Thellier, Microwave and Shaw-DHT palaeointensity techniques were carried out on whole rocks specimens from each location, producing highly varied results: virtual dipole moments (VDMs) ranging from 0.5 to 6.4 $Am^2 \times 10^{22}$ are obtained and compared against current data. Many of the results agree with recent ultralow palaeointensity data obtained from Ediacaran rocks and may support that the dynamo was on the brink of collapse in the Neoproterozoic prior to a young inner core formation date. However, there is also substantial disagreement with this hypothesis raised by new high field-strength values at 755 Ma that are difficult to explain. Comparisons of VDMs using these new data suggest that the Proterozoic palaeomagnetic field was highly variable on timescales of 10s to 100s Myrs, and that the use of sparse datasets may introduce bias when used as a model constraint or to infer the occurrence of significant deep earth events.

Contents

List of Figures

List of Tables

List of Acronyms

α .... Angular difference between the anchored and unanchored best-fit directions

AF .... Alternating frequency

ANC .... Ancient

API .... Absolute palaeointensity

(p)ARM .... (partial) Anhysteretic remanent magnetisation

ARM_{AQ} .... Stepwise ARM acquisition

β .... Relative scatter around the best-fit line

B .... Magnetic flux density

B_c .... Coercivity

B_{cr} .... Coercivity of remanence

B_i .... Induced magnetic field

BiCEP .... Bias Corrected Estimation of Paleointensity

BMO .... Basal magma ocean

BSE .... Backscatter electron

CDRAT .... Cumulative DRAT (see DRAT)

ChRM .... Characteristic remanent magnetisation

CMB .... Core-mantle boundary

CNS .... Cretaceous normal-polarity Superchron

CRM .... Chemical remanent magnetisation

DAC .... Diamond-Anvil cell experiments

DANG .... The deviation angle selection criterion

DC .... Direct current

DHT .... Double heating technique

DFT .... Density function theory

DRAT .... Maximum absolute difference produced by a pTRM check

$DRAT_{TAIL}$ .... Maximum absolute difference produced by a pTRM tail check

DRM .... Detrital remanent magnetisation

E_d .... Magnetostatic anisotropy energy or demagnetising energy

E_k .... Magnetocrystalline anisotropy energy

EDS .... Electron-dispersive X-ray spectrometry

f_{RESID} .... Palaeointensity slope is origin-trending, and the

f (or fN) .... Fraction of NRM used on an Arai diagram by vector difference

FRAC .... Fraction of NRM used for the best-fit on an Arai diagram

FeO .... Iron oxide

FORC .... First-order reversal curve

GAD .... Geocentric axial dipole

GPTS .... Geomagnetic polarity time scale

GRM .... Gyroscopic remanent magnetisation

H .... Magnetic field strength

H_c .... Coercivity

H_d .... Demagnetising field

I .... Infield step

ICB .... Inner core boundary

ICN .... Inner core nucleation

IRM .... Isothermal remanent magnetisation

KTT .... Königsberger-Thellier-Thellier

k' .... Curvature parameter

κ .... Bulk magnetic susceptibility

LAB .... Laboratory

LIP .... Large igneous province

LLSVP .... Large low-shear-velocity province

LTD .... Low-temperature demagnetisation

M .... Magnetisation

M_{rs} .... Remanent saturation magnetisation

M_s .... Saturation magnetisation

m .... Magnetic moment

MAD .... Maximum angular deviation

MD .... Multi domain

MgO .... Magnesium oxide

NRM .... Natural remanent magnetisation

PINT .... Palaeointensity

PRM .... Piezo remanent magnetisation

PSD .... Pseudo single domain

PSV .... Palaeosecular variation

PsT .... Pseudo-Thellier

QDM .... Quantum diamond magnetic mapping

QG-MAC .... Quasi-geostrophic forces - Magnetic, Archimedean, Coriolis

QPI .... Quality of palaeointensity

QPM .... Quality of palaeomagnetic models

R^2*corr* .... Square of the Pearson correlation

rN .... R^2*corr* for $slope_N$

rT .... R^2*corr* for $slope_T$

RESET .... Repeated Thellier-Series Experiment

S .... Angular dispersion

SAF .... Subduction area flux

SCP .... Single crystal palaeointensity

SEM .... Scanning electron microscope

SD .... Single domain

SHRIMP .... Sensitive high-resolution ion microprobe

SiO2 .... Silicon oxide

$Slope_N$ (sN) .... Shaw method palaeointensity slope

$Slope_T$ (sT) .... Shaw method corrected TRM slope

Slope$_A$ (sA)........Shaw method ARM slope

SQUID ....Superconducting quantum interference device

T........Temperature

T_b........Blocking temperature

T_c........Curie temperature

T_{ub}........Unblocking temperature

T_v........Temperature required to remove viscous component

TAF........Time-averaged field

TBL........Thermal boundary layer

TCRM ....Thermo-chemical remanent magnetisation

TDM........True dipole moments

(p)TRM........(partial) Thermal remanence magnetisation

ν........Viscous coefficient

V(A)DM ....Virtual (axial) dipole moment

VGP........Virtual geomagnetic pole

VRM........Viscous remanent magnetisation

χ ....Magnetic susceptibility

Z........zero-field step

Declaration of authorship

I, Simon J. Lloyd, declare that the thesis entitled “Palaeomagnetic field behaviour in the Neoproterozoic; providing constraints on Inner Core Nucleation”, and the work presented in the thesis are both my own, and have been generated by me as the result of my own original research. I confirm that:

- this work was done wholly while in candidature for a research degree at this University;
- where any part of this thesis has previously been submitted for a degree or at this University or any other institution, this has been clearly stated;
- where I have consulted the published work of others, this is always clearly attributed;
- where I have quoted from the work of others, the source is always given. With the exception of such quotations, this thesis is entirely my own work;
- I have acknowledged all main sources of help;
- where the thesis is based on work done by myself jointly with others, I have made clear exactly what was done by others and my contribution;
- parts of this work have been accepted for publication as:

Lloyd, S. J., Biggin, A. J., Halls, H., & Hill, M. J. (2021). First Palaeointensity Data from the Cryogenian and their potential implications for Inner Core Nucleation Age. Geophysical Journal International. https://doi.org/10.1093/gji/ggab090

Lloyd, S. J., Paterson, G. A., Thallner, D., & Biggin, A. J. (2021). Improvements to the Shaw-Type Absolute Palaeointensity Method. Frontiers in Earth Science, 9(July), 1–11. https://doi.org/10.3389/feart.2021.701863

Lloyd, S. J., Biggin, A. J., & Li, Z.-X. (2021). New paleointensity data suggest possible Phanerozoic-type paleomagnetic variations in the Precambrian. Geochemistry, Geophysics, Geosystems, https://doi.org/10.1029/2021GC009990

Signed: ....

Date: ... 20/10/2021 ....

This PhD thesis by

Simon James Lloyd

has been produced under the supervision of the following persons

Supervisors:

Andrew J. Biggin
Mimi J. Hill

I would firstly like to thank my primary supervisor, Andy Biggin. I will always feel enormous gratitude to Andy for giving me this opportunity in the first place. His continuous support, friendship and patience over the last several years has made my time in the lab incredibly rewarding. It is also thanks to Andy's leadership and encouragement that I have been able to enjoy being part of such a great, dynamic and engaging team. Andy, I will be sticking around until I can beat you at tennis, so until retirement :)

I have appreciated working with some incredibly knowledgeable and supportive teammates and I would like to thank them all for their help and friendship. I have so many good memories of team nights out, 'away meetings', and of course, field work. A special thanks to Greig for his friendship, endless patience and our many invaluable discussions which have helped me hugley, and for which I am incredibly grateful. Also to Richard for all his invaluable help. A special thanks to Mimi for all the guidance and support, especially in helping me get my first paper across the line at a time when I was losing my confidence. Of course, I also have to give big love to my two main 'oppos' Dan and Yael who have made my time infinitely more fun on a daily basis. We've learned, laughed and had some amazing times together, in and out of work and it would never have been the same without you both. Also to Ben, I know you shaved your hair to look like me, and I was glad to be your role model ;) Thank you also, to top tech guru Elliot for fixing everything I broke and blamed on Yael :)

Thank you to Leverhulme for providing the funding which allowed me the opportunity to pursue my PhD. Thanks to the University of Liverpool, which has been a special place for me over the last seven years. Thanks to Prof. Zheng-Xiang Li and Josh Beardmore at Curtin University for the incredible fieldwork experience. Thanks to Phil McCausland and Henry Halls for the fieldwork and collaborations; you helped me get my studies off the ground. Thanks to Elliot Wood and Matt Bilton, both electron microscopy specialists at UoL SEM Shared Research Facility, for all the help.

It's been extremely tough at times in getting to this point, and it would simply not have been possible without the love and support of my family. I want to thank my parents for their never-ending love and support, I love you both dearly. Clare has been my rock, and has always done whatever she can to help and support me in all aspects of our lives, despite it being really tough for her too. Amber has been a superstar, just in general but especially for helping me out whenever she can to look after my little boy Jesse. I would like to thank Jesse too, for making things twice as difficult (I like a challenge) but mainly for being the most amazing little loving person in the world.

Chapter 1

Introduction and background

1.1 Introduction

The question of when the inner core formed is one of deep Earth sciences greatest debates. This hugely significant event in Earth history provided new power sources for the geodynamo and may have prevented its complete collapse (Bono et al., 2019). Earth's sustained magnetic field has been able to continue to protect all life by neutralising the constant bombardment of cosmic radiation which would otherwise erode the atmosphere, leading to surface heating (Tarduno et al., 2010, 2014; Zossi et al., 2019).

The timing of Inner core formation is intrinsically linked to many complex deep earth processes. Most of these processes and conditions are associated with large uncertainties, and an accurate inner core nucleation (ICN) age would be invaluable in reducing the uncertainties in the parameterisation of numerical geodynamo and global mantle convection models. These parameters include processes such as thermal convection and thermal conductivity in the outer core, total heat flux across the core-mantle boundary (CMB), and core stratification.

It would also provide a primary constraint on thermochemical evolution models, which also feature many related and poorly constrained processes. It may therefore help to answer some big questions such as what is the total planetary energy budget, geochemical abundances within the core, and its structure. These models are also more broadly related to processes such as plate tectonics through the cooling history of Earth; in addition, subducting slabs and mantle plumes affect the temperature gradients across the CMB and thereby, the heat flow.

Formation and growth of the inner core changes the dynamical regime in the core considerably (Biggin et al., 2015), providing a source of compositional convection and the release of latent heat to power the geodynamo. The vigorously convecting region of the outer core is responsible for providing the geomagnetic field and so substantial changes to the regime are likely to affect the magnetic field. The addition of these new forces, which are much more efficient than thermal convection alone, are expected to produce a corresponding change, on average, in the strength and/ or morphology of the geomagnetic field as observed at the earth surface (Biggin et al., 2015). The Neoproterozoic era coincides with most of the recent model age estimates for ICN (see Chapter 2, Figure 2.1); there exists, however, a severe paucity of palaeointensity data during this time period with just a handful of single estimates spanning ~500 Myr.

The primary focus of this research is to obtain reliable palaeointensity data for key periods of the Neoproterozoic, addressing the substantial sparsity of data during this time. The compiled data from my research are integrated with published palaeomagnetic data and analysed to provide an improved understanding of the palaeomagnetic field and determine whether a signature for ICN is detected in the higher resolution palaeointensity records. This forms a fundamental part of a larger group of projects who's overarching aim is to improve our understanding of Earth's deep interior through the application of palaeomagnetism. In addition to the aim of constraining ICN age, other important questions are investigated; for example, whether geomagnetic field behaviour follows an approximate 200 Myr cycle and, if so, why? The larger project is set to achieve its goals through several key strategic areas of focus: 1) The development and application of new field characterisation techniques and improved statistical modelling. 2) A series of new numerical geodynamo that conform to earth-like behaviour, as defined by point (1). 3) Better integration of these and other new palaeomagnetic results with existing data, to produce comprehensive models of geomagnetic evolution through Earth's history.

1.2 Thesis structure

The remainder of this chapter is devoted to providing background information on rock magnetic theory and palaeointensity methodology. The fundamental principles covered here explain how we are able to use palaeomagnetism and they provide the basis for the approach to our studies.

Given that the aims set out in this thesis are intrinsically related to many deep earth processes, I feel that an extended background on this subject is important; this forms chapter 2. The chapter is a review of the most current literature that is relevant to the subject of ICN and acts as a detailed background on deep earth structure and the processes that affect ICN. The relationship between these geodynamic processes and the palaeomagnetic field is discussed, including how palaeomagnetism is used to constrain many deep earth processes. The chapter also provides context for the motivations behind the studies I have carried out herewith; I also provide a comprehensive list and analysis of the most current ICN age estimates.

The remaining chapters of the thesis are presented as published manuscripts. The first of three paper-based chapters (Chapter 3) is one that looks in detail at the Shaw-DHT (LTD) palaeointensity method. This method is becoming more popular in studies of ancient rocks and is relied on throughout my studies; this is, in part, due to how well it can be adapted to modern day equipment such as the RAPID magnetometer. Although it has been in use for several decades, with subsequent amendments, the reliability of the Shaw method has remained unclear. Given these considerations, it needed testing in terms of its accuracy and precision on a wide range of rock types and ages. This thesis is also able to demonstrate several improvements to the selection criteria used in analysing the data, most notably replacing the correlation coefficient (R^2corr) with the curvature parameter ($|k'|$) to assess linearity. Improving reliability in the palaeointensity methodology used in these studies allows for greater confidence in any forthcoming geodynamo models that rely on these data as a constraint. I drove the project forward and rationalised many of the key concepts along with G. Paterson and A. Biggin, who also provided me with continual support. I carried out most of the experiments alongside D. Thallner who also wrote the code for the Shaw data analysis and down-sampling.

Chapter 4 is a palaeointensity study on widespread Neoproterozoic dykes and sills from the high Arctic of Canada and Greenland. The results obtained from dykes and sills of the 720 Ma Franklin Large Igneous Province (LIP) are the first in a ~300 Myr gap in palaeointensity records, providing a crucial insight into field behaviour during this time. Multiple palaeointensity techniques were applied and compared in this study, in addition to various rock magnetic experiments and microscopy work to ensure accurate, reliable results. The new data approximately correspond in time to the most recent estimates of ICN age, for which they may provide a valuable constraint. I carried out all of the experiments and data analysis for this chapter. A. Biggin developed the ideas and research behind the project and provided me with continual advice and support. The sample collection was carried out by Henry Halls who also provided me with guidance along the way. M. Hill gave advice and support, particularly at the writing stage.

A further palaeointensity study of Precambrian aged rocks from Western Australia forms chapter 5. The Mundine Wells dykes (755 Ma) and the Bangemall Sills (1070 Ma) were studied to provide further insight into Precambrian field behaviour. Their ages are close to the previously mentioned Franklin LIP and anomalously high intensity results from the Mid-Continent Ridge (1087 Ma; Kulakov et al., 2013; Sprain et al., 2018). This study provides a unique opportunity to examine dipole moment variability and questions whether values for the Precambrian were similar to those in the Phanerozoic by making appropriate comparisons of both periods. A highly variable field coupled with extremely sparse palaeointensity data has implications for the reliability for such data, particularly when drawing significant conclusions. This project was mainly developed by A. Biggin. The field work was carried out by all authors, for which Z-X. Li was invaluable. I then performed all of the experiments, data analysis and research.

Additional palaeomagnetic work was undertaken on the Chatham Grenville (531 Ma) and Mont Riguad (533 Ma) stocks, located in Western Canada. The work was based on previously directional published results by McCausland et al. (2007) and is mentioned briefly in Chapter 6. Just a small number of the original sites were located, with the remaining sampling being carried out near to the description of the sites. Analysis of the directions revealed large scatter with very few site means agreeing with the original study; out of these, just one site (one of the original dykes) give successful and consistent palaeointensity results (Appendix D).

Finally, my conclusions bring together the results from all the Precambrian palaeointensity studies and relate these to the latest estimates for ICN age. I also suggest potential future work needed to further expand our understanding of this highly debated subject.

1.3 Rock magnetic principles

In order to achieve my goals, an understanding of the various rock magnetic properties and principles, and how they affect palaeomagnetic experiments is vital. This intricate discipline has been studied extensively over many years, leading to an expansive and well-documented knowledge from which to refer. Next, I summarise some of the most relevant of these topics, including some recent advances, acknowledging that a vast amount of the overall subject is not included here.

1.3.1 Physics of magnetism

The field of palaeomagnetism is ultimately made possible by the capability of certain magnetic minerals to acquire a remanent magnetisation in nature, which reflects the direction and strength (or relative strength) of Earth's magnetic field. The magnetic moment generated in such materials is a result of electron motions and the forces applied to them by an external magnetic field.

1.3.1.1 Diamagnetism and Paramagnetism

There are two sources of magnetic moments in electronic motions: the orbits and the spins of unpaired electrons. The orbital motion of electrons alters to align in the presence of an external field, producing a small magnetisation antiparallel to the applied magnetic field. This fundamental property of all materials is called diamagnetism. Diamagnetic materials comprise of atoms with no atomic magnetic moments; their electrons orbit the nucleus in pairs which spin in opposite direction, cancelling out their magnetic moment. Magnetic susceptibility is small and negative, and is temperature independent (Tauxe et al., 2008).

Materials (commonly, iron-bearing transition element solids) are described as paramagnetic if the order of their electrons are such that they possess unpaired electrons. The spin directions of these unpaired electrons align in an external magnetic field to produce a net magnetisation. Thermal energy constantly excites the crystal lattice opposing the ordering of magnetic moments which become randomised once the external field is removed and the net magnetisation returns to zero. Thermal energy at room temperature is many thousand times the aligning energy, hence, net magnetisation is small even in a significant magnetising field (Butler, 2004). Susceptibility is temperature dependent (because increasing thermal energy opposes aligning energy) and is proportional to $1/T$ and is C/T for a specific material (C = Curie constant).

1.3.1.2 Ferromagnetism

Ferromagnetism is a particular case of Paramagnetism where there is a strong magnetic coupling between adjacent atoms; as a result, the magnetisation is orders of magnitude higher than Paramagnetism for a given magnetic field. The strong interaction between atoms is a result of exchange energy. This exchange energy is minimised by the parallel or antiparallel alignment of adjacent magnetic moments; however, it is of a complex quantum nature and is related to the partial overlap of electron probability distributions of atoms packed in a crystalline structure (Tauxe, 2008). It is the crystal structure and density of packing that determines whether a solid containing transition elements is paramagnetic (no overlapping orbitals and no exchange coupling) or ferromagnetic (significant orbital overlap and resulting exchange coupling).

The balance of magnetic and thermal energies within a grain dictates its magnetic behaviour; in particular, whether a magnetic moment remains oriented along an "easy axis" (in an energy minima) or is able to overcome an energy barrier, and reorientate. Ferromagnetic materials are able to retain a remanent magnetisation (M_r) in the absence of an external field and therefore display hysteresis (see Section 1.3.6). The external field provides the energy required for individual magnetic moments to overcome the anisotropic energy barriers within a grain which would otherwise prevent their rotation. Once removed, a net alignment of magnetic moments remains because thermal excitation energy at room temperature is insufficient to overcome the energy barriers in many grains. There are several magnetic anisotropic energy barriers that can be present within a grain, which are influenced by and relate to its geometry, crystal structure and internal or external stresses (Butler, 2004; Dunlop & Ozdemir, 2007).

1.3.1.3 Antiferromagnetism and Ferrimagnetism

Antiferromagnetism occurs when the electron spins of two crystal sublattices oppose each other and are therefore antiparallel. In this case, their magnetisations are equal, resulting in a net zero spontaneous magnetisation. Hematite is a special case of antiferromagnetism whereby the atomic moments in its sublattices are not perfectly antiparallel due to spin canting (the two crystal lattices are not quite antiparallel), allowing for a net magnetisation; this is known as canted antiferromagnetism. Magnetite is ferrimagnetic, which means that the magnetisations of each sublattice are not equal because of different numbers of Fe^{2+} and Fe^{3+} cations at different sites, resulting in a net magnetic moment (Dunlop & Ozdemir, 2007).

1.3.1.4 Superparamagnetism

Superparamagnetism refers to the state in which a particles thermal energy can easily overcome any anisotropic barriers. This occurs in very small particles, which are analogous to paramagnets in their behaviour except they posses thousands of coupled electron spins, and exchange energy is not overcome by thermal energy. Magnetic moments flip continuously, and if a particle were observed on a very short timescale, it may appear single domain-like (Butler, 2004).

1.3.2 Domain theory

Domains occur in magnetic particles in order to reduce the magnetostatic energy (E_d). For SD particles, the lowest energy state is achieved when its magnetisation is saturated in a single direction. As particle size increases, so does E_d until a point is reached where lower overall energy can be achieved by creating two or more domains, each with their saturation magnetisation (M_s) vectors antiparallel or otherwise depending on anisotropic conditions (Dunlop and Ozdemir, 2007). E_d is proportional to M^2, and so particles of weakly magnetised minerals such as hematite have a larger critical grain size (the point at which domain walls form) than, for example, magnetite.

The nucleation of domain walls is required to separate adjacent domains; these walls are regions of increased energy because electron spins are forced into opposite directions. Exchange energy would be too large if this were to occur abruptly and so a gradual change is favoured; however, this places spins in the domain wall in positions with higher magnetocrystalline energy. Domain walls are easily displaced and can often become pinned to local imperfections since this reduces their energy; however, the demagnetising magnetic field (H_d) can force domain walls from local pinning as the lowest magnetisation state is sought. When domain walls are displaced, they tend to reform in a new local energy minimum during remagnetisation; this changes the total magnetisation and makes multi-domain (MD) particles unsuitable for palaeointensity experiments (Tauxe et al., 2008).

So-called pseudo single-domain (PSD) refer to those particles (slightly larger than SD) in which it remains energetically favourable to remain free of domain walls, but produce magnetic states that are much more complex than a single uniaxial domain. Micromagnetic modelling has shown that a form of “vortex” magnetic state occurs, followed by a “flower” state as the particle grows (Muxworthy & Williams, 2006). Small PSD particles with an easy-aligned, single-vortex domain state have been found to display SD behaviour, in that their magnetic domain structure can coherently switch between stable states (Nagy et al., 2017). Recent modelling suggests that PSD particles may have as many as 60 local energy minima, although many of these would quickly decay to create a more stable vortex state during the acquisition process. Magnetic remanence associated PSD grains are considered to be less stable than in SD grains; however, fast cooling rates can stabilise metastable flower domain states and can create very stable remanence magnetisations (Fabian & Shcherbakov, 2018). Recent studies have even found that a hard-aligned single vortex can be more stable than SD (Nagy et al., 2019).

1.3.3 Remanent magnetisations

There are many types of remanent magnetisation, detailed below:

1.3.3.1 Natural remanent magnetisation (NRM)

An NRM is the general term given to a remanent magnetisation acquired in nature, by either chemical, thermal or depositional processes and can be composed of multiple components. A ‘primary’ component of a thermal NRM is acquired as a rock originally cools after formation; this may subsequently be overprinted by a secondary component, either viscous or by reheating. The most stable retained component is referred to as the characteristic remanent magnetisation (ChRM), and may not necessarily be primary.

1.3.3.2 Thermoremanent magnetisation (TRM)

A TRM is acquired in magnetic particles as they cool through their Curie temperature (T_c) in an external magnetic field. This can occur in igneous rocks when they originally cool or from a subsequent reheating. As the rock cools and thermal energy decreases, anisotropic energy barriers become too great for the magnetic moment to rotate beyond. It effectively becomes locked in position; this occurs at a particle’s blocking temperature. The distribution of blocking temperatures varies according to the distribution of particle mineralogy, size and shape within the rock. Collectively, there is a statistical preference of alignment to the external magnetic field. Magnetisations will gradually relax and individual particles will unblock; for SD particles at ambient temperatures, this can take billions of years. Néel (1949) provided an explicit theory for the relaxation time (τ) of non-interacting SD particles. This defines the time it takes for the magnetisation to fall to 1/e of its original value.

1.3.3.3 Viscous remanent magnetisation (VRM)

A magnetic particle exposed to a weak magnetic field over a prolonged period of time is more likely to have the energy to overcome the anisotropy barriers that prevent rotation of its magnetic moment. This tendency toward magnetic equilibrium enables the acquisition of a VRM in a similar way to TRM but at ambient temperatures. Larger particles with lower energy barriers are more susceptible to this process according to Néels theory of relaxation time (τ). However, extremely stable VRM have been observed in some studies (e.g., De Groot et al., 2014), which is supported by recent micromagnetic modelling of cubic PSD particles (Fabian & Shcherbakov, 2018).

1.3.3.4 Chemical remanent magnetisation (CRM)

A CRM can be acquired when new magnetic minerals form below their critical blocking temperature in the presence of an external magnetic field. Initially very small particles are dominated by thermal energy and are therefore superparamagnetic. As the newly formed particles grow through a critical size, the anisotropic energy increases relative to thermal energy and the magnetisation becomes blocked (Mcclelland, 1996). This type of grain-growth CRM typically occurs through exsolution of iron-oxides from an iron-rich non-magnetic matrix. This type of remanence acquisition is thermally controlled and is dependent on the alignment of particles as they become blocked; it can therefore be modelled as a TRM according to Néel theory (1949).

A CRM can also occur when an existing magnetic mineral, such as titanomagnetite, exsolves into magnetite and ilmenite lamellae. Alternatively, magnetite can transform into a new mineral such as maghemite; where this occurs over geologic timescale, it tends to involve low temperature oxidation. Alteration of a pre-existing mineral in laboratory experiments is often associated with titanomagnetites that undergo reduction or oxidation (Collinson, 1983).

Where chemical changes occur simultaneously with temperature and volume changes, the remanent magnetisation is referred to as thermochemical (TCRM; Dunlop and Ozdemir, 1997). TCRM is described by Fabian (2009) as being acquired through recrystallisation processes rather than CRM grain growth, whereby the original blocked TRM is not erased, but is altered or added to by the chemical changes. In the strict sense, a TCRM would be acquired as a rock is cooling, and is below its Curie temperature.

1.3.3.5 Isothermal remanent magnetisation (IRM)

This is a remanence acquired at a constant temperature and by strict definition can include, and is occasionally referred to by, other remanence magnetisations such as CRM, VRM and ARM. Typically, however, it is acquired by short applications of a strong magnetic field such as in the measurement of a hysteresis loop; it is also commonly induced in nature through lightning strikes.

1.3.3.6 Anhysteretic remanent magnetisation (ARM)

ARM is the net magnetisation acquired by applying a continuous direct current (DC) bias field and simultaneous decaying alternating field (AF) of initially large amplitude (Figure 1.1). Without a bias field, as the amplitude of the AF decays, particles of decreasing coercivity are blocked in opposing AF directions, effectively cancelling each other out. The AF is either applied in a single direction with the sample tumbling, or with in three perpendicular directions, with the sample in a static position, thereby randomising particle magnetisations. A stepwise increase in the applied AF field results in progressive AF demagnetisation of particles with higher coercivities. A small DC bias field imposes a statistical preference in the direction of the bias field for the remagnetised particles. A partial remanence (pARM) can be imparted by only turning on the DC field for part of the AF cycle, analogous to pTRM acquisition during cooling, or by using a peak field that is less than the maximum coercivity of the sample.

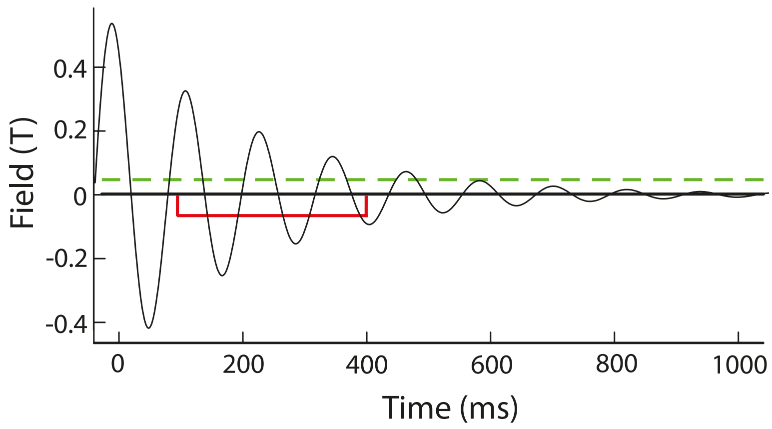

Figure 1.1 Acquisition of pARM using a decaying AF (black line) and DC bias field (dashed green line). The solid red line indicates the duration that the DC is applied. Image adapted from Tauxe et al. (2008).

Other remanent magnetisations not mentioned here include detrital remanent magnetisation (DRM), pressure or piezo remanent magnetisation (PRM), and gyromagnetic remanent magnetisation (GRM).

1.3.4 Magnetic minerology

There are many magnetic minerals that are exist in nature; however, there are two iron-oxide "solid solutions" (their original atoms can be substituted without changing the structure) that are most important for palaeomagnetism, ulvospinel-magnetite and ilmenite-hematite; these are shown in a ternary diagram (Figure 1.2). In both series, titanium is the most common substitute, and can be present in any abundance in the complete solid solution above the temperature at which crystallisation occurs. As the rock cools, many compositions become unstable causing titatanium concentrations to exsolve into ti-rich and ti-poor lamellae, toward their end members. If cooling is sufficiently fast, i.e., the rock is quenched, the exsolution process is impeded, allowing any composition of titanium-substituted metastable states to exist in nature (Dunlop & Özdemir, 1997).

Low-temperature oxidation can occur for a given titanomagnetite composition (z direction, Figure 1.2), by solid-state diffusion; two thirds of the original Fe^{2+} become Fe^{3+} while one third of the original Fe^{2+} are removed from the B sublattice Because ferrimagnetism of magnetite results from Fe^{2+} in the B sublattice (Fe^{3+} cancel each other out), removal of one third of these cations decreases saturation magnetisation (Butler, 2004).

1.3.4.1 Magnetite

Magnetite is the most common magnetic mineral on Earth. It is the magnetic end member of the stoichiometric ulvospinel-magnetite solid solution. It has a cubic lattice with inverse spinel structure (Fe^{2+}(A) Fe_2^{3+}(B) O^4). Titanomagnetite is formed by the substitution of iron cations with non-magnetic titanium cations ($2Fe^{3+} \rightarrow Fe^{2+} + Ti^{4+}$); this weakens the A-B exchange interactions in the inverse spinel structure (where A and B represent the two antiparallel sublattices). An increase in the amount of titanium substitution (x direction, Figure 1.2) results in a near linear reduction in T_c (Dunlop & Ozdemir, 2007; Tauxe, 2008).

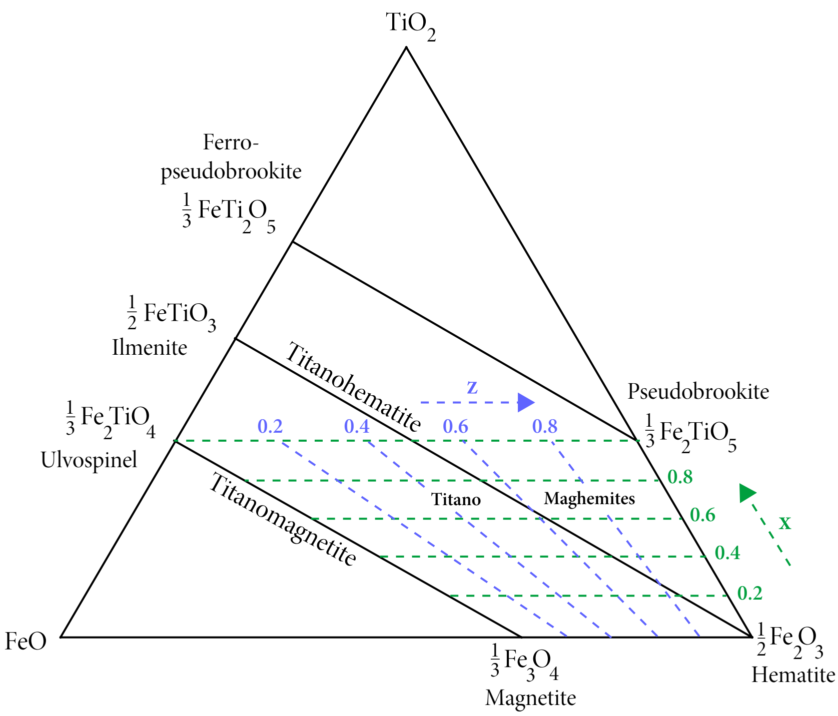

Figure 1.2. Ternary diagram of titanium and iron oxides. The dashed area indicate the solid solution series of titanomaghemites; x and z represent the titanium concentration and oxidation parameter respectively. Redrawn after Dunlop and Özdemir (2007).

Magnetite is associated with a large M_s (480 kAm^{-1}) and small changes from an equant geometry tend to dominate the magnetic anisotropy energy. A characteristic feature of magnetite and titanomagnetite is that they undergo a Verwey transition whereby their cubic lattice distorts to monoclinic at ~110 K for magnetite. The specific temperature is affected by the amount of titanium substitution and by oxidation, whereby maghematisation suppresses the transition altogether. Magnetocrystalline anisotropy (E_k) increases substantially, leading to a loss of magnetisation. The effect is minor for SD particles because they tend to be dominated by E_d rather than E_k, but domain walls can be affected considerably and thereby so can MD remanence. This forms the basis for low-temperature demagnetisation techniques used in palaeointensity methods.

1.3.4.2 Hematite

Hematite has a rhombohedral crystal structure, and is antiferromagnetic whereby the magnetisation of its sublattices are cantered. It can form in a melt by primary high-temperature oxidation of titanomagnetite, or by several secondary processes such as oxidation of magnetite over long periods at ambient temperatures (Dunlop & Ozdemir, 1997). Hematite does not have a curie temperature (this is restricted to ferromagnets), but rather a Néel temperature of 675 °C. M_s is more than an order of magnitude weaker than magnetite; ~2 kAm^{-1} at ambient temperatures (Butler, 2004). It is affected by the so-called Morin transition which occurs at ~ -20 °C, whereby the net anisotropy changes and so too does the crystallographic easy axis. When cooling through this temperature, which is affected by titanium substitution and particle size, spin-canting disappears and magnetisation held in the basal plane is lost, although some is regained as it warms.

Coercivity (H_c) can be very high (hundreds of mT) but varies greatly with particle size, increasing steadily from nano-particles to its maximum; after a particle size of ~15 µm it falls off linearly with particle size (Banjeree, 1971; Tauxe et al., 2008). Its high coercivity can be attributed to magnetoelastic anisotropy in SD crystals caused by internal stress due to crystal twinning; its magnetostriction is similar to magnetite but H_c is proportional to M_s.

1.3.5 Rock magnetic methods

1.3.5.1 Hysteresis

Measurements of hysteresis loops are performed on bulk specimens (Figure 1.3), in which assemblages of particles are fixed in position with random dipole moments. Assuming a combined magnetisation (M) of zero (demagnetised), dipole moments align through torque with B until the magnetisation reaches saturation. This forces the rotation of many dipole moments beyond an anisotropic barrier, to rest in a new preferred 'easy' orientation that is closer to the direction of B once the field is removed; this results in a saturation remanent magnetisation (M_{rs}). If the direction of B is reversed, the field required to return the magnetisation to zero is the bulk coercivity (B_c). The coercivity of remanence (B_{cr}; not shown) is the antiparallel field required to irreversibly rotate half of the dipole moments (for single domain uniaxial particles, $M_r/M_s = 0.5$), reducing M_{rs} to zero.

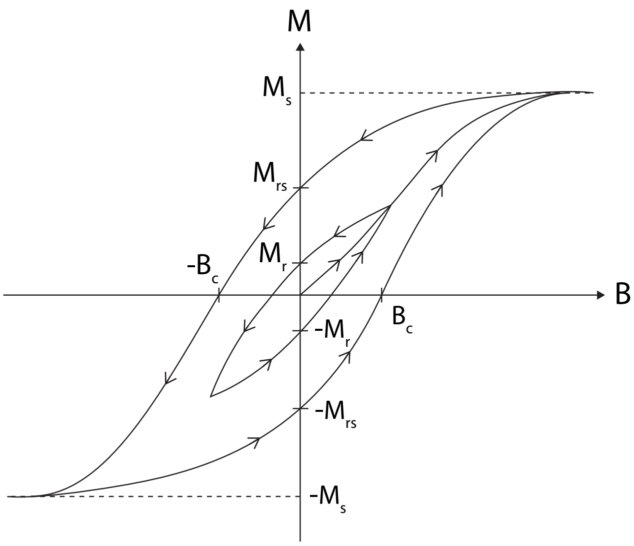

Figure 1.3. Minor and major hysteresis loops. M, magnetisation; B, applied field; M_s, saturation magnetisation; M_{rs}, saturation remanent magnetisation; Mr, isothermal remanent magnetisation (minor loop); B_c, coercivity (Dunlop & Özdemir, 1997).

Parameters from hysteresis measurements are typically used to identify bulk domain properties of a sample. This is achieved historically by comparing the ratio of hysteresis parameters, M_{rs}/ M_s and B_{cr}/ B_c in a Day et al. (1977) plot; however, a recent study conclude that this method is not reliable, even for single-exsolved silicate crystals (Nikolaisen et al., 2020).

1.3.5.2 First-order reversal curves

A first-order reversal curves (FORC) is a partial magnetic hysteresis curve, measured at a series of evenly spaced points in a stepwise changing applied field (Mayergoyz, 1986). A FORC diagram is constructed from multiple FORCs which start from increasing reversed field points (B_a) to positive saturation (B_s). The magnetisation along any curve is represented by M (B_a, B) at a point toward positive M_s. Measurement points from a grid of consecutive FORCs are used to determine the FORC distribution by taking a mixed second derivative. A smoothing factor is applied to reduce the experimental noise.

FORC diagrams are superior to the ambiguous parametric-ratio methods for domain state classification; their interpretation is based on an extensive testing of well-defined samples and through numerical and micromagnetic modelling (Roberts et al., 2014). The distribution is transformed to B_i, B_c, representing the shifting field due to local interactions (or sensitivity to the various domain states) and the coercivity distribution respectively. Characteristic signatures can be identified for the various domain states that exist, as well as more precise observations on anisotropy energies and magnetostatic interactions within the particle (Harrison et al., 2019). The FORC signal can also be separated into three unique signals; remanent, induced and transient FORC (Zhao et al., 2017). These can each identify different features and address some of the ambiguity related to overlapping magnetic processes such as domain wall movement, vortex state-changes and moment rotation.

1.3.5.3 Thermomagnetic measurements

M_s decreases with increasing temperature, becoming zero at a particular materials Curie temperature (T_c); this is because inter-atomic distances increase during thermal expansion and therefore the strength of exchange coupling (and resultant M_s) decrease with increasing temperature. At T_c these distances have increased to the point at which exchange coupling no longer occur, and the material becomes paramagnetic. Thermomagnetic measurements of M_s as a function of temperature (M_s-T) can therefore be used to determine the T_c of the dominant magnetic mineral, either by using the second derivative or extrapolation method (Leonhardt, 2006; Moskowitz, 1981; Petrovský & Kapička, 2006).

High-temperature susceptibility (κ-T) is used to determine the reversibility of susceptibility during a heating and cooling experiment. The reversibility of the heating and cooling curves indicates whether magnetic material has increased or reduced during heating, and cyclic experiments can precisely identify the temperatures at which the alteration has occurred. Irreversible but parallel curves suggest that no new mineral type has formed.

1.3.5.4 Anisotropy of magnetic susceptibility (AMS)

AMS is an important technique that has applications in the study of plate tectonics, palaeosols and detrital remanence magnetisations. It is also useful in providing information on the strain history and initial fluid flow of volcanic lava flows and dykes. The manner in which magnetic susceptibility relates the external field to magnetisation is generally regarded as a scalar property; however, if anisotropy of magnetic susceptibility is large, the orientation of the applied field can affect the outcome of palaeointensity measurements and it is appropriate to consider magnetic responses as a tensor.

Anisotropy of remanence can affect certain palaeointensity results and may be assessed by applying an ARM in at least three orientations (but typically more), and demagnetised along the axis of the following ARM between each step, and the residual is vector subtracted from the subsequent ARM. Each ARM step gives three orthogonal remanence components from which a correction can be applied to obtain an anisotropy corrected intensity (Tauxe et al., 2008).

1.4 Palaeointensity methodology

The emphasis throughout all of this research has been to ensure that robust and reliable palaeointensity information is obtained. Reliable palaeointensity data is intrinsically difficult to acquire, particularly for periods extending back into the Precambrian era. Magnetic particles with relaxation times of up to several billions of years are required; in addition, the integrity of the magnetic signal must be preserved in rocks that are subjected to ever changing conditions over geologic time. As the lack of data for the Neoproterozoic suggests, identifying suitable rocks of a particular Precambrian age is problematic. Locating and dating rocks from particular key periods spanning hundreds of millions of years is non-trivial; rocks are often weathered with limited or no exposure or have been reheated and possibly metamorphosed during subsequent geological events. This can cause much, if not all, of the original magnetic signal to become overprinted to record the field at the time of secondary reheating and cooling. Those rocks that have not been reheated can often slowly oxidise in nature, causing alteration of the original magnetic minerals and growth of new magnetic minerals; this can produce a CRM or modify a TRM into a TCRM; either of these would alter the magnetic signal that was originally recorded as the rock cooled.

Significant problems further arise from the need to reheat the rock specimens in the laboratory to high temperatures which may exceed the Tc of the magnetic minerals (e.g., 580 °C for Magnetite). Alteration is common and can produce a CRM or TCRM, thereby damaging the fidelity of the specimen. Many rocks, particularly those that are slow-cooled, contain an excessive abundance of large 'multi-domain' particles. When reheated during laboratory experiments, the domain walls of these larger particles shift to new localised energy minima; this causes a lack of reciprocity between cooling and heating blocking temperatures and can lead to substantially biased palaeointensity results.

Various rock magnetic techniques are employed to minimise the use of unsuitable samples in palaeointensity experiments; this includes specimens with a high percentage of multi-domain particles, or those that are prone to thermal or chemical alteration. Despite efforts to select the best quality rock samples, these problems can persist, particularly in non-ideal samples such as those from the Precambrian.

1.4.1 Theory of palaeointensity

The idea of obtaining palaeointensity information using thermally induced magnetisations on rocks and archaeological materials was initially proposed by Folgheraiter (1899). Several decades later, Koenigsberger (1936) developed an experimental protocol in which the NRM could be compared with a laboratory induced TRM. The same fundamental protocol was subsequently adapted by Thellier and Thellier (1959) and has been the subject of many variations since (Section 1.4.2). In addition, many alternative techniques have been developed (Section 1.4.3), all of which compare the characteristic (ChRM) component of the NRM with either a TRM or ARM.

Palaeointensity is made possible because the NRM, which is assumed to be a TRM, acquired by rocks are approximately linearly related to the applied field for low fields such as the Earth's (Néel, 1949). That is, MNRM is proportional to the ancient field (B_{anc}) by some constant (v_{anc}); similarly, M_{lab} is proportional to the laboratory field (B_{lab}) by a constant (v_{lab}). If these two proportionality constants are equal, for which an assumption is made (for pTRMs) that the remanence is carried by non-interacting SD particles (Néel, 1949; Thellier & Thellier, 1959), then the relationships can be arranged:

Eq 1.1

$$B_{anc} = \frac{M_{NRM}}{M_{lab}} \times B_{lab}$$

Equation 1.1 is the basis for obtaining palaeointensity information; however, there are many complications, as previously mentioned. Arguably, the most important step in a palaeointensity study is to determine whether the NRM is of a primary thermal nature, and has not undergone chemical alteration or remagnetisation; i.e., the magnetisation that we are measuring at least has the potential to give us the correct answer.

Palaeomagnetic field tests provide crucial information on the characteristic nature of the NRM; they are the most direct methods for establishing whether rocks retain ancient magnetisation (Graham, 1949). These tests are related to the palaeomagnetic direction, and are designed to determine the timing of the remanent magnetisation relative to their depositional environment. A reliable direction should be associated with a palaeointensity otherwise it cannot be considered as a reliable primary magnetisation. The field tests are briefly described below:

Baked contact test – The country rock immediately adjacent to igneous rocks should be baked during the formation of the igneous rock so that they both acquire a TRM that should agree in direction (and strength). Older country rock, further away, that has not been baked should carry a ChRM that is distinct; this constitutes a pass of the test and suggests that the ChRM is primary.

Conglomerate and fold tests – A random distribution of ChRM directions in conglomerate clasts is evidence that the magnetisation predates the deposition of the conglomerate. This constitutes a positive conglomerate test and provides very strong evidence that the ChRM is primary (Butler, 2004). The fold test exists to determine the timing of NRM relative to local or regional folding events. If palaeomagnetic directions converge after a structural correction is made to the bedding, the magnetisation predates the folding event.

A reversal test can also be performed on the directional data; this is based on the understanding that the time-averaged field for normal and reversed polarity intervals should be antiparallel (180 ° apart). If normal and reversed polarity ChRM averaged directions from a given suite of sites are antiparallel, this indicates that secular variation is adequately averaged during both intervals (Butler, 2004). If the angle is significantly less, then geomagnetic secular variation is likely not averaged; this is useful data but it is important to distinguish between time-averaged and time-instantaneous results.

For palaeointensity, there is an additional requirement to that of obtaining a reliable direction; there must be evidence that the TRM has not been chemically altered; this requires a physical analysis of the magnetic grains. There are several methods that can be used, such as high-resolution scanning electron microscopy (SEM), sensitive high-resolution ion microprobe (SHRIMP), quantum diamond magnetic (QDM) mapping and many more; these are complex disciplines in their own right and are not discussed further here. We focus instead, on palaeointensity, outlining the most common methods and discus how they attempt to overcome the many problems to achieve reliable results.

1.4.2 KTT methods

The Königsberger-Thellier-Thellier (KTT) family of experiments use a step-wise approach to replacing NRM with pTRM. The original Thellier method (Thellier & Thellier, 1959) and its subsequent variations (Aitken et al., 1988; Coe, 1967a; Tauxe & Staudigel, 2004; Yu & Tauxe, 2005) are widely regarded as the most robust of palaeointensity methods. They rely on a set of three assumptions provided by Thellier (1938); the so-called "Thellier's Laws".

The Law of Independence states that a pTRMs acquired between two temperatures are independent (in direction and intensity) of those acquired between any two other temperature steps. If this holds true then so too should the law of additivity, which states that the sum of all pTRMs acquired below T_c should be equal to the total TRM. A third law of Reciprocity assumes that a magnetisation acquired by cooling from a particular temperature is fully replaced by reheating to that same temperature under the same conditions; in other words, the blocking

(T_b) and unblocking (T_{ub}) temperature are identical. However, these assumptions are only valid for SD particles, and break down as individual grain sizes or the interactions between grains increase (e.g., Biggin & Böhnel, 2003; Dunlop & Özdemir, 2001; Xu & Dunlop, 2004).

Advances in technology over the last several decades and improved protocols, have resulted in several variations to the method. We discuss some of these below.

1.4.2.1 The Thellier-Thellier protocol (Thellier and Thellier, 1959)

Referred to as an "II" technique because it uses two in-field heatings for each temperature step. A sample is first heated and cooled to temperature (T_1) in the presence of a B field, imparting a pTRM; this is then repeated under the same conditions, but with the sample positioned so that the field is now antiparallel (–B), thereby imparting a pTRM in the opposite direction. The NRM remaining and the pTRM gained at each temperature step can be determined through vector subtraction and addition respectively. This is then repeated at increasing temperature steps until all of the NRM is replaced by pTRM, and the palaeointensity may be estimated using equation 1.1.

1.4.2.2 The Coe protocol (Coe, 1967a)

Until recently, this was the most commonly used Thellier protocol. Referred to as the 'ZI" method because it heats and cools a sample firstly in a zero-field, and repeats the process in-field for each temperature step T_i. The NRM loss can be measured directly from the "Z" step; the pTRM gained is determined from the "I" step. A modified version of the Coe protocol reversed the steps to "IZ" (Aitken et al. 1988).

A repeated in-field step at lower temperature was introduced (Coe, 1967a, b) to check for chemical alteration by comparing a newly imparted pTRM with the original. These so-called "pTRM checks" meant that the step-wise approach could now repeatedly test for alteration and then limit the temperature at which a palaeointensity is determined according to the amount of alteration that is observed. However, the check only determines the amount of alteration at that temperature step or below; it cannot identify alteration that may have occurred in particles with higher unblocking temperatures. A problem can occur, in which the zero-field step proceeding an in-field step of a Coe experiment causes alteration that is not captured by pTRM checks. This can continue undetected throughout an experiment, causing a shallowing of the palaeointensity slope as the pTRM capacity is increased (Wang & Kent, 2021).

To address this, Wang and Kent (2021) use a "Repeated Thellier-Series Experiment" (RESET), previously known as the MD-correction technique (Wang & Kent, 2013). Here, a repeated experiment uses a synthetic NRM from an imparted TRM to check for changes in NRM unblocking and pTRM acquisition between both experiments. The pTRM gains of each experiment, when plotted together (tTRM check), must be linear and well-correlated in order to satisfy the method. Similarly, the NRM (one is the synthetic NRM) unblocking of both experiments are compared and meet the same requirements. These additional checks can identify alteration that may have been missed by standard pTRM checks. The method also uses this NRM slope as a palaeointensity slope corrected for MD bias (Wang and Kent, 2013, 2021). Since MD tails can accumulate iteratively, a vital criterion for assessing MD effects in this way is to repeat the initial experiment precisely, which includes the exact number and type of steps in an identical order.

At lower temperatures, non-SD particles tend to have reduced capacity to acquire pTRM compared to how capably they demagnetise, causing a concave-up curve in a Coe Arai diagram (Xu & Dunlop, 1995). However, this is not always the case, and their effects can go undetected creating bias in the palaeointensity estimate. A failure of the law of reciprocity results in high and low-temperature pTRM "tails"; a high-temperature tail is a pTRM that is not fully demagnetised reheating in a zero-field to T_b, ($T_{ub} > T_b$) (Shashkanov & Metallova, 1972), whereas the low-temperature tail $T_{ub} < T_b$ (Dunlop & Ozdemir, 2001). Riisager and Riisager (2001) developed the so-called "pTRM tail check" by applying an additional "Z" step, so that the Coe sequence becomes "ZI-Z"; it determines whether the pTRM gained is entirely removed by reheating to the same temperature step in a zero-field. Both the Coe (1967a) and Aitken et al. (1988) variants also show a strong angular dependence on the applied filed resulting from pTRM tails, which can substantially affect the outcome of results (Yu et al., 2004).

With the introduction of the Arai diagram (e.g., Figure 1.4; Nagata et al., 1963), the visualisation and assessment of palaeointensity slope linearity and pTRM checks could be achieved by plotting NRM lost against pTRM gained at each temperature step.

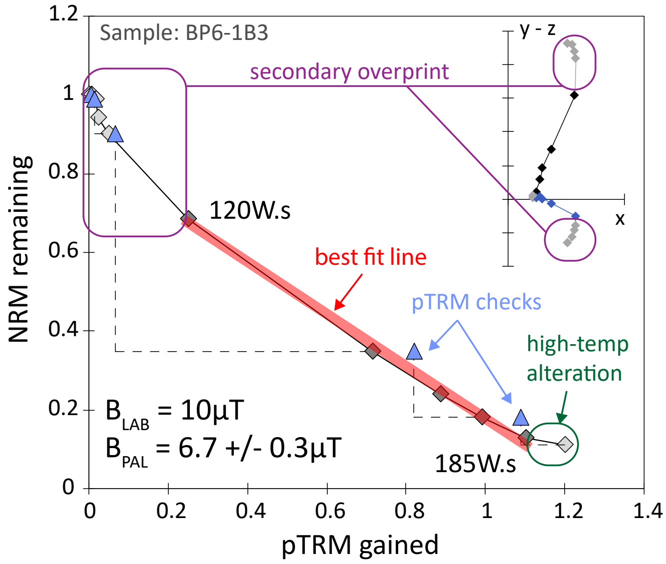

Figure 1.4. Example of an Arai diagram (Nagata et al., 1963) used in the analysis of a Thellier-style experiment (the sample shown is from data in chapter 4). Associated palaeomagnetic directions are shown in an orthogonal plot (top right). The best-fit slope (red) for the calculation of B_{pal} (Palaeointensity) is determined from the selected points (dark grey) and are interpreted to represent the primary magnetisation. pTRM checks (blue triangles) test for alteration. A secondary (viscous) overprint from a slightly stronger ambient field is highlighted in the low blocking temperature area and in the orthogonal plot (purple). High temperature laboratory induced alteration is interpreted to produce a change in slope in the high blocking temperature region (green).

1.4.2.3 The IZZI protocol (Tauxe and Staudigel, 2004)

Here, the "ZI" of Coe (1967a) and the "IZ" of Aitken et al. (1988) are combined, somewhat misleadingly according to the protocol name, in the sequence "ZIIZP", with "P" being a pTRM check (Figure 1.5). It is the component magnitudes of the Z-I and I-Z pairs of steps that are plotted together to make a single point on the Arai diagram (Figure 1.4).

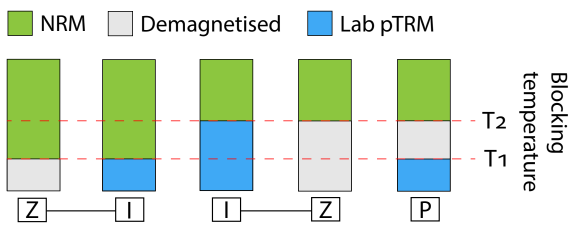

Figure 1.5. Schematic diagram for the IZZI protocol. Z, zero-field step; I, infield step; P, pTRM

check (infield). Z-I pairs of steps are heated to the same temperature (joined by a horizontal line).

This method easily detects the angular dependence on the applied field, and negates the need for a pTRM tail check. This is because the tails influence the two sets of alternating ZI and IZ steps independently, creating a zigzag effect on the Arai diagram that is proportional to size of pTRM tails (Yu & Tauxe, 2005).

1.4.2.4 Data analysis

A prominent two-slope phenomenon can occur in "IZZI" Arai diagrams (and other protocols) that may not be due to MD effects. If the break in slope corresponds to a change in the direction of the recorded field, then this may be explained as the cause, provided that the associated palaeointensity values of both slopes are Earth-like. Where no change in direction is observed, interpretation becomes more difficult. Historically, palaeointensity values have been accepted from the lower temperature slopes with the logic that this approach should avoid high temperature alteration (e.g., Thomas & Piper, 1992, 1995; Thomas, 1993). This can result in an over-estimation of the field strength; whereas, accepting high-temperature segments of two-slope Aria diagrams can result in under-estimation. High-temperature segments are generally favoured more recently due to the association with more stable remanence; however, further justification is necessary to accept such results. For example, if similar results are obtained from single-slope Arai diagrams or from different palaeointensity techniques, alongside rock magnetic evidence to support the results. The lack of pTRM acquisition corresponding to significant NRM loss at low temperatures is not well understood; it may be due to an annealing effect (Kosterov & Prévot, 1998), lightening induced IRM or some other rock magnetic effect.

A new method of analysing KTT data is the so-called Bias Corrected Estimation of Paleointensity (BiCEP; Cych et al., 2021). Rather than using what the authors describe as binary selection criteria to determine between "good" and "bad" data, a Bayesian approach is used to consider all data. Results are compared to a model which assumes a linear relationship between a samples palaeointensity estimate and its Arai diagram linearity (as defined by the k′ parameter; Paterson, 2011). The Bayesian method for calculating k′ also provides an uncertainty for the zigzagging Arai diagram produced in an IZZI experiment. This new way of statistically analysing KTT palaeointensity results does not affect the experimental procedure and can be compared against the more standard data analyses that use a set of selection criteria to produce an overall more robust set of results.

When assessing the quality of a palaeointensity estimate from an Arai diagram, linearity is of strict importance. A recent study identified a phenomenon, whereby a curved Arai diagram, after receiving a fresh TRM in a repeated experiment, is not reproducible (became straight); so-called "Fragile curvature". This was followed by a subsequent growth of curvature in aged TRM experiments over two years (Santos & Tauxe, 2019; Tauxe et al., 2021). This is very different to the curvature resulting from MD particles, which are reproducible. The cause of this fragility requires further explanation.

It should be noted that linearity does not guarantee a reliable palaeointensity estimate. It is experimentally possible for a CRM to produce a linear Arai diagram (Kono, 1987); stringent checks for alteration should therefore remain in place. Linear Arai diagrams that consist of (T)CRM can be explained by the strong magnetic interactions that form between the new magnetic particles, randomly modifying their intrinsic blocking/unblocking temperatures (Draeger et al., 2006).

1.4.3 Other methods

1.4.3.1 Microwave method

The Geomagnetism Laboratory at the University of Liverpool operates a Triston microwave palaeointensity system with low-temperature SQUID magnetometer (Suttie et al., 2010). Demagnetisation of a sample occurs by ferromagnetic resonance, in which a high frequency (~14.5 GHz) microwave field couples with the magnetic system within the sample, producing magnons (quasi-particles associated with spin waves) which demagnetise the sample as the energy is increased (Hill et al., 2002). The magnetic minerals are excited directly, avoiding significant heating to the sample matrix. This has been demonstrated to have the effect of reducing thermal alteration during palaeointensity experiments in both natural rock samples and archaeological material (e.g., Casas et al., 2005; Hill et al., 2002, 2005). All of the same previously mentioned thermal Thellier protocols can be used, producing similar results to those from thermal Thellier-style experiments (Biggin et al., 2007; Grappone et al., 2019).

1.4.3.2 Shaw method

The Shaw-DHT (LTD) method compares the stepwise AF demagnetisation of NRM with that of a laboratory induced TRM. It uses ARM to measure the amount of alteration and uses this to apply a correction to the palaeointensity slope. This method has a full chapter (3) devoted to it.

1.4.3.3 Multi-specimen method

Another common palaeointensity method is the multi-specimen method (MSP-DB; Dekkers & Böhnel, 2006). This method uses multiple specimens to determine a single palaeointensity, and firstly requires that all specimens are heated to a temperature that removes any viscous component (T_v), as determined in a sister specimen, to leave only the natural remanent magnetisation. A single heating is then applied, to a chosen temperature $T_v < T < T_c$, in multiple specimens, applying a different bias field to each specimen. The single heating reduces the potential for thermo-chemical alteration; however, it should still be able to sufficiently unblock a significant fraction of the NRM. By overprinting the original NRM by different amounts in each specimen, the field at which the overprinted remanence is equal to the original NRM can be determined statistically. An additional heating is applied to T_v, in order to test for alteration.

A fraction-corrected (MSP-FC) variation corrects for the fraction of NRM used in the best-fit slope of the individual MSP plot, in order to reduce the overall scatter. Additionally, the original method has been shown to overestimate the field where MD particles are present and $T_b \neq T_{ub}$ (Fabian & Leonhardt, 2007). As a result, Fabian and Leonhardt (2010) developed a domain-state corrected (MSP-DSC) variation of the method. Here, the domain-state bias is estimated by imparting and comparing a series of additional pTRMs to T_1, including in a field that is antiparallel (-B) to the initial in-field pTRM. The domain-state correction is based on the relative size of pTRM tails using individual magnetisations and susceptibilities of TRM acquisition, based on a phenomenological model.

1.4.3.4 Pseudo-Thellier method

Where thermal alteration is too difficult to overcome, the Pseudo-Thellier (PsT) method can be utilised to produce results, since it does not require any heating. It was designed for basalts with low Ti magnetite, and originally constructed as a method of obtaining relative palaeointensities (Tauxe et al., 1995); it has since been possible to convert results into an absolute palaeointensity method by means of a calibration factor (de Groot et al., 2013, 2016; Paterson et al., 2016; Yu, 2010). The NRM is AF demagnetised, after which a stepwise ARM acquisition (ARM_{AQ}) is applied using the same coercivity steps; the fully acquired ARM is then demagnetised. The ARM acquisition and demagnetisation are plotted together to determine the reciprocity of coercivity; these should produce a linear, unit slope. The pseudo-Thellier slope is derived from NRM/ARM_{AQ}.

A strong grain-size dependence exists in the ratio of TRM/ARM which affects the PsT slope, particularly in grain sizes 0.1 - 1 μm (Dunlop & Argyle, 1997; Yu et al., 2003). As a result, a grain size indicator was established as a selection criterion by de Groot et al. (2013); defined as the magnitude of the AF for which half of the maximum ARM is imparted ($B_{1/2}$ ARM). Comparing the ratio of PsT slopes and expected palaeointensities with $B_{1/2}$ ARM, determined that the optimal range for $B_{1/2}$ ARM is 23 – 63 mT (de Groot et al., 2013). There are fundamentally different methods for calibrating the results to produce an absolute palaeointensity. Arguably, the most well-established method of calibration defines a linear relationship between PsT slopes and palaeointensity results from thermal methods (de Groot et al., 2013, 2015, 2016). The resultant straight-line equation, which is based on using an ARM bias field of 40 μT, has been refined in the latter study to:

Eq 1.2

$$B_{anc} = 7.718\ x \mid slope_{PsT} \mid + 14.6$$

The reliability of the calibration relation has not yet been established for weak intensities of less than ~24 μT; furthermore, it is the nonlinear relationship towards lower intensities that is suggested to explain the non-zero y-axis intercept. Paterson et al. (2016) proposed a new calibration that resolves the non-zero intercept, whilst providing an accurate estimate of the associated uncertainties. Thermally stable samples were given full TRMs in different DC bias fields; the PsT results were plotted against the TRM field strength, where various rock magnetic parameters and best line fits were considered, including grain size to determine a generalised calibration factor of 3.28 (± 0.83) to be used with any ARM bias field (Paterson et al., 2016), noting that additional studies are needed to determine the influence of ARM bias field. Yu (2010) similarly determines a calibration factor using the ratio of susceptibilities χNRM/

χARM for a group of samples, such that:

Eq 1.3

$$\frac{\chi_{NRM}}{\chi_{ARM}} = \frac{M_{NRM}/B_{anc}}{M_{ARM}/B_{ARM}} = 2.6\ (\pm 1.32)$$

Rearranged to solve for B_{anc}:

Eq 1.4

$$B_{anc} = B_{ARM}\ x\ \frac{M_{NRM}/M_{ARM}}{2.6}$$

1.4.3.5 Single crystal palaeointensity (SCP) technique

Palaeointensity experiments on single crystals have become increasingly popular during the last two decades. Zircon crystals, which house magnetite inclusions, are resistant to chemical alteration and can be dated using radiometric methods (Tarduno et al., 2014). Magnetic inclusions within plagioclase and quartz crystals can also be suitable for palaeointensity experiments (Kato et al., 2018). Several types of palaeointensity techniques can be adapted for use, e.g., KTT and Shaw; however, a specialised holder is required in order to accurately maintaining a specimen's position, owing to the small size (~5mm once they are mounted).

SCP using zircons have been found to accurately recover the palaeointensity when compared with high precision whole rock results from the 767 ka Bishop Tuff (Fu et al., 2017). However, quantum diamond magnetic (QDM) mapping identified that the bulk of remanent magnetisation was carried by apatite inclusions which can be susceptible to alteration. This emphasises the importance of careful characterisation of the magnetic carrier and their primary nature.

The SCP method has been used on the Jack Hills Hadean-zircon bearing rocks, located in Western Australia; which are argued to contain some of the oldest palaeointensity recorders on Earth (Tarduno et al., 2015, 2020). Weiss et al. (2015) argued that the Jack Hills Hadean-zircon bearing rocks at Erawandoo Hill were either completely remagnetised, or lacked stable magnetisation; however, these findings were strongly disputed (Bono et al., 2016).

1.4.4 Multi-method approach

Several of the experimental problems outlined may be mitigated by a departure from the traditional, single palaeointensity method (usually a variant of the Thellier-Thellier method) approach, and instead utilised multiple methods. Higher success rates have attributed to this multi-technique approach (e.g., de Groot et al., 2016; Thallner et al., 2021), and similar results achieved using different methods are arguably more robust. Reliance on a single method can result in success rates so small that they are not of value.

In this thesis, we focus on the first three methods outlined; the Multi-specimen and Pseudo-Thellier methods do not form part of this research because only a limited number of the ancient specimens were available to study, many of which carried large overprints. The Pseudo-Thellier method was also not performed because many of the palaeointensities reported in this thesis are less than 10 μT. In addition, large uncertainties of up to ~25 % may be associated with the calibration factor required to convert the relative results to absolute palaeointensities (Paterson et al., 2016).

1.5 References cited

Aitken, M. J., Allsop, A. L., Bussell, G. D., & Winter, M. B. (1988). Determination of the intensity of the Earth's magnetic field during archaeological times: Reliability of the Thellier technique. *Reviews of Geophysics*, *26*(1), 3–12.

Banjeree, S. K. (1971). New Grain Size Limits for Palaeomagnetic Stability in Haematite. *Nature Physical Science*, *232*, 15–16.

Biggin, A. J., & Böhnel, H. N. (2003). A method to reduce the curvature of Arai plots produced during Thellier palaeointensity experiments performed on multidomain grains. *Geophysical Journal International*, *155*(3). https://doi.org/10.1111/j.1365-246X.2003.02089.x

Biggin, A. J., Piispa, E. J., Pesonen, L. J., Holme, R., Paterson, G. A., Veikkolainen, T., & Tauxe, L. (2015). Palaeomagnetic field intensity variations suggest Mesoproterozoic inner-core nucleation. *Nature*, *526*(7572), 245–248. https://doi.org/10.1038/nature15523

Biggin, Andrew J., Perrin, M., & Shaw, J. (2007). A comparison of a quasi-perpendicular method of absolute palaeointensity determination with other thermal and microwave techniques. *Earth and Planetary Science Letters*, *257*(3–4), 564–581. https://doi.org/10.1016/j.epsl.2007.03.016

Bono, R. K., Tarduno, J. A., & Cottrell, R. D. (2016). Comment on: Pervasive remagnetization of detrital zircon host rocks in the Jack Hills, Western Australia and implications for records of the early dynamo. *Earth and Planetary Science Letters*, *450*, 406–408. https://doi.org/10.1016/j.epsl.2016.06.006

Bono, R. K., Tarduno, J. A., Nimmo, F., & Cottrell, R. D. (2019). Young inner core inferred from Ediacaran ultra-low geomagnetic field intensity. *Nature Geoscience*, *12*(2), 143–147. https://doi.org/10.1038/s41561-018-0288-0

Butler, R. (2004). Paleomagnetism : Magnetic Domains to Geologic Terranes. *Blackwell Science Inc.*

Casas, L., Shaw, J., Gich, M., & Share, J. A. (2005). High-quality microwave archaeointensity determinations from an early 18th century AD English brick kiln. *Geophysical Journal International*, *161*(3), 653–661. https://doi.org/10.1111/j.1365-246X.2005.02631.x

Coe, R. S. (1967a). Paleo-intensities of the Earth's magnetic field determined from Tertiary and Quaternary rocks. *Journal of Geophysical Research*, *72*(12), 3247–3262. https://doi.org/10.1029/jz072i012p03247

Coe, R. S. (1967b). The Determination of Paleo-Intensities of the Earth's Magnetic Field with Emphasis on Mechanisms Which Could Cause Non-Ideal Behavior in Thellier's Method. *Journal of Geomagnetism and Geoelectricity*, *19*(3), 157–179. https://doi.org/10.5636/jgg.19.157

Collinson, D. W. (1983). Methods in Rock Magnetism and Palaeomagnetism. Techniques and Instrumentation. xiv+503 pp., numerous figs. London: Chapman & Hall. *Geological Magazine*, *121*(3), 258. https://doi.org/DOI: 10.1017/S0016756800028375

Cych, B., Morzfeld, M., & Tauxe, L. (2021). Bias Corrected Estimation of Paleointensity (BiCEP): An Improved Methodology for Obtaining Paleointensity Estimates. *Geochemistry, Geophysics, Geosystems*, *22*(8), 1–25. https://doi.org/10.1029/2021gc009755

Day, R., Fuller, M., & Schmidt, V. A. (1977). Hysteresis properties of titanomagnetites: Grain-size and compositional dependence. *Physics of the Earth and Planetary Interiors*, *13*(4), 260–267. https://doi.org/10.1016/0031-9201(77)90108-X

Dekkers, M. J., & Böhnel, H. N. (2006). Reliable absolute palaeointensities independent of magnetic domain state. *Earth and Planetary Science Letters*, *248*(1–2), 508–517. https://doi.org/10.1016/j.epsl.2006.05.040

Draeger, U., Prévot, M., Poidras, T., & Riisager, J. (2006). Single-domain chemical, thermochemical and thermal remanences in a basaltic rock. *Geophysical Journal International*, *166*(1), 12–32. https://doi.org/10.1111/j.1365-246X.2006.02862.x

Dunlop, D. J., & Özdemir, Ö. (1997). Rock Magnetism. Fundamentals and Frontiers. Cambridge Studies in Magnetism. *Geological Magazine*, *135*(2), 287–300. https://doi.org/DOI:10.1017/S0016756898218437

Dunlop, D. J., & Özdemir, Ö. (2001). Beyond Néel's theories: Thermal demagnetization of narrow-band partial thermoremanent magnetizations. *Physics of the Earth and Planetary Interiors*, *126*(1–2), 43–57. https://doi.org/10.1016/S0031-9201(01)00243-6

Dunlop, D J, & Özdemir, Ö. (2015). 5.08 - Magnetizations in Rocks and Minerals. In G. B. T.-T. on G. (Second E. Schubert (Ed.) (pp. 255–308). Oxford: Elsevier. https://doi.org/https://doi.org/10.1016/B978-0-444-53802-4.00102-0

Dunlop, David J., & Argyle, K. S. (1997). Thermoremanence, anhysteretic remanence and susceptibility of submicron magnetites: Nonlinear field dependence and variation with grain size. *Journal of Geophysical Research: Solid Earth*, *102*(B9), 20199–20210. https://doi.org/10.1029/97jb00957

Fabian, K., & Leonhardt, R. (2007). Theoretical analysis and experimental tests of multiple specimen absolute paleointensity determination techniques. *Geophysical Research Abstracts*, (GU2007-A-04510.).

Fabian, Karl, & Leonhardt, R. (2010). Multiple-specimen absolute paleointensity determination: An optimal protocol including pTRM normalization, domain-state correction, and alteration test. *Earth and Planetary Science Letters*, *297*(1–2), 84–94. https://doi.org/10.1016/j.epsl.2010.06.006

Fabian, Karl, & Shcherbakov, V. P. (2018). Energy barriers in three-dimensional micromagnetic models and the physics of thermoviscous magnetization. *Geophysical Journal International*, *215*(1), 314–324. https://doi.org/10.1093/gji/ggy285

Folgheraiter, G. (1899). Ricerche sull'inclinazione magnetica nel I sec. a.C. e nel I sec. dell'era volgare calcolata dai vasi fittili di Arezzo e Pompei. *Reports of the Regia Accademia Dei Lincei*, *5(8)*, 176–188.

Fu, R. R., Weiss, B. P., Lima, E. A., Kehayias, P., Araujo, J. F. D. F., Glenn, D. R., et al. (2017). Evaluating the paleomagnetic potential of single zircon crystals using the Bishop Tuff. *Earth and Planetary Science Letters*, *458*, 1–13. https://doi.org/10.1016/j.epsl.2016.09.038

Graham, J. W. (1949). The Stability and Significance of Magnetism in Sedimentary Rocks. *Journal of Geophysical Research*, *51*.

Grappone, J. M., Biggin, A. J., & Hill, M. J. (2019). Solving the mystery of the 1960 Hawaiian lava flow: Implications for estimating Earth's magnetic field. *Geophysical Journal International*, *218*(3), 1796–1806. https://doi.org/10.1093/gji/ggz252

de Groot, L. V., Biggin, A. J., Dekkers, M. J., Langereis, C. G., & Herrero-Bervera, E. (2013). Rapid regional perturbations to the recent global geomagnetic decay revealed by a new hawaiian record. *Nature Communications*, *4*, 1–7. https://doi.org/10.1038/ncomms3727

de Groot, Lennart V., Béguin, A., Kosters, M. E., van Rijsingen, E. M., Struijk, E. L. M., Biggin, A. J., et al. (2015). High paleointensities for the Canary Islands constrain the Levant geomagnetic high. *Earth and Planetary Science Letters*, *419*, 154–167. https://doi.org/10.1016/j.epsl.2015.03.020

de Groot, Lennart V., Pimentel, A., & Di Chiara, A. (2016). The multimethod palaeointensity approach applied to volcanics from Terceira: Full-vector geomagnetic data for the past 50 kyr. *Geophysical Journal International*, *206*(1), 590–604. https://doi.org/10.1093/gji/ggw095

de Groot, Lennart V., Fabian, K., Bakelaar, I. A., & Dekkers, M. J. (2014). Magnetic force microscopy reveals meta-stable magnetic domain states that prevent reliable absolute palaeointensity experiments. *Nature Communications*, *5*. https://doi.org/10.1038/ncomms5548

Harrison, R. J., Zhao, X., Hu, P., Sato, T., Heslop, D., Muxworthy, A. R., et al. (2019). Simulation of Remanent, Transient, and Induced FORC Diagrams for Interacting Particles With Uniaxial, Cubic, and Hexagonal Anisotropy. *Journal of Geophysical Research: Solid Earth*, *124*(12), 12404–12429. https://doi.org/10.1029/2019JB018050

Hill, M. J., Gratton, M. N., & Shaw, J. (2002). A comparison of thermal and microwave palaeomagnetic techniques using lava containing laboratory induced remanence. *Geophysical Journal International*, *151*(1), 157–163. https://doi.org/10.1046/j.1365-246X.2002.01745.x

Hill, M. J., Shaw, J., & Herrero-Bervera, E. (2005). Palaeointensity record through the Lower Mammoth reversal from the Waianae volcano, Hawaii. *Earth and Planetary Science Letters*, *230*(3–4), 255–272. https://doi.org/10.1016/j.epsl.2004.11.012

Kato, C., Sato, M., Yamamoto, Y., Tsunakawa, H., & Kirschvink, J. L. (2018). Paleomagnetic studies on single crystals separated from the middle Cretaceous Iritono granite. *Earth, Planets and Space*, *70*(1). https://doi.org/10.1186/s40623-018-0945-y

Koenigsberger, J. G. (1936). Die Abhängigkeit der natürlichen remanenten Magnetisierung bei Eruptivgesteinen von deren Alter und Zusammensetzung. *Beitr. Angew. Geophys*, *5*, 193–246.

Kono, M. (1987). Changes in TRM and ARM in a basalt due to laboratory heating. *Physics of the Earth and Planetary Interiors*, *46*(1–3), 1–8. https://doi.org/10.1016/0031-9201(87)901671

Kosterov, A. A., & Prévot, M. (1998). Possible mechanisms causing failure of Thellier palaeointensity experiments in some basalts. *Geophysical Journal International*, *134*(2), 554–572. https://doi.org/10.1046/j.1365-246X.1998.00581.x

Leonhardt, R. (2006). Analyzing rock magnetic measurements: The RockMagAnalyzer 1.0 software. *Computers and Geosciences*, *32*(9), 1420–1431. https://doi.org/10.1016/j.cageo.2006.01.006

Mayergoyz, I. D. (1986). Mathematical Models of Hysteresis. *Physical Review Letters*, *56*(15), 1518–1521. https://doi.org/10.1103/PhysRevLett.56.1518

McCausland, P. J. A., Van der Voo, R., & Hall, C. M. (2007). Circum-Iapetus paleogeography of the Precambrian-Cambrian transition with a new paleomagnetic constraint from Laurentia. *Precambrian Research*, *156*(3–4), 125–152. https://doi.org/10.1016/j.precamres.2007.03.004

McClelland, E. (1996). Theory of CRM acquired by grain growth, and its implications for TRM discrimination and palaeointensity determination in igneous rocks. *Geophysical Journal International*, *126*(1), 271–280. https://doi.org/https://doi.org/10.1111/J.1365-246X.1996.TB05285.X

Moskowitz, B. M. (1981). Methods for estimating Curie temperatures of titanomaghemites from experimental Js-T data. *Earth and Planetary Science Letters*, *53*(1), 84–88. https://doi.org/10.1016/0012-821X(81)90028-5

Muxworthy, A. R., & Williams, W. (2006). Critical single-domain/multidomain grain sizes in noninteracting and interacting elongated magnetite particles: Implications for magnetosomes. *Journal of Geophysical Research: Solid Earth*, *111*(12), 3–9. https://doi.org/10.1029/2006JB004588

Nagata, T., Arai, Y., & Momose, K. (1963). Secular Variation of the Geomagnetic Total Force during the Last 5000 Years. *Journal of Geophysical Research*, *68*(18), 5277–5281. https://doi.org/10.1029/j.2156-2202.1963.tb00005.x

Nagy, L., Williams, W., Muxworthy, A. R., Fabian, K., Almeida, T. P., Conbhuí, P., & Shcherbakov, V. P. (2017). Stability of equidimensional pseudo–single-domain magnetite over billion-year timescales. *Proceedings of the National Academy of Sciences of the United States of America*, *114*(39), 10356–10360. https://doi.org/10.1073/pnas.1708344114

Nagy, L., Williams, W., Tauxe, L., & Muxworthy, A. R. (2019). From Nano to Micro: Evolution of Magnetic Domain Structures in Multidomain Magnetite. *Geochemistry, Geophysics, Geosystems*, *20*(6), 2907–2918. https://doi.org/10.1029/2019GC008319

Néel, L. (1949). Théorie du traînage magnétique des ferromagnétiques en grains fins avec application aux terres 5 cuites. *Annals de Géophysique*, *5*(2), 99–136.

Nikolaisen, E. S., Harrison, R. J., Fabian, K., & McEnroe, S. A. (2020). Hysteresis of Natural Magnetite Ensembles: Micromagnetics of Silicate-Hosted Magnetite Inclusions Based on Focused-Ion-Beam Nanotomography. *Geochemistry, Geophysics, Geosystems*, *21*(11), 1–20. https://doi.org/10.1029/2020GC009389

Paterson, G. A., Heslop, D., & Pan, Y. (2016). The pseudo-Thellier palaeointensity method: New calibration and uncertainty estimates. *Geophysical Journal International*, *207*(3), 1596–1608. https://doi.org/10.1093/gji/ggw349

Petrovský, E. D., & Kapička, A. (2006). On determination of the Curie point from thermomagnetic curves. *Journal of Geophysical Research: Solid Earth*, *111*(12), 1–10. https://doi.org/10.1029/2006JB004507

Roberts, A. P., Heslop, D., Zhao, X., & Pike, C. R. (2014). Understanding fine magnetic particle systems through use of first-order reversal curve diagrams. *Reviews of Geophysics*, *52*, 557–602. https://doi.org/10.1029/88EO01108

Santos, C. N., & Tauxe, L. (2019). Investigating the Accuracy, Precision, and Cooling Rate Dependence of Laboratory-Acquired Thermal Remanences During Paleointensity Experiments. *Geochemistry, Geophysics, Geosystems*, *20*(1), 383–397. https://doi.org/10.1029/2018GC007946

Shashkanov, V. A., & Metallova, V. V. (1972). Violation of Thellier's law for partial thermoremanent magnetizations. *Izv. Akad. Nauk SSSR, Fiz. Zemli*, *3*(3), 80–86.

Suttie, N., Shaw, J., & Hill, M. (2010). Direct demonstration of microwave demagnetization of a whole rock sample with minimal heating. *Earth and Planetary Science Letters*, *292*, 357–362. https://doi.org/10.1016/j.epsl.2010.02.002

Tarduno, J. A., Cottrell, R. D., Davis, W. J., Nimmo, F., & Bono, R. K. (2015). A Hadean to Paleoarchean geodynamo recorded by single zircon crystals. *Science*, *349*(6247), 521–524.

Tarduno, J. A., Cottrell, R. D., Watkeys, M. K., Hofmann, A., Doubrovine, P. V., Mamajek, E. E., et al. (2010). Geodynamo, solar wind, and magnetopause 3.4 to 3.45 billion years ago. *Science*, *327*(5970), 1238–1240. https://doi.org/10.1126/science.1183445

Tarduno, J. A., Blackman, E. G., & Mamajek, E. E. (2014). Detecting the oldest geodynamo and attendant shielding from the solar wind: Implications for habitability. *Physics of the Earth and Planetary Interiors*, *233*, 68–87. https://doi.org/10.1016/j.pepi.2014.05.007

Tarduno, J. A., Cottrell, R. D., Bono, R. K., Oda, H., Davis, W. J., Fayek, M., et al. (2020). Paleomagnetism indicates that primary magnetite in zircon records a strong Hadean geodynamo. *Proceedings of the National Academy of Sciences of the United States of America*, *117*(5), 2309–2318. https://doi.org/10.1073/pnas.1916553117

Tauxe, L., Pick, T., & Kok, Y. S. (1995). Relative paleointensity in sediments: A Pseudo-Thellier Approach. *Geophysical Research Letters*, *22*(21), 2885–2888. https://doi.

org/10.1029/95GL03166

Tauxe, L., Santos, C. N., Cych, B., Zhao, X., Roberts, A. P., Nagy, L., & Williams, W. (2021). Understanding Nonideal Paleointensity Recording in Igneous Rocks: Insights From Aging Experiments on Lava Samples and the Causes and Consequences of "Fragile" Curvature in Arai Plots. *Geochemistry, Geophysics, Geosystems*, *22*(1), 1–24. https://doi.org/10.1029/2020GC009423

Tauxe, L., & Staudigel, H. (2004). Strength of the geomagnetic field in the cretaceous normal superchron: New data from submarine basaltic glass of the troodos ophiolite. *Geochemistry, Geophysics, Geosystems*, *5*(2). https://doi.org/10.1029/2003GC000635

Tauxe, L., Banerjee, S. K., Butler, R. L., & Voo, R. Van Der. (2008). Essentials of Rock and Paleomagnetism, 496. Retrieved from http://www.amazon.com/Essentials-Paleomagnetism-Lisa-Tauxe/dp/0520260317

Thallner, D., Biggin, A. J., & Halls, H. C. (2021). An extended period of extremely weak geomagnetic field suggested by palaeointensities from the Ediacaran Grenville dykes (SE Canada). *Earth and Planetary Science Letters*, *568*, 117025. https://doi.org/10.1016/j.epsl.2021.117025

Thellier, E., & Thellier, O. (1959). Sur l'intensité du champ magnétique terrestre dans le passé historique et géologique. *Annales de Géophysique*, *15*, 285–376.

Thomas, D. N., & Piper, J. D. A. (1992). A revised magnetostratigraphy for the Mid-Proterozoic Gardar lava succession, South Greenland. *Tectonophysics*. https://doi.org/10.1016/0040-1951(92)90172-3

Thomas, N. (1993). An integrated rock magnetic approach to the selection or rejection of ancient basalt samples for palaeointensity experiments. *Physics of the Earth and Planetary Interiors*, *75*(4), 329–342. https://doi.org/10.1016/0031-9201(93)90008-W

Wang, H., & Kent, D. V. (2013). A paleointensity technique for multidomain igneous rocks.

Geochemistry, Geophysics, Geosystems, *14*(10), 4195–4213. https://doi.org/10.1002/ggge.20248

Wang, H., & Kent, D. V. (2021). RESET: A Method to Monitor Thermoremanent Alteration in Thellier-Series Paleointensity Experiments. *Geophysical Research Letters*, *48*(5), 1–10. https://doi.org/10.1029/2020GL091617

Weiss, B. P., Maloof, A. C., Tailby, N., Ramezani, J., Fu, R. R., Hanus, V., et al. (2015). Pervasive remagnetization of detrital zircon host rocks in the Jack Hills, Western Australia and implications for records of the early geodynamo. *Earth and Planetary Science Letters*, *430*, 115–128. https://doi.org/10.1016/j.epsl.2015.07.067

Xu, S., & Dunlop, D. J. (1995). Towards a better understanding of the Lowrie-Fuller test. *Journal of Geophysical Research*, *100*, 533–542.

Xu, Song, & Dunlop, D. J. (2004). Thellier paleointensity theory and experiments for multidomain grains. *Journal of Geophysical Research: Solid Earth*, *109*(7), 1–13. https://doi.org/10.1029/2004JB003024

Yu, Y. (2010). Paleointensity determination using anhysteretic remanence and saturation isothermal remanence. *Geochemistry, Geophysics, Geosystems*, *11*(2), 1–12. https://doi.org/10.1029/2009GC002804

Yu, Y., & Tauxe, L. (2005). Testing the IZZI protocol of geomagnetic field intensity determination. *Geochemistry, Geophysics, Geosystems*, *6*(5). https://doi.org/10.1029/2004GC000840

Yu, Y., Dunlop, D. J., & Özdemir, Ö. (2003). Are ARM and TRM analogs? Thellier analysis of ARM and pseudo-Thellier analysis of TRM. *Earth and Planetary Science Letters*, *205*(3–4), 325–336. https://doi.org/10.1016/S0012-821X(02)01060-9

Zossi, B., Fagre, M., Amit, H., & Elias, A. G. (2019). Polar caps during geomagnetic polarity reversals. *Geophysical Journal International*, *216*(2), 1334–1343. https://doi.org/10.1093/gji/ggy494

Chapter 2

Extended background

2.1 Introduction

It had long been understood that the source of Earth's magnetic field is within its centre (Gilbert, 1600). A significant advance in our understanding came in 1839 thanks to Carl Friedrich Gauss, who was able to model Earth's magnetic field using spherical harmonic analysis (Gauss, 1839), and who's principles are still used in present-day geomagnetic field models. Earth's core was first discovered by R. D. Oldham after identifying a seismic discontinuity (using P waves) at the core mantle boundary (CMB) in 1906. It took twenty years to establish that the core was liquid (Jeffreys, 1926); this was further confirmed along with the discovery of a solid inner core in 1936 by Inge Lehmann (Brush, 1980).

It is now understood that the geomagnetic field is generated by self-sustaining dynamo process which was first proposed by Joseph Larmor in 1920. The geodynamo process responsible for generating the magnetic field is powered in Earth's convecting, rotating outer core, and is driven by the motion of electrically-conducting liquid iron. There are many thermal and chemical processes that are intrinsically linked to this process, many of which have varied in degree over the course of Earth history.

It is generally accepted that some sort of geodynamo process has existed for most of Earth history, with evidence for a geomagnetic field dating back to ~3.4 Ga (Biggin et al., 2011) and possibly 4.2 Ga (Tarduno et al., 2015). The early geodynamo, prior to the onset of inner core nucleation (ICN), was most likely enabled purely by thermal convection (Gubbins et al., 2004; Lister & Buffett, 1995). Early core temperatures allowed for rapid cooling from within, and this was controlled by the temperature gradients in the liquid core and across the core-mantle boundary (CMB).

The cooling continued until conditions were reached that enabled a phase change in the liquid core, facilitating the nucleation of an inner core. Its formation brought about substantial change in conditions, bringing about new forces to drive the geodynamo. As the liquid iron solidifies and grows, lighter elements are released into the outer core, these more buoyant elements rise through the outer core and generate compositional convection. In addition to this, latent heat is released during the phase change, also acting to provide buoyancy. A combination of slow cooling and solidification of the inner core then results in thermo-chemical convection. Unlike in the mantle, chemically-driven convection is more efficient than thermally-driven convection and becomes the dominant driving force (Davies et al., 2015; Labrosse, 2003). This is due in part to the difference in thermal diffusivity; heat conducts very slowly in the mantle whereas adiabatic heat flow in the outer core is very large which makes thermal convection far less efficient than in mantle. The density difference across the inner core boundary (ICB) dictates the energy provided by compositional convection, however, this is poorly constrained (Hirose et al., 2013; Labrosse, 2015).

The enigmatic age of the solid inner core is determined by a series of hierarchical events and processes which start with the formation of the Earth and its core. Models which seek to define the Earth's thermal history and timing of ICN are governed largely by the entropy balance within the core, which must adhere to several thermodynamical constraints (Labrosse et al 2003). The additional forces associated with arrival of the inner core substantially increase entropy production in the outer core; because CMB heat flow is essentially fixed over short timescales, limited by how fast the mantle can extract heat, the additional entropy can drive the geodynamo (Nimmo, 2015).

In this chapter, we examine the conditions and processes that have taken place in earth's core and how these affect the geodynamo, and ultimately ICN. We use the most up-to-date set of palaeointensity observations, taken from the PINT database (Biggin et al., 2015), to describe the geomagnetic field through time and examine how this can inform on core conditions. Estimates for ICN are examined by comparing the latest observational-based statistical models and those based on numerical geodynamo simulations, exploring any correlations and/ or contradictions.

2.2 The Earth's core

2.2.1 Formation

The Earth formed through accretion within a period of ~50 Myrs from solar system formation; a process that occurred through a series impact events (Rubie et al., 2004). Gravitational energy caused the differentiation of elements according to their density, into a metallic core and silicate mantle. Processes such as percolation and diapirism would facilitate differentiation of siderophile elements, which eventually partition into a central core. Geochemistry identifies these siderophile elements as depleted in the mantle by comparing element abundances to chondrites (Walter et al., 2000).

It has generally been considered that metal-silicate separation took place at the bottom of a global magma ocean (Rubie et al., 2003). However, alternative models suggest that a large collision event may have produced the magma ocean (Tonks & Melosh, 1992). Large collision events, such as that which is believed to have led to the formation of the moon, would increase temperatures and cause melting on a very large-scale. The energy to achieve the temperatures required for core formation likely arose from a combination of the differentiation process which reduces gravitational potential energy, from the decay of radioactive nuclides, and the kinetic energy from collision events.

Secular cooling of the Earth over time reduced core temperatures sufficiently to allow crystallisation of the liquid iron core. In addition to approaching temperatures at which macroscopic solid metal can become thermodynamically stable, a stable crystalline cluster of atoms must form. This requires that they overcome the nucleation energy barrier (Christian, 2002). Analyses show that this energy barrier to homogeneous nucleation from a purely liquid alloy in the deep core is loo large unless critical supercooling occurred to the order of 1000 K. This level of supercooling has been estimated to be vastly unachievable in the core unless the entire core was supercooled (Huguet et al., 2018). Possible solutions come with substantial caveats to overcome; despite this, we know the inner core exists. This is referred to as the core nucleation paradox.

2.2.2 Physical properties

The composition of Earth's core is an almost pure metallic alloy of ~85 % iron and probably up to ~10 % nickel (Davies et al., 2015; Li et al., 2021; Vocadlo, 2013). Calculations based on observed seismic velocities, density functional theory (DFT) and thermal-pressure equations of state, reveal an overall density deficiency in the outer core of ~10 % (Alfè et al., 2002; Nimmo, 2015; Pozzo et al., 2013; Vocadlo, 2013) with as low as ~5 % reported (Anderson & Isaak, 2002). The deficit can be accounted for by a mixture of lighter elements. Recent studies show that the core likely formed in oxidising conditions (Georg & Shahar, 2015; Siebert et al., 2013) and given the abundance of silicate mantle, the most likely lighter elements appear to be silicon, sulphur and oxygen (Badro et al., 2014; Morard et al., 2014; Siebert et al., 2013). These do not fully account for the deficit, which requires elements such as C, P, and H (Davies et al., 2015; Poirier, 1994). The lighter elements cannot substitute for iron and are released into the outer core as the inner core freezes. As such, a notable difference exists in the amount light elements between the inner (~3 %) and outer (~10 %) core (Nimmo, 2015).

Fundamental properties such as temperature, pressure and density vary with depth. Temperatures are poorly constrained, however, in a vigorously convecting outer core, they are expected to be close to the adiabat. Present day values (including pressure) are estimated to be in the range of 5650 ± 600 K (329 Gpa) at the ICB, and extrapolated to 4180 K ± 400 K (135 GPa) at the CMB (Alfe et al., 2007; Alfè et al., 2003; Nimmo, 2015). Density values can be determined from seismic observations and these increase with depth. The density jump at the ICB occurs due to the phase change and the difference in concentration of light elements. This density difference, which is also poorly constrained, dominates compositional convection in the outer core. The difference calculated from seismic waves is higher than that derived from first principles, with recent best estimates between 3 and 7 % or 400 – 800 kg m^{-3} (Nimmo 2015).

The vigorously convecting outer core sustains the Earth's magnetic field against ohmic dissipation (Buffett, 2015). The well-mixed outer core is implied from its seismic density profile, and this further implies that the temperature gradient is close to adiabatic (Peter Olson, 2013). The very small fluid viscosity in the outer core (e.g., Perrillat et al., 2010; Poirier, 1988) implies a large range of complicated flow length scales are present, however, the first-order flow is dominated by three forces; the Coriolis force, which is comparable to the buoyancy and the Lorentz forces combined; collectively referred to as the Magnetic, Archimedean, Coriolis (MAC) state (Yadav et al., 2016). Higher-order quasi-geostrophic forces complete the force balance (QG-MAC).

Analysis of P-wave velocities provide a seismologically complex picture of the inner core, whereby its anisotropic structure varies radially and longitudinally (Lasbleis & Deguen, 2015). Dominant observations include a hemispherical dichotomy, whereby the eastern hemisphere is seismically faster and more isotropic than the western hemisphere (Alboussière et al., 2010; Aubert et al., 2008). This may be explained, in part, by East-West translation of the inner core, whereby inner core convection produces a heat flux parallel to the equator which causes the eastern side to melt, and the colder, western side to crystallise. Lateral variations of iron grains are produced in the process, as they are allowed to grow during their transportation (Monnereau et al., 2010). Thermal heterogeneity within the inner core shifts Earth's centre of mass towards the crystalising side and isostatic equilibrium is continually restored by the translation.

Equatorial Taylor column convection is generated in the outer core due to the Coriolis force; the columns are aligned with, and sit just outside of the inner core tangent cylinder and only come in to contact with the inner core at the equator. This causes more efficient heat transport and faster equatorial cooling, producing preferential equatorial inner core growth (Aubert et al., 2008; Frost et al., 2021; Yoshida et al., 1996). The stress imparted on the inner core produces deformation and preferential alignment of crystals (Bergman, 1997; Yoshida et al., 1996). Deformation mechanisms such as solidification texturing (Bergman, 1997) would allow creeping deformation along a preferred orientation. A more recently proposed mechanism is the self-diffusion of body-centred cubic iron phase (instead of hexagonally close-packed), which at core temperatures and pressures, would allow easy texturing of iron in response to stress (Belonoshko et al., 2017).

2.3 Thermal conductivity

Notwithstanding the importance of constraining CMB heat flux, or indeed the age of ICN, the thermal conductivity in earth's core is one of the most important geophysical parameters in understanding many of deep earth dynamics and evolution. It is intrinsically linked to the thermal history of the core, the amount of power available for the geodynamo, and the age of inner core nucleation. All of these properties rely fundamentally on realistic values of thermal conductivity. Unfortunately, it is one of the most poorly constrained quantities in deep Earth science, with estimates varying by approximately a factor of 6 (Williams, 2018). Difficulties lie in computationally factoring or experimentally replicating the immense pressures (135 – 360 GPa) and temperatures (~5000 K) that are present in the core. Its value relies on other poorly constrained parameters such as the fractional concentration of the specific light elements present.

Until recently, estimates of thermal conductivity and electrical resistivity have been based on extrapolations of resistivity measurements in shock-compressed Fe and Fe–Si alloys (Bi et al., 2002; Keeler & Mitchell, 1969; Matassov, 1977; Stacey & Loper, 2007; Stacey & Anderson, 2001). Various alternative methods for calculating thermal conductivity have since been adopted; such as Density Functional Theory (Pozzo et al., 2012, 2013, 2014; Xu et al., 2018) and Diamond-Anvil cell experiments (DAC) to higher, more core-like pressures of 100 – 170 GPa (Gomi et al., 2013, 2016; Gomi & Hirose, 2015; Konôpková et al., 2016; Ohta et al., 2016; Zhang et al., 2020). Most of these recent studies (Gomi et al., 2013, 2016; Gomi & Hirose, 2015; De Koker et al., 2012; Pozzo et al., 2012, 2013, 2014; Xu et al., 2018; Zhang et al., 2020) similarly estimate much higher thermal conductivity values (~90 – 130 $Wm^{-1} K^{-1}$) than previously assumed. A recent DAC experiment, however, achieves lower results of 18 – 44 $Wm^{-1} K^{-1}$ (Konopkova et al., 2016), and further recent studies (Hsieh et al., 2020; Zhang et al., 2021) support these findings (approaching the CMB), noting that a slight increase silicon percentage in the outer core considerably increases electrical resistivity and thereby reduces thermal conductivity.

If the higher values are accurate, it requires a revision of the adiabat gradient to ~ 12 to 15 TW in order to maintain a well-mixed vigorously convecting core. This is equal to, or exceeds the most recent estimates of total CMB heat flux (Nimmo, 2015). If the thermal conduction along the adiabat is equal to, or greater than the total heat flux across the CMB then thermal convection would be inhibited and a stratified layer would form at the top of the core. High CMB heat flux is also found to be required to maintain the two large low shear-wave velocity provinces (LLSVPs) in the lower mantle (McNamara & Zhong, 2004; Peter Olson et al., 2015). The discovery of several results of similarly high thermal conductivities from 2012 onwards, led to the question of how could the geodynamo sustain itself for much of Earth history, in the absence of an inner core? This was described as ‘the new core paradox’ by Olsen (2013).

A possible, and almost certain solution would require a higher CMB heat flux to allow for thermal convection to maintain the geodynamo for an extensive part of Earth history, prior to the formation of the inner core (Davies, 2015; Labrosse, 2015; Pozzo et al., 2012). Subsequent model results find that a higher present-day CMB heat flow of ~ 15 TW avoids the new Core paradox, allowing the for thermal conductivity values of up to 130 Wm^{-1} K^{-1} (P. Driscoll & Bercovici, 2014).

Estimates of internal field strength (determined indirectly from ohmic losses in the outer core) place constraints on the power required for the geodynamo (Buffett, 2010; Christensen & Tilgner, 2004; Jackson & Livermore, 2009); however, the power available is usually determined from estimations of total heat flux across the CMB. This changes on timescales limited by the mantle (several 100 Myrs) and the same solutions may not apply for all of Earth history (Buffet, 2015). CMB heat flow is poorly constrained due, in part, to its dependence on equally, if not even more poorly constrained parameters such as the rate at which the mantle can extract heat (Lay et al., 2008), and thermal conductivity in the outer core. Estimates are obtained using various methods to measure temperature differences across the CMB thermal boundary layer; for example, seismological detection of phase transitions average at ~9 TW (Lay et al., 2006) and a statistical model of the D" region produced 13 ± 3 TW (Wu et al., 2011). Based on these and other results, a modern-day estimate is ~7 – 17 TW (Buffett, 2015; Davies et al., 2021; Davies, 2015; Lhuillier et al., 2019; Nimmo, 2015).

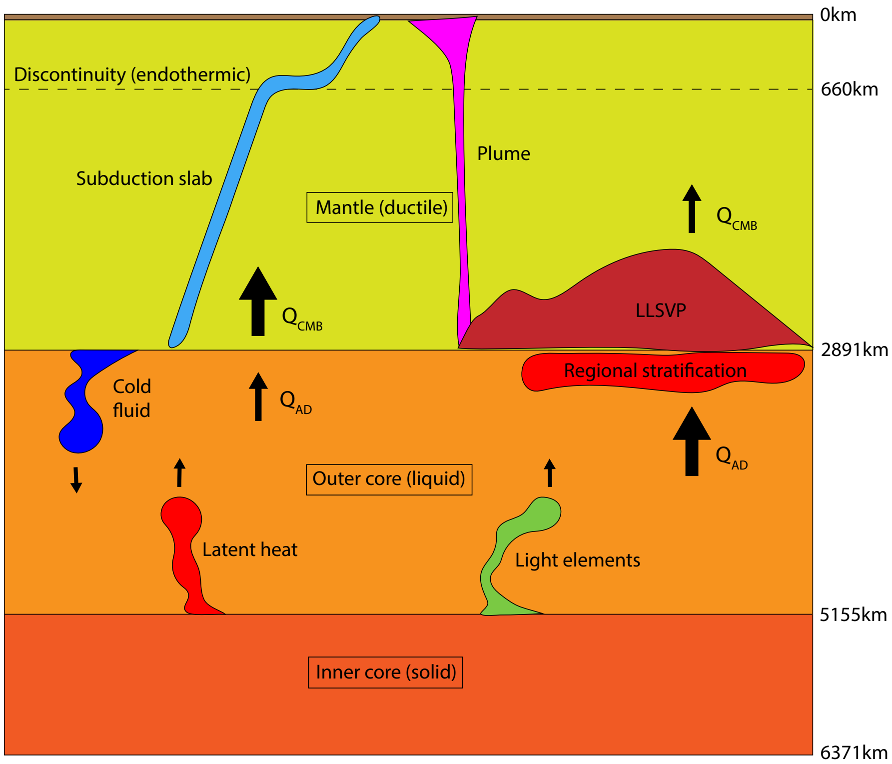

Figure 2.1. Cartoon illustration of some key deep Earth processes, with vertical distances to scale. Depicts two scenario's whereby Q_{AD} (adiabatic heat flow in the outer core) < Q_{CMB} (heat flow across the core-mantle boundary) and the opposite. The first scenario aids thermal convection as the liquid at the top of the outer core is able to cool and sink. Where Q_{CMB} < Q_{AD}, a thermal or chemically stratified layer builds beneath the CMB. A regionaly stratified layer would most likely lie underneath an LLSVP (large low shear velocity province) since this relatively hot material would restrict Q_{CMB}.

2.4 Stratification in the outer core

There have been many seismological observations over the last several decades of significant P-wave velocity reductions (relative to PREM) near the top of the outer core, suggesting the existence of a stably stratified layer (Helffrich & Kaneshima, 2010; Kaneshima, 2018; Lay & Young, 1990; Tanaka, 2007; Tang et al., 2015). Other studies, however, interpret the seismic observations differently and favour little to no stratification at the top of the core (Alexandrakis & Eaton, 2010; Irving et al., 2018).

In the scenario where the heat transferred along the adiabatic gradient is greater than that across the CMB (Figure 2.1, right side), the mantle is unable to remove the conducted heat and excess heat accumulated at the top of the core. This prevents the process of thermal convection, which requires buoyant material to cool and sink. This sub-adiabatic regime, which appears necessary due to recent increases in thermal conductivity values, creates some form of stably stratified layer near the top of the outer core (Buffett, 2015; De Koker et al., 2012; Pozzo et al., 2012). A chemically stratified layer can also arise from the accumulation of light elements beneath the CMB, forming a buoyant layer (Braginsky, 2006). However, theoretical calculations suggest an increase in P-wave velocity would be required, rather than the observed seismological decrease, with increased light element (Brodholt & Badro, 2017; Buffett & Seagle, 2010).

The properties of any layer, such as the thickness and extent of stratification is unclear; or indeed, whether this layer would be thermally or chemically generated (Gastine et al., 2020). Recent thermodynamic numerical models place upper bounds on the thickness of any stable layer of 250 – 400 km, although it is noted that if the convective layer can significantly entrain the fluid at the base of the stable layer, the upper bound on layer size quickly becomes zero

(Greenwood et al., 2021). A separate recent suite of numerical models also supports the absence of a stable layer. By comparing numerical field models for their Earth likeness at the CMB, they find that only models which require a fully convecting core, or penetration distance spanning the entire layer yield good agreement (Gastine et al., 2020); this implies no stratification.

The implications of a thick stratified layer may also be somewhat at odds with geomagnetic observations of secular variation (Gubbins, 2007). Reverse flux patches appear to require thin to no stratification in these regions, and imply that regional stratification is a strong possibility. Recent models find that the stratification is indeed restricted to regions (Figure 2.1), and that this would allow the geodynamo to operate in a sub-adiabatic regime on average, provided there were regional anomalies with super-adiabatic heat flux (Gubbins et al., 2015; Labrosse, 2015; Mound et al., 2019). The most likely scenario is heterogeneous thermo-chemical stratification, which allows laterally-dependent convection (Mound et al., 2019; Olson, 2016). In support, CMB heat flux is also not likely to be laterally homogeneous (Buffet, 2015: Mound et al., 2019; Davies et al., 2021). This may be due to influence from the mantle.

2.5 Core/ mantle interactions

Various thermal, chemical, mechanical and electromagnetic interactions occur between the two giant heat engines of the mantle and core at the CMB (Buffet, 2015). Long-term variations (tens to hundreds of millions of years) in the palaeomagnetic field are not typically associated with the outer core, for which the convective turnover time is estimated to be a few centuries (Hongre et al., 1998). These variations are likely forced through mantle processes changing the total heat flux across the CMB and its lateral distribution (Buffett, 2015; Gubbins, 1994). The mantle therefore likely exerts some dominance over the outer core and the geodynamo on mantle flow timescales (mm yr^{-1}). Mantle control of the geodynamo can be determined through numerical coupled core-mantle models (Olson, 2016; Olson et al., 2015) and through observations of palaeomagnetic behaviour (Biggin et al., 2012).

CMB heat flow plays a fundamental part in controlling the vigour of convection which drives the geodynamo, and it depends on the temperature difference across the mantle's basal thermal boundary layer (TBL). Sources of substantial influence on the TBL include, in particular, the LLSVPs situated under the Pacific and Africa. These long-term features of the lower mantle

(Evans, 2010; Torsvik et al., 2010) are interpreted to consist of dense thermochemical piles, although others interpret these to be purely thermal "superplumes" (Davies et al., 2012); nevertheless, they are likely to restrict heat flux across the CMB in these regions (Garnero et al., 2007). Vertical flux of relatively hotter or colder mantle material can also influence the TBL in a similar manner; major examples of this include mantle plumes departing from the CMB, subducted slabs reaching the lower mantle. These large-scale movements of mass can also cause episodes of true polar wander (TPW), in which the non-hydrostatic moment of inertia tensor is perturbed by the movement of mass of the Earth and seeks to realign itself with Earth's rotation.

On the basis of numerical geodynamo simulations (e.g., Olson, 2007), it is argued that, to first order, CMB heat flow and reversal frequency are positively correlated (Biggin et al., 2012), whereby average polarity reversals may be more frequent when core heat flow is high and infrequent when it is low (Courtillot & Olson, 2007). The long-term variations of the field, in the context of polarity reversal rates, is considered to follow a non-stationary process throughout much of the Phanerozoic era, with three, near evenly-spaced superchrons separated by periods of normal and hyperactive reversal rates. Decreases in average polarity reversals tend to be observed to be a precursor to the onset of the Cretaceous superchron (Gallet & Pavlov, 2016), and may be a feature prior to the other two superchrons (Hounslow et al., 2018).

Periods of weak palaeointensity are recently reported to occur 10–100 Myr prior to the onset of the three Phanerozoic superchrons (Bono et al., 2019; Doubrovine et al., 2019; Hawkins et al., 2019; Shcherbakova et al., 2017, 2020); this suggests an approximate 180 Myr quasi-periodicity in dipole strength. Further support for this feature is provided by a recent study that identifies a potential mid-Palaeozoic dipole low (Hawkins et al., 2021).

Such long-term recurring feature may be related to lithospheric subduction flux, with several studies relating the effects of sinking slabs with the stability of the geomagnetic field (e.g., Gaffin, 1987; Pétrélis et al., 2011). A statistically significant, positive correlation between subduction area flux (SAF) and reversal rates during the Phanerozoic has been identified, with SAF leading a time delay of 120 Ma (Hounslow et al., 2018). The same study details the many complexities and uncertainties in calculating these two phenomena, such as deficiencies in plate models and reversal records, SAF does not represent volume or thermal mass, and the dynamics of the lowermost mantle are poorly understood. The timescale for subducting slabs reaching the CMB can also vary substantially. Some can stagnate at the 660 km discontinuity (Fukao et al., 2001), slowing their arrival. On the other hand, the effects of a subducting slab can be realised long before (100's kms) they reach the CMB since they likely displace hot mantle ahead of them, thinning the TBL, causing the neighbouring TBL to thicken (Steinberger & Torsvik, 2012; Tan et al., 2002). A plausible subduction rate of ~1.5 cm yr^{-1} (Biggin et al., 2012; Goes et al., 2008) would equate 2700km to 180 Myr travel time.

Positive correlations have also been made between reversal rates and large igneous province (LIP) activity, with a lag ~50 Myr (Biggin et al., 2012); this lag agrees with model estimates of rise-times of plumes that are rooted in the lowermost mantle (van Hinsbergen et al., 2011).

2.6 Early dynamo

The prediction of models that incorporate higher CMB heat flow is a younger inner core. The faster core cooling rates required to produce the increased heat flow place constraints on inner core age due to its current size; this in turn implies that the initial core was much hotter than previously estimated. Large uncertainties are associated with early evolution of core temperature (Badro et al., 2016), however, geochemical constraints on mantle cooling may not allow for too high initial core temperatures (Keller & Schoene, 2018; Mittal et al., 2020). To avoid mantle catastrophe, whereby the mantle becomes mostly molten when it is known to be solid, requires a reduction in the mantle secular cooling rate to ~11 TW (Driscoll & Bercovici, 2014).

A younger inner core requires a dynamo capable of generating a geomagnetic field for ~3 Ga without the additional forces that are provided by core solidification (O'Rourke et al., 2017; Pozzo et al., 2012; Tarduno et al., 2010). Provided that at least parts of the core remained super-adiabatic, it may be possible that there was sufficient initial heat available for thermal convection to be the sole power source. There are, however, hypotheses in support of alternative early power sources. The dynamo may have benefited from additional power provided by the precipitation of light elements such as magnesium (Badro et al., 2016; Liu et al., 2020; Mittal et al., 2020; O'Rourke & Stevenson, 2016). The precipitation of magnesium oxide (MgO) in the core is a more efficient source of buoyancy than the compositional convection from inner-core growth by an order of magnitude (O'Rouke & Stevenson, 2016).

Theoretical models propose that MgO exsolution in the core (O'Rouke & Stevenson, 2016) provided a substantial energy source for the geodynamo. They also demonstrate that partitioning of non-siderophiles (such as Mg & O) into the core, could occur through 'two-stage accretion', whereby increased temperatures are generated by major impact events such as the moon impact (O'Rouke et al., 2017; Liu et al., 2019). Giant impacts were able to superheat parts of the earth to temperatures that permit some metal-silicate equilibration (O'Rouke & Stevenson, 2016). In support, recent laboratory impact experiments that account for the previously neglected inertia of massive impacts (Landeau et al., 2021), demonstrate that the mass transfer between metal and silicates is substantially larger than previous estimates, reducing the accretion timescale and the equilibration pressure. Experimental evidence also shows that MgO can dissolve in core-forming iron melt at very high temperatures (Badro et al., 2016). MgO solubility depends only on temperature, and so as the core cooled, the gravitational energy generated by this precipitation gradually decreased. This is hypothesised to explain a gradually decreasing Precambrian geomagnetic field intensity (Badro et al., 2016; Liu et al., 2019).

Recent coupled chemical thermodynamic models allow for various combinations of MgO, SiO_2, and FeO precipitation (Mittal et al., 2020). The results indicate that for a wide range of parameter space, precipitation of either (or multiple) of these species is capable of supporting the geodynamo across earth history, producing spikes in entropy at various times. All of the model parameters adhere to initial and present-day constraints and produce ICN ages between 400 – 700 Ma, typically 550 Ma.

There is also increasing evidence to suggest that the early geomagnetic field was generated in the lowermost mantle (Soubiran & Militzer, 2018; Stixrude et al., 2020; Ziegler & Stegman, 2013). Moon impact sized events can create temperatures high enough to remelt the silicate mantle (Pahlevan & Stevenson, 2007). Evidence suggests that a deep molten mantle can be negatively or neutrally buoyant (Mosenfelder et al., 2007; Stixrude et al., 2009); this would cause crystallisation of the magma to occur at mid-levels, expanding in both vertical directions; two distinct liquid mantles would then form, including an isolated basal magma ocean (BMO). DFT-based molecular dynamics simulations show that electrical conductivity values of liquid silicate melt at temperatures and pressures of a BMO exceed the requirement (10,000 S/m) for dynamo action (Stixrude et al., 2020). In addition, the other two fundamental constraints for generating (convective velocities of 1 mm s^{-1} or higher) and maintaining (magnetic Reynolds number > 40) the early geomagnetic field are also likely exceeded (Soubiran & Militzer, 2018; Stixrude et al., 2020). The theoretical field strength produced by these calculations is argued to be in excellent agreement with paleointensity observations (Stixrude et al., 2020).

Ziegler and Stegman (2013) model a change in the power source of the geomagnetic field from mantle to core at ~2.5 Ga, which may coincide with the change from a stagnant lid regime (Driscoll and Bercovici 2014). At the same approximate time, the only punctuation occurs in a generally continuous trajectory of decreasing compatible element concentrations in preserved continental basalts over the last 4 Gyr (Keller and Schoene, 2018); spikes in entropy production in the core have also recently been predicted by models to have occurred at ~2.5 Ga (Mittal et al., 2020).

2.7 Palaeomagnetism

The geomagnetic field we observe at the surface originates in the outer core, with a small external influence. Therefore, it displays many quantifiable characteristics that can be related to, and inform on geodynamic processes in the fluid core (Aubert et al., 2010; Biggin et al., 2008; Driscoll, 2016). Here we establish the characteristic traits of the geomagnetic field, discussing some recent advances in our understanding, and examine how these relate to deep earth processes.

2.7.1 Palaeofield characteristics

The geometry of the geomagnetic field is well established and is approximated by a geocentric axial dipole (GAD) at Earth's centre that is aligned with the earth's rotation axis. It can be described through spherical harmonics which use gauss coefficients of varying degree and order; these are obtained (and calculated) from a set of globally distributed observations. More observations enable the field to be described to higher orders but the lower order terms dominate the field. Degree one accounts for 90 % of the power though geocentric dipoles about the spin axis ($g^0{}_1$) and two equatorial axes ($h^0{}_1$ and $h^1{}_1$); the total dipole is the vector sum of these.

The field exhibits variability on all timescales, and instantaneous observations record this temporal variability, in which the field departs from a GAD. However, averaging these observations over ~104 years, provides a good approximation of the observed GAD-like magnetic field (Opdyke & Henry, 1969). It is important to note that small, systematic time-averaged departures from GAD have been observed in studies spanning several decades (Johnson & McFadden, 2015). These are thought to arise from vortices in the tangent cylinder (tangent to the inner core), which create 'flux lobes' in the polar regions of the core. Spherical harmonic models (to degree 13) using satellite data observe large variation in the radial component of the geomagnetic field at high northern latitudes (Hulot et al., 2002). These non-axisymmetric vortices persist in the time average of the main field over the past 400 years.

2.7.2 Polarity reversals

The time-averaged field (TAF) is determined by taking the average of multiple global directional measurements; that is, an independent average of all Gauss coefficients before using their ratios to define its properties. Records of relative palaeointensity obtained from sediment cores spanning the last 800 kyr, suggest that the TAF was stronger on average during periods of low reversal rates (Valet et al., 2005). In addition, during the Phanerozoic, periods of high reversal rate such as part of the Jurassic (140 – 200 Myr ago), may be also associated with lower-than-average dipole moment (Biggin et al., 2012).

The stability of the geomagnetic field is defined by the frequency of polarity reversals. A reversal of the magnetic field coincides with a large decrease in the axial dipole moment, which can typically occur over ~20 kyr (Valet et al., 2005), and an associated increase in higher-order, non-dipole components (Amit et al., 2010). However, there is also evidence for a precursor and rebound phase in field strength, tens of thousands of years either side of a reversal, which itself can take as little as a few thousand years (Valet et al., 2012).

Reversal rates over the last ~83 Myr can be obtained from the geomagnetic polarity time scale (GPTS), from which it can be seen that 184 polarity intervals have occurred. The average geomagnetic reversal rate during the Cenozoic is 2 – 3 Myr^{-1}, with the most recent reversal ~780 kyr ago (Leonhardt and Fabian, 2007). There are intervals, such as the mid-Cretaceous, during which the geomagnetic field did not undergo a reversal for ~40 Myr (Ogg, 2020); the cretaceous normal polarity superchron (CNS). There are also periods of hyper-reversals with rates of ~5 Myr^{-1} such as in the mid-Jurassic, pre-CNS and the last 10 Myr (Biggin et al., 2012; Doubrovine et al., 2019).

Reversal frequency is commonly described as a largely stochastic process (Biggin et al., 2012); however, the sequence of superchrons can be characterised by long term correlations (Jonkers, 2003). Long term changes in the average frequency of polarity reversals are likely to be linked to changes in CMB heat flow; a correlation can be observed between numerical simulations of CMB heat flow variation and reversal frequency (Carbone et al., 2020; Driscoll & Olson, 2011). It has been suggested that the geodynamo is maintained near to a critical point between an ordered and chaotic system (Jonkers, 2003); the geodynamo may exist in a regime whereby, for example, the change from non-reversing (superchron) to reversing would take a relatively small amount of additional CMB heat flow (Courtillot & Olson, 2007).

Excursions also frequently occur throughout Earth history; although these are harder to demonstrate in the magnetic records, there appears to have been more than ten since the last reversal (Lund et al., 2021). These may be described as failed reversals, whereby it is energetically favourable for the axial dipole to regain power in the same polarity. A detailed study of PSV and excursions during the interval 130–243 ka, identified four periods of low palaeointensity and that corresponded ('one-to one') with four periods of high angular dispersion (Lund et al., 2021); suggesting that a correlation may exist between high VGP scatter and low palaeointensity. Two recent excursions that have been studied in detail are that of the Laschamp (41.3 ± 0.6 ka), which lasted ~1500 yr, and the Mono Lake 4.25 ± 1.2 ka. The palaeointensity is reported to recover to almost non-transitional values during the ~6 ka between the two excursions (Laj et al., 2014).

2.7.3 Secular variation

The secular variation, or rate of change of the field, is an important characteristic of the geomagnetic field. Variation over the last several hundred years can be determined through direct observations, whereas longer periods require indirect, palaeomagnetic measurements. Palaeosecular variation (PSV) is a measure of spatial and temporal variation of the palaeofield over broad time scales ranging from hundreds to millions of years. Measurements are typically provided by sequences of sediments and lava flows, from which a time-series of palaeomagnetic records can be produced (Jackson & Finlay, 2015).

Angular dispersion (S) in the direction of virtual geomagnetic poles (VGPs) is a measure of temporal variability in the magnetic field. PSV analyses should distinguish between temporal variations during stable periods and polarity reversals by excluding transitional data captured during a reversal. These data, which substantially deviate from a GAD, bias any analysis which aims to define PSV for a given time period.
The transitional data is assessed by their VGP latitude, using a method such as that proposed by Vandamme (1994) to determine the optimal cut-off angle. The method which was originally tested on synthetic VGP data, assumes a Fisherian distribution of data (Fisher, 1953); it was later found to work well on real palaeomagnetic data for the period or 0 – 5 Ma (McElhinny & McFadden, 1997).

The statistical analysis of PSV has often employed Model G (McFadden et al., 1988), whereby S can be characterised by a covarying latitudinal dependence ($S^2 = a^2 + \lambda b^2$); where λ is the latitude, and parameters a and b are constants that represent equatorially symmetric (l – m even) and anti-symmetric (l – m odd) spherical harmonic terms of gauss coefficients with respect to the axial dipole. These two families of gauss coefficients are semi-independent from each other and are claimed to be latitude-invariant and dependent respectively. A recent study, however, found Model G to provide an unacceptable statistical fit for selected reliable PSV data of the last 5 – 10 Ma (Doubrovine et al., 2019).

A strong power law relation was recently derived between median dipole dominance and the Model G 'a' parameter (Biggin et al., 2020). Dynamo simulations demonstrate that as the dipole dominance increases, VGP dispersion decreases and so too does its latitudinal dependence. This useful relation (dipole dominance/ Model G 'a') can be applied to any time period, and is particularly useful for Precambrian times where field morphology is very poorly constrained due to a severe paucity in data. It uses directional data, which is easier to obtain than intensity data, and is therefore more readily available. It allows the morphology to be defined in a more quantitative way than using Model G; this can be used as a further constraint on geodynamo models and may inform on the types of regimes required to generate such morphology.

However, the authors found that dipole dominance was remarkably similar throughout much of Earth history which indicates that similar field geometry existed through significant changes in core regimes. It is also important to note that the median dipole dominance values obtained are the average of multiple instantaneous field morphologies; this different to how the time-averaged GAD field is determined, which is the independent average of the gauss coefficients of multiple directional measurements. Despite this, the dynamo simulations show some correlation between their Model G parameters and the TAF allowing a modicum of insight into this too.

VGP dispersion, considered as a function of latitude, has been suggested to correlate with geomagnetic reversal frequency (Mcfadden, 1991); however, this relationship was later found to be equivocal (Biggin et al., 2008; Tarduno et al., 2002). More recently, an in-depth study (Doubrovine et al., 2019) analysed PSV data from the Cretaceous Normal Superchron (CNS; average reversal rate = 0.05 Myr^{-1}), the pre-CNS (reversal rate = 4.6 Myr^{-1}), and the last 10 million years (reversal rate = ~4.4 – 4.8 Myr^{-1}). They found similar parameter values for periods or high and low reversal frequency and thus, that a and b/a are not a reliable proxy for the reversal frequency. Very different latitudinal dependencies of VGP dispersion were also identified for two distinct periods; the CNS and the highly reversing Early Cretaceous-Jurassic interval. VGP dispersion in the latter was found to be almost latitude-invariant, and therefore cannot be explained by Model G. It was concluded, however, that a distinct increase of VGP dispersion with latitude can be present during periods high and low reversal rates (Doubrovine et al., 2019).

It has been argued that the latitudinal dependence of VGP scatter may arise from long-term changes in core-mantle interactions, which causes changes in the equatorially symmetric or antisymmetric relative contributions of the geodynamo (McFadden, 1991; Aubert et al., 2010). It is not clear whether periods of long-term stability, such as the CNS, are coincidental with a strongly antisymmetric geomagnetic field (dominated by the axial dipole g^0_1). If the outer core is regionally stratified, as described by Mound et al (2019), it is feasible that subadiabatic, stably stratified regions of the uppermost outer core located under the LLSVPs may be influencing PSV, while the bottom-driven buoyancy powering the geodynamo operates almost independently in dichotomous regions. This may explain why VGP scatter and model G parameters are found to be similar during times of high and low reversal.

Measurements of PSV provide a vital insight into geodynamo behaviour and can be used to produce inverse models which map the advective flow within the outer core (Aubert, 2013; Calkins, 2018; Hulot et al., 2002). They also provide constraints on forward models which aim to determine, for example, the degree of stable stratification in the core (section 2.4). High secular variation also helps to identify long-term, prominent anomalous features that exist in the geomagnetic field, such as an area of relatively weaker intensity over the South Atlantic region (Engbers et al., 2020). The persistence of the South Atlantic anomaly may suggest a connection to the lower mantle where it coincides with the margin of an LLSVPs (Tarduno et al., 2015). Alternatively, it may be associated with long-term processes in the outer core (Aubert et al., 2013; Engbers et al., 2020). It has long been claimed that a westward, eccentric planetary gyre exists in the outer core (Bloxham & Jackson, 1991; Bullard, 1950; Dumberry & More, 2020; Finlay et al., 2010; Halley, 1692). There is evidence of its persistence over hundreds and possibly thousands to millions of years (Aubert, 2013). The flux patches associated with this westward gyre, causes PSV to be most prominent at low latitudes in the Atlantic region, and less so over the Pacific (Aubert et al., 2013).

2.8 Long-term evolution of the palaeomagnetic field

The sparsity of Precambrian palaeointensity data make analyses of long-term evolution of the geomagnetic field non-trivial. The stability of the field is very difficult to ascertain with reasonable certainty. It has been suggested that reversal rate of the palaeofield was low in the Precambrian (Biggin et al., 2008; Coe & Glatzmaier, 2006; Dunlop & Yu, 2004); however, data is significantly limited for much of this time, and so this may reflect a failure to capture many polarity reversals. For example, sequences from the interval 1100 to 800 Myr record numerous reversals as high as 5 – 10 per Myr and potential superchrons (Pavlov & Gallet, 2010).

Despite the limited data, an ever-increasing palaeointensity database (v.2015.05; http://earth.liv.ac.uk/pint/; Biggin et al., 2015) has allowed improved statistical analyses of the average long-term palaeomagnetic field (e.g., Biggin et al., 2015; Bono et al., 2019). In addition, recent advances in assessing the quality of palaeointensity (Q_{PI}) data have been made with the introduction of a system of quality scoring, using ten Q_{PI} criteria (Biggin & Paterson, 2014); this has enabled more systematic analyses of data reliability. The application of the Q_{PI} criteria is tested by observing the misfit in the known relationship between palaeointensity and palaeomagnetic inclination for a dipole-dominated field with a varying Q_{PI} cut-off. As the Q_{PI} score increases, a reduction in the misfit is observed across the PINT database (Biggin et al., 2015). However, a robust analysis is difficult across geologic time because the field characteristics, such as the dipole moment and its variability, are unknown; the effect of applying a Q_{PI} cut-off on the uncertainty of palaeointensity estimates is therefore difficult to determine. While it is also possible that certain Q_{PI} criteria may need more weighting than others, the QPI framework is now the benchmark for how palaeointensity experiments should be planned and executed.

Biggin et al. (2009) reported a moderately reliable VDM of ~50 ZAm^2 at approximately 2750 Ma, and suggested that a Proterozoic period of low average dipole existed between two periods of higher field intensity. Following on from this, Biggin et al. (2015) produced a comprehensive statistical analysis of Precambrian palaeointensity. Data was QPI scored and binned into four key periods; later than 1.3 Ga (Late & Recent), earlier than 2.4 Ga (Early) and the intervening (Mid) interval. Approximately half of the VDM measurements in the Early and Late time periods are high (greater than 50 ZAm2) compared with just 5% during the Mid period. In agreement, Smirnov (2017) also found that relatively high palaeointensity values in the Neoarchean and early Palaeoproterozoic were followed by a sustained period of weak dipole strength. These late Archean highs were hypothesised to be the results of a basal magma ocean until ~2.5 Gyr (Ziegler & Stegman, 2013).

Estimation of the average field strength and interpretations made from such data can vary depending on data used. An alternative approach to selecting data was adopted by Bono et al (2019), in which only slow cooled units were accepted for analyses, rather than the average of time-instantaneous palaeointensity values. In the same study, a long-term, decaying trend was identified from the early Archean until ICN at ~565 Ma. Whilst this ICN age compares well with recent numerical geodynamo models (discussed in section 2.9), the approach meant that many Precambrian palaeointensity data were excluded from the analysis and some periods of high dipole moment were perhaps not given enough consideration.

Regardless of the approach, it is generally accepted that a dipole low preceded ICN (Bono et al., 2019; Driscoll, 2016; Landeau et al., 2017); however, it is unclear whether this low extended through the Neoproterozoic era due to a severe lack of data (Biggin et al., 2015). If it did, the

Ediacaran may be of primary interest as the period leading up to ICN due to well-documented unusual field behaviour (e.g., Halls et al., 2015), recently reported low field strengths (Bono et al., 2019; Shcherbakova et al., 2020; Thallner et al., 2021) and recent numerical geodynamo model estimates of ICN. Alternatively, further recent weak palaeointensity data (Shcherbakova et al., 2017; Hawkins et al, 2019) suggest that the dipole low may be extended even further to ~400 Ma; this is supported by some model ICN age estimates (Pozzo et al., 2012; Davies et al., 2015).

Numerical modelling is an important tool in determining the long-term evolution of the deep Earth; they provide information on many fundamental parameters, on Earths total energy budget and on key events such as ICN. However, as previously outlined, many fundamental parameters are associated with large uncertainties. Palaeomagnetic observations provide real data constraints on numerical geodynamo simulations, as well as allowing for statistical models that inform on core evolution (Aubert et al., 2009; Driscoll & Evans, 2016). They enable comparison of synthetic and real statistical global field data, such as true dipole moments (TDM) and virtual dipole moments (VDM), polarity reversals and PSV (Bouligand et al., 2005; McMillan et al., 2001). These two fields of research have made considerable independent advances over the last decade or so; however, only a handful of studies (e.g., Aubert et al., 2009; Driscoll, 2016; Davies et al., 2021) have combined the statistical analysis of palaeomagnetic data with the model outputs. This is an upcoming and exciting area uniquely equipped to answer important questions on deep Earth evolution and long term-morphology of the field.

Improved integration of statistical palaeomagnetic analysis is necessary to ensure that geodynamo models accurately reproduce real world observations. A recent system used palaeomagnetic observational constraints to determine the quality of palaeomagnetic (geodynamo) models (Q_{PM}) with respect to capturing earth-like variability (Sprain et al., 2019). The basis for this is that models should capture the geometry of the TAF and the temporal variations that are known to occur, including polarity reversals. The study found that all of the 46 models tested failed to capture the main aspects of the observed variability with only a few passing three of the five outlined criteria, with large total misfits. A further study used the Q_{PM} criteria to test whether a new set of geodynamo simulations could reproduce the paleomagnetic field behaviour of the last 10 Myrs (Meduri et al., 2021). The authors reported the first numerical simulations known to reproduce the fundamental characteristics of the paleomagnetic field since 10 Ma. They found that the dipole dominance (axial dipole terms/ non-axial terms to spherical harmonic degree and order 12 at the CMB) can be used as a proxy for all five Q_{PM} observable criteria, regardless of the input parameters used.

Such palaeomagnetic observations are important real constraints on deep Earth processes in the geologic past. However, there is a severe lack of data for extended periods of the ancient past, and there is a need for many more high-quality, palaeointensity data in particular. These data are absolutely key when it comes to having confidence in the models that determine our understanding of the conditions that helped shape the earth we see today.

2.9 Latest estimates of ICN age

There has been much activity and advances in numerical geodynamo modelling over the last decade, particularly since the discovery of higher thermal conductivity values (de Koker et al., 2012; Pozzo et al., 2012). Many studies set out to explain how the geodynamo could sustain a magnetic field throughout most of Earth history (Olson, 2013; Driscoll et al., 2014; Davies et al., 2015; Tarduno et al., 2010); these required re-evaluation regarding some key deep Earth processes and parameters including the age of ICN.

Pozzo et al (2012) were the first to produce a range of ICN ages that were modelled on updated thermal conductivity values. They highlighted a wide range of possible ages based on varying several uncertain parameters, however, ages older than ~1 Ga are seen as unlikely due to constraints on the thickness of a stably stratified layer (e.g., Greenwood et al., 2021). Their model no.5 (ICN age = 0.4 Ga) was perhaps the most earth-like, with CMB heat flux just high enough to operate in an adiabatic regime, without a stably stratified layer or any radiogenic heating; both of which would increase ICN age slightly. This model was reproduced independently by Nimmo (2015) and was focussed on further by Davies et al. (2015) who compared the effect of different parameterisations of core structure, which produced a mean ICN age of 0.46 ± 0.04 Ga (N = 10).

Several other suites of unique numerical geodynamo and core evolution models have been used; each of which had varying key thermodynamic and chemical parameters (e.g., Davies et al., 2015; Labrosse, 2015). These include models that are driven by whole-planet thermal history

(Driscoll et al., 2016) and global circulation models of the mantle, from which CMB heat flux is derived (Olsen et al., 2015). More recently, thermal conductivity values were re-evaluated for Fe and FeNi under Earth's outer core conditions to obtain ICN ages (Li et al., 2021). Another recent study used modern seismology data combined with growth models and mineral physics calculations (Frost et al., 2021). Statistical models of time-averaged palaeointensity data are also used to determine ICN age estimates (Biggin et al., 2015; Bono et al., 2019). These models are formed, in part, on the expectation that an observable average increase in palaeointensity is recorded immediately following ICN due to the increase in compositional buoyancy force it provides. Collectively, this is a multi-disciplinary approach to solving (and revising) ICN age that has produced similar values (Figure 2.2).

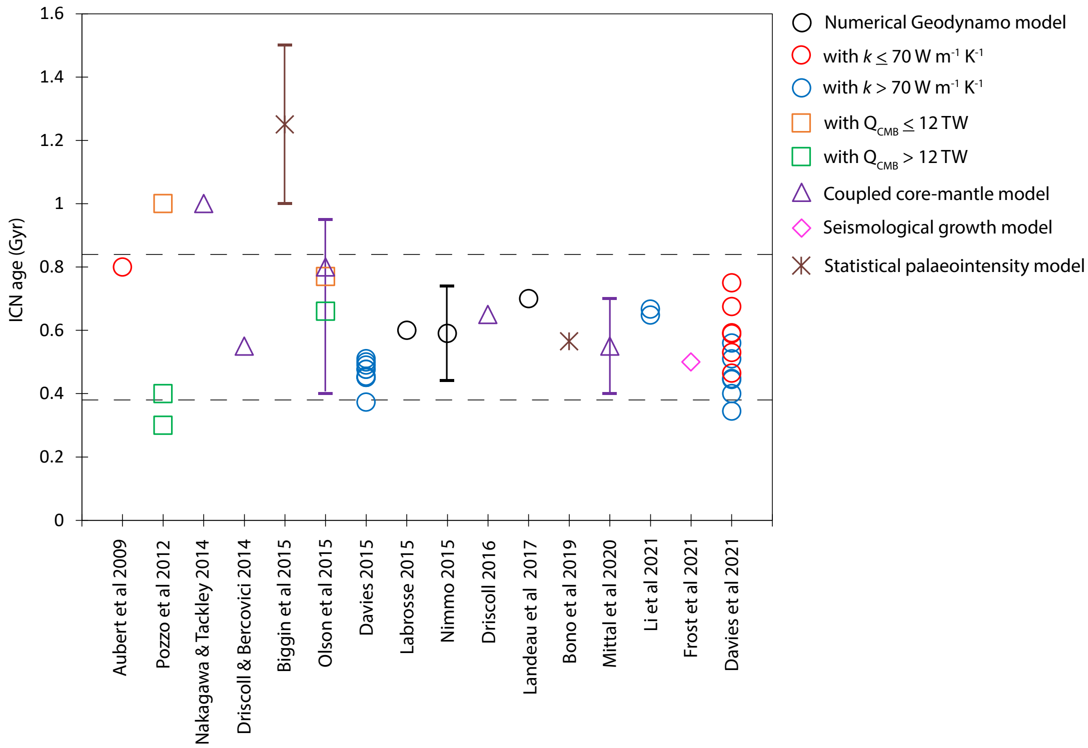

Figure 2.2. ICN age estimates from several studies and based on various approaches. Q_{CMB}, core-mantle boundary heat flux; k, thermal conductivity; solid line, mean ICN age; dashed lines, standard deviation, which takes each of the upper and lower bound markers as an age unit (Olson et al., 2015; Nimmo 2015; Mittal et al., 2020). Several age estimates from the included studies are omitted as they are arguably less reliable. Aubert et al. (2009) omits a low Q_{CMB} (6 TW), low K (50 W m^{-1} K^{-1}) model estimate of 1.8 Ga. For Pozzo et al. (2012), we omit several model-estimates due to recent upper constraints on the thickness of a stably

stratified layer. Only the favoured model of Nakagawa & Tackley (2014) is shown, although they produce a range of estimates, and only their estimate of 0.4 Ga is highlighted in Davies et al. (2021). The latter study also produces age estimates (0.8 – 1.6 Ga) using high MgO precipitation rates which are omitted. It should be noted that a part of the data used (The Garder lava flows; Thomas & Piper 1992, 1995; Thomas 1993) in the analysis of Biggin et al (2015) was later found to be an over-estimation of the palaeofield strength Kodama et al. (2019). This has the effect of reducing the originally interpreted increase in palaeointensity.

High power models, which require high CMB heat flux to accommodate high thermal conductivity, all favour a younger ICN age; these also appear to be the most agreed upon. A consequence of this requirement is that moderate radiogenic heating has a relatively small effect on ICN (Labrosse, 2015). While these consistent estimates are promising, numerical models remain poorly constrained due to large parameter uncertainties. For example, a recent suite of thermal evolution models predicts significantly different ages (>1 Ga) according to the degree of MgO precipitation (Davies et al., 2021). However, the same study produces a narrow range of inner core ages regardless of other uncertain parameters such as the ICB density jump. Thermal conductivity values of 100 W m^{-1} K^{-1} produce age estimates of ~0.4 – 0.6 Ga; these extend to ~0.8 Ga when using 70 W m^{-1} K^{-1}.

Despite recent advances in numerical geodynamo simulations, the models cannot reach certain Earth-like parameters such as the Ekman number (ratio of viscous forces to Coriolis forces). This is due to the immense computational requirements to simulate small scale convection in the outer core. It also remains difficult to reduce the large uncertainty associated with many of the input parameters, or to comprehensively include the complexities that likely exist in core and mantle processes, such as heterogeneous layers and heating influences (Aubert et al., 2010). The balance of forces used may also bear different results (Aubert, 2019; Yadav et al., 2016). It therefore remains vitally important to compare these models to observable data, such as records of palaeointensity and palaeosecular variation.

2.10 Contribution of this research

We can see from Figure 2.1 that an agreement exists in model estimates of ICN, falling within the Neoproterozoic period (~0.5 – 1 Ga). The importance of correlating model-based estimates to the constraints provided by palaeointensity data has also previously been emphasised. It is therefore crucial that a sufficient coverage of high-quality palaeointensity data from this period is available for analysis; unfortunately, an almost complete sparsity of data exits, with just a handful of studies to account for 500 Myrs of Earth history. The Neoproterozoic period seems to be hampered by a lack of suitable target rocks, and additional problems associated with long complicated weathering histories which causes alteration of the magnetic minerals and affects their fidelity as original magnetic recorders.

Our focus was to obtain reliable palaeointensity data from key periods in the Neoproterozoic. We targeted rocks from Chatham Grenville in Canada (530 Ma), the Franklin Large Igneous Province (755 Ma) in high Arctic Canada, Mundine Wells dykes (720 Ma) and Bangemall Sills (1070 Ma) in Western Australia. We carried out detailed rock magnetic and palaeomagnetic experiments on samples from each of these locations, which revealed some interesting results that are difficult to reconcile with the expectation from model predictions. These new data provide some important insight into the Precambrian palaeomagnetic field and allow comparisons to be made with existing Precambrian data and also with palaeofield characteristics in the Phanerozoic. We also provide new constraints for numerical geodynamo simulations and statistical field models which aim to determine the age of ICN.

2.11 References cited

Alboussière, T., Deguen, R., & Melzani, M. (2010). Melting-induced stratification above the Earth's inner core due to convective translation. *Nature*, *466*(7307), 744–747. https://doi.org/10.1038/nature09257

Alexandrakis, C., & Eaton, D. W. (2010). Precise seismic-wave velocity atop Earth's core: No evidence for outer-core stratification. *Physics of the Earth and Planetary Interiors*, *180*(1–2), 59–65. https://doi.org/https://doi.org/10.1016/j.pepi.2010.02.011

Alfe, D., Gillan, M. J., & Price, G. D. (2007). Temperature and composition of the Earth's core. *Contemporary Physics*, *48*(2), 63–80. https://doi.org/10.1080/00107510701529653

Alfè, D., Gillan, M. J., & Price, G. D. (2002). Ab initio chemical potentials of solid and liquids solutions and the chemistry of the Earth's core. *Journal of Chemical Physics*, *116*(16), 7127–7137. https://doi.org/10.1063/1.1464121

Alfè, D., Gillan, M., & Price, G. (2003). Thermodynamics from first principles: temperature and composition of the Earth's core. *Mineralogical Magazine - MINER MAG*, *67*, 113–123. https://doi.org/10.1180/0026461026610089

Amit, H., Leonhardt, R., & Wicht, J. (2010). Polarity reversals from paleomagnetic observations and numerical dynamo simulations. *Space Science Reviews*, *155*(1–4), 293–335. https://doi.org/10.1007/s11214-010-9695-2

Anderson, O. L., & Isaak, D. G. (2002). Another look at the core density deficit of Earth's outer core. *Physics of the Earth and Planetary Interiors*, *131*(1), 19–27. https://doi.org/10.1016/S0031-9201(02)00017-1

Aubert, J. (2013). Flow throughout the earth's core inverted from geomagnetic observations and numerical dynamo models. *Geophysical Journal International*, *192*(2), 537–556. https://doi.org/10.1093/gji/ggs051

Aubert, J. (2019). Approaching Earth's core conditions in high-resolution geodynamo simulations. *Geophysical Journal International*, *219*, S137–S151. https://doi.org/10.1093/gji/ggz232

Aubert, J., Amit, H., Hulot, G., & Olson, P. (2008). Thermochemical flows couple the Earth's inner core growth to mantle heterogeneity. *Nature*, *454*(7205), 758–761. https://doi.org/10.1038/nature07109

Aubert, J., Labrosse, S., & Poitou, C. (2009). Modelling the palaeo-evolution of the geodynamo. *Geophysical Journal International*, *179*(3), 1414–1428. https://doi.org/10.1111/j.1365-246X.2009.04361.x

Aubert, J., Tarduno, J. A., & Johnson, C. L. (2010). Observations and models of the long-term evolution of earth's magnetic field. *Space Science Reviews*, *155*(1–4), 337–370. https://doi.

org/10.1007/s11214-010-9684-5

Aubert, J., Finlay, C. C., & Fournier, A. (2013). Bottom-up control of geomagnetic secular variation by the Earth's inner core. *Nature*, *502*(7470), 219–223. https://doi.org/10.1038/nature12574

Badro, J., Côté, A. S., & Brodholt, J. P. (2014). A seismologically consistent compositional model of Earth's core. *Proceedings of the National Academy of Sciences of the United States of America*, *111*(21), 7542–7545. https://doi.org/10.1073/pnas.1316708111

Badro, J., Siebert, J., & Nimmo, F. (2016). An early geodynamo driven by exsolution of mantle components from Earth's core. *Nature*, *536*(7616), 326–328. https://doi.org/10.1038/nature18594

Belonoshko, A. B., Lukinov, T., Fu, J., Zhao, J., Davis, S., & Simak, S. I. (2017). Stabilization of body-centred cubic iron under inner-core conditions. *Nature Geoscience*, *10*(4), 312–316. https://doi.org/10.1038/ngeo2892

Bergman, M. I. (1997). Measurements of electric anisotropy due to solidification texturing and the implications for the Earth's inner core. *Nature*, *389*(6646), 60–63. https://doi.org/10.1038/37962

Bi, Y., Tan, H., & Jing, F. (2002). Electrical conductivity of iron under shock compression up to 200 GPa. *Journal of Physics: Condensed Matter*, *14*(44), 10849–10854. https://doi.org/10.1088/0953-8984/14/44/389

Biggin, A. J., Steinberger, B., Aubert, J., Suttie, N., Holme, R., Torsvik, T. H., et al. (2012). Possible links between long-term geomagnetic variations and whole-mantle convection processes. *Nature Geoscience*, *5*(8), 526–533. https://doi.org/10.1038/ngeo1521

Biggin, A. J., Piispa, E. J., Pesonen, L. J., Holme, R., Paterson, G. A., Veikkolainen, T., & Tauxe, L. (2015). Palaeomagnetic field intensity variations suggest Mesoproterozoic inner-core nucleation. *Nature*, *526*(7572), 245–248. https://doi.org/10.1038/nature15523

Biggin, A. J., & Paterson, G. A. (2014). A new set of qualitative reliability criteria to aid inferences on palaeomagnetic dipole moment variations through geological time. *Frontiers in Earth Science*, *2*(October), 1–9. https://doi.org/10.3389/feart.2014.00024

Biggin, A. J., Strik, G. H. M. A., & Langereis, C. G. (2008). Evidence for a very-long-term trend in geomagnetic secular variation. *Nature Geoscience*, *1*(6), 395–398. https://doi.org/10.1038/ngeo181

Biggin, A. J., van Hinsbergen, D. J. J., Langereis, C. G., Straathof, G. B., & Deenen, M. H. L. (2008). Geomagnetic secular variation in the Cretaceous Normal Superchron and in the Jurassic. *Physics of the Earth and Planetary Interiors*, *169*(1–4), 3–19. https://doi.org/10.1016/j.pepi.2008.07.004

Biggin, A. J., Strik, G. H. M. A., & Langereis, C. G. (2009). The intensity of the geomagnetic field in the late-Archaean: New measurements and an analysis of the updated IAGA palaeointensity database. *Earth, Planets and Space*, *61*(1), 9–22. https://doi.org/10.1186/BF03352881

Biggin, A. J., de Wit, M. J., Langereis, C. G., Zegers, T. E., Voûte, S., Dekkers, M. J., & Drost, K. (2011). Palaeomagnetism of Archaean rocks of the Onverwacht Group, Barberton Greenstone Belt (southern Africa): Evidence for a stable and potentially reversing geomagnetic field at ca. 3.5Ga. *Earth and Planetary Science Letters*, *302*(3–4), 314–328. https://doi.org/10.1016/j.epsl.2010.12.024

Biggin, A. J., Bono, R. K., Meduri, D. G., Sprain, C. J., Davies, C. J., Holme, R., & Doubrovine, P. V. (2020). Quantitative estimates of average geomagnetic axial dipole dominance in deep geological time. *Nature Communications*, *11*(1), 1–9. https://doi.org/10.1038/s41467-020-19794-7

Bloxham, J., & Jackson, A. (1991). Fluid flow near the surface of Earth's outer core. *Reviews of Geophysics*, (90), 97–120.

Bono, R. K., Tarduno, J. A., Nimmo, F., & Cottrell, R. D. (2019). Young inner core inferred from Ediacaran ultra-low geomagnetic field intensity. *Nature Geoscience*, *12*(2), 143–147. https://doi.org/10.1038/s41561-018-0288-0

Bouligand, C., Hulot, G., Khokhlov, A., & Glatzmaier, G. A. (2005). Statistical palaeomagnetic field modelling and dynamo numerical simulation. *Geophysical Journal International*, *161*(3), 603–626. https://doi.org/10.1111/j.1365-246X.2005.02613.x

Braginsky, S. I. (2006). Formation of the stratified ocean of the core. *Earth and Planetary Science Letters*, *243*(3), 650–656. https://doi.org/https://doi.org/10.1016/j.epsl.2006.01.029

Tonks, W., & Melosh, J. H. (1992). Core formation by giant impacts. *Icarus*, *100*(2), 326–346. https://doi.org/10.1016/0019-1035(92)90104-F

Brodholt, J., & Badro, J. (2017). Composition of the low seismic velocity E′ layer at the top of Earth's core. *Geophysical Research Letters*, *44*(16), 8303–8310. https://doi.org/https://doi.org/10.1002/2017GL074261

Brush, S. G. (1980). Discovery of the Earth's core. *American Journal of Physics*, *48*(9), 705–724. https://doi.org/10.1119/1.12026

Buffett, B. A. (2015). Core-Mantle Interactions. *Treatise on Geophysics: Second Edition*, *8*, 213–224. https://doi.org/10.1016/B978-0-444-53802-4.00148-2

Buffett, B. A. (2010). Tidal dissipation and the strength of the Earths internal magnetic field. *Nature*, *468*(7326), 952–954. https://doi.org/10.1038/nature09643

Buffett, B. A, & Seagle, C. T. (2010). Stratification of the top of the core due to chemical interactions with the mantle. *Journal of Geophysical Research: Solid Earth*, *115*(B4). https://doi.org/https://doi.org/10.1029/2009JB006751

Bullard, E. C. (1950). The Transfer of heat from the core of the Earth. *Geophysical Journal International*, *6*(s1), 36–41. https://doi.org/https://doi.org/10.1111/j.1365-246X.1950.tb02971.x

Calkins, M. A. (2018). Quasi-geostrophic dynamo theory. *Physics of the Earth and Planetary Interiors*, *276*, 182–189. https://doi.org/10.1016/j.pepi.2017.05.001

Carbone, V., Alberti, T., Lepreti, F., & Vecchio, A. (2020). A model for the geomagnetic field reversal rate and constraints on the heat flux variations at the core-mantle boundary. *Scientific Reports*, *10*(1), 1–9. https://doi.org/10.1038/s41598-020-69916-w

Christensen, U. R., & Tilgner, A. (2004). Power requirement of the geodynamo from ohmic losses in numerical and laboratory dynamos. *Nature*, *429*(6988), 169–171. https://doi.org/10.1038/nature02508

Christian, J. W. (2002). *The Theory of Transformations in Metals and Alloys*. Newnes.

Coe, R. S., & Glatzmaier, G. A. (2006). Symmetry and stability of the geomagnetic field. *Geophysical Research Letters*, *33*(21), 1–5. https://doi.org/10.1029/2006GL027903

Courtillot, V., & Olson, P. (2007). Mantle plumes link magnetic superchrons to phanerozoic mass depletion events. *Earth and Planetary Science Letters*, *260*(3–4), 495–504. https://doi.org/10.1016/j.epsl.2007.06.003

Davies, C. J., Pozzo, M., Gubbins, D., & Alfè, D. (2015). Constraints from material properties on the dynamics and evolution of Earth's core. *Nature Geoscience*, *8*(9), 678–685. https://doi.org/10.1038/ngeo2492

Davies, C. J. (2015). Cooling history of Earth's core with high thermal conductivity. *Physics of the Earth and Planetary Interiors*, *247*, 65–79. https://doi.org/10.1016/j.pepi.2015.03.007

Davies, C. J., Bono, R. K., Meduri, D. G., Aubert, J., Greenwood, S., & Biggin, A. J. (2021). Dynamo constraints on the long-term evolution of Earth's magnetic field strength. *Geophysical Journal International*, *228*(1), 316–336. https://doi.org/10.1093/gji/ggab342

Davies, D. R., Goes, S., Davies, J. H., Schuberth, B. S. A., Bunge, H. P., & Ritsema, J. (2012).

Reconciling dynamic and seismic models of Earth's lower mantle: The dominant role of thermal heterogeneity. *Earth and Planetary Science Letters*, *353–354*, 253–269. https://doi.org/10.1016/j.epsl.2012.08.016

Doubrovine, P. V., Veikkolainen, T., Pesonen, L. J., Piispa, E., Ots, S., Smirnov, A. V., et al. (2019). Latitude Dependence of Geomagnetic Paleosecular Variation and its Relation to the Frequency of Magnetic Reversals: Observations From the Cretaceous and Jurassic. *Geochemistry, Geophysics, Geosystems*, *20*(3), 1240–1279. https://doi.org/10.1029/2018GC007863

Driscoll, P., & Bercovici, D. (2014). On the thermal and magnetic histories of Earth and Venus: Influences of melting, radioactivity, and conductivity. *Physics of the Earth and Planetary Interiors*, *236*, 36–51. https://doi.org/10.1016/j.pepi.2014.08.004

Driscoll, P., & Olson, P. (2011). Superchron cycles driven by variable core heat flow. *Geophysical Research Letters*, *38*(9), 1–5. https://doi.org/10.1029/2011gl046808

Driscoll, P. E. (2016). Simulating 2 Ga of geodynamo history. *Geophysical Research Letters*, *43*(11), 5680–5687. https://doi.org/10.1002/2016GL068858

Driscoll, P. E., & Evans, D. A. D. (2016). Frequency of Proterozoic geomagnetic superchrons. *Earth and Planetary Science Letters*, *437*, 9–14. https://doi.org/10.1016/j.epsl.2015.12.035

Dumberry, M., & More, C. (2020). Weak magnetic field changes over the Pacific due to high conductance in lowermost mantle. *Nature Geoscience*, *13*(7), 516–520. https://doi.org/10.1038/s41561-020-0589-y

Dunlop, D. J., & Yu, Y. (2004). Intensity and polarity of the geomagnetic field during precambrian time. *Geophysical Monograph Series*, *145*, 85–100. https://doi.org/10.1029/145GM07

Engbers, Y. A., Biggin, A. J., & Bono, R. K. (2020). Elevated paleomagnetic dispersion at Saint Helena suggests long-lived anomalous behavior in the South Atlantic. *Proceedings of the National Academy of Sciences of the United States of America*, *117*(31), 18258–18263.

https://doi.org/10.1073/pnas.2001217117

Evans, D. A. D. (2010). Proposal with a ring of diamonds. *Nature*, *466*, 326–327.

Finlay, C. C., Dumberry, M., Chulliat, A., & Pais, M. A. (2010). Short timescale core dynamics: Theory and observations. *Space Science Reviews*, *155*(1–4), 177–218. https://doi.org/10.1007/s11214-010-9691-6

Fisher, R. A. (1953). Dispersion on a sphere. *Proceedings of the Royal Society of London. Series A. Mathematical and Physical Sciences*, *217*(1130), 295–305. https://doi.org/10.1098/rspa.1953.0064

Frost, D. A., Lasbleis, M., Chandler, B., & Romanowicz, B. (2021). Dynamic history of the inner core constrained by seismic anisotropy. *Nature Geoscience*, *14*(7), 531–535. https://doi.org/10.1038/s41561-021-00761-w

Fukao, Y., Widiyantoro, S., & Obayashi, M. (2001). Stagnant slabs in the upper and lower mantle transition region. *Reviews of Geophysics*, *39*(3), 291–323. https://doi.org/10.1029/1999RG000068

Gaffin, S. (1987). Phase difference between sea level and Magnetic Reversal Rate. *Nature*, *329*, 816–819.

Gallet, Y., & Pavlov, V. E. (2016). Three distinct reversing modes in the geodynamo. *Izvestiya, Physics of the Solid Earth*, *52*(2), 291–296. https://doi.org/10.1134/S106935131602004X

Garnero, E. J., Lay, T., & McNamara, A. (2007). Implications of lower-mantle structural heterogeneity for the existence and nature of whole-mantle plumes. *Special Paper of the Geological Society of America*, *430*(05), 79–101. https://doi.org/10.1130/2007.2430(05)

Gastine, T., Aubert, J., & Fournier, A. (2020). Dynamo-based limit to the extent of a stable layer atop Earth's core. *Geophysical Journal International*, *222*(2), 1433–1448. https://doi.org/10.1093/GJI/GGAA250

Gauss, C. F. (1839). Allgemeine Theorie des Erdmagnetismus, Resultate aus den Beobachtungen des magnetischen Vereins im Jahre 1838. *Wilhelm Weber, Leipzig.*, 1–57.

Georg, R. B., & Shahar, A. (2015). The accretion and differentiation of Earth under oxidizing conditions. *American Mineralogist*, *100*(11–12), 2739–2748. https://doi.org/doi:10.2138/am-2015-5153

Gilbert, W. (1600). De magnete, magneticisque corporibus, et de magno magnete tellure; Physiologia nova, plurimis & argumentis, & experimentis demonstrata. *Peter Short*.

Goes, S., Capitanio, F. A., & Morra, G. (2008). Evidence of lower-mantle slab penetration phases in plate motions. *Nature*, *451*(7181), 981–984. https://doi.org/10.1038/nature06691

Gomi, H., & Hirose, K. (2015). Electrical resistivity and thermal conductivity of hcp Fe–Ni alloys under high pressure: Implications for thermal convection in the Earth's core. *Physics of the Earth and Planetary Interiors*, *247*, 2–10. https://doi.org/https://doi.org/10.1016/j.pepi.2015.04.003

Gomi, H., Ohta, K., Hirose, K., Labrosse, S., Caracas, R., Verstraete, M. J., & Hernlund, J. W. (2013). The high conductivity of iron and thermal evolution of the Earth's core. *Physics of the Earth and Planetary Interiors*, *224*, 88–103. https://doi.org/10.1016/j.pepi.2013.07.010

Gomi, H., Hirose, K., Akai, H., & Fei, Y. (2016). Electrical resistivity of substitutionally disordered hcp Fe-Si and Fe-Ni alloys: Chemically-induced resistivity saturation in the Earth's core. *Earth and Planetary Science Letters*, *451*, 51–61. https://doi.org/10.1016/j.epsl.2016.07.011

Greenwood, S., Davies, C. J., & Mound, J. E. (2021). On the evolution of thermally stratified layers at the top of Earth's core. *Physics of the Earth and Planetary Interiors*, *318*, 106763. https://doi.org/10.1016/j.pepi.2021.106763

Gubbins, D. (1994). Geomagnetic polarity reversals: A connection with secular variation and core-mantle interaction? *Reviews of Geophysics*, *32*(1), 61–83. https://doi.org/https://doi.org/10.1029/93RG02602

Gubbins, D. (2007). Geomagnetic constraints on stratification at the top of Earth's core. *Earth, Planets and Space*, *59*(7), 661–664. https://doi.org/10.1186/BF03352728

Gubbins, D., Alfè, D., Masters, G., Price, G. D., & Gillan, M. (2004). Gross thermodynamics of two-component core convection. *Geophysical Journal International*, *157*(3), 1407–1414. https://doi.org/10.1111/j.1365-246X.2004.02219.x

Gubbins, D., Alfè, D., Davies, C., & Pozzo, M. (2015). On core convection and the geodynamo: Effects of high electrical and thermal conductivity. *Physics of the Earth and Planetary Interiors*, *247*, 56–64. https://doi.org/10.1016/j.pepi.2015.04.002

Halley, E. (1692). An account of the cause of the change of the variation of the magnetical needle. with an hypothesis of the structure of the internal parts of the earth: as it was proposed to the Royal Society in one of their late meetings. *Philosophical Transactions of the Royal Society of London*, *17*(195), 563–578. https://doi.org/10.1098/rstl.1686.0107

Halls, H. C., Lovette, A., Hamilton, M., & Söderlund, U. (2015). A paleomagnetic and U-Pb geochronology study of the western end of the Grenville dyke swarm: Rapid changes in paleomagnetic field direction at ca. 585Ma related to polarity reversals? *Precambrian Research*, *257*, 137–166. https://doi.org/10.1016/j.precamres.2014.11.029

Hawkins, L. M.A., Anwar, T., Shcherbakova, V. V., Biggin, A. J., Kravchinsky, V. A., Shatsillo, A. V., & Pavlov, V. E. (2019). An exceptionally weak Devonian geomagnetic field recorded by the Viluy Traps, Siberia. *Earth and Planetary Science Letters*, *506*, 134–145. https://doi.org/10.1016/j.epsl.2018.10.035

Hawkins, Louise M.A., Grappone, J. M., Sprain, C. J., Saengduean, P., Sage, E. J., Thomas-Cunningham, S., et al. (2021). Intensity of the Earth's magnetic field: Evidence for a Mid-Paleozoic dipole low. *Proceedings of the National Academy of Sciences of the United States of America*, *118*(34). https://doi.org/10.1073/pnas.2017342118

Helffrich, G., & Kaneshima, S. (2010). Outer-core compositional stratification from observed core wave speed profiles. *Nature*, *468*(7325), 807–810. https://doi.org/10.1038/nature09636

Hirose, K., Labrosse, S., & Hernlund, J. (2013). Composition and State of the Core. *Annual Review of Earth and Planetary Sciences*, *41*(1), 657–691. https://doi.org/10.1146/annurev-earth-050212-124007

Hongre, L., Hulot, G., & Khokhlov, A. (1998). An analysis of the geomagnetic field over the past 2000 years. *Physics of the Earth and Planetary Interiors*, *106*(3), 311–335. https://doi.org/https://doi.org/10.1016/S0031-9201(97)00115-5

Hounslow, M. W., Domeier, M., & Biggin, A. J. (2018). Subduction flux modulates the geomagnetic polarity reversal rate. *Tectonophysics*, *742–743*(July 2017), 34–49. https://doi.org/10.1016/j.tecto.2018.05.018

Hsieh, W. P., Goncharov, A. F., Labrosse, S., Holtgrewe, N., Lobanov, S. S., Chuvashova, I., et al. (2020). Low thermal conductivity of iron-silicon alloys at Earth's core conditions with implications for the geodynamo. *Nature Communications*, *11*(1), 1–7. https://doi.org/10.1038/s41467-020-17106-7

Huguet, L., Van Orman, J. A., Hauck, S. A., & Willard, M. A. (2018). Earth's inner core nucleation paradox. *Earth and Planetary Science Letters*, *487*, 9–20. https://doi.org/10.1016/j.epsl.2018.01.018

Hulot, G., Eymin, C., Langlais, B., Mandea, M., & Olsen, N. (2002). Small-scale structure of the geodynamo inferred from Oersted and Magsat satellite data. *Nature*, *416*(6881), 620–623. https://doi.org/10.1038/416620a

Irving, J. C. E., Cottaar, S., & Lekic, V. (2018). Seismically determined elastic parameters for Earth's outer core. *Science Advances*, *4*(6), 1–10. https://doi.org/10.1126/sciadv.aar2538

Jackson, A., & Finlay, C. (2015). Geomagnetic Secular Variation and Its Applications to the Core. *Treatise on Geophysics: Second Edition*, *5*, 137–184. https://doi.org/10.1016/B978-0-444-53802-4.00099-3

Jackson, Andrew, & Livermore, P. (2009). On Ohmic heating in the Earth's core I: Nutation constraints. *Geophysical Journal International*, *177*(2), 367–382. https://doi.org/10.1111/j.1365-246X.2008.04008.x

Jeffreys, H. (1926). The Rigidity of the Earth's Central Core. *Geophysical Journal International*, *1*(s7), 371–383. https://doi.org/https://doi.org/10.1111/j.1365-246X.1926.tb05385.x

Johnson, C. L., & McFadden, P. (2015). *The Time-Averaged Field and Paleosecular Variation*. *Treatise on Geophysics: Second Edition* (Vol. 5). Published by Elsevier Inc. https://doi.org/10.1016/B978-0-444-53802-4.00105-6

Jonkers, A. R. T. (2003). Long-range dependence in the Cenozoic reversal record. *Physics of the Earth and Planetary Interiors*, *135*(4), 253–266. https://doi.org/10.1016/S0031-9201(03)00036-0

Kaneshima, S. (2018). Array analyses of SmKS waves and the stratification of Earth's outermost core. *Physics of the Earth and Planetary Interiors*, *276*, 234–246. https://doi.org/https://doi.org/10.1016/j.pepi.2017.03.006

Keeler, R. N., & Mitchell, A. C. (1969). Electrical conductivity, demagnetization, and the high-pressure phase transition in shock-compressed iron. *Solid State Communications*, *7*(2), 271–274. https://doi.org/https://doi.org/10.1016/0038-1098(69)90397-4

Keller, B., & Schoene, B. (2018). Plate tectonics and continental basaltic geochemistry throughout Earth history. *Earth and Planetary Science Letters*, *481*, 290–304. https://doi.org/https://doi.org/10.1016/j.epsl.2017.10.031

Kodama, K. P., Carnes, L. K., Tarduno, J. A., & Berti, C. (2019). Palaeointensity of the 1.3 billion-yr-old Gardar basalts, southern Greenland revisited: No evidence for onset of inner core growth. *Geophysical Journal International*, *217*(3), 1974–1987. https://doi.org/10.1093/gji/ggz126

de Koker, N., Steinle-Neumann, G., & Vlček, V. (2012). Electrical resistivity and thermal conductivity of liquid Fe alloys at high P and T, and heat flux in Earth's core. *Proceedings of the National Academy of Sciences of the United States of America*, *109*(11), 4070–4073. https://doi.org/10.1073/pnas.1111841109

Konôpková, Z., McWilliams, R. S., Gómez-Pérez, N., & Goncharov, A. F. (2016). Direct measurement of thermal conductivity in solid iron at planetary core conditions. *Nature*, *534*(7605), 99–101. https://doi.org/10.1038/nature18009

Labrosse, S. (2003). Thermal and magnetic evolution of the Earth's core. *Physics of the Earth and Planetary Interiors*, *140*(1–3), 127–143. https://doi.org/10.1016/j.pepi.2003.07.006

Labrosse, S. (2015). Thermal evolution of the core with a high thermal conductivity. *Physics of the Earth and Planetary Interiors*, *247*, 36–55. https://doi.org/10.1016/j.pepi.2015.02.002

Laj, C., Guillou, H., & Kissel, C. (2014). Dynamics of the earth magnetic field in the 10-75 kyr period comprising the Laschamp and Mono Lake excursions: New results from the French Chaîne des Puys in a global perspective. *Earth and Planetary Science Letters*, *387*, 184–197. https://doi.org/10.1016/j.epsl.2013.11.031

Landeau, M., Aubert, J., & Olson, P. (2017). The signature of inner-core nucleation on the geodynamo. *Earth and Planetary Science Letters*, *465*, 193–204. https://doi.org/10.1016/j.epsl.2017.02.004

Landeau, M., Deguen, R., Phillips, D., Neufeld, J. A., Lherm, V., & Dalziel, S. B. (2021). Metal-silicate mixing by large Earth-forming impacts. *Earth and Planetary Science Letters*, *564*, 116888. https://doi.org/10.1016/j.epsl.2021.116888

Lasbleis, M., & Deguen, R. (2015). Building a regime diagram for the Earth's inner core. *Physics of the Earth and Planetary Interiors*, *247*, 80–93. https://doi.org/10.1016/j.pepi.2015.02.001

Lay, T., & Young, C. J. (1990). The stably-stratified outermost core revisited. *Geophysical Research Letters*, *17*(11), 2001–2004. https://doi.org/https://doi.org/10.1029/GL017i011p02001

Lay, T., Hernlund, J., Garnero, E. J., & Thorne, M. S. (2006). A post-perovskite lens and D″ heat flux beneath the central Pacific. *Science*, *314*(5803), 1272–1276. https://doi.org/10.1126/science.1133280

Lay, T., Hernlund, J., & Buffett, B. A. (2008). Core – mantle boundary heat flow. *Nature Geoscience*, *1*, 25–32.

Lhuillier, F., Hulot, G., Gallet, Y., & Schwaiger, T. (2019). Impact of inner-core size on the dipole field behaviour of numerical dynamo simulations. *Geophysical Journal International*, *218*(1), 179–189. https://doi.org/10.1093/gji/ggz146

Li, W. J., Li, Z., He, X. T., Wang, C., & Zhang, P. (2021). Constraints on the thermal evolution of Earth's core from ab initio calculated transport properties of FeNi liquids. *Earth and Planetary Science Letters*, *562*. https://doi.org/10.1016/j.epsl.2021.116852

Lister, J. R., & Buffett, B. A. (1995). The strength and efficiency of thermal and compositional convection in the geodynamo. *Physics of the Earth and Planetary Interiors*, *91*(1–3), 17–30. https://doi.org/10.1016/0031-9201(95)03042-U

Liu, W., Zhang, Y., Yin, Q. Z., Zhao, Y., & Zhang, Z. (2020). Magnesium partitioning between silicate melt and liquid iron using first-principles molecular dynamics: Implications for the early thermal history of the Earth's core. *Earth and Planetary Science Letters*, *531*, 115934. https://doi.org/10.1016/j.epsl.2019.115934

Lund, S., Acton, G., Clement, B., Okada, M., & Keigwin, L. (2021). On the relationship between paleomagnetic secular variation and excursions – Records from MIS 6 and 7 - ODP Leg 172. *Physics of the Earth and Planetary Interiors*, *318*(May). https://doi.org/10.1016/j.pepi.2021.106727

Matassov, G. (1977, November 1). The Electrical Conductivity of Iron-Silicon Alloys at High Pressures and the Earth's Core. *Ph.D. Thesis*. AA(California Univ., Davis). Retrieved from https://ui.adsabs.harvard.edu/abs/1977PhDT........67M

McElhinny, M. W., & McFadden, P. L. (1997). Palaeosecular variation over the past 5 Myr based on a new generalized database. *Geophysical Journal International*, *131*(2), 240–252. https://doi.org/10.1111/j.1365-246X.1997.tb01219.x

Mcfadden, P. L. (1991). Reversals of the Earth ' s Magnetic Field and Temporal Variations of the Dynamo Families. *Journal of Geophysical Research: Solid Earth*, *96*, 3923–3933.

McFadden, P. L., Merrill, R. T., & Mcelhinny, M. W. (1988). Dipole / Quadrupole Family Modeling of Paleosecular Variation. *Journal of Geophysical Research*, *93*(7), 11,583-11,588.

McMillan, D. G., Constable, C. G., Parker, R. L., & Glatzmaier, G. A. (2001). A statistical analysis of magnetic fields from some geodynamo simulations. *Geochemistry, Geophysics, Geosystems*, *2*(11), n/a-n/a. https://doi.org/10.1029/2000gc000130

McNamara, A. K., & Zhong, S. (2004). Thermochemical structures within a spherical mantle: Superplumes or piles? *Journal of Geophysical Research: Solid Earth*, *109*(7), 1–14. https://doi.org/10.1029/2003JB002847

Meduri, D. G., Biggin, A. J., Davies, C. J., Bono, R. K., Sprain, C. J., & Wicht, J. (2021). Numerical Dynamo Simulations Reproduce Paleomagnetic Field Behavior. *Geophysical Research Letters*, *48*(5), 1–10. https://doi.org/10.1029/2020GL090544

Mittal, T., Knezek, N., Arveson, S. M., McGuire, C. P., Williams, C. D., Jones, T. D., & Li, J. (2020). Precipitation of multiple light elements to power Earth's early dynamo. *Earth and Planetary Science Letters*, *532*, 116030. https://doi.org/10.1016/j.epsl.2019.116030

Monnereau, M., Calvet, M., Margerin, L., & Souriau, A. (2010). Lopsided growth of Earth's inner core. *Science*, *328*(5981), 1014–1017. https://doi.org/10.1126/science.1186212

Morard, G., Andrault, D., Antonangeli, D., & Bouchet, J. (2014). Properties of iron alloys under the earth's core conditions. *Comptes Rendus - Geoscience*, *346*(5–6), 130–139. https://doi.org/10.1016/j.crte.2014.04.007

Mosenfelder, J. L., Asimow, P. D., & Ahrens, T. J. (2007). Thermodynamic properties of Mg2SiO4 liquid at ultra-high pressures from shock measurements to 200 GPa on forsterite and wadsleyite. *Journal of Geophysical Research: Solid Earth*, *112*(6). https://doi.org/10.1029/2006JB004364

Mound, J., Davies, C., Rost, S., & Aurnou, J. (2019). Regional stratification at the top of Earth's core due to core–mantle boundary heat flux variations. *Nature Geoscience*, *12*(7), 575–580. https://doi.org/10.1038/s41561-019-0381-z

Nakagawa, T., & Tackley, P. (2014). Influence of combined primordial layering and recycled MORB on the coupled thermal evolution of Earth's mantle and core. *Geochemistry, Geophysics, Geosystems*, *15*, 619–633. https://doi.org/https://doi.org/10.1002/2013GC005128

Nimmo, F. (2015). Thermal and Compositional Evolution of the Core. In *Treatise on Geophysics: Second Edition*. https://doi.org/10.1016/B978-0-444-53802-4.00160-3

O'Rourke, J. G., & Stevenson, D. J. (2016). Powering Earth's dynamo with magnesium precipitation from the core. *Nature*, *529*(7586), 387–389. https://doi.org/10.1038/nature16495

O'Rourke, J. G., Korenaga, J., & Stevenson, D. J. (2017). Thermal evolution of Earth with magnesium precipitation in the core. *Earth and Planetary Science Letters*, *458*, 263–272. https://doi.org/10.1016/j.epsl.2016.10.057

Ogg, J. G. (2020). *Geomagnetic Polarity Time Scale*. *Geologic Time Scale 2020*. https://doi.org/10.1016/b978-0-12-824360-2.00005-x

Ohta, K., Kuwayama, Y., Hirose, K., Shimizu, K., & Ohishi, Y. (2016). Experimental determination of the electrical resistivity of iron at Earth's core conditions. *Nature*, *534*(7605), 95–98.

https://doi.org/10.1038/nature17957

Olson, P. (2007). Gravitational dynamos and the low-frequency geomagnetic secular variation. *Proceedings of the National Academy of Sciences*, *104*(51), 20159 LP – 20166. https://doi.org/10.1073/pnas.0709081104

Olson, P. (2016). Mantle control of the geodynamo: Consequences of top-down regulation. *Geochemistry, Geophysics, Geosystems*, 1935–1956. https://doi.org/10.1002/2016GC006334. Received

Olson, P. (2013). The new core paradox. *Science*. https://doi.org/10.1126/science.1243477

Olson, P., Deguen, R., Rudolph, M. L., & Zhong, S. (2015). Core evolution driven by mantle global circulation. *Physics of the Earth and Planetary Interiors*, *243*, 44–55. https://doi.org/10.1016/j.pepi.2015.03.002

Opdyke, N. D., & Henry, K. W. (1969). A test of the dipole hypothesis. *Earth and Planetary Science Letters*, *6*(2), 139–151. https://doi.org/10.1016/0012-821X(69)90132-0

Pahlevan, K., & Stevenson, D. J. (2007). Equilibration in the aftermath of the lunar-forming giant impact. *Earth and Planetary Science Letters*, *262*(3), 438–449. https://doi.org/https://doi.org/10.1016/j.epsl.2007.07.055

Pavlov, V., & Gallet, Y. (2010). Variations in geomagnetic reversal frequency during the earth's middle age. *Geochemistry, Geophysics, Geosystems*, *11*(1). https://doi.org/10.1029/2009GC002583

Perrillat, J. P., Mezouar, M., Garbarino, G., & Bauchau, S. (2010). In situ viscometry of high-pressure melts in the Paris-Edinburgh cell: Application to liquid FeS. *High Pressure Research*, *30*(3), 415–423. https://doi.org/10.1080/08957959.2010.494844

Pétrélis, F., Besse, J., & Valet, J. P. (2011). Plate tectonics may control geomagnetic reversal frequency. *Geophysical Research Letters*, *38*(19), 2–5. https://doi.org/10.1029/2011GL048784

Poirier, J. P. (1988). Transport properties of liquid metals and viscosity of the Earth's core. *Geophysical Journal*, *92*(1), 99–105. https://doi.org/10.1111/j.1365-246X.1988.tb01124.x

Poirier, Jean Paul. (1994). Light elements in the Earth's outer core: A critical review. *Physics of the Earth and Planetary Interiors*, *85*(3–4), 319–337. https://doi.org/10.1016/0031-9201(94)90120-1

Pozzo, M., Davies, C., Gubbins, D., & Alfè, D. (2012). Thermal and electrical conductivity of iron at Earth's core conditions. *Nature*, *485*(7398), 355–358. https://doi.org/10.1038/nature11031

Pozzo, M., Davies, C., Gubbins, D., & Alfè, D. (2013). Transport properties for liquid silicon-oxygen-iron mixtures at Earth's core conditions. *Physical Review B - Condensed Matter and Materials Physics*, *87*(1), 1–10. https://doi.org/10.1103/PhysRevB.87.014110

Pozzo, M., Davies, C., Gubbins, D., & Alfè, D. (2014). Thermal and electrical conductivity of solid iron and iron-silicon mixtures at Earth's core conditions. *Earth and Planetary Science Letters*, *393*, 159–164. https://doi.org/10.1016/j.epsl.2014.02.047

Rubie, D. C., Melosh, H. J., Reid, J. E., Liebske, C., & Righter, K. (2003). Mechanisms of metal-silicate equilibration in the terrestrial magma ocean. *Earth and Planetary Science Letters*, *205*(3–4), 239–255. https://doi.org/10.1016/S0012-821X(02)01044-0

Rubie, D. C., Gessman, C. K., & Frost, D. J. (2004). Partitioning of oxygen during core formation on the Earth and Mars. *Nature*, *429*, 58–61.

Shcherbakova, V. V., Biggin, A. J., Veselovskiy, R. V., Shatsillo, A. V., Hawkins, L. M. A., Shcherbakov, V. P., & Zhidkov, G. V. (2017). Was the Devonian geomagnetic field dipolar or multipolar? Palaeointensity studies of Devonian igneous rocks from the Minusa Basin (Siberia) and the Kola Peninsula dykes, Russia. *Geophysical Journal International*, *209*(2), 1265–1286. https://doi.org/10.1093/gji/ggx085

Shcherbakova, V. V., Bakhmutov, V. G., Thallner, D., Shcherbakov, V. P., Zhidkov, G. V., & Biggin, A. J. (2020). Ultra-low palaeointensities from East European Craton, Ukraine support a globally anomalous palaeomagnetic field in the Ediacaran. *Geophysical Journal International*, *220*(3), 1920–1946. https://doi.org/10.1093/gji/ggz566

Siebert, J., Badro, J., Antonangeli, D., & Ryerson, F. J. (2013). Terrestrial Accretion Under Oxidizing Conditions. *Science*, *339*(March), 1194–1198.

Smirnov, A. V. (2017). Intensity of geomagnetic field in the Precambrian and evolution of the Earth's deep interior. *Izvestiya, Physics of the Solid Earth*, *53*(5), 760–768. https://doi.org/10.1134/S1069351317050123

Soubiran, F., & Militzer, B. (2018). Electrical conductivity and magnetic dynamos in magma oceans of Super-Earths. *Nature Communications*, *9*(1). https://doi.org/10.1038/s41467-018-06432-6

Sprain, C. J., Biggin, A. J., Davies, C. J., Bono, R. K., & Meduri, D. G. (2019). An assessment of long duration geodynamo simulations using new paleomagnetic modeling criteria (QPM). *Earth and Planetary Science Letters*, *526*. https://doi.org/10.1016/j.epsl.2019.115758

Stacey, F. D., & Loper, D. E. (2007). A revised estimate of the conductivity of iron alloy at high pressure and implications for the core energy balance. *Physics of the Earth and Planetary Interiors*, *161*(1), 13–18. https://doi.org/https://doi.org/10.1016/j.pepi.2006.12.001

Stacey, F. D., & Anderson, O. L. (2001). Electrical and thermal conductivities of Fe–Ni–Si alloy under core conditions. *Physics of the Earth and Planetary Interiors*, *124*(3), 153–162. https://doi.org/https://doi.org/10.1016/S0031-9201(01)00186-8

Steinberger, B., & Torsvik, T. H. (2012). A geodynamic model of plumes from the margins of Large Low Shear Velocity Provinces. *Geochemistry, Geophysics, Geosystems*, *13*(1). https://doi.org/10.1029/2011GC003808

Stixrude, L., de Koker, N., Sun, N., Mookherjee, M., & Karki, B. B. (2009). Thermodynamics of silicate liquids in the deep Earth. *Earth and Planetary Science Letters*, *278*(3–4), 226–232. https://doi.org/10.1016/j.epsl.2008.12.006

Stixrude, L., Scipioni, R., & Desjarlais, M. P. (2020). A silicate dynamo in the early Earth. *Nature Communications*, *11*(1), 6–10. https://doi.org/10.1038/s41467-020-14773-4

Tan, E., Gurnis, M., & Han, L. (2002). Slabs in the lower mantle and their modulation of plume formation. *Geochemistry, Geophysics, Geosystems*, *3*(11), 1–24. https://doi.org/10.1029/2001gc000238

Tanaka, S. (2007). Possibility of a low P-wave velocity layer in the outermost core from global SmKS waveforms. *Earth and Planetary Science Letters*, *259*(3), 486–499. https://doi.org/https://doi.org/10.1016/j.epsl.2007.05.007

Tang, V., Zhao, L., & Hung, S. H. (2015). Seismological evidence for a non-monotonic velocity gradient in the topmost outer core. *Scientific Reports*, *5*, 1–5. https://doi.org/10.1038/srep08613

Tarduno, J.A., Cottrell, R. D., Davis, W. J., Nimmo, F., & Bono, R. K. (2015). A Hadean to Paleoarchean geodynamo recorded by single zircon crystals. *Science*, *349*(6247), 521–524.

Tarduno, J. A., Cottrell, R. D., Watkeys, M. K., Hofmann, A., Doubrovine, P. V., Mamajek, E. E., et al. (2010). Geodynamo, solar wind, and magnetopause 3.4 to 3.45 billion years ago. *Science*, *327*(5970), 1238–1240. https://doi.org/10.1126/science.1183445

Tarduno, J. A., Watkeys, M. K., Huffman, T. N., Cottrell, R. D., Blackman, E. G., Wendt, A., et al. (2015). Antiquity of the South Atlantic Anomaly and evidence for top-down control on the geodynamo. *Nature Communications*, *6*. https://doi.org/10.1038/ncomms8865

Tarduno, J. A., Cottrell, R. D., & Smirnov, A. V. (2002). The Cretaceous superchron geodynamo: Observations near the tangent cylinder. *Proceedings of the National Academy of Sciences*, *99*(22), 14020 LP – 14025. https://doi.org/10.1073/pnas.222373499

Thallner, D., Biggin, A. J., & Halls, H. C. (2021). An extended period of extremely weak geomagnetic field suggested by palaeointensities from the Ediacaran Grenville dykes (SE Canada). *Earth and Planetary Science Letters*, *568*, 117025. https://doi.org/10.1016/j.epsl.2021.117025

Torsvik, T. H., Burke, K., Steinberger, B., Webb, S. J., & Ashwal, L. D. (2010). Diamonds sampled by plumes from the core-mantle boundary. *Nature*, *466*(7304), 352–355. https://doi.org/10.1038/nature09216

Valet, J. P., Meynadier, L., & Guyodo, Y. (2005). Geomagnetic dipole strength and reversal rate over the past two million years. *Nature*, *435*(7043), 802–805. https://doi.org/10.1038/nature03674

Valet, J. P., Fournier, A., Courtillot, V., & Herrero-Bervera, E. (2012). Dynamical similarity of geomagnetic field reversals. *Nature*, *490*(7418), 89–93. https://doi.org/10.1038/nature11491

Vandamme, D. (1994). A new method to determine paleosecular variation. *Physics of the Earth and Planetary Interiors*, *85*(1–2), 131–142. https://doi.org/10.1016/0031-9201(94)90012-4

Vocadlo, L. (2013). Core composition revealed. *Nature*, *495*, 177–178.

Walter, M., Newsom, H., Ertel-Ingrisch, W., & Holzheid, A. (2000). Siderophile Elements in the Earth and Moon: Metal/Silicate Partitioning and Implications for Core Formation. *Origin of the Earth and Moon*, *1*, 265–289.

Williams, Q. (2018). The Thermal Conductivity of Earth's Core: A Key Geophysical Parameter's Constraints and Uncertainties. *Annual Review of Earth and Planetary Sciences*, *46*, 47–66. https://doi.org/10.1146/annurev-earth-082517-010154

Wu, B., Driscoll, P., & Olson, P. (2011). A statistical boundary layer model for the mantle D″ region. *Journal of Geophysical Research: Solid Earth*, *116*(12), 1–17. https://doi.org/10.1029/2011JB008511

Xu, J., Zhang, P., Haule, K., Minar, J., Wimmer, S., Ebert, H., & Cohen, R. E. (2018). Thermal Conductivity and Electrical Resistivity of Solid Iron at Earth's Core Conditions from First Principles. *Physical Review Letters*, *121*(9), 96601. https://doi.org/10.1103/PhysRevLett.121.096601

Yadav, R. K., Gastine, T., Christensen, U. R., Wolk, S. J., & Poppenhaeger, K. (2016). Approaching a realistic force balance in geodynamo simulations. *Proceedings of the National Academy of Sciences of the United States of America*, *113*(43), 12065–12070. https://doi.org/10.1073/pnas.1608998113

Yoshida, S., Sumita, I., & Kumazawa, M. (1996). Growth model of the inner core coupled with the outer core dynamics and the resulting elastic anisotropy. *Journal of Geophysical Research B: Solid Earth*, *101*(12), 28085–28103. https://doi.org/10.1029/96jb02700

Zhang, Y., Hou, M., Liu, G., Zhang, C., Prakapenka, V. B., Greenberg, E., et al. (2020). Reconciliation of Experiments and Theory on Transport Properties of Iron and the Geodynamo. *Physical Review Letters*, *125*(7), 78501. https://doi.org/10.1103/PhysRevLett.125.078501

Zhang, Y., Hou, M., Driscoll, P., Salke, N. P., Liu, J., Greenberg, E., et al. (2021). Transport properties of Fe-Ni-Si alloys at Earth's core conditions: Insight into the viability of thermal and compositional convection. *Earth and Planetary Science Letters*, *553*. https://doi.org/10.1016/j.epsl.2020.116614

Ziegler, L. B., & Stegman, D. R. (2013). Implications of a long-lived basal magma ocean in generating Earth's ancient magnetic field. *Geochemistry, Geophysics, Geosystems*, *14*(11), 4735–4742. https://doi.org/10.1002/2013GC005001

Chapter 3

Improvements to the Shaw-type absolute palaeointensity method

This chapter is published as Lloyd, S. J., Paterson, G. A., Thallner, D., & Biggin, A. J. (2021). Improvements to the Shaw-Type Absolute Palaeointensity Method. Frontiers in Earth Science, 9(July), 1–11. https://doi.org/10.3389/feart.2021.701863

Abstract

Palaeointensity information enables us to define the strength of Earth's magnetic field over geological time, providing a window into Earth's deep interior. The difficulties in acquiring reliable measurements are substantial, particularly from older rocks. Two of the most significant causes of experimental failure are laboratory induced alteration of the magnetic remanence carriers and effects relating to multidomain magnetic carriers. One method that has been claimed to overcome both of these problems is the Shaw method. Here we detail and evaluate the method, comparing various selection criteria in a controlled experiment performed on a large, non-ideal dataset of mainly Precambrian rocks. Monte Carlo analyses are used to determine an optimal set of selection criteria; the end result is a new, improved experimental protocol that lends itself very well to the automated Rapid 2G magnetometer system enabling experiments to be carried out expeditiously and with greater accuracy.

3.1 Introduction

The acquisition of absolute palaeointensity data is problematic. The minerals that carry magnetic remanence are prone to various types of alteration in nature and in the laboratory. The matrix can also alter to form new magnetic minerals. This alteration affects the original magnetic signal and can lead to inaccurate estimates of past field strength. The pre-requisite that reliable palaeomagnetic directions and ages are obtained from suitable rocks is followed by time-consuming experiments, which often yield low success rates. To aid the process, there are several different methods with which a palaeointensity can be determined. Of these, variants of the thermal Thellier method (Thellier & Thellier, 1959; Coe, 1967; Tauxe & Staudigel, 2004) remains the most robust for assemblages of non-interacting uniaxial SD grains, due to its explicit theoretical basis grounded in the work of Néel (1949). However, it does have disadvantages that may be overcome by using alternative techniques such as the Shaw method (Shaw 1974; Tsunakawa & Shaw 1994, Yamamoto et al., 2003).

The Thellier method can only be used to calculate a palaeointensity at temperatures below those at which alteration occurs. The primary magnetic remanence of ancient rocks is often carried by grains associated with high unblocking temperatures and any thermo-chemical alteration that may influence the primary remanence during heating in the laboratory is not usually corrected for. The method can also suffer from multidomain (MD) effects associated with a failure of Thellier's laws of thermoremanence, causing non-linear Arai plots, which can lead to erroneous palaeointensity estimates (Levi & Merrill, 1976; Shcherbakov et al., 2001; Paterson, 2011). This can lead to significant problems because of an oft-present multi-slope phenomenon that is not easily overcome, causing under/over-estimations of the field strength (Thomas & Piper 1992; Xu & Dunlop 2004; Smirnov et al., 2017).

Compared with other palaeointensity methods, the imparted laboratory remanence in a Shaw experiment is somewhat more analogous to that acquired in nature, in that it is acquired during a single cooling from above the Curie temperature rather than during multiple stepwise heating-cooling cycles with lower peak temperatures. In principle, this makes it less prone to the multidomain effects associated with blocking and unblocking of partial thermoremanent magnetisations, and is said to be domain-state independent (Biggin & Paterson, 2014). Repeated measurements (before and after heating) of anhysteretic remanent magnetisation (ARM) are used to correct any physiochemical alteration of the magnetic minerals; this allows palaeointensities to be calculated from a thermal remanent magnetisation (TRM) at higher temperatures that would otherwise be beyond the range of a Thellier experiment. However, it should be noted that heating above the Curie temperature (T_c) can induce alteration affecting the whole specimen. Additional uncertainties are associated with the Shaw method and its subsequent variations; in particular, the use of ARM as an analogous substitute for TRM, given the well-established grain size dependency of the ratio of ARM and TRM (Tanaka & Komuro, 2009).

The palaeointensity average for the past 0–5 Ma is also noticeably lower when using the Shaw method compared with the Thellier method according to the PINT database (v.2015.05; http://earth.liv.ac.uk/pint/; Biggin et al., 2015). This discrepancy requires that both methods be scrutinised for any systematic biases that they may introduce.

Here we aim to provide a practical evaluation of several aspects of the Shaw-DHT method using a large dataset of wellcharacterised samples. A base set of selection criteria are applied to all data, after which, two linearity parameters with varying selection criteria are applied to the palaeointensity slope and compared. These include the curvature parameter (|k′|; Paterson 2011; Paterson et al., 2014b) and the R^2 correlation coefficient (R^2_{corr}; Paterson et al., 2016). R^2_{corr} is the square of the Pearson correlation (R_{corr}) used in other Shaw palaeointensity studies (Yamamoto et al., 2003). The aim is to determine the most effective set of selection criteria and provide a quantitative measure of their accuracy and precision. We also examine any potential effects of varying the high-temperature hold durations used in the experimental heatings.

3.2 The Shaw method

The Shaw method produces a palaeointensity estimate by comparing the alternating frequency (AF) demagnetisation spectra of a natural remanent magnetisation (NRM) with that of a TRM that is acquired in a single step. Alteration is measured by comparing the demagnetisation spectra of an ARM imparted prior to, and following the laboratory heating; the difference is calculated for each coercivity step and applied as a correction to the TRM (Figure 3.1).

Originally proposed by Shaw (1974), the current method is the product of modifications that allow a palaeointensity to be calculated in the presence of alteration (Kono 1978; Rolph & Shaw 1985). The double heating technique (DHT) was further added (Tsunakawa & Shaw, 1994) with the purpose of testing the reliability of the ARM corrections. This involves a controlled repeat of the initial experiment, replacing the NRM with a laboratory TRM. If subsequent ARM corrections lead to the recovery the TRM, it suggests that the initial corrections are reliable.

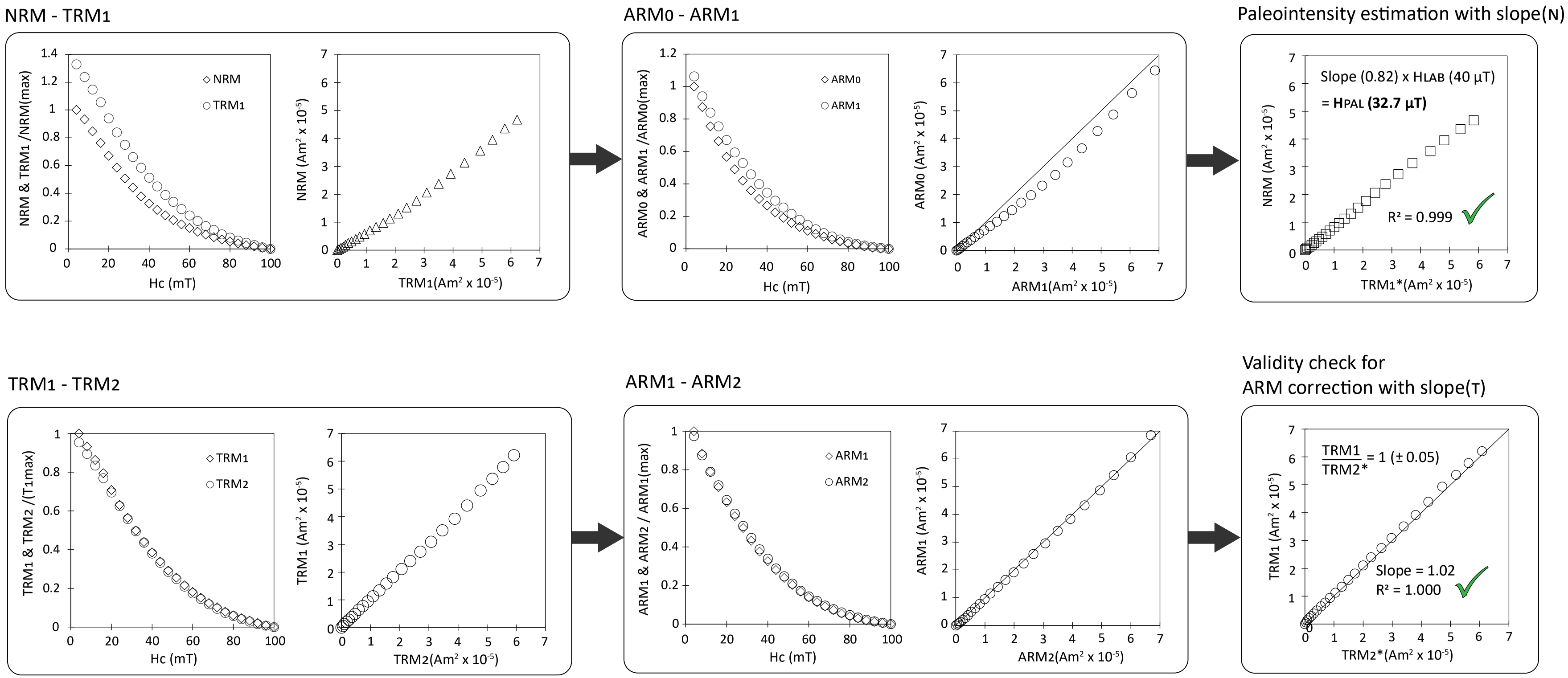

Figure 3.1. Schematic view of the data analyses process for the Shaw-type experiment using a specimen from Mount Etna. Top (Biggin et al., 2007) row is the palaeointensity experiment, where any alteration to the TRM_1 demagnetisation spectra is corrected by multiplying by the ARM slope (ARM_0/ARM_1) to produce TRM1. Bottom row is a repeat experiment to test the validity of the ARM corrections. This ARM validity check uses additional remanence acquisitions (TRM_2 and ARM_2) and should produce a unit slope. Note that the values shown in these figures are after vectoral subtraction of the remanences at the maximum AF step.*

The Shaw-DHT method (referred to as the Tsunakawa-Shaw method) now includes low-temperature demagnetisation (LTD; Yamamoto et al., 2003), which is said to preferentially remove remanence magnetisation held by MD grains (c.f. Ahn et al. 2016). The validity of the Shaw LTD-DHT method has been recognised in historical lavas (Mochizuki et al., 2004; Oishi et al., 2005; Yamamoto et al., 2003; Yamamoto & Hoshi, 2008) and in archaeological samples (Yamamoto et al., 2015).

The inclusion of LTD treatment is optional with respect to the theory behind the DHT. Recent studies of rocks that were moderately to highly MD (15 – 28 %), obtained very similar palaeointensity estimates from LTD and non-LTD sister specimens (Yamamoto et al., 2007; Lloyd et al., 2021a) and other studies successfully use the method without LTD (Thallner et al., 2021). However, the incorporation of LTD can be important, not only for removing MD-like remanence, but also for the additional information it provides. The remanence loss due to LTD can be measured in the NRM, ARM and TRM steps; this can be used to quantify the size of the MD component, differences in the various remanent magnetisation losses and in general how the LTD influences the coercivity spectra.

Here we outline the full experimental LTD-DHT method; note that the LTD method also requires an LTD treatment prior to demagnetising the NRM and TRMs (steps 1,3 and 5). These are then compared with the LTD treated ARMs (steps 2b, 4b and 6b; italics). The procedural steps are as follows:

1) (NRM) Stepwise AF demagnetisation of the NRM, usually up to 100–180 mT.

2a) (ARM_0) An ARM is imparted over the full coercivity range that was used in the NRM demagnetisation, and then progressively AF demagnetised using the same steps as for the NRM. The ARM direct current (DC) bias field is usually 2–3 times higher than the TRM DC bias field to compensate for a weaker ARM acquisition. The ARM AF demagnetising field must always equal the maximum AF demagnetisation
step of the NRM.

2b) (ARM_{00}) LTD-ARM; the same as step 2a but with LTD treatment prior to AF demagnetisation.

3) (TRM_1) A TRM is imparted by heating in a magnetically shielded oven to above T_c (typically to 600 °C for magnetite), with heating and cooling in a constant DC bias field. This is then stepwise AF demagnetised to the same maximum level as the preceding steps. The DC bias field should be close to the expected palaeointensity or a sensible moderate value, i.e., 20 μT.

4a) (ARM_1) A second ARM is imparted over the full coercivity range, as before, and stepwise AF demagnetised to the same maximum level.

4b) (ARM_{10}) LTD-ARM; the same as step 4a but with LTD treatment prior to AF demagnetisation.

5) (TRM_2) A second TRM is imparted and demagnetised in an identical manner to step (3), usually with a longer hold duration.

6a) (ARM_2) A third ARM is imparted and demagnetised in an identical manner to steps (2a and 4a).

6b) (ARM_{20}) LTD-ARM; the same as step 6a but with LTD treatment prior to demagnetisation.

The key parameters obtained from a Shaw experiment are defined as follows:

• $TRM_1*(i)$ $TRM_1(i) \times [ARM_0(i)/ARM_1(i)]$; TRM_1 is corrected at each AF demagnetisation step for the ARM_0/ARM_1 ratio at the same AF step.

• $Slope_N$ (NRM/TRM_{1*}) is the palaeointensity slope calculated using the corrected TRM_1.

• $TRM_2*(i)$ $TRM_2(i) \times [ARM_1(i)/ARM_2(i)]$; TRM_2 is corrected at each AF demagnetisation step for the ARM_1/ARM_2 ratio at the same AF step $Slope_T$ (TRM_1/TRM_2*) is the correction validation made using the slope between TRM_1 and the corrected TRM_2 and should be within 5% of unity.

The AF demagnetisation spectra used for all slopes corresponds to the coercivity range determined as the ChRM, except $slope_T$, which should use the full coercivity range or close to it, but no less than the ChRM. Heating of samples are often conducted in a vacuum in order to repress high-temperature oxidation during laboratory heatings (Mochizuki et al., 2004). The Shaw LTD-DHT studies after Mochizuki et al. (2004) usually used vacuum heating.

The hold durations used for heating steps are chosen somewhat arbitrarily and have varied across different studies. It is common practice to prolong the second hold duration to allow a similar amount of alteration to occur in a specimen that has presumably undergone some thermal stabilisation. Some examples of first (second) heat hold durations are: 30 (60) minutes (Tsunakawa and Shaw, 1994), 10 (20) minutes (Yamamoto et al., 2003), 24 (48) minutes (Yamamoto & Hoshi, 2008), 20–35 (30–45) minutes (Mochizuki et al., 2011), 15 (30) minutes (Yamamoto & Yamaoka, 2018), and 30 (40) minutes (Okayama et al., 2019). Specimens must be held above the Curie temperature of their remanence bearing minerals for enough time to homogeneously heat the specimen; however, heating durations have been shown to alter the ARM/TRM ratio and potentially affect the palaeointensity estimate (Tanaka & Komuro, 2009) and should therefore be subject to scrutiny.

ARM corrections are performed at each measurement point rather than applying a single correction obtained from the best fit slope of ARM_0/ARM_1; although the slope is a linear fit, the plot of ARM_0/ARM_1 need not be linear. This means that a unit slope does not necessarily mean that no alteration has taken place. In the results that will be discussed, we find that the curvature observed in $slope_A$ (k'_A) tends to be inversely proportional to the difference in curvature between the corrected and uncorrected palaeointensity slope ($\Delta k'$), so that $k'_A \approx -\Delta k'$ (Supplementary Figure A1.1). This is indicative of the non-linear behaviour of the ARM_0/ARM_1 data being transferred to the NRM/TRM* plot by the ARM correction.

3.3 Samples and experimental procedures

3.3.1 Monte Carlo Down-Sampling and Testing Linear Parameters

A large dataset of measurements undertaken on 426 individual specimens was compiled from multiple Shaw-DHT experiments, mostly carried out at the University of Liverpool over the last 3 years. Full multi-method palaeointensities are now published on many of these sample sets (Lloyd et al., 2021; Thallner et al., 2021). The experiments were performed using a wide variety of varying input parameters, including differences in the laboratory TRM bias field, ARM bias field, hold durations, sample positions, oven used and number of measurement steps. Most, but not all were heated in a vacuum, and many were subjected to LTD treatment. Here, we do not test how LTD impacts on the palaeointensity estimates although this is something that could be done in the future.

Rock type	***Age***	***N***
Dolerite Sills	*1070 Ma*	*48*
Dolerite Dykes	*755 Ma*	*69*
Dolerite Dykes	*720 Ma*	*43*
Dykes	*590 Ma*	*33*
Lavas	*570 Ma*	*112*
Lavas	*551 Ma*	*23*
Grenville Dyke	*531 Ma*	*23*
Andesitic Lava	*1914 & 46 AD*	*51*
Kiln wall samples	*< 2 Ka*	*24*

Table 3.1. Summary of all samples used in the dataset. Included are specimens from studies by Thallner et al. (2021) and Lloyd et al. (2021a) and other submitted work.

The specimens (Table 3.1) vary widely in lithology and age, from present day lavas and igneous rocks reheated in the walls of a kiln, to Precambrian dolerite dykes and sills extending to more than 1Ga. These ancient samples are non-ideal recorders with various degrees of magnetominerological alteration. Included in the modern-day lavas are Shaw LTD-DHT data available in the MagIC database from a study on the andesitic lavas of Sakurajima (Yamamoto & Hoshi 2008). The deliberately large proportion of extremely non-ideal samples, which includes specimens that were originally determined to be unsuitable for palaeointensity based on rock magnetic results, is meant to ensure that the results represent a worst-case scenario.

A simulated palaeointensity experiment was constructed (similar to Pan et al., 2002) by utilising the data from steps 3-6 of the standard Shaw-DHT method (see method description). A full TRM was imparted on all specimens, resetting their primary remanence and replacing it with a new thermal remanence (step 3 in the method description); importantly, this does not render them all thermally stable, since alteration is still observed in the majority of slopes$_{A2}$ (Supplementary Table A2.2). This laboratory induced TRM becomes the control that we aim to recover by comparing it with an additional, ARM corrected TRM (steps four to six in the method description). If a unit slope is produced when comparing the control TRM with the subsequent corrected TRM, the ARM correction is determined to be successful in exactly the same way as slope$_T$ in a standard Shaw-DHT experiment.

The simulated palaeointensities produced here are the original slope$_T$ values. The fundamental difference between this and a normal Shaw-DHT experiment is that here, there is no double heating; ARM corrections can be tested directly, whereas in the standard method, slope$_T$ is an indirect test of the corrections performed in steps 1 and 2. We begin by applying a base set of selection criteria to the entire dataset (Table 3.2), these include f_{RESID} (Paterson et al., 2016) which ensures that the palaeointensity slope is origin-trending, and the scatter parameter β (Coe et al., 1978), which is used to assess the slope uncertainty. After the base selection criteria are applied, the remaining data are randomly down-sampled ten thousand times with increasing number of specimens (N; starting at N = 3), as follows;

1. Three specimens are randomly sampled from the dataset, and this is repeated ten thousand times.

2. Every sampled specimen is analysed to determine a simulated palaeointensity (TRM_1/TRM_{2*}) using their full coercivity spectra.

3. For each set of three randomly sampled specimens, a mean palaeointensity and standard deviation is calculated. This produces ten thousand mean palaeointensities and standard deviations, each from an N of 3.

4. The ten thousand mean palaeointensities are sorted to calculate their 95 % confidence limit and then averaged to produce an overall mean palaeointensity for an N of 3.

5. The ten thousand standard deviations are sorted to calculate their 95% confidence limit and then averaged to produce a mean standard deviation.

6. This iterative process is repeated, generating an overall mean palaeointensity and mean standard deviation with their respective 95 % confidence limits for each increasing N. The accuracy and standard deviation of the mean is assessed as a function of N.

After we establish a set of results using the base set of selection criteria, the entire process (steps 1–6) is repeated four more times, after various additional selection criteria are applied to the data. R^2_{corr} is applied with two minima, $R^2_{corr} \geq 0.990$ and $R^2_{corr} \geq 0.995$; $|k'|$ is also applied with two minima, $|k'| \leq 0.2$ and $|k'| \leq 0.1$. Each selection criterion is added individually to the base set of selection criteria and the results are randomly down-sampled ten thousand times each time, producing a total of five sets of down-sampled results for comparison.

Parameter	***Criterion***
α	*≤ 15 º*
DANG	*≤ 15 º*
MAD_{ANC}	*≤ 15 º*
MAD_{FREE}	*≤ 15 º*
β	*≤ 0.1*
f_{RESID}	*≤ 0.1*

Table 3.2. Base set of selection that is applied to the entire dataset, and in addition to each of the parameters tested in this study. All parameters follow the Standard Palaeointensity Definitions (Paterson et al., 2014).

These parameters (R^2_{corr} and $|k'|$) are used to assess Shaw plot linearity–the importance of strict linearity in the Shaw NRM-TRM_1* plot has previously been highlighted (Tanaka & Komuro, 2009) and is considered further in the Discussion. Since all the specimens are thermally reset, the full coercivity range is used for all simulated palaeointensity slope fits; this removes any user bias that can result from the slope selection of a preferred coercivity range. Performance is measured by determining the number of specimens required to achieve an acceptable level (±10 % of the correct mean) of accuracy and precision with 95 % confidence.

The selection criteria are also compared using the published Sakurajima data (Yamamoto & Hoshi 2008). We are also able to determine how effective the DHT is at rejecting unreliable results in the same study because the expected field strength is known.

3.3.2 Testing the double heating technique

The DHT is designed to provide additional confidence in the Shaw method, however, variations in the heating hold durations may influence the palaeointensity results that are obtained, particularly since TRM/ARM ratios have been demonstrated to evolve with excessive heating time (Tanaka & Kamuro, 2009). Here, we examine the effect of varying experimental hold durations to determine if any heating time-dependency exists. To do this, we carried out a Shaw-DHT palaeointensity experiment on a set of 23 specimens, using hold durations that are shorter than usual whilst ensuring that equilibrium above T_c is reached. We then compared the

$slope_T$ values with sister specimens that underwent longer hold durations.

The samples from this experiment were from seven different sites and two different ages (five dolerite dykes aged 755 Ma and two sills aged 1070 Ma; Supplementary Table A2.1). The 23 half-inch length cylindrical cores were heated in a vacuum to 610 °C and held for 15 minutes for the acquisition of both TRM_1 and TRM_2 (the second hold would normally be approximately twice as long). The TRMs were imparted using a 20 μT bias field. A third TRM was then imparted on three specimens from one site (MD6) to observe any differences in their AF demagnetisation spectra. The specimens were held at 610 °C for 40 minutes using a 20 μT DC bias field.

Sister-specimens of the specimens used in this experiment yielded reversible high- temperature susceptibility curves (Supplementary Figure A1.2) and high-quality thermal Thellier results with a narrow distribution of remanence-bearing single-domain magnetite grains (Supplementary Figure A1.3). Their well-defined mineralogy and characteristics make them suitable to use in this comparison of hold duration effects.

3.4 Results

3.4.1 Whole data set results

Results obtained after applying all of the selection criteria to the entire data set of 426 specimens (without down-sampling) are given in Table 3.3 and Supplementary Table A2.2. These simulated palaeointensity results are exactly equivalent to the $slope_T$ values in the original experiments. Irrespective of the selection criteria used, an accurate mean palaeointensity is obtained (0.99-1.0). The standard deviations of results, however, differ considerably. Overall standard deviations range from 21% using only the base selection criteria to 9 % for results with the additional criterion $|k'| \leq 0.1$.
Using $|k'|$ with a threshold of ≤ 0.2 produces improved results to that of $R^2_{corr} \geq 0.995$ and notably improved over the results from $R^2_{corr} \geq 0.990$, which is widely used in current analyses (Table 3.2; Figures 3.2 and 3.3). A further improvement is observed when decreasing the curvature minimum to ≤ 0.1, however, given that the difference is small, and its use may potentially discard specimens unnecessarily, we consider that a minimum acceptable curvature of ≤ 0.2 is optimal.

The results in Table 3.3 all have a base set of selection criteria (Table 3.2) applied to them, which remove 24 of the 426 results. In Figure 3.2, we compare the two linearity parameters with selected minima ($R^2_{corr} \geq 0.990$ and $|k'| \leq 0.2$) on the full dataset of 426 specimens. No base selection criteria are applied in this comparison of the two parameters; therefore, the values differ slightly from those in Table 3.3. Use of the single criterion $|k'| \leq 0.2$ appears to be more effective at rejecting non-ideal results, producing a mean result of 1.00 ± 0.12; this is compared to the criterion $R^2_{corr} \geq 0.990$ which rejects fewer specimens and produces a higher standard deviation (mean = 1.01 ± 0.17).

	overall results			down sampled results
Parameter	Mean PI	SD (%)	N	N (CI PI ± 10 %)
Base only	0.99	20.8	402	18
$R^2_{corr} \geq 0.990$	1.00	16.4	360	15
$R^2_{corr} \geq 0.995$	1.00	11.6	308	7
$\lvert k' \rvert \leq 0.2$	0.99	11.0	341	6
$\lvert k' \rvert \leq 0.1$	1.00	9.4	286	4

Table 3.3. Simulated palaeointensity results and standard deviations according to the selection criteria used. The base selection criteria (Table 3.2) are applied in all scenarios. Overall results: Mean PI, mean palaeointensity; SD (%), standard deviation; N, number of results to pass the selection criteria. Down sampled results: N (CI PI ± 10 %), number of randomly sampled results required for the 95 % confidence interval to be within 10 % of the correct mean result (the lower the better).

3.4.2 Down-sampling results

The Monte Carlo down-sampling also produced accurate mean palaeointensities, regardless of the number of specimens averaged (Figure 3.3a, Table 3.3 and Supplementary Table A2.3; see Lloyd et al., 2021b). All selection criteria yield an accurate mean intensity, but with varying scatter (standard deviation) and number of accepted results. Of the four sets with additional linearity checks, those that assess curvature yield the lowest result scatter (~9-11 %), while retaining 70-80 % of the pre-screened results. When assessing plot curvature, we also observe consistently smaller numbers of specimens required to obtain a mean palaeointensity estimate that has a confidence interval within 10 % of the mean. That is, using |k′| ≤ 0.2 or |k′| ≤ 0.1, in addition to the base selection criteria can yield a more precise palaeointensity estimate from fewer specimens (4-6 specimens) than using the R^2_{corr} (7-15 specimens). Furthermore, we observe that with our proposed selection we have a much smaller 95 % confidence interval around the mean standard deviation (Figure 3.3b) which indicates that we can obtain a more constrained estimate of the data scatter than with other selection criteria.

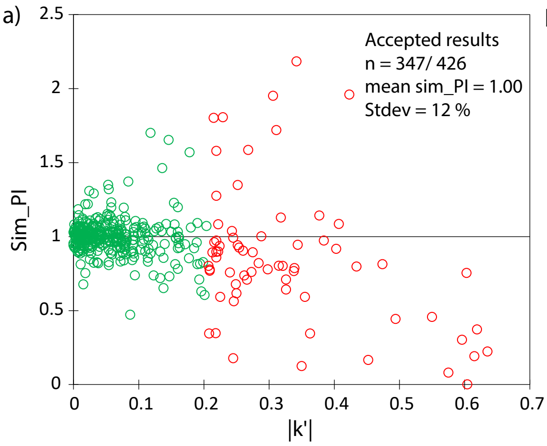

Figure 3.2. The full dataset of 426 simulated palaeointensity results are plotted against linearity parameters |k′| (a) and R^2_{corr} (b). Here, no base selection criteria (Table 3.2) are applied before we plot the data, therefore, the values in these figures differ slightly to those in Table 3.3. Green circles, accepted results at the selected minima; red circles, rejected results at |k′| > 0.2 and R^2_{corr} < 0.990. A few rejected results are not observed as they are outliers, falling outside the selected scale.

4.3 True palaeointensity comparison

The selection criteria were also tested on the original Shaw LTD-DHT palaeointensity results from Sakurajima. The single linearity criterion (|k′| ≤ 0.2) was compared with the main two current Shaw-DHT selection criteria, (R^2_{corr} ≥ 0.990 combined with $slope_T$ = 1 ± 0.05; Yamamoto & Hoshi 2008). All specimen results pass the R^2_{corr} and |k′| criteria; the only difference is due to the $slope_T$ criterion, which causes six specimens to be rejected in the original published data (Figure 3.4a). Intensity error fractions for all but one of the rejected palaeointensity results are less than 8 % and are closer to the expected geomagnetic field intensity than many of the successful results (Figure 3.4a). The results obtained using the single criterion |k′| are slightly improved over the current Shaw-DHT selection criteria (without the use of a second heating) in terms of the number of successful results, the mean palaeointensity result, and the standard deviation (Figure 3.4b).

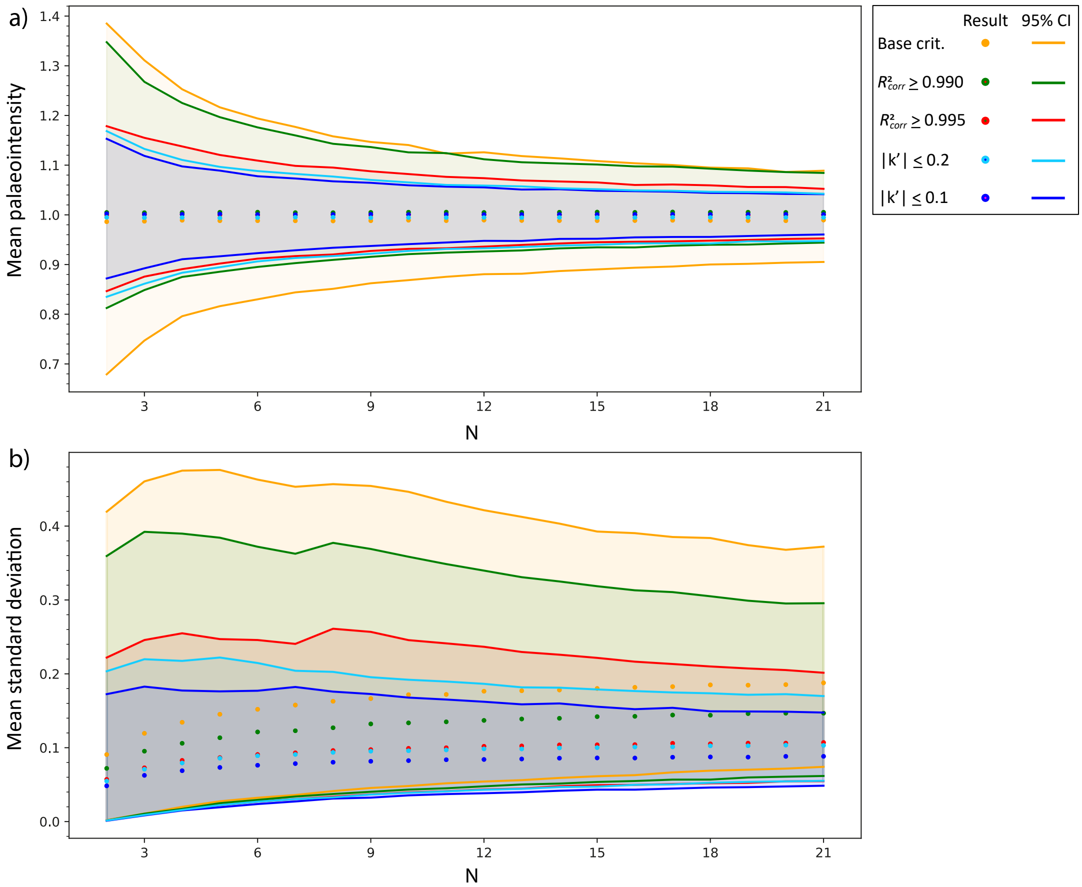

Figure 3.3. Plots of the down-sampled results with increasing N, shown up to N = 21. a) Mean palaeointensity (dots) are the (N) mean of ten thousand randomly sampled specimens, and associated 95% confidence interval (solid lines) results after applying each set of the tested selection criteria. b) Mean standard deviation (dots) is the (N) mean of ten thousand randomly sampled specimens and associated 95 % confidence interval (solid lines) results after applying each set of the tested selection criteria.

3.4.4 DHT hold time results

As part of the original palaeointensity experiments that were carried out on the specimens in this study, one Shaw-DHT experiment was carried out on a subset that included specimens from seven different sites and three localities (Figure 3.5a). The experiment was designed to explore the effect of varying hold durations on the palaeointensity estimates and associated

$slope_T$ values. The effect of shorter hold durations on some $slope_T$ values were not expected and are highlighted here. The $slope_T$ values obtained were unusually high for several, but not all, specimens and they appear to cluster according to site (Figure 3.5a).

We compared the high $slope_T$ results from site MD6 with sister specimens that were subjected to longer hold durations, and noted that the values are affected by the hold duration used (Figure 3.5b). Sister specimens that underwent shorter hold durations (those in Figure 3.5a) produced high $slope_T$ values. This is in contrast to sister specimens with a combined hold duration of 80 minutes, which produced a near unit $slope_T$ (Figure 3.5b and Supplementary Figure A1.4).

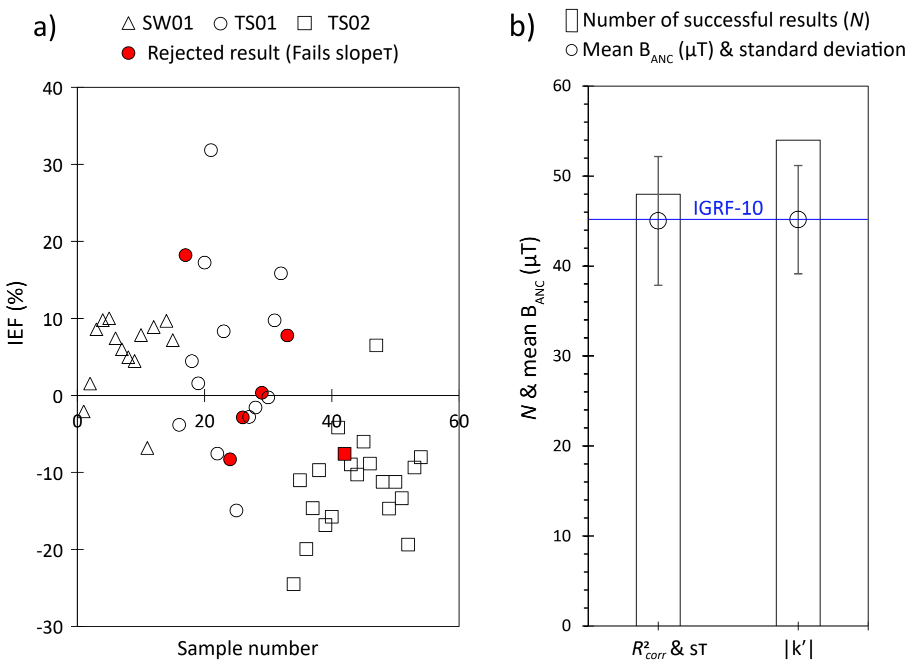

Figure 3.4. Palaeointensity results of the two volcanic lava flows from Sakurajima, (Yamamoto & Hoshi 2008). IGRF values are 45.7 and 46.0 μT. a) All individual palaeointensity results using the current Shaw (LTD)-DHT selection criteria. Results separated according to Yamamoto and Hoshi (2008). The only rejected results are due to a failure of the $slope_T$ criterion (highlighted in red). IEF (%) is the intensity error fraction ((m-μ)/ μ x 100); m, estimated mean geomagnetic field intensity; μ, expected geomagnetic field intensity determined from IGRF-10 data. b) A comparison of the results when applying the same Shaw-DHT selection criteria; R^2_{corr} ≥ 0.990 and $slope_T$ (sT) = 1 ± 0.05 (left) versus |k'| ≤ 0.2 (right). The blue horizontal line represents the mean expected palaeointensity according to IGRF-10.

It has recently been noted that $Slope_T$ values may be dependent on hold duration (Lloyd et al., 2021a); this is now further supported in more detail here. To analyse the cause of these latest observations, we subjected three of the specimens from site MD6 to a third TRM, heating to 610 °C using a hold duration of 40 minutes and compared the AF demagnetisation spectra. In Figure 3.6 we show that a large decrease in the magnitude of TRM_2 is the cause of the high $slope_T$ value in all three specimens, and this was brought about by the corresponding short hold duration (Figure 3.5b).

Alteration appears to have continued to affect TRM during the acquisition of TRM_3, but has caused a reversal of TRM magnitude which finishes close to the original TRM_1 position. The changes in demagnetisation spectra (Figure 3.6) infer that the heating would cause a change in $slope_T$ (TRM_1–TRM_2* plot) depending on the time spent at high temperature. This result is in agreement with specimens from site MD6 that had longer hold durations and unit $slope_T$ values (Figure 3.5). It is also worth noting that ARM appears to be unaffected by the apparent alteration to TRM.

3.5 Discussion

3.5.1 Summary of results and significance

Notably improved results are achieved by replacing the R^2_{corr} with the curvature parameter $|k'|$. This is because it provides a more direct measure of linearity, the fundamental characteristic that should be tested for in the Shaw-type palaeointensity slope. A non-linear ARM-corrected Shaw palaeointensity slope suggests that changes in ARM are not behaving as an analogous substitute for TRM changes, most likely due to non-uniform high-temperature alteration affecting certain grain sizes (coercivity ranges) more than others. ARM/TRM ratios have previously been shown to differ with grain size and heating times (Tanaka & Komuro, 2009). The R^2_{corr} parameter does not perform as well because it has a strong dependence on the number of points selected in the best-fit slope, which allows for increased curvature for a larger number of points. It can also be sensitive to random noise, which can decrease correlation despite a general linear trend in the data. In this sense, R^2_{corr} measure both NRM-TRM reciprocity (i.e., linearity) as well data scatter. We argue it is more appropriate to use two criteria more attuned to testing for reciprocity and scatter separately. For example combining curvature ($|k'|$) with the β parameter; The ratio of the standard error of the slope to the absolute value of the slope (Coe et al., 1978; Paterson et al., 2014). These data pass the β minimum as part of the base selection criteria which suggests that the noise is acceptable.

The results based on using |k′| as a primary selection criterion are improved over existing data selection. The notable improvement in accuracy and precision when using $|k'| \leq 0.2$ instead of $R^2_{corr} \geq 0.990$ does not come at the expense of a lower success rate; these remain similar at 350 and 329 respectively from a potential 426; this is because the R^2_{corr} criterion is rejecting more of the accurate palaeointensities than the |k′| criterion. The improved results are also obtained without a second heating (viewed as though the simulated experiment data were from an initial heating) and therefore, without using the DHT.

With the use of modern equipment such as a Rapid 2G, this new version of the method, with improved palaeointensity slope selection criteria (|k′|, f_{RESID}, β) and without the DHT, can be almost fully automated and able to produce as many as 100 palaeointensity and directional results per week using high resolution AF steps, while other more time-consuming methods may take up to ten times longer.

3.5.2 Observations on the DHT

The validity of the DHT for natural rocks has been discussed by Tsunakawa and Shaw (1994) using historical or young lavas, where it was found to detect non-ideal behaviour or non-unity in the slope of TRM_1-TRM_2* plots. The results from such specimens were viewed as unreliable because they could potentially give an erroneous slope in the NRM-TRM_1* plots (Tsunakawa & Shaw, 1994; Yamamoto et al., 2003).

The initial findings presented in this study, however, suggest that it may be possible for the DHT to allow alteration to occur undetected in certain samples and that $slope_T$ values could potentially be dependent on the hold duration used (c.f. Lloyd et al., 2021a). This is highlighted in Figure 3.5b where sister specimens with varying hold durations produced very different $slope_T$ values.

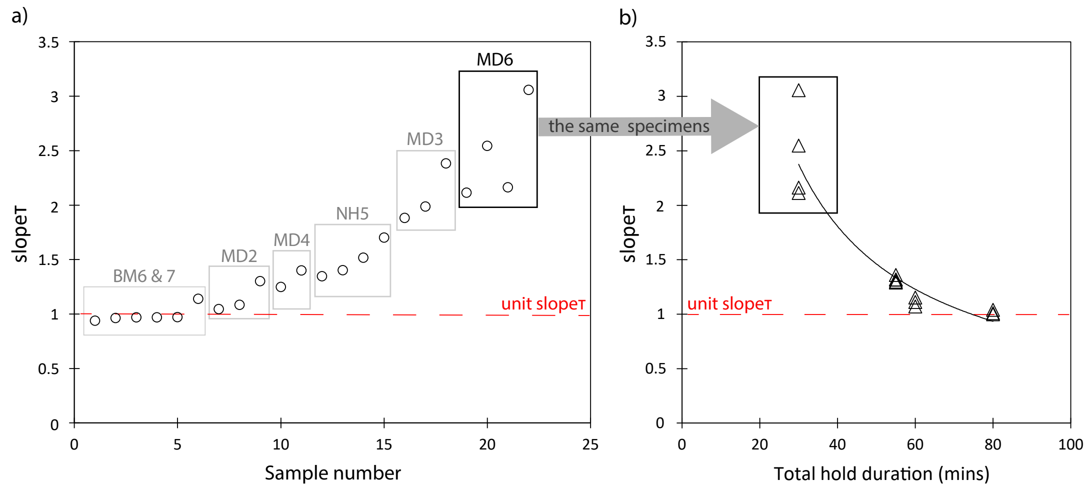

Figure 3.5. Comparison of slope$_T$ results. a) Results from a single Shaw-DHT experiment designed to test the effect of varying hold durations on palaeointensity estimates and slopeT values using hold durations of 15 minutes for TRM$_1$ and TRM$_2$. Values are plotted by site in ascending order. b) Comparison of slope$_T$ results from site MD6 as a function of total hold duration. The high slope$_T$ values (boxed) are the same specimens from box in figure 3.4A; these are compared with sister specimens from other Shaw-DHT experiments that had longer total hold durations.

TRM and ARM can both be affected independently by alteration (Tsunakawa & Shaw, 1994; Tanaka & Komuro, 2009), which is demonstrated by the existence of non-unit slope$_T$ values, however, the magnitude of their remanent magnetisation can also increase and decrease in the same experiment (Figure 3.6). These results are preliminary, and require further study to understand the cause of, and extent to which the observed phenomena can occur; however, the reversibility of remanent magnetisation magnitudes after prolonged heating may not be uncommon. We often see results where slope$_{A1}$ and slope$_{A2}$ are opposite in magnitude, where the ARM slopes are less than and more than one, or vice versa (e.g., Yamamoto & Tsunakawa, 2005; Yamamoto et al., 2007); this implies that the ARM magnitudes are reversing. If slopeA$_1$ (ARM$_0$/ARM$_1$) < 1, the heating has caused an overall increase in ARM over the coercivity steps used; if then, the slopeA$_2$ (ARM$_1$/ARM$_2$) > 1, the ARM magnitude is altering in the opposite sense during the second heating. It is also possible that this occurs undetected in a single heating.

The cause of reversing magnitude in TRM and or ARM, which can occur in either remanence independently, is unclear. The loss of TRM observed in Figure 3.6 may be due to the oxidation of magnetite to hematite, however, this does not explain the subsequent increase in TRM_3. It is possible for new minerals to form that will acquire an increased TRM, but with coercivities too high to contribute to the ARM. This may account for the slight increase in residual magnetisation observed in TRM_3 (Figure 3.6c), but does not explain the reversing magnitude of the full TRM, which appears to require more than one mechanism.

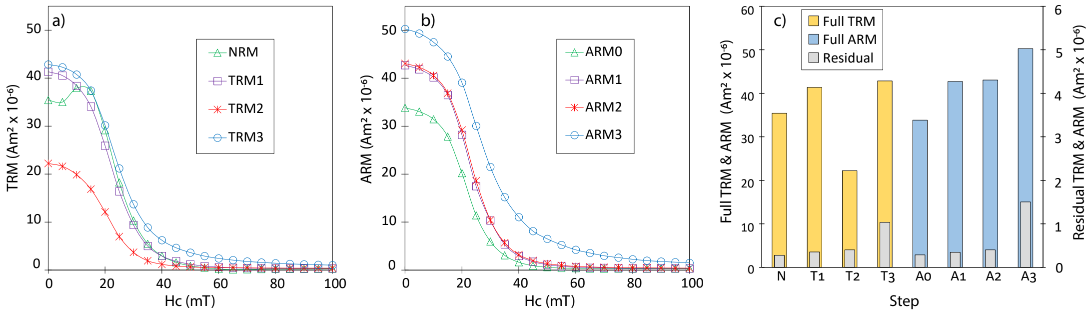

Figure 3.6. AF demagnetisation information for specimen 6.2A of site MD6. (a) Vector-subtracted TRM AF demagnetisation spectra. (b) Vector-subtracted ARM AF demagnetisation spectra. (c) Magnitudes of the remanence and residual magnetisations.

A requirement of the Shaw-DHT method is that sufficient alteration occurs in the second heating in order to validate the initial ARM corrections. It is this second alteration correction that provides an indication of whether ARM and TRM are acting as analogues within the specimen. There are currently no criteria to prevent a specimen from becoming thermally stable during the first heating (alteration has saturated), which is inferred by a non-unit $slope_{A1}$ combined with a unit $slope_{A2}$ (e.g., Yamamoto & Tsunakawa 2005; Yamamoto et al., 2007). Where a specimen experiences little to no initial alteration, it should be expected to behave similarly in the subsequent heating, in which case, both $slope_{A1}$ and $slope_{A2}$ should be close to unity.

The technique also tends to remove accurate palaeointensity results, rather than outliers in the original Sakurajima palaeointensity study (Figure 3.4a); in this case it appears to say little about the accuracy of the palaeointensity estimate. It should be acknowledged, however, that any criterion designed for rejecting inaccurate estimates, can reject some of the accurate estimates.

An alternative and arguably more useful technique to test the validity of the alteration corrections would be to vary hold durations with sister specimens during their one and only heating. This enables a more direct assessment of alteration effects and ARM corrections at the palaeointensity level of the experiment, rather than the assessment coming from separate ARM corrections after further and excessive heating. Variations in palaeointensity values from sister specimens can be quantified and large standard deviations can be rejected.

3.6 Conclusions

We have identified a set of improved selection criteria for the Shaw-type palaeointensity method by down-sampling simulated palaeointensity results from a large dataset of 426 individual specimens. Use of the improved selection criteria demonstrate notably increased accuracy and precision of mean palaeointensity results. This comes with only a minor reduction in the number of successful results and, importantly, without the use of a second heating. We also highlight an additional measure as a safeguard to detect undesirable behaviour that requires varying the hold duration in sister specimens; however, the exact usage and interpretation of this approach requires further investigation.

We find that the DHT may allow alteration to occur undetected, and that $slope_T$ appears to be dependent on the hold durations used in certain instances. In the analysis of historical lavas from Sakurajima, the effectiveness of the DHT was not demonstrated. We therefore suggest that a larger scale study of the DHT efficacy is required. The results suggest that it may not be necessary to include the DHT, however, more work is needed to better understand the broad spectrum of how alteration affects remanence magnetisations in the method. The removal of the DHT allows the method to be carried out much more expeditiously and almost fully automated if used in conjunction with modern equipment such as the Rapid 2G system.

3.7 References cited

Ahn, H. S., Kidane, T., Yamamoto, Y., & Otofuji, Y. I. (2016). Low geomagnetic field intensity in the Matuyama Chron: Palaeomagnetic study of a lava sequence from Afar depression, East Africa. Geophysical Journal International, 204(1), 127–146. https://doi.org/10.1093/

gji/ggv303

Biggin, A. J., Perrin, M., & Dekkers, M. J. (2007). A reliable absolute palaeointensity determination obtained from a non-ideal recorder. Earth and Planetary Science Letters, 257(3–4), 545–563. https://doi.org/10.1016/j.epsl.2007.03.017

Biggin, A. J., Piispa, E. J., Pesonen, L. J., Holme, R., Paterson, G. A., Veikkolainen, T., & Tauxe, L. (2015). Palaeomagnetic field intensity variations suggest Mesoproterozoic inner-core nucleation. Nature, 526(7572), 245–248. https://doi.org/10.1038/nature15523

Biggin, A. J., & Paterson, G. A. (2014). A new set of qualitative reliability criteria to aid inferences on palaeomagnetic dipole moment variations through geological time. Frontiers in Earth Science, 2(October), 1–9. https://doi.org/10.3389/feart.2014.00024

Coe, R. S. (1967). The Determination of Paleo-Intensities of the Earth's Magnetic Field with Emphasis on Mechanisms Which Could Cause Non-Ideal Behavior in Thellier's Method. Journal of Geomagnetism and Geoelectricity, 19(3), 157–179. https://doi.org/10.5636/jgg.19.157

Coe, R. S., Grommé, S., & Mankinen, E. A. (1978). Geomagnetic paleointensities from radiocarbon-dated lava flows on Hawaii and the question of the Pacific nondipole low. Journal of Geophysical Research: Solid Earth, 83(B4), 1740–1756. https://doi.org/10.1029/jb083ib04p01740

Kono, M. (1978). Reliability of palaeointensity methods using alternating field demagnetization and anhysteretic remanence. Geophysical Journal of the Royal Astronomical Society. https://doi.org/10.1111/j.1365-246X.1978.tb04258.x

Levi, S., & Merrill, R. T. (1976). A comparison of ARM and TRM in magnetite. Earth and Planetary Science Letters, 32(2), 171–184. https://doi.org/10.1016/0012-821X(76)90056-X

Lloyd, S. J., Biggin, A. J., Halls, H., & Hill, M. J. (2021a). First Palaeointensity Data from the Cryogenian and their potential implications for Inner Core Nucleation Age. Journal of

Geophysical Research.

Lloyd, S. J., Paterson, G. A., Thallner, D., & Biggin, A. J. (2021b). Improvements to the Shaw-Type Absolute Palaeointensity Method. *Frontiers in Earth Science*, *9*(July), 1–11. https://doi.org/10.3389/feart.2021.701863

Mochizuki, N., Tsunakawa, H., Oishi, Y., Wakai, S., Wakabayashi, K. I., & Yamamoto, Y. (2004). Palaeointensity study of the Oshima 1986 lava in Japan: Implications for the reliability of the Thellier and LTD-DHT Shaw methods. Physics of the Earth and Planetary Interiors, 146(3–4), 395–416. https://doi.org/10.1016/j.pepi.2004.02.007

Mochizuki, N., Oda, H., Ishizuka, O., Yamazaki, T., & Tsunakawa, H. (2011). Paleointensity variation across the Matuyama-Brunhes polarity transition: Observations from lavas at Punaruu Valley, Tahiti. Journal of Geophysical Research: Solid Earth, 116(6), 1–17. https://doi.org/10.1029/2010JB008093

Oishi, Y., Tsunakawa, H., Mochizuki, N., Yamamoto, Y., Wakabayashi, K. I., & Shibuya, H. (2005). Validity of the LTD-DHT Shaw and Thellier palaeointensity methods: A case study of the Kilauea 1970 lava. Physics of the Earth and Planetary Interiors, 149(3–4), 243–257. https://doi.org/10.1016/j.pepi.2004.10.009

Okayama, K., Mochizuki, N., Wada, Y., & Otofuji, Y. ichiro. (2019). Low absolute paleointensity during Late Miocene Noma excursion of the Earth's magnetic field. Physics of the Earth and Planetary Interiors, 287(August 2018), 10–20. https://doi.org/10.1016/j.pepi.2018.12.006

Paterson, G. A. (2011). A simple test for the presence of multidomain behavior during paleointensity experiments. Journal of Geophysical Research: Solid Earth, 116(10), 1–12. https://doi.org/10.1029/2011JB008369

Paterson, G. A., Tauxe, L., Biggin, A. J., Shaar, R., & Jonestrask, L. C. (2014a). On improving the selection of Thellier-type paleointensity data. Geochemistry, Geophysics, Geosystems, 15(4), 1180–1192. https://doi.org/10.1002/2013GC005223.Received

Paterson, G. A., Tauxe, L., Biggin, A. J., Shaar, R., & Jonestrask, L. C. (2014b). Standard Paleointensity Definitions v1.1, 0–43. Retrieved from http://www.paleomag.net/SPD/spdweb.html

Paterson, G. A., Heslop, D., & Pan, Y. (2016). The pseudo-Thellier palaeointensity method: New calibration and uncertainty estimates. Geophysical Journal International, 207(3), 1596–1608. https://doi.org/10.1093/gji/ggw349

Rolph, T. C., & Shaw, J. (1985). A new method of palaeofield magnitude correction for thermally altered samples and its application to Lower Carboniferous lavas. Geophysical Journal of the Royal Astronomical Society, 773–781.

Shaw, J. (1974). A New Method of Determining the Magnitude of the Palaeomagnetic Field: Application to five historic lavas and five archaeological samples. Geophysical Journal of the Royal Astronomical Society, 39(1), 133–141. https://doi.org/10.1111/j.1365-246X.1974.tb05443.x

Shcherbakov, V. P., Shcherbakova, V. V., & Vinogradov, Y. K. (2001). On a thermomagnetic criterion for the identification of the domain structure. Izvestiya - Physics of the Solid Earth.

Smirnov, A. V., Kulakov, E. V., Foucher, M. S., & Bristol, K. E. (2017). Intrinsic paleointensity bias and the long-term history of the geodynamo. Science Advances, 3(2), 1–8. https://doi.org/10.1126/sciadv.1602306

Tanaka, H., & Komuro, N. (2009). The Shaw paleointensity method: Can the ARM simulate the TRM alteration? Physics of the Earth and Planetary Interiors, 173(3–4), 269–278. https://doi.org/10.1016/j.pepi.2009.01.003

Tauxe, L., & Staudigel, H. (2004). Strength of the geomagnetic field in the cretaceous normal superchron: New data from submarine basaltic glass of the troodos ophiolite. Geochemistry, Geophysics, Geosystems, 5(2). https://doi.org/10.1029/2003GC000635

Thallner, D., Biggin, A. J., & Halls, H. C. (2021). An extended period of extremely weak geomagnetic field suggested by palaeointensities from the Ediacaran Grenville dykes (SE Canada). Earth and Planetary Science Letters, 568, 117025. https://doi.org/10.1016/j.epsl.2021.117025

Thellier, E., & Thellier, O. (1959). Sur l'intensité du champ magnétique terrestre dans le passé historique et géologique. Annales de Géophysique, 15, 285–376.

Thomas, D. N., & Piper, J. D. A. (1992). A revised magnetostratigraphy for the Mid-Proterozoic Gardar lava succession, South Greenland. Tectonophysics. https://doi.org/10.1016/0040-1951(92)90172-3

Tsunakawa, H., & Shaw, J. (1994). The Shaw method of palaeointensity determinations and its application to recent volcanic rocks. Geophysical Journal International, 118(3), 781–787. https://doi.org/10.1111/j.1365-246X.1994.tb03999.x

Xu, S., & Dunlop, D. J. (2004). Thellier paleointensity theory and experiments for multidomain grains. Journal of Geophysical Research: Solid Earth, 109(7), 1–13. https://doi.org/10.1029/2004JB003024

Yamamoto, Y., Tsunakawa, H., & Shibuya, H. (2003a). Palaeointensity study of the Hawaiian 1960 lava: Implications for possible causes of erroneously high intensities. Geophysical Journal International, 153(1), 263–276. https://doi.org/10.1046/j.1365-246X.2003.01909.x

Yamamoto, Y., Tsunakawa, H., & Shibuya, H. (2003b). Palaeointensity study of the Hawaiian 1960 lava: Implications for possible causes of erroneously high intensities. Geophysical Journal International, 153(1), 263–276. https://doi.org/10.1046/j.1365-246X.2003.01909.x

Yamamoto, Y., Tsunakawa, H., Shaw, J., & Kono, M. (2007). Paleomagnetism of the Datong monogenetic volcanoes in China: Paleodirection and paleointensity during the middle to early Brunhes Chron. Earth, Planets and Space, 59(7), 727–746. https://doi.org/10.1186/BF03352736

Yamamoto, Y., & Hoshi, H. (2008). Paleomagnetic and rock magnetic studies of the Sakurajima 1914 and 1946 andesitic lavas from Japan: A comparison of the LTD-DHT Shaw and Thellier paleointensity methods. Physics of the Earth and Planetary Interiors, 167(1–2), 118–143. https://doi.org/10.1016/j.pepi.2008.03.006

Yamamoto, Y., & Tsunakawa, H. (2005). Geomagnetic field intensity during the last 5 Myr: LTD-DHT Shaw palaeointensities from volcanic rocks of the Society Islands, French Polynesia. Geophysical Journal International, 162(1), 79–114. https://doi.org/10.1111/j.1365-246X.2005.02651.x

Yamamoto, Y., & Yamaoka, R. (2018). Paleointensity study on the holocene surface lavas on the island of Hawaii using the Tsunakawa–Shaw method. Frontiers in Earth Science, 6(May), 1–10. https://doi.org/10.3389/feart.2018.00048

Yamamoto, Y., Torii, M., & Natsuhara, N. (2015). Archeointensity study on baked clay samples taken from the reconstructed ancient kiln: Implication for validity of the Tsunakawa-Shaw paleointensity method. *Earth, Planets and Space, 67*(1), 1–13. https://doi.org/10.1186/s40623-015-0229-8

Chapter 4

First palaeointensity data from the cryogenian and their potential implications for inner core nucleation age

This chapter is published as Lloyd, S. J., Biggin, A. J., Halls, H., & Hill, M. J. (2021). First Palaeointensity Data from the Cryogenian and their potential implications for Inner Core Nucleation Age. Geophysical Journal International. https://doi.org/10.1093/gji/ggab090

Abstract

The timing of inner core nucleation is a hugely significant event in Earth's evolution and has been the subject of intense debate. Some of the most recent theoretical estimates for the age of nucleation fall throughout the Neoproterozoic era; much younger than previously thought. A young inner core requires faster recent core cooling rates and a likely hotter early core; knowledge of its age would be invaluable in understanding Earth's thermal history and total energy budget. Predictions generated by numerical dynamo models need to be tested against such data, but records are currently much too sparse to constrain the event to a precise period of time. Here, we present results from 720 Ma dolerite dykes (and one sill) from the Franklin Large Igneous Province, which fall within a crucial 300 Myr gap in palaeointensity records. This study uses three independent techniques on whole rocks from 11 sites spread across High Arctic Canada and Greenland to produce virtual dipole moments ranging from 5 to 20 ZAm^2 (mean 11 ZAm^2); almost one order of magnitude lower than the present-day field. These weak-field results agree with recent ultralow palaeointensity data obtained from Ediacaran rocks formed ~150 Myr later and may support that the dynamo was on the brink of collapse in the Neoproterozoic prior to a young inner core formation date.

4.1 Introduction

A fundamental and intensely debated topic in Earth science relates to the question: when did inner core nucleation (ICN) occur? (e.g. Gubbins et al., 2014; Biggin et al., 2015; O'Rourke & Stevenson, 2016; Bono et al., 2019). Palaeomagnetic information recorded in rocks can potentially be used to constrain events which occurred in the deep Earth in the ancient past.

ICN is expected to have had a major impact on core convection, providing additional power to the geodynamo and moving the primary buoyancy source to much greater depths (Aubert et al., 2009). As liquid iron freezes, lighter elements are released, causing compositional convection and the release of latent heat (Nimmo, 2015). The location of the dominant buoyancy release changes from a top driven regime at the core–mantle boundary, to one which is bottom driven (Landeau et al., 2017). These are competing factors on the resultant geomagnetic field intensity (palaeointensity) observed at Earth's surface because the additional power is being dissipated ~3500 km further away. Post nucleation, however, it is plausible that we would see an increase in the geomagnetic field intensity at Earth's surface, followed by a higher time-averaged field (Aubert et al., 2009; Driscoll, 2016). Unfortunately, there are currently insufficient palaeointensity data to provide conclusive tests of such hypotheses.

The current challenge in elucidating long-term observational trends, which might act as a proxy for ICN, has led to wildly varying age estimates and much conjecture. Assessment of existing palaeomagnetic data with new reliability criteria (Q_{PI}; Biggin & Paterson, 2014; Kulakov et al., 2019) enabled an increase in the Earth's magnetic field between 1.0 and 1.5 Ga to be claimed and hypothesized to have signified ICN (Biggin et al., 2015). This was immediately questioned, however (Smirnov et al., 2016), and should be considered in light of new palaeomagnetic data gathered from relevant time periods (Sprain et al., 2018; Bono et al., 2019; Kodama et al., 2019; Veselovskiy et al., 2019). Furthermore, various numerical dynamo models, using recent increased thermal conductivity estimates in the outer core (de Koker et al., 2012; Pozzo et al., 2012), tend toward a younger nucleation age of between 500 and 800 Ma (Driscoll & Bercovici, 2014; Labrosse, 2014; Davies et al., 2015). These younger ages are in closer agreement to recent ultralow palaeointensity results obtained using single crystals (as opposed to whole rock samples) of Ediacaran age (Bono et al. 2019), hypothesized to be caused by a geodynamo on the brink of collapse immediately prior to ICN. Equally relevant, however, are recent thermal conductivity studies of conflicting values (Konopkova et al., 2016; Ohta et al., 2016; Zhang et al. 2020); this emphasizes the urgent requirement for more reliable quantitative constraints that palaeointensity data may provide.

Here, we present crucial new palaeointensity data from the mid-Neoproterozoic (~720 Ma), close in time to when some of the recent dynamo models predict ICN to have occurred (e.g., Labrosse, 2014; Driscoll, 2016; Landeau et al., 2017). These new data are the first to emerge for this time-period, falling in the midst of a critical 300 Myr palaeointensity data gap, with the aim of providing a further constraint on thermal evolution models seeking to address the timing of ICN. The difficulties in obtaining reliable palaeointensity data for the Precambrian are substantial; rocks of the correct age are scarce, the magnetic minerals are likely to have been subjected to reheating, low-temperature oxidation, and other alteration since the time of emplacement. Ideal magnetic recorders should be free from these effects, displaying thermal stability and evidence that the initial thermal remanence magnetization has remained pure, to be confident that the results are unbiased. Previous work (Denyszyn et al., 2004) has shown that many of the Franklin dykes (which are the focus of this study) show typical signs of varying hydrous alteration and as such, a conservative approach is adopted here in reporting results, with particular emphasis on assessing reliability and potential bias from alteration and multidomain (MD) effects.

4.2 Franklin Large Igneous Province (LIP)

The Franklin LIP is a widespread (2.25 M km^2) mafic sill and dyke swarm province in the high Arctic Canada and Greenland (Figure 4.1a). The dolerite dykes sampled in this study, from Devon Island, Ellesmere Island and Greenland, are plagioclase-pyroxene cumulates which are petrologically uniform (Denyszyn et al., 2004). The dykes are on average 30m wide with well-preserved chilled margins. The surrounding host rocks are high-grade, granitic gneiss of Archean to Palaeoproterozoic age, overlain by flat-lying Palaeozoic carbonate and mudstone. The original palaeodirection study (Denyszyn et al. 2009) reports variable amounts of hydrous alteration present in many samples, varying from mild to extensive sericitization of plagioclase. U - Pb ages are available from three sites (BG, CG and QA; Figure 4.1) and the remaining sites are estimated to be of similar age (721 ±4 Ma; Denyszyn et al. 2009). Similar ages have previously been obtained from other Franklin sills and lavas dated at 723 ± 4 and 718 ± 2 Ma (Heaman et al., 1992), and dykes 720 ± 8 and 716 ± 4 Ma (Pehrsson & Buchan, 1999).

Palaeomagnetic poles obtained from the dykes (mean pole 8.4 °N, 163.4 °E; Denyszyn et al., 2009) are considered robust and agree with multiple previous studies from other regions of the Franklin LIP, such as the Victoria Island sills,Natkusiak volcanics, the Coronation sills and the Thule sills of Greenland (Palmer et al., 1983; Park, 1994; Buchan et al., 2000; Shellnutt et al., 2004). The original study (Denyszyn et al. 2009) includes a successful baked contact test at site GR and includes reversed-polarity directions (sites SG2 and NU1). Directional results obtained as part of the palaeointensity study carried out here will be compared to the published results to ensure consistency.

A total of 106 standard 1-inch size cylindrical specimens were donated from the original study by Denyszyn et al. (2009) for palaeointensity experiments. A total of 17 sites are included in this study, with samples per site ranging from 3 to 13. The locations of the 17 sites are shown in Figure 4.1a and the corresponding site mean palaeomagnetic directions from Denyszyn et al. (2009) are shown in Figure 4.1b.

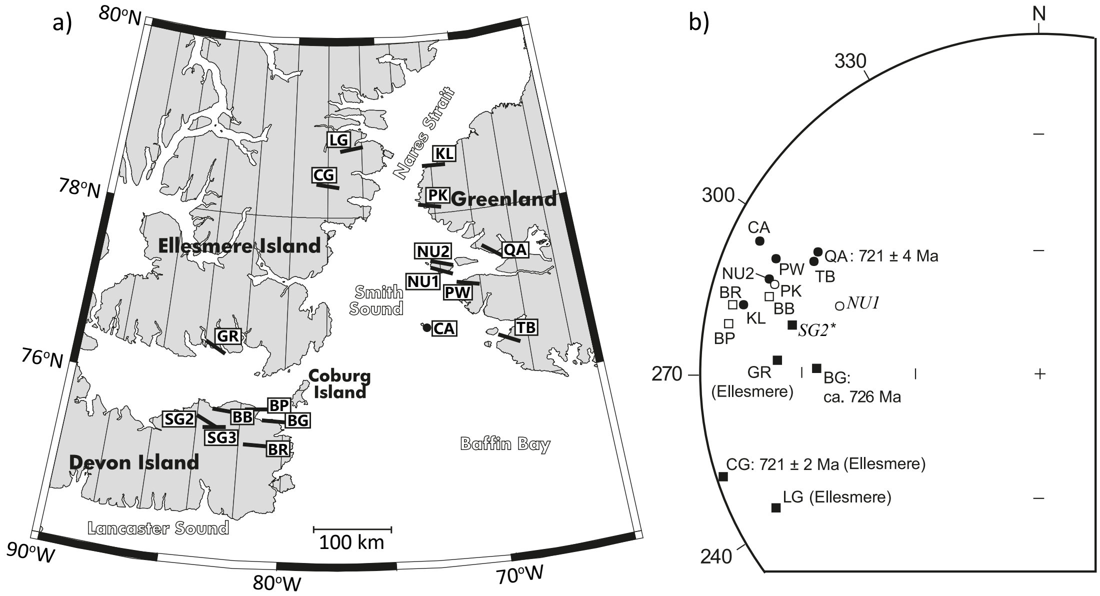

Figure 4.1. a) Map showing the position of the Franklin dykes and one sill used in this study. Dykes (black lines) are identified by their site names (in boxes). b) Equal-area stereoplot of the quality-filtered, site-mean palaeomagnetic characteristic remanence magnetisation directions obtained by Denyszyn et al. (2009) relating to the Franklin dykes and sill (site CA) in this study. Circles, Greenland data; squares, Canada data; solid, lower hemisphere; open, upper hemisphere. Italics indicate reversed polarity directions (sites NU1 and SG2). Asterisk indicates that directions were taken with magnetic compass only. Where ages are available these are given beside the site. [(a) and (b) are adapted from Denyszyn et al. (2009).] Site SG3 is not shown in (b) as its directions are transitional and was not included in the main table of the original paper by Denyszyn et al. (2009), although its location is identified in (a).

4.3 Methods

4.3.1 Rock magnetic experiments and microscopy

Hysteresis parameters were obtained alongside thermomagnetic curves of the saturation magnetisation (M_s-T) and isothermal remanent magnetisation (IRM) acquisition curves using a Magnetic Measurements Ltd Variable Field Translation Balance (VFTB) which was housed in a magnetically shielded room. All experiments were undertaken in ambient air. Due to the limited availability of material, an average of two powdered subsamples with masses in the order of 150 mg were used to represent each site.

The magnetic susceptibility of representative specimens (one or two per site) was measured using a MFK1-FA Kappabridge susceptometer with CS-3 furnace (AGICO) to high temperature (up to 700 °C) in an argon gas atmosphere. Several partial curves were measured with increasing maximum temperatures. A Viscous Remanent Magnetisation (VRM) experiment (Prévot, 1981) was carried out on 35 samples to identify their viscous coefficient (v), where;

(Eq. 4.1)

$$v = \frac{|\vec{M}_1 - \vec{M}_2|}{|\vec{M}_1 + \vec{M}_2|}$$

Samples were orientated with the Earth's field in the Z- position for three weeks (M_1), and the same in the Z+ position (M_2) followed by 3 weeks in a zero-field environment; declination, inclination and intensity were measured after each stage. Thin sections (one from each of four sites) were selected to represent a mixture of magnetomineralogies, as determined by rock magnetic results. These were examined using the Zeiss GeminiSEM 450 based within the University of Liverpool SEM Shared Research Facility. Backscatter electron imaging (BEI) and energy dispersive X-ray spectroscopy (EDS) were used for mineral identification and semi-quantitative elemental analyses

4.3.2 Absolute palaeointensities

All original one-inch specimens were halved to make 212 separate A and B half-inch specimens. Microwave specimens which are smaller were drilled from a half inch specimen. Specimen names consist of the site identifier; first two letters (or two letters and a number plus a dash in the case of sites SG2 and SG3), followed by the core number; a dash then separates the specimen number and whether it is from the A or B half of the original provided specimen. For example, specimen BB5-1A is from site BB, core 5, specimen 1A. Microwave specimens have an additional number at the end where more than one specimen is from the same half inch core e.g. BP6-1B3 indicates that this is the third microwave specimen obtained from specimen 1B, core 6, site BP. Sister specimens are defined as adjacent specimens from the same core, or microwave specimens from the same half-inch specimen. These are compared where possible using a multiple technique approach to assess palaeointensity, which can increase the experimental success rates and allow for cross-technique comparisons.

Three main methods were used here; the Shaw double heating technique (DHT; Tsunakawa & Shaw, 1994, Yamamoto et al., 2003), thermal Thellier (Thellier & Thellier, 1959, Tauxe & Staudigel, 2004) and the microwave method (Walton et al., 1992, Hill et al., 2002). All thermal Thellier and Shaw-DHT measurements were performed using a RAPID 2G superconducting rock magnetometer in a magnetically shielded cage where the residual field was less than 100 nT. The microwave experiments were carried out using the 14.2 GHz Tristan microwave palaeointensity system at the University of Liverpool (Hill et al., 2008).

The Shaw double heating technique (DHT) experiments (Tsunakawa & Shaw, 1994; Yamamoto et al., 2003) were undertaken using varying laboratory protocols to improve robustness of results. At a basic level, a palaeointensity can be derived by comparing the demagnetisation spectra of a natural remanent magnetisation (NRM) with a laboratory induced thermal remanent magnetisation (TRM). Any alteration that occurs due to the laboratory heating is estimated by comparing the demagnetisation spectra of an anhysteretic remanent magnetisation (ARM) imparted prior to, and post laboratory heating; the difference in ARM is a direct result of the alteration and is applied as a correction to the TRM. The ARM corrections are then performed again on a second laboratory heating in order to recover the initially imparted known field, thereby acting as a reliability check on the corrections used for the palaeointensity calculation (the DHT part).

All specimens were heated in a vacuum at a rate of 60 °C/ minute to 500 °C, followed by 5 °C/ minute to 610 °C where they were held at temperature before cooling. Thirty-three specimens were held at 610 °C for 45 minutes for the first and second heating. Laboratory TRM was imparted in a 20 μT DC field along the z-axis of the samples while ARM was imparted using a 100 μT bias field. A further 16 specimens were held for 20 (60) minutes the first (second) heating with a laboratory TRM of 20 μT DC field and an ARM bias field of 70 μT. The purpose for changing the input variables was to increase the robustness of the results by minimising any input biases. Specimens were stepwise demagnetised using alternating frequency (AF) steps of 5 – 10 mT to a maximal field of 100 mT. ARM's were imparted at 100 mT to coincide with the maximum AF demagnetisations.

Two Shaw-DHT experiments included the use of low-temperature demagnetisation (LTD), which is known to preferentially target remanence carried by multidomain grains (Yamamoto et al., 2003). LTD specimens were soaked in liquid nitrogen in a plastic dewar for 10 minutes and then removed and allowed to warm to room temperature in a zero field for 60 minutes. In the first instance, 16 specimens from 10 sites were subjected to a full Shaw LTD-DHT experiment with the addition of a non-LTD ARM (ARM_0); the two ARM_0 treatments were compared in order to quantify the MD component of remanence. We also compared Shaw-DHT results from two separate experiments, where one set of samples were treated with LTD and one set without. These were carried out on sister samples to check for any systematic bias that the treatment may have on the results.

Thermal Thellier experiments were used to measure 36 specimens from ten sites; these consisted of a sequence of paired heatings in air, to a set of increasing temperatures. The IZZI+ protocol was used (Tauxe & Staudigel 2004) which alternates the zero-field and infield steps, with partial thermal remanent magnetization (pTRM) checks after every two step pairs. The sequence of steps was repeated up to an average of 600 °C, with an infield laboratory bias field of 20 μT. A pre-treatment 5 mT AF cleanse was used in some experiments and compared to those without the treatment.

Twenty-six further experiments were carried out using the microwave system. Small cylindrical cores (5 mm diameter) are centred in the resonant cavity, where the microwave field couples with the magnetic system to demagnetise the sample. The IZZI+ protocol (as with the thermal Thellier experiments) was used with an additional requirement that the ChRM make an angle of at least 45 ° with the lab field; this achieves a compromise between minimising any non-ideal behaviour arising from multi domain effects while also being able to detect its presence (Yu and Tauxe, 2005; Hawkins et al., 2019). The microwave method has been demonstrated to produce equivalent results to thermal Thellier-style experiments (Biggin et al., 2007), and in some cases, improved results (Grappone et al., 2019). To further check the reliability of the successful palaeointensity estimates, we assessed potential biases related to anisotropy of remanence. We compared the angular difference between the last pTRM step used for the palaeointensity determination and the applied field direction (γ).

Palaeointensity results were quantitatively assessed using selection criteria parameters set out in the standardised palaeointensity definitions (Paterson et al., 2014) and are similar to those used in other studies (Yamamoto et al., 2003, Shcherbakova et al., 2017a).

For all experiments:

A maximum angular deviation; MAD $\leq$ 10 °

The angle between an anchored and unanchored fit of the directional data to the origin of an orthogonal vector plot; $\alpha \leq 15$ °

Number of measurements used for palaeointensity determination (N) ≥ 4

For Shaw (LTD)-DHT experiments:

The linear segment of the palaeointensity slope should include the maximum AF step identified as characteristic remanence, thereby reducing ambiguities in the calculation of palaeointensity.

The R^2 correlation (rN) of the palaeointensity $slope_N$ (demagnetisation spectra NRM/ TRM_1*; Yamamoto et al., 2003) ≥ 0.990

$Slope_T$ (demagnetisation spectra TRM_1/ TRM_2*; Yamamoto et al., 2003) = 1 ± 0.05 (Class A result) and ± 0.10 (Class B result)

The R^2 correlation (rT) of the $slope_T \geq 0.990$

Fraction of coercivity used in palaeointensity determination (fN) ≥ 0.25 (Class A result) and ≥ 0.20 (Class B result)

Thellier IZZI+ (thermal and microwave)

NRM fraction used for the best-fit on the plot of NRM lost versus TRM gained (Arai diagram) determined entirely by vector difference sum calculation; *FRAC* ≥ 0.35 (Class A result) and ≥ 0.25 (Class B result)

The slope of the best-fit line of the selected TRM and NRM points on the Arai plot, or scatter parameter; $\beta \leq 0.1$

Number of pTRM checks > 2

The maximum absolute difference produced by a pTRM check, normalized by the total TRM (dCK) ≤ 20 %

The maximum absolute difference produced by a pTRM check, normalized by the length of the best-fit line (DRAT) ≤ 15 %

The sum of the absolute pTRM difference (CDRAT) ≤ 20 %

The curvature of the linear section of a selected palaeointensity slope (k′) ≤ 0.48

4.4 Results

4.4.1 Rock magnetic and microscopy

Rock magnetic and microscopy results are presented in Figures 4.2 and 4.3 and Supplementary Figures B1.1 and B1.2. Hysteresis parameters of representative specimens are consistent with grain populations located predominantly in the so-called pseudo single-domain state and are summarised in a Day plot (Day et al. 1977) (Figure 4.2a). A small number of subsamples (QA11-1, QA4-1A & BB7-5A) locate close to the MD section however, samples from site QA also locate in the main cluster of results. VRM coefficients (v) are generally acceptable (≤ 10 %), however, higher values of 14 % or greater are observed from sites GR, LG, PK, BB, and samples from site BG exceed 100% (Figure 4.2b).

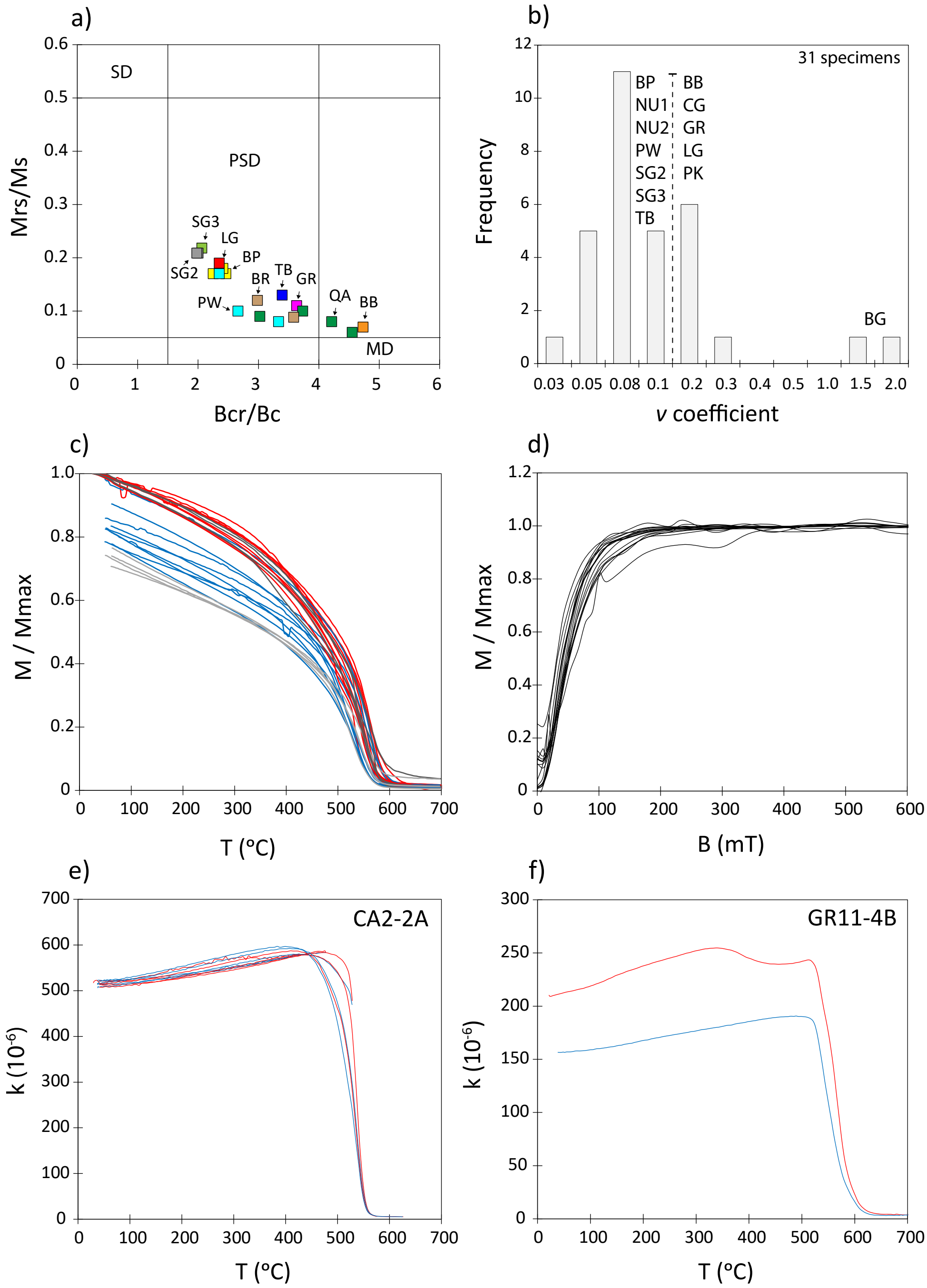

Figure 4.2. a) Day plot of the hysteresis parameters (Day et al., 1977). M_{rs}/M_s, remanent saturation magnetisation/ saturation magnetisation; B_{cr}/B_c, coercivity of remanence/ coercivity. b) Histogram of VRM results. The dashed line separates sites according to whether they have v coefficients of less

or more than 0.1 (10 %). c) Accepted M_s-T curves; red, heating; blue, cooling; rejected M_s-T curves; dark grey, heating; light grey, cooling. M/ M_{MAX}, magnetisation normalised by the maximum value; T, temperature. d) IRM curves normalised. e & f) Representative high-temperature/ susceptibility reversible (e) and non-reversible (f) curves. κ, susceptibility; T, temperature. Diagram (f) also shows an inflection ~300 °C. Red lines, heating curve; blue lines, cooling curve.

M_s-T curves (Figure 4.2c) indicate single Curie temperatures of between 550 and 590 °C suggesting that the main magnetic carriers are low titanium-titanomagnetite (Dunlop et al., 1998). Curves are separated according to their reversibility at room temperature with a 20 % threshold, however, consistent behaviour is observed across all specimens and sites with only small differences in reversibility. IRM curves saturate by 180 mT (Figure 4.2d) with no indication of high coercivity minerals present suggesting that the remanence is most likely carried by (titano) magnetite.

Susceptibility on heating (κ-T) curves show a range of reversibility and suggest equivalent Curie temperatures to M_s-T curves. Many samples show no clear evidence of alteration (Figure 4.2e), however, as expected from rocks of this age, some κ-T curves are less reversible and show a slight inflection at ~300 °C (Figure 4.2f), indicating mild low-temperature oxidation; these are likely in response to reported hydrous alteration (Denyszyn et al., 2009); these require more careful handling (diagrams of additional κ-T curves are found in Supplementary Figure B1.1).

SEM results show two distinct opaque grains, indicating that samples from a particular site would either comprise of sizes ~5 µm (Figures 4.3a & b), and ~100 µm (Figures 4.3c & d). Larger grains appear to show alteration textures consistent with low-temperature oxidation. Grains in one sample (Figure 4.3d) had also undergone oxyexsolution, likely during primary cooling, such that lamellae of ilmenite and Ti-poor titanomagnetite were visible. Details of the EDS spot analysis is found in Supplementary Figure B1.2. Although these much larger grains are not the stable remanence carriers, potential alteration effects in samples from these sites are considered in detail, later in the manuscript.

The rock magnetic and microscopy results suggest that approximately half of the 17 sites (BP, CA, NU1, NU2, PW, SG3, QA and TB) show promise for producing reliable palaeointensities and that the remainder have either been subjected to various degrees of alteration or are likely to suffer from alteration in any laboratory heatings.

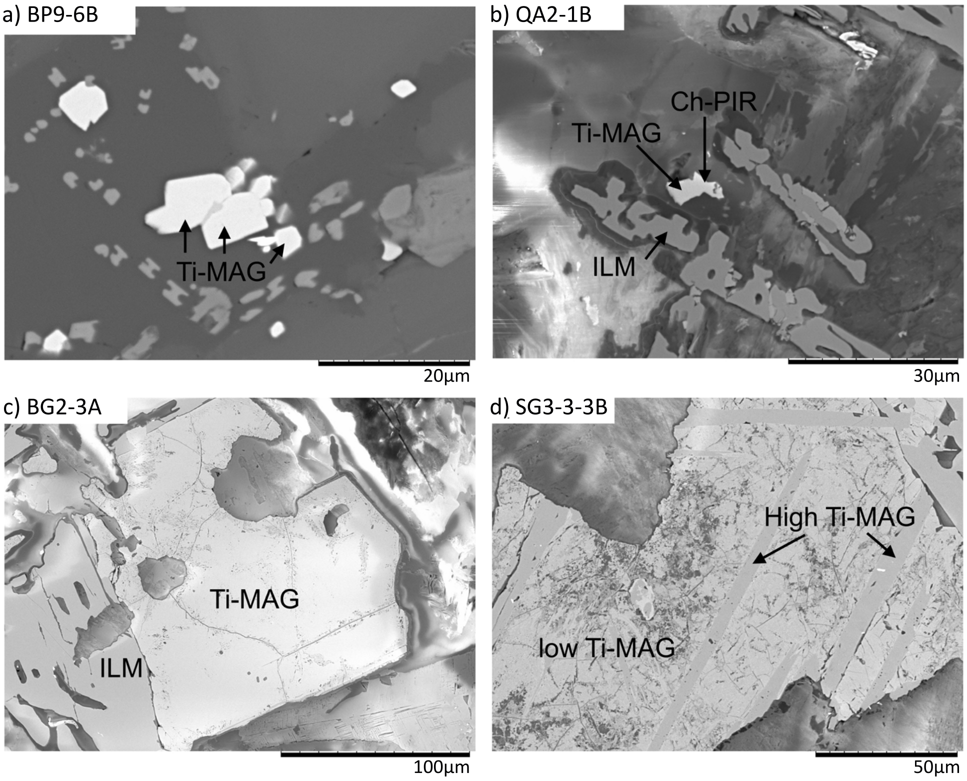

Figure 4.3. Examples of mineral fabrics observed using a scanning electron microscope from four sites. a & b) Specimens BP9-6B and QA2-1B showing fine low-Ti titanomagnetite grains which appear pristine. c) Specimen BG2-3A shows much larger ilmenite and low-Ti titanomagnetite grains (~100um), with cracks consistent with alteration. d) Specimen SG3-3-3B shows large, altered grains with further evidence of alteration. Ti-MAG, Titanomagnetite; ILM, Ilmenite, Ch-PIR, Chalcopyrite.

4.4.2 Absolute palaeointensities

Pilot Shaw-DHT experiments were combined with preliminary rock magnetic results to identify the most suitable sites and specimens for palaeointensity analysis. Sites BB and PK were rejected after this stage due to poor VRM coefficients, uninterpretable demagnetisation of the NRM or failed palaeointensity experiments (Supplementary Table B2.1). Successful palaeointensity results were obtained using all three methods, from 10 out of 16 sites, ranging from 1.1 to 9.9 μT. Three of these sites (BG, BR and GR) yield less than three individual results per site and are not used to calculate a VDM. Site-mean palaeointensity estimates were determined from the unweighted average of successful results from all methods from a given site. Specimen level results are found in Supplementary Tables B2.1 – B2.3 for Shaw-DHT, Thermal Thellier IZZI+, and microwave IZZI+ respectively and representative sample plots are shown in Figures 4.4 and 4.5. A summary of all successful palaeointensity results is presented in Table 4.1.

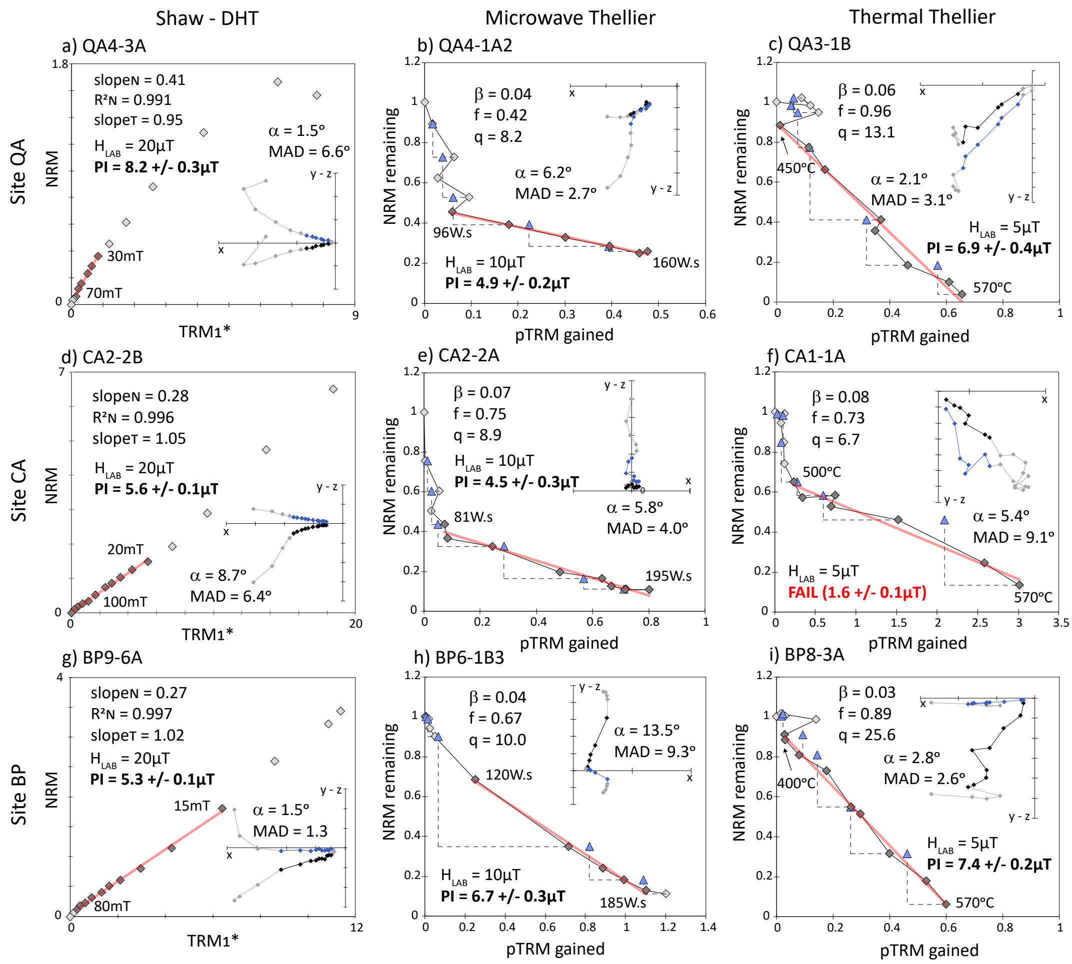

Figure 4.4. A selection of Arai plots from the microwave and thermal Thellier experiments, and Shaw pseudo-Arai plots (units 10^{-6} Am²). Each column includes only results from the same method; each row includes only results from the same site. CA2-2A and CA2-2B are sister specimens. Red line, best-fit line for palaeointensity points used; blue triangles, pTRM checks; dashed lines, link the pTRM check to the position that the check was carried out. Dark grey points are used in palaeointensity determination; light grey points are not used. Orthogonal plot data corresponding to (Pseudo)-Arai plots are highlighted in black and blue with the remaining points greyed out. An explanation of the selection criteria is given in Section 4.3.2.

The Shaw-DHT method produced the most successful paleointensities with 24/ 59 specimens yielding positive results across nine sites (Figures 4a, d & g; Supplementary Table B2.4;). Shaw (LTD)-DHT results range from 1.1 to 9.9 μT (4.8 μT mean). A comparison of LTD treated ARM versus non-LTD treated ARM (Supplementary Figure B1.3) shows that LTD-prone remanence was completely removed by 25 mT for all specimens. In addition, no systematic intensity differences were observed between specimens which underwent LTD and those that did not (Supplementary Figure B1.4); most sister specimen results are within 1 – 2 μT. SlopeA_1 (ARM_0/ ARM_1), which is a measure of ARM alteration, indicates that a mean correction of 28 % was applied. A slight correlation was observed in which larger corrections (slopeA_1 further from 1) are associated with higher palaeointensity results (Supplementary Table B2.1).

Changing the first heating duration from 45 minutes to 20 minutes, and the second heating from 45 to 60 minutes, in the Shaw-DHT experiments, produced a $slope_T$ further from unity in sister samples but did not appear to affect the palaeointensity results. We therefore allow for a slightly relaxed $slope_T$ criterion (See selection criteria, section 4.3.2) and define these results as class B. Additionally, class B results are also defined in results with a single relaxed criterion (fN > 0.2; Supplementary Table B2.1); the inclusion of these results does not significantly affect the within-site scatter and they are in close agreement with results using the stricter criterion. Where a relaxed fN is accepted, the minimum number of steps required in the palaeointensity slope (N) is increased from four to six.

Unsuccessful specimens typically failed to meet criteria associated with the correlation of the NRM-TRM slope or due to a lack of reproducibility ($slope_T$ criterion); in some cases, the characteristic directions were also not sufficiently well-defined. The directions obtained from the successful Shaw-DHT paleointensity results here are consistent with those from the original study (Denyszyn et al., 2009: Supplementary Table B2.1).

Thermal Thellier and microwave experiments produced 5/ 36 and 10/ 26 accepted results (Supplementary Tables B2.2 & B2.3) respectively. The results are similar to those of the Shaw experiments, with Microwave ranging from 3.5 to 6.7 μT (4.5 μT mean) and thermal Thellier from 1.0 to 7.4 μT (4.6 μT mean). In some accepted results, Arai diagrams display two-slope behaviour, the change in which corresponds to a change between secondary and characteristic remanence direction (e.g., Figures 4.4f & 4.5b), rather than requiring multi-domain effects to explain (Smirnov et al., 2017, Hawkins et al., 2019). The high-temperature sections of most two-slope Arai plots correspond to the primary remanence, as observed in the associated orthogonal diagram; this is particularly apparent in the very low result (1.6 µT) of specimen BG1-4B (Figure 4.5a). An instance where this is slightly more difficult to discern is observed in the Arai diagram for specimen BP5-1A (Figure 4.5b); here, a prominent two-slope is associated with a less clear change in direction, however, a maximum of two earlier steps could be interpreted as primary and would not change the result. A straight-line fit from 20 °C to 565 °C was also determined for this sample and would only alter the palaeointensity result from 1 µT to 2.6 µT (Supplementary Figure B1.5).

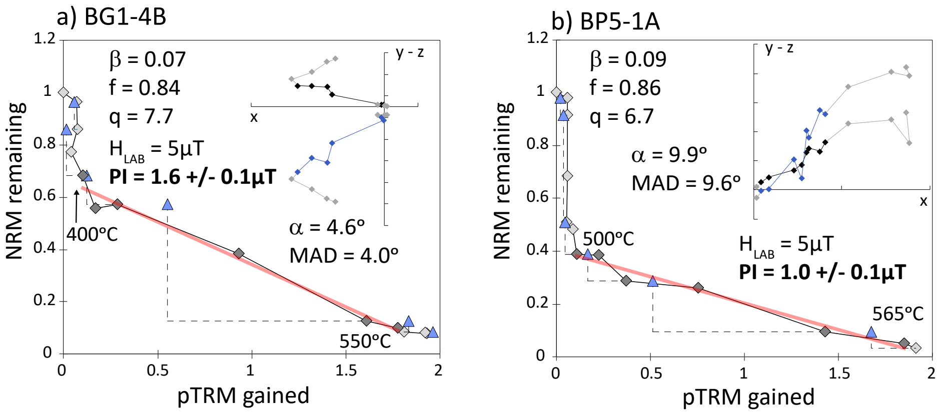

Figure 4.5. a & b) Additional thermal Thellier Arai diagrams with associated orthogonal plots. See selection criteria (section 4.3.2) and caption in Figure 4.4 for further details.

Common reasons for failure in microwave and thermal Thellier IZZI experiments, associated with multi-domain behaviour and alteration of the magnetic carriers, are excessive 'zigzagging' and failure of pTRM checks in Arai-plots (Supplementary Figure B1.6). Several specimens did not produce interpretable Arai-plots; these were mostly from specimens where no AF pre-measurement steps were applied. A relaxed criterion is used (*FRAC* ≥ 0.25) in a class B result for microwave specimen QA4-1A2. The results from a direct comparison of eleven sister specimens from Shaw-DHT and microwave methods are in good agreement (Supplementary Figure B1.7), producing an R^2 correlation of 0.63; this is improved by the removal of a single outlier to R^2 = 0.90.

The highest success rate is achieved from the Shaw-DHT experiments, most likely because the method applies a correction for any alteration caused by heating in the laboratory. Shaw type experiments are also expected to be less prone to domain state effects than Thellier-type because they use a single full heating which means that Thellier's laws of independence, additivity and reciprocity are less likely to fail. Microwave Thellier experiments are also more successful than thermal; this may be because the microwave / magnon system (analogous to heat/ phonon) may reduce bulk specimen heating (e.g. Hill & Shaw, 2000, Suttie et al., 2010). The thermal Thellier results are in agreeance with, and supported by, the partial reliance on non-Thellier data, which come from two separate and well-documented palaeointensity methods (Tsunakawa & Shaw, 1994, Hill & Shaw, 1999, Hill & Shaw, 2000, Yamamoto et al., 2003). Results were also tested using a stricter set of selection criteria; this had no notable effect on site-mean results other than to decrease the success rates slightly (Supplementary Table B2.5).

A consistently weak field is recorded with successful results obtained from eleven sites and by all three palaeointensity methods (Table 4.1). Site-mean inclinations (Denyszyn et al., 2009) were used to calculate virtual dipole moments (VDMs) that ranged between 3.6 and 19.3 ZAm^2. Four of the eleven site-means are defined by fewer than three palaeointensities, consequently no VDM is determined for these sites; they are retained for comparison only.

4.5 Discussion

4.5.1 Palaeointensity reliability

Rock magnetic and palaeointensity results largely concur; sites associated with κ-T curves which share common features such as slight inflections at ~300 °C (CG, LG, KL; Figures 4.3h to j) fail to produce any successful palaeointensities. Sites associated with high (> 10 %) VRM coefficients (GR, LG, BG) also fail to produce successful palaeointensity results with the exception of one result from site BG and one from GR, neither of which are used in the final determination of VDM results because the number of successful results from these sites are less than three. SEM backscatter electron images depicting fine grains are from two sites with the highest palaeointensity success rates (BP and QA) in contrast with those with large, altered grains (sites BG and SG3).

Site	*U/Pb date* (Ma)	*Type*	*Lat* (°N)	*Lon* (°W)	*Dec* (°)	*Inc* (°)	*Ndir*	*k*	a_{95} (°)	*F* (μT)	$б_F$ (μT)	N_{PI}	N_{mic}	N_{Shaw}	N_{Thel}	*VDM* ($Z\,Am^2$)	Q_{PI}
BB	-	*Dyke*	*75.7*	*83.0*	*286.0*	*-18.0*	*9*	*91*	*5.4*	-	-	-	-	-	-	-	-
BG	*726 (+/- 24)*	*Dyke*	*75.6*	*80.2*	*271.3*	*34.5*	*7*	*24*	*12.6*	*1.6*	-	*1*	-	-	*1*	*3.6*	*5*
BP	-	*Dyke*	*75.8*	*81.3*	*279.2*	*-7.5*	*9*	*70*	*5.2*	*5.5*	*2.5*	*7*	*1*	*3*	*3*	*14.1*	*8*
BR	-	*Dyke*	*75.5*	*81.6*	*282.6*	*-7.5*	*7*	*226*	*4.0*	*4.9*	*0.3*	*2*	*2*	-	-	*12.6*	*6*
CA	-	*Sill*	*76.7*	*73.2*	*295.4*	*9.3*	*5*	*234*	*5.0*	*3.9*	*1.8*	*4*	*2*	*2*	-	*9.9*	*6*
CG	-	*Dyke*	*78.3*	*77.1*	*251.9*	*1.8*	*7*	*46*	*9.0*	-	-	-	-	-	-	-	-
GR	-	*Dyke*	*76.4*	*83.0*	*272.9*	*23.3*	*8*	*190*	*4.0*	*2.3*	-	*1*	-	*1*	-	*5.6*	*6*
KL	-	*Dyke*	*78.7*	*70.7*	*283.0*	*10.9*	*8*	*74*	*6.5*	-	-	-	-	-	-	-	-
LG	-	*Dyke*	*78.7*	*75.7*	*243.1*	*13.7*	*7*	*91*	*6.4*	-	-	-	-	-	-	-	-
NU1	-	*Dyke*	*77.4*	*71.6*	*108.3*	*37.7*	*8*	*59*	*7.3*	-	-	-	-	-	-	-	-
NU2	-	*Dyke*	*77.4*	*71.5*	*289.9*	*16.3*	*8*	*123*	*5.0*	*4.4*	-	*1*	-	*1*	-	*11.0*	*6*
PK	-	*Dyke*	*77.9*	*72.2*	*288.7*	*-18.5*	*7*	*132*	*5.3*	-	-	-	-	-	-	-	-
PW	-	*Dyke*	*77.2*	*70.8*	*293.6*	*15.9*	*7*	*144*	*5.1*	*3.1*	*0.3*	*4*	-	*4*	-	*7.9*	*6*
QA	*720 (+/-3)*	*Dyke*	*77.5*	*68.9*	*298.8*	*26.1*	*6*	*106*	*6.5*	*8.1*	*0.8*	*5*	*1*	*3*	*1*	*19.3*	*9*
SG2	-	*Dyke*	*75.7*	*84.0*	*101.2*	*-26.4*	*6*	*103*	*6.6*	*2.4*	*1.3*	*4*	*2*	*2*	-	*5.7*	*6*
SG3(T)	-	*Dyke*	*~75.7*	*~84.0*	*68.9*	*61.4*	*10*	*123*	*4.4*	*2.9*	*0.2*	*3*	-	*3*	-	*4.8*	*5*

Table 4.1. A summary of paleomagnetic results. D (°), magnetic declination; I (°), magnetic inclination; Ndir, number of specimens used to determine the mean direction; k, the Fisher precision parameter; α95, 95 % confidence limit on the mean direction; F, field intensity; σ_P, absolute standard deviation; N_{PI}, number of palaeointensity results; N_{mic}, N_{Shaw}, N_{Thel} are the number of results for each method; VDM, virtual dipole moment; Q_{PI}, quality score of palaeointensity; ~, SG3 site lat & long estimated from map in Denyszyn et al. (2009). Directions are from Denyszyn et al. (2009). Italics denote sites with n < 3; (T), Transitional. Site-mean palaeointensity results are unweighted average of all successful results from all methods for a given site.

These correlations suggest that the applied palaeointensity selection criteria were successful in filtering out unreliable recorders. A small number of specimens (e.g. those from site QA) have hysteresis parameters that suggest they were some of the least suitable (Figure 4.2a) but were retained on the basis of their κ-T curves and SEM observations (Figure 4.3) and gave high quality palaeointensity results.

Due to vortex domain-state bulk properties and the potential of field underestimation from using high-temperature segments of two-slope Arai diagrams, careful scrutiny of the data is applied to determine the possibility, if any, of MD bias in the final palaeointensity estimations. We find that there are numerous lines of evidence to suggest that the successful results are free from such bias:

There is reasonable evidence (high *FRAC* with low β, low curvature, domain state independent method) that the final presented estimates are not significantly biased by multidomain behaviour during the experiment; and as such, we award a pass in our assessment of the quality of palaeointensity (Q_{PI}; Biggin & Paterson, 2014) for the MD criterion; evidence that the final estimate was not significantly biased by multidomain behaviour. All sites are assigned Q_{PI} scores which range between 5 and 9 (Table 4.1 and Supplementary Table B2.6). Only two sites (BG and QA) are associated with specific radiometric ages but as part of a single large igneous province, all dykes from this study can reasonably be assumed to have been emplaced over just a few million years (Bryan & Ernst, 2008) and their palaeointensities are derived from an interpreted primary component of remanence, which satisfies the AGE criterion; a reliable age and palaeomagnetic behaviour consistent with palaeointensity derived from a primary component of remanence.

All sites also pass ALT criterion; reasonable evidence that the final estimate was not significantly biased by alteration occurring during the experiment. Any steps associated with alteration were identified by pTRM checks and excluded, or corrected using the ARM technique (Shaw method) which was itself subsequently checked. SEM images indicate that for two sites (BP and QA), the remanence is carried by unaltered grains that may reasonably be assumed to have formed during primary cooling, and therefore satisfy the TRM criterion; evidence that the component of remanence in the bulk of samples is likely a TRM, whereas the poor quality observed in thin sections from sites SG3 and BG are cause for failure. We adopt a cautious and strict approach to the remaining sites where no SEM evidence is available; these sites are also are not awarded a pass, although there is no reason to expect at least some of these sites would pass, particularly the sites with the highest quality rock magnetic results.

The low field values made it difficult to pass the STAT criterion; a minimum of 5 individual sample estimates per unit with low dispersion, as they are associated with a higher relative standard deviation. It is worth highlighting that the absolute standard deviations are small, ranging between 0.2 μT and 2.6 μT. All sites pass the ACN criterion; the final estimate was not significantly biased by anisotropy of TRM, cooling rate effects, and nonlinear TRM effects. Calculations of γ -values indicate minimal anisotropy; cooling rate is considered unproblematic because the specimens were collected from dyke margins, with rock magnetic evidence of vortex-state grains, and finally, nonlinear TRM effects were tested by using several bias fields in the multiple palaeointensity experiments.

5.2 Significance of results for the geodynamo

While we note that palaeointensity estimates from seven rapidly cooled units are unlikely to provide a strong averaging of secular variation, we nevertheless highlight their consistent low values across well-dispersed sites (and methods), ranging from 1.0 to 9.9 μT with a median of 4.4 μT. We therefore consider it very likely that the time-average field was low at this time, noting also, that the presence of several reversed-polarity directions suggests at least one reversal of the geomagnetic field has been captured. These new data allow the first characterisation of the geomagnetic field from any time within the mid-Neoproterozoic.

An analysis of the virtual geomagnetic pole (VGP) dispersion of the Franklin LIP data from Denyszyn et al. (2009) yields Angular dispersion of 11.6 ° ± 3.7 ° at a palaeolatitude of 7 °N (N = 23). This is approximately equivalent to that expected from analysis of the PSV10 data set of volcanics from the last 10 Myr (Cromwell et al., 2018; Doubrovine et al., 2019; Supplementary Table B2.4 & Supplementary Text B3). This supports the Franklin LIP being emplaced during a time period when the average axial dipole dominance was similar to recent times (Biggin et al., 2020) despite the substantially reduced average dipole moment.

We provide an interpretation of the most current palaeointensity global database for the 300 – 2500 Ma period. All data is taken from the PINT database (v.2015.05; http://earth.liv.ac.uk/pint/; Biggin et al., 2015). Data older than 500 Ma has been assessed according to the Q_{PI} criteria and assigned scores (Biggin et al., 2015). A filter has been applied to all of this data to only include those with a Q_{PI} score of 3 of more. In addition, a limit is applied so that a minimum of three samples per cooling unit have been used to calculate the VDM. These generalised minimum criteria are accompanied by the removal of results of the ~1300 Ma Gardar lava flows in Greenland (Thomas & Piper, 1992, 1995; Thomas, 1993) believed now to be over-estimations of the palaeofield, and have been superseded by (Kodama et al., 2019).

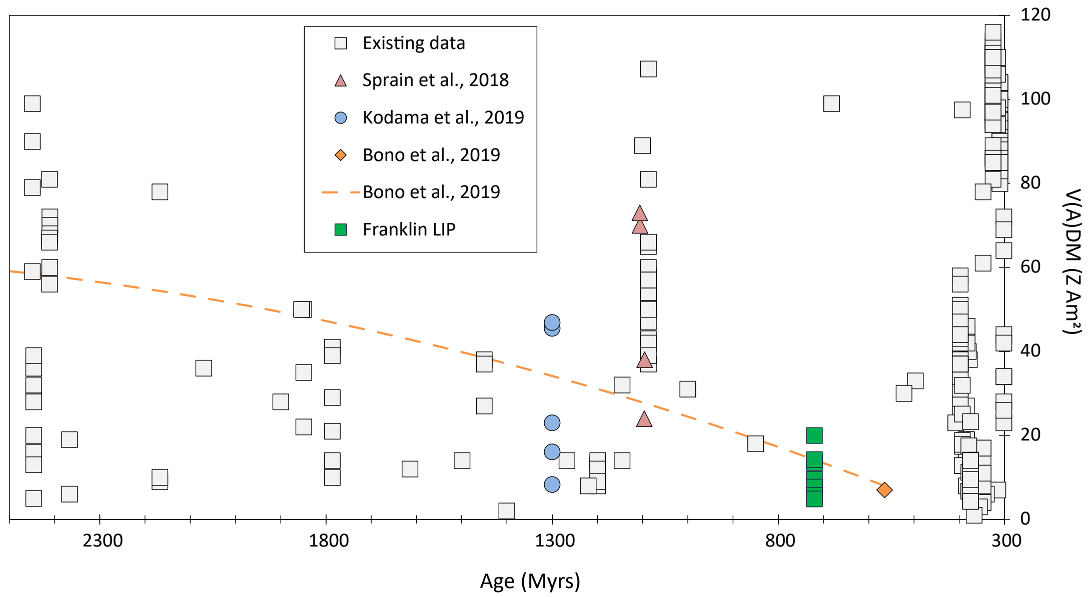

Figure 4.6. Virtual (axial) dipole moment data (V(A)DM) through time (300 – 2500 Ma). Data taken from the PINT database (v.2015.05; http://earth.liv.ac.uk/ pint/; Biggin et al., 2015) with the addition of recent data from Shcherbakova et al., 2017, Sprain et al., 2018, Hawkins et al., 2019, Kodama et al., 2019 and Bono et al., 2019. The dashed line is the weighted second-order polynomial regression of Precambrian field strength data by Bono et al., 2019. Data > 500 Myr has been filtered to exclude VDM data with Q_{PI} < 3, N <3.

These new data provide an additional test of recent numerical models and statistical hypotheses which suggest alternative ages for ICN spanning more than 300 Ma (Labrosse, 2014; Driscoll, 2016; Landeau et al., 2017). Driscoll (2016) predicts that the geodynamo entered a weak-field state during the period prior to ICN (~1000– 650 Ma), following a dipole high (1.0–1.7 Ga). Palaeointensity data do not support the long-term dipole high for the early part of this interval (Figure 4.6), with the only reliable high VDM estimates (> 60 ZAm^2) recorded at ~1.1 Ga from the Midcontinent Rift (Kulakov et al., 2013, Sprain et al., 2018). However, the hypothesis provided by Driscoll for the long-term intensity trend of Earth history fits well with these most recent observations. The unique high at ~1.1 Ga is otherwise difficult to explain apart from that it may result from substantial variation about the long- term trend because of changing core–mantle boundary conditions, despite the decline in thermal convection reducing the core to a low power state.

Biggin et al. (2015) hypothesised that nucleation may be linked to an increase observed in the average VDM between 1 and 1.5 Ga. Our results do not support this hypothesis but, similarly, cannot yet rule it out. There remains a severe paucity of data in the interval 600–1100 Ma and, considering the fluctuations that are observed in the Phanerozoic geomagnetic field (Biggin et al., 2012), it is possible that any of the Precambrian studies may capture a temporally or spatially limited anomaly that is not representative of the very long-term average.

Additional complications may exist in using palaeointensity as a proxy for ICN. Palaeointensity records are currently too sparse to allow a meaningful time-series analysis of variations occurring even on 100 Myr timescales through Precambrian time. Recent work supports periodic low-field observations occurring 10–100 Myr prior to the onset of three Phanerozoic superchrons (Shcherbakova et al., 2017, 2020; Bono et al., 2019; Doubrovine et al., 2019; Hawkins et al., 2019). This approximately 200 Myr quasi-periodicity in dipole strength most likely reflects mantle forcing of the geodynamo via changes in the core–mantle heat flux (Biggin et al., 2012). It is possible that such an oscillation extending back into the Proterozoic could account for variations observed back to at least 1100 Ma. If this were the case, then any signature of ICN and growth will be modulated by a higher frequency mantle signal, requiring a good deal more data in poorly sampled time periods.

Whilst there remains some uncertainty over the agreement of compiled datasets with the various hypotheses, we note that these new results are consistent with an inner core which had not yet formed. A palaeofield at ~720 Ma of slightly higher strength than the recent ultralow results found ~160 Ma later in the Ediacaran (Bono et al., 2019) fits well on the long-term polynomial trend modelled in the same paper (Figure 4.6); however, many more data are required to say anything meaningful regarding the age of ICN with any degree of certainty.

4.6 Conclusions

We have reported the first palaeointensity results from the middle of a 300 Myr mid-Neoproterozoic gap in the global palaeointensity database. Providing evidence of a weak time-averaged geomagnetic field at ~720 Myr, our estimates of the VDM, ranging from 3.6 to 19.3 ZAm^2 ($N \geq 3$), are acquired from six widespread dykes and one sill of the Franklin Large Igneous Province. A further four sites reporting equivalent successful results with $N < 3$ are not used to determine VDMs. Consistently low field values are observed within and between site (and method), with 39 results ranging from 1.1 to 9.9 μT. Displaying a high degree of consistency in absolute terms, site mean standard deviations are less than 3 μT. The results are also associated with high Q_{PI} values (between 5 and 9).

These new results are consistent with an inner core which had yet to form, although a severe paucity in global records remains, particularly for the Neoproterozoic era, making any meaningful conclusions regarding the age of ICN unfeasible. They do provide a real constraint at a crucial time, on recent numerical models and statistical hypotheses, and may be significant in narrowing the argument for alternative ages for ICN.

4.7 References cited

Aubert, J., Labrosse, S., & Poitou, C. (2009). Modelling the palaeo-evolution of the geodynamo. *Geophysical Journal International*, *179*(3), 1414–1428. https://doi.org/10.1111/j.1365-246X.2009.04361.x

Biggin, Bono, Meduri, Sprain, Davies, Holme, Doubrovine, P. . (2020). Quantitative estimates of average geomagnetic axial dipole dominance in deep geological time. *Nature Communications*.

Biggin, A. J., Steinberger, B., Aubert, J., Suttie, N., Holme, R., Torsvik, T. H., et al. (2012). Possible links between long-term geomagnetic variations and whole-mantle convection processes. *Nature Geoscience*, *5*(8), 526–533. https://doi.org/10.1038/ngeo1521

Biggin, A. J., Piispa, E. J., Pesonen, L. J., Holme, R., Paterson, G. A., Veikkolainen, T., & Tauxe, L. (2015). Palaeomagnetic field intensity variations suggest Mesoproterozoic inner-core nucleation. *Nature*, *526*(7572), 245–248. https://doi.org/10.1038/nature15523

Biggin, A.J., Perrin, M., & Shaw, J. (2007). A comparison of a quasi-perpendicular method of absolute palaeointensity determination with other thermal and microwave techniques. *Earth and Planetary Science Letters*, *257*(3–4), 564–581. https://doi.org/10.1016/j.epsl.2007.03.016

Biggin, A. J., & Paterson, G. A. (2014). A new set of qualitative reliability criteria to aid inferences on palaeomagnetic dipole moment variations through geological time. *Frontiers in Earth Science*, *2*(October), 1–9. https://doi.org/10.3389/feart.2014.00024

Biggin, A. J., Strik, G. H. M. A., & Langereis, C. G. (2009). The intensity of the geomagnetic field in the late-Archaean: New measurements and an analysis of the updated IAGA palaeointensity database. *Earth, Planets and Space*, *61*(1), 9–22. https://doi.org/10.1186/BF03352881

Bono, R. K., Tarduno, J. A., Nimmo, F., & Cottrell, R. D. (2019). Young inner core inferred from Ediacaran ultra-low geomagnetic field intensity. *Nature Geoscience*, *12*(2), 143–147. https://doi.org/10.1038/s41561-018-0288-0

Bryan, S. E., & Ernst, R. E. (2008). Revised definition of Large Igneous Provinces (LIPs). *Earth-Science Reviews*, *86*(1–4), 175–202. https://doi.org/10.1016/j.earscirev.2007.08.008

Buchan, K. L., Mertanen, S., Park, R. G., Pesonen, L. J., Elming, S. Å., Abrahamsen, N., & Bylund, G. (2000). Comparing the drift of Laurentia and Baltica in the Proterozoic: The importance of key palaeomagnetic poles. *Tectonophysics*, *319*(3), 167–198. https://doi.org/10.1016/S0040-1951(00)00032-9

Cromwell, G., Johnson, C. L., Tauxe, L., Constable, C. G., & Jarboe, N. A. (2018). PSV10: A Global Data Set for 0–10 Ma Time-Averaged Field and Paleosecular Variation Studies. *Geochemistry, Geophysics, Geosystems*, *19*(5), 1533–1558. https://doi.org/10.1002/2017GC007318

Davies, C., Bono, R.K., Meduri, D.G., Greenwood, S., Biggin, A. J. (2021). Dynamo constraints on the long-term evolution of Earth's magnetic field strength. *Geophysical Journal International*.

Davies, C., Pozzo, M., Gubbins, D., & Alfè, D. (2015). Constraints from material properties on the dynamics and evolution of Earth's core. *Nature Geoscience*, *8*(9), 678–685. https://doi.org/10.1038/ngeo2492

Day, R., Fuller, M., & Schmidt, V. A. (1977). Hysteresis properties of titanomagnetites: Grain-size and compositional dependence. *Physics of the Earth and Planetary Interiors*, *13*(4), 260–267. https://doi.org/10.1016/0031-9201(77)90108-X

Denyszyn, S. W., Halls, H. C., & Davis, D. W. (2004). A paleomagnetic, geochemical and U-Pb geochronological comparison of the thule (Greenland) and Devon Island (Canada) dyke swarms and its relevance to the nares strait problem. *Polarforschung*, *74*(1–3), 63–75.

Denyszyn, S. W., Halls, H. C., Davis, D. W., & Evans, D. A. D. (2009). Paleomagnetism and U-Pb geochronology of Franklin dykes in high arctic Canada and Greenland: A revised age and paleomagnetic pole constraining block rotations in the Nares Strait region. *Canadian Journal of Earth Sciences*, *46*(9), 689–705. https://doi.org/10.1139/E09-042

Doubrovine, P. V., Veikkolainen, T., Pesonen, L. J., Piispa, E., Ots, S., Smirnov, A. V., et al. (2019). Latitude Dependence of Geomagnetic Paleosecular Variation and its Relation to the Frequency of Magnetic Reversals: Observations From the Cretaceous and Jurassic. *Geochemistry, Geophysics, Geosystems*, *20*(3), 1240–1279. https://doi.org/10.1029/2018GC007863

Driscoll, P., & Bercovici, D. (2014). On the thermal and magnetic histories of Earth and Venus: Influences of melting, radioactivity, and conductivity. *Physics of the Earth and Planetary Interiors*, *236*, 36–51. https://doi.org/10.1016/j.pepi.2014.08.004

Driscoll, P. E. (2016). Simulating 2 Ga of geodynamo history. *Geophysical Research Letters*, *43*(11), 5680–5687. https://doi.org/10.1002/2016GL068858

Dunlop, D., Özdemir, Ö., & Fuller, M. D. (1998). Rock Magnetism: Fundamentals and Frontiers. *Physics Today*. https://doi.org/10.1063/1.882466

Grappone, J. M., Biggin, A. J., & Hill, M. J. (2019). Solving the mystery of the 1960 Hawaiian lava flow: Implications for estimating Earth's magnetic field. *Geophysical Journal International*, *218*(3), 1796–1806. https://doi.org/10.1093/gji/ggz252

Gubbins, D., Alfè, D., Davies, C., & Pozzo, M. (2015). On core convection and the geodynamo: Effects of high electrical and thermal conductivity. *Physics of the Earth and Planetary Interiors*, *247*, 56–64. https://doi.org/10.1016/j.pepi.2015.04.002

Hawkins, L. M. A., Anwar, T., Shcherbakova, V. V., Biggin, A. J., Kravchinsky, V. A., Shatsillo, A. V., & Pavlov, V. E. (2019). An exceptionally weak Devonian geomagnetic field recorded by the Viluy Traps, Siberia. *Earth and Planetary Science Letters*, *506*, 134–145. https://doi.org/10.1016/j.epsl.2018.10.035

Heaman, L. M., LeCheminant, A. N., & Rainbird, R. H. (1992). Nature and timing of Franklin igneous events, Canada: Implications for a Late Proterozoic mantle plume and the break-up of Laurentia. *Earth and Planetary Science Letters*, *109*(1–2), 117–131. https://doi.org/10.1016/0012-821X(92)90078-A

Hill, M. J., & Shaw, J. (1999). Palaeointensity results for historic lavas from Mt Etna using microwave demagnetization/remagnetization in a modified Thellier-type experiment. *Geophysical Journal International*. https://doi.org/10.1046/j.1365-246X.1999.00980.x

Hill, M. J., & Shaw, J. (2000). Magnetic field intensity study of the 1960 Kilauea lava flow, Hawaii, using the microwave palaeointensity technique. *Geophysical Journal International*, *142*(2), 487–504. https://doi.org/10.1046/j.1365-246X.2000.00164.x

Hill, M. J., Gratton, M. N., & Shaw, J. (2002). A comparison of thermal and microwave palaeomagnetic techniques using lava containing laboratory induced remanence. *Geophysical Journal International*, *151*(1), 157–163. https://doi.org/10.1046/j.1365-246X.2002.01745.x

Kodama, K. P., Carnes, L. K., Tarduno, J. A., & Berti, C. (2019). Palaeointensity of the 1.3

billion-yr-old Gardar basalts, southern Greenland revisited: No evidence for onset of inner core growth. *Geophysical Journal International*, *217*(3), 1974–1987. https://doi.org/10.1093/gji/ggz126

de Koker, N., Steinle-Neumann, G., & Vlček, V. (2012). Electrical resistivity and thermal conductivity of liquid Fe alloys at high P and T, and heat flux in Earth's core. *Proceedings of the National Academy of Sciences of the United States of America*, *109*(11), 4070–4073. https://doi.org/10.1073/pnas.1111841109

Konôpková, Z., McWilliams, R. S., Gómez-Pérez, N., & Goncharov, A. F. (2016). Direct measurement of thermal conductivity in solid iron at planetary core conditions. *Nature*, *534*(7605), 99–101. https://doi.org/10.1038/nature18009

Kulakov, E. V., Sprain, C. J., Doubrovine, P. V., Smirnov, A. V., Paterson, G. A., Hawkins, L., et al. (2019). Analysis of an Updated Paleointensity Database (QPI-PINT) for 65–200 Ma: Implications for the Long-Term History of Dipole Moment Through the Mesozoic. *Journal of Geophysical Research: Solid Earth*, *124*(10), 9999–10022. https://doi.org/10.1029/2018JB017287

Kulakov, Evgeniy V., Smirnov, A. V., & Diehl, J. F. (2013). Absolute geomagnetic paleointensity as recorded by ~1.09 Ga Lake Shore Traps (Keweenaw Peninsula, Michigan). *Studia Geophysica et Geodaetica*, *57*(4), 565–584. https://doi.org/10.1007/s11200-013-0606-3

Labrosse, S. (2015). Thermal evolution of the core with a high thermal conductivity. *Physics of the Earth and Planetary Interiors*, *247*, 36–55. https://doi.org/10.1016/j.pepi.2015.02.002

Landeau, M., Aubert, J., & Olson, P. (2017). The signature of inner-core nucleation on the geodynamo. *Earth and Planetary Science Letters*, *465*, 193–204. https://doi.org/10.1016/j.epsl.2017.02.004

Nimmo, F. (2015). Thermal and Compositional Evolution of the Core. In *Treatise on Geophysics: Second Edition*. https://doi.org/10.1016/B978-0-444-53802-4.00160-3

O'Rourke, J. G., & Stevenson, D. J. (2016). Powering Earth's dynamo with magnesium precipitation from the core. *Nature*, *529*(7586), 387–389. https://doi.org/10.1038/nature16495

Ohta, K., Kuwayama, Y., Hirose, K., Shimizu, K., & Ohishi, Y. (2016). Experimental determination of the electrical resistivity of iron at Earth's core conditions. *Nature*, *534*(7605), 95–98. https://doi.org/10.1038/nature17957

Palmer, H. C., Baragar, W. R. A., Fortier, M., & Foster, J. H. (1983). Paleomagnetism of Late Proterozoic rocks, Victoria Island, Northwest Territories, Canada. *Canadian Journal of Earth Sciences*, *20*(9), 1456–1469. https://doi.org/10.1139/e83-131

Park, J. K. (1994). Palaeomagnetic constraints on the position of Laurentia from middle Neoproterozoic to Early Cambrian times. *Precambrian Research*, *69*(1–4), 95–112. https://doi.org/10.1016/0301-9268(94)90081-7

Paterson, G. A., Tauxe, L., Biggin, A. J., Shaar, R., & Jonestrask, L. C. (2014). Standard Paleointensity Definitions v1.1, 0–43. Retrieved from http://www.paleomag.net/SPD/spdweb.html

Pehrsson, S. J., & Buchan, K. L. (1999). Borden dykes of Baffin Island, northwest territories: A Franklin U-Pb baddeleyite age and a paleomagnetic reinterpretation. *Canadian Journal of Earth Sciences*. https://doi.org/10.1139/e98-091

Pozzo, M., Davies, C., Gubbins, D., & Alfè, D. (2012). Thermal and electrical conductivity of iron at Earth's core conditions. *Nature*, *485*(7398), 355–358. https://doi.org/10.1038/nature11031

Prévot, M. (1981). Some aspects of magnetic viscosity in subaerial and submarine volcanic rocks. *Geophysical Journal of the Royal Astronomical Society*, *66*(1), 169–192. https://doi.org/10.1111/j.1365-246X.1981.tb05952.x

Shcherbakova, V. V., Biggin, A. J., Veselovskiy, R. V., Shatsillo, A. V., Hawkins, L. M. A., Shcherbakov, V. P., & Zhidkov, G. V. (2017a). Was the Devonian geomagnetic field dipolar or multipolar? Palaeointensity studies of Devonian igneous rocks from the Minusa Basin (Siberia) and the Kola Peninsula dykes, Russia. *Geophysical Journal International*, *209*(2), 1265–1286. https://doi.org/10.1093/gji/ggx085

Shcherbakova, V. V., Biggin, A. J., Veselovskiy, R. V., Shatsillo, A. V., Hawkins, L. M. A., Shcherbakov, V. P., & Zhidkov, G. V. (2017b). Was the Devonian geomagnetic field dipolar or multipolar? Palaeointensity studies of Devonian igneous rocks from the Minusa Basin (Siberia) and the Kola Peninsula dykes, Russia. *Geophysical Journal International*, *209*(2), 1265–1286. https://doi.org/10.1093/gji/ggx085

Shcherbakova, V. V., Bakhmutov, V. G., Thallner, D., Shcherbakov, V. P., Zhidkov, G. V., & Biggin, A. J. (2020). Ultra-low palaeointensities from East European Craton, Ukraine support a globally anomalous palaeomagnetic field in the Ediacaran. *Geophysical Journal International*, *220*(3), 1920–1946. https://doi.org/10.1093/gji/ggz566

Shellnutt, J. G., Dostal, J., & Keppie, J. D. (2004). Petrogenesis of the 723 Ma Coronation sills, Amundsen basin, Arctic Canada: Implications for the break-up of Rodinia. *Precambrian Research*, *129*(3–4), 309–324. https://doi.org/10.1016/j.precamres.2003.10.006

Smirnov, A. V., Tarduno, J. A., Kulakov, E. V., McEnroe, S. A., & Bono, R. K. (2016). Palaeointensity, core thermal conductivity and the unknown age of the inner core. *Geophysical Journal International*, *205*(2), 1190–1195. https://doi.org/10.1093/gji/ggw080

Smirnov, A. V., Kulakov, E. V., Foucher, M. S., & Bristol, K. E. (2017). Intrinsic paleointensity bias and the long-term history of the geodynamo. *Science Advances*, *3*(2), 1–8. https://doi.org/10.1126/sciadv.1602306

Sprain, C. J., Swanson-Hysell, N. L., Fairchild, L. M., & Gaastra, K. (2018). A field like today's? The strength of the geomagnetic field 1.1 billion years ago. *Geophysical Journal International*, *213*(3), 1969–1983. https://doi.org/10.1093/gji/ggy074

Suttie, N., Shaw, J., & Hill, M. J. (2010). Direct demonstration of microwave demagnetization of a whole rock sample with minimal heating. *Earth and Planetary Science Letters*. https://doi.org/10.1016/j.epsl.2010.02.002

Tauxe, L., & Staudigel, H. (2004). Strength of the geomagnetic field in the cretaceous normal superchron: New data from submarine basaltic glass of the troodos ophiolite. *Geochemistry, Geophysics, Geosystems*, *5*(2). https://doi.org/10.1029/2003GC000635

Thellier, E., & Thellier, O. (1959). Sur l'intensité du champ magnétique terrestre dans le passé historique et géologique. *Annales de Géophysique*, *15*, 285–376.

Thomas, D. N., & Piper, J. D. A. (1995). Evidence for the existence of a transitional geomagnetic field recorded in a Proterozoic lava succession. *Geophysical Journal International*. https://doi.org/10.1111/j.1365-246X.1995.tb03553.x

Thomas, D. N., & Piper, J. D. A. (1992). A revised magnetostratigraphy for the Mid-Proterozoic Gardar lava succession, South Greenland. *Tectonophysics*. https://doi.org/10.1016/0040-1951(92)90172-3

Thomas, D. N. (1993). An integrated rock magnetic approach to the selection or rejection of ancient basalt samples for palaeointensity experiments. *Physics of the Earth and Planetary Interiors*, *75*(4), 329–342. https://doi.org/10.1016/0031-9201(93)90008-W

Tsunakawa, H., & Shaw, J. (1994). The Shaw method of palaeointensity determinations and its application to recent volcanic rocks. *Geophysical Journal International*, *118*(3), 781–787. https://doi.org/10.1111/j.1365-246X.1994.tb03999.x

Veselovskiy, R. V., Samsonov, A. V., Stepanova, A. V., Salnikova, E. B., Larionova, Y. O., Travin, A. V., et al. (2019). 1.86 Ga key paleomagnetic pole from the Murmansk craton intrusions – Eastern Murman Sill Province, NE Fennoscandia: Multidisciplinary approach and paleotectonic applications. *Precambrian Research*, *324*(December 2018), 126–145. https://doi.org/10.1016/j.precamres.2019.01.017

Walton, D., Shaw, J., Share, J., & Hakes, J. (1992). Microwave demagnetization. *Journal of Applied Physics*, *71*(3), 1549–1551. https://doi.org/10.1063/1.351230

Yamamoto, Y., Tsunakawa, H., & Shibuya, H. (2003). Palaeointensity study of the Hawaiian 1960 lava: Implications for possible causes of erroneously high intensities. *Geophysical Journal International*, *153*(1), 263–276. https://doi.org/10.1046/j.1365-246X.2003.01909.x

Zhang, Y., Hou, M., Liu, G., Zhang, C., Prakapenka, V. B., Greenberg, E., et al. (2020). Reconciliation of Experiments and Theory on Transport Properties of Iron and the Geodynamo. *Physical Review Letters*, *125*(7), 78501. https://doi.org/10.1103/PhysRevLett.125.078501

Chapter 5

New palaeointensity data suggest possible Phanerozoic-type paleomagnetic variations in the Precambrian

This chapter is published as Lloyd, S. J., Biggin, A. J., & Li, Z.-X. (2021). New paleointensity data suggest possible Phanerozoic-type paleomagnetic variations in the Precambrian. Geochemistry, Geophysics, Geosystems, https://doi.org/10.1029/2021GC009990

Abstract

The state of the geomagnetic field throughout the Precambrian era is largely unknown. Approximately 8% of global paleointensity records account for ~ 4 Billion years of Earth history. Despite this severe sparsity, the data is used to constrain models that predict the timing of significant deep earth events such as inner core nucleation. This carries with it the assumption that the Precambrian palaeomagnetic field was less variable when compared to the Phanerozoic, or at least that the sparse data can be averaged to accurately represent a particular time period. This study reports new paleointensities from the West Australian Craton at 755 Ma (the Mundine Wells dyke swarm) and 1070 Ma (the Bangemall Sills); both of which occurred within ~30 Ma from times at which extremely weak and anomalously strong fields, respectively, have been reported. Virtual dipole moments of 6.3 ± 0.1 Am^2 x 10^{22} and 1.8 ± 1.2 Am^2 x 10^{22} have been obtained from the two suites of mafic rock units which are substantially different to the previous measurements for the two respective ages. The findings suggest that field variability over tens of Myrs in the Precambrian was greater than has previously been assumed. This is supported by comparisons of paleosecular variation and distributions of virtual dipole moments (VDM). If variability in the Precambrian field is similar to that observed in the Phanerozoic, spatial or temporal anomalies may introduce significant bias to statistical analyses and model constraints, implying that caution should be employed in the interpretation of the Precambrian dipole moment records.

5.1 Introduction

Palaeointensity has been used to either constrain or signify the onset of deep earth events such as the formation of the inner core (Biggin et al., 2015; Smirnov 2016; Driscoll, 2016; Bono et al., 2019; Lloyd et al. 2021a). An important requirement is that the data accurately represents the true palaeofield. Systematic biases can affect the fidelity of specimen and site-level palaeointensity results (Smirnov & Tarduno, 2005, Smirnov et al., 2017) and non-ideal effects such as natural thermo-chemical and laboratory induced alteration, multi-domain carriers and other causes of Arai-slope curvature must be overcome (Kosterov & Prévot, 1998, Biggin & Böhnel, 2003, Shaar & Tauxe, 2015, Shcherbakov et al., 2019). Further complications exist when interpreting the data; for example, a fundamental assumption is made in long term statistical analyses, that the field is adequately defined for binned periods (Biggin et al., 2015, Kulakov et al., 2019). This requires that fluctuations occurring in both direction and intensity as a result of palaeosecular variation are sufficiently represented by good data.

Evidence suggests that Earth's geomagnetic field has existed for ~3.5 - 4.0 Ga (Biggin et al., 2011; Tarduno et al., 2020); however, 90 % of global palaeointensity data is from the last 50 Ma. Therefore, understanding the long-term evolution of the geodynamo in the Precambrian, currently requires models which are either constrained by, or based on, limited data with gaps of up to hundreds of millions of years (PINT database v.2015.05; http://earth.liv.ac.uk/pint/ Biggin et al., 2015; Bono et al., 2019; Smirnov et al., 2017; Lloyd et al., 2021a). Such sparse data may lead to the possibility of bias or aliasing, depending on whether long-term variations are reliably averaged out. For example, substantial periods of extreme variation in dipole stability are observed in the Phanerozoic between 65 Ma and 200 Ma related to changes in the average polarity reversal rate (Kulakov et al., 2019).

Here we set out to determine whether long-term variations in field strength (tens to hundreds of Myrs) in the Precambrian are comparable to those observed in the Phanerozoic, and to gain a better appreciation of whether existing models are accurately representing these long-term variations where a severe paucity of data exists. We target two important periods in the Precambrian era, approximal either to a large number (7) of weak-field observations which are linked to the onset of inner core nucleation (ICN) (720 Ma; Lloyd et al., 2021a) or to the anomalously high intensities from the Mid-Continent Ridge (1087 Ma; Kulakov et al., 2013, Sprain et al., 2018). Reported here are the first late Precambrian palaeointensity data from the West Australian Craton: that of the Mundine Wells dyke swarm (755 ± 3 Ma) and the Bangemall Sills (1070 ± 6 Ma). Both rock units were originally studied with the aim of better defining the apparent polar wander path for the Australian continent with respect to Laurentia during Precambrian supercontinent cycles (Wingate & Giddings, 2000: Wingate et al., 2002). The palaeomagnetic poles obtained are considered robust for palaeogeographic reconstruction (Li et al., 2008; Meert & Torsvik, 2003). Multiple lines of evidence for primary TRMs are reported from both localities, providing good potential for palaeointensity investigation. These includes positive fold and baked-contact tests, low within-site dispersion, high unblocking temperatures of single-domain (SD) magnetite, and little reported alteration in high temperature-susceptibility experiments (Wingate & Giddings, 2000; Wingate et al., 2002).

The temporal proximity of these rock units to existing data allows for more accurate comparisons of Precambrian field characteristics and intensity variations to those observed in the Phanerozoic. A similar order of variability combined with a severe sparsity of data may introduce considerable bias to statistical analyses, and would suggest a more cautious approach may be required when using such data to constrain key Earth events.

5.2 Background and geological setting

The Mundine Wells dyke swarm (MDS) and Bangemall Sills (BMS) are located close to one another in Western Australia (Figure 5.1a), with the former cross-cutting the latter in places. The extensive MDS intrude into Archean and Proterozoic rocks of the Pilbara Craton, trending mainly NNE. The dykes represent the last known igneous event in the region and are essentially undeformed, cutting vertically across all older rocks. The Bangemall Supergroup was deposited in the Edmund and Collier Basins of Western Australia during the Mesoproterozoic. The quartz dolerite BMS intrude into these clastic and carbonate sedimentary rocks, and are widely distributed across the basins. The sills are typically ~100m thick and are generally conformable with the hosting strata.

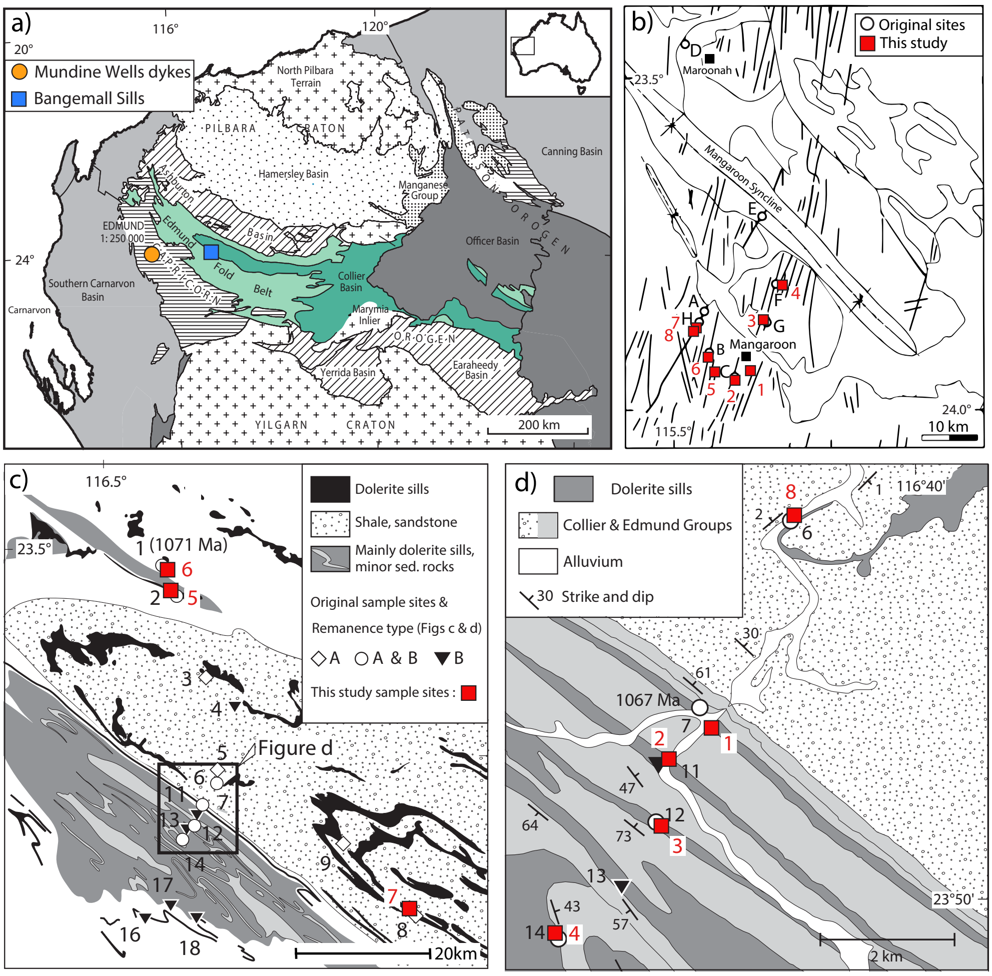

Figure 5.1. a) Map showing the geological setting of MDS and BMS studied here. b) MDS original palaeomagnetic site locations (black open circles) with sites from this study overlaid (solid red squares). c & d) BMS site locations and remanence types. All maps based on Wingate & Giddings (2000) and Wingate et al. (2002). Original images courtesy of the Geological Survey and Resource Strategy, Department of Mines, Industry Regulation and Safety. © State of Western Australia 2021.

5.2.1 Background - MDS

The dykes are typically ~30m wide and consist of fine to medium grained quartz dolerites; plagioclase, interstitial quartz and quartz-feldspar is commonly contained in most samples, with orthopyroxene and clinopyroxene found less commonly (Wingate & Giddings, 2000). U-Pb dating put MDS emplacement at 755 ± 3 Ma (Wingate & Giddings, 2000). Alteration in the quartz dolerites is reported to be slight to moderate in places and is variable between dykes and between cores from the same dyke; plagioclase is locally sericitised, and pyroxenes may be partially altered.

Wingate and Giddings (2000) interpreted a low coercivity component as resulting from a lightning induced isothermal remanent magnetisation (IRM) and noted that this was removed by an AF pre-treatment to 15 or 20 mT. The high coercivity remanence of most specimens are consistently oriented to NNE with shallow to moderate downwards inclination. Thermal demagnetisation of one specimen from each of four dykes yielded similar directions with unblocking temperatures in the range 570 to 580 °C. The dominant magnetic carrier is interpreted to be SD magnetite, which is supported by high-temperature susceptibility results which show well-defined Hopkinson peaks close to 580 °C, indicative of the presence of SD magnetite (Schmidt, 1993).

Positive baked contact tests at sites A and C agree with positive results from a contact test at site E (Wingate & Giddings, 2000), where the dyke crosscuts an older Bangemall sill. Here, there is evidence of primary remanence based on agreement in direction between magnetisations in the dyke and the baked dolerite sill near the contact and a stable coherently directed remanence in the unbaked dolerite sill which is different in direction from that of the dyke.

A total of eight dykes were sampled in the current study, four of which were positively identified from the original study by drill holes. The remaining dykes were close to the original ones based on the description and GPS coordinates although we failed to locate the former drill holes (Figure 5.1b). An average of eight cores were drilled at each dyke, providing a total of 320 half-inch specimens which were oriented in-situ using a sun compass. The overall mean direction of the MDS dykes here is reported as D = 014 °, I = 36 ° ($\alpha95$ = 5 °), with an associated palaeopole at 134 °E, 44 °N (Wingate & Giddings, 2000).

5.2.2 Background - BMS

The extensive quartz dolerite sills, typically ~100m thick, are medium-grained with exposed chilled margins. Most samples contain plagioclase, augite, orthopyroxene, and magnetite, with minor quartz and K-feldspar. Some secondary minerals, such as hornblende and biotite, are reported to be the result of deuteric alteration; they are classified geochemically as high-Ti continental tholeiites (Muhling & Brakel, 1985). A palaeomagnetic and U–Pb geochronological study of sills was carried out by Wingate et al. (2002) in which statistically indistinguishable ages were obtained (1071 ± 8, 1067 ± 14 and 1068 ± 22 Ma) from three of the sampling sites.

Two types of magnetisation were originally identified; type-A, a consistently directed, thermally stable magnetisation isolated in 15 sites (including the three dated sills) with magnetite reported as the dominant remanence carrier (Wingate et al., 2002). Type-B magnetisation is a chemical remanent magnetisation (CRM) most likely carried by maghemite, and is present in several sites alongside type-A.

Site mean directions obtained from type-A magnetisation converge after correction for bedding tilt, with an overall mean direction of D = 339°, I = 46.5° ($\alpha95 = 8.3$, N = 11). The magnetisation is argued to be primary due to multiple factors including positive fold and baked contact tests with no evidence of thermal events that could cause remagnetisation. Polarity reversals are also reported between, but not within intrusions (Wingate et al., 2002).

We positively identified and sampled five of the originally studied sills, and a further three sites at the same GPS position as originally reported (Figures 5.1c & d) but where we were unable to locate the original drill holes. An average of eight cores were drilled at five sites, and hand samples were collected in-situ at the remaining three sites. Baked contact was identified at two sites, where a further four cores were drilled. All drill cores were oriented using a sun compass and the combined samples were converted in to 330 half-inch specimens.

5.3 Methods

The methods laid out in this section apply to both the Mundine and Bangemall localities.

5.3.1 Rock-magnetic and SEM

We examined the mineralogy of opaque grains from polished thin-sections (two from each locality) using a low-voltage, high-resolution Zeiss GeminiSEM 450 based within the University of Liverpool SEM Shared Research Facility. Backscatter electron imaging (BSE) and energy dispersive X-ray spectroscopy (EDS) were used for the identification and semi-quantitative elemental analysis of the magnetic grains.

Representative rock magnetic measurements were performed on an average of three samples per site. Hysteresis loops, backfield coercivity, saturation Isothermal Remanence Magnetisation (sIRM) and high-field thermomagnetic curves of the saturation magnetisation, M_s (T), were obtained using a Magnetic Measurements Ltd Variable Field Translation Balance. Hysteresis loops were corrected for the paramagnetic contribution to the slope above 0.5 T, with ratios of the hysteresis parameters, remanent saturation magnetisation/ saturation magnetisation (B_{cr}/ B_c) and coercivity of remanence/ coercivity (M_{rs}/ M_s), used to determine bulk domain stability (Paterson et al., 2017). Curie temperatures (T_c) were calculated using the second derivative of the M_s (T) heating curves with a 3-point running average applied. High-temperature susceptibility, κ (T), experiments were carried out up to 600 °C and 700 °C using a MFK1-FA Kappabridge susceptometer with CS-3 furnace (AGICO).

5.3.2 Palaeointensity experiments

A total of 293 individual specimens were subject to palaeointensity experiments. Details of specimen labelling are located in Supplementary Text C3. The thermal Thellier method is considered the most robust of palaeointensity techniques (Dunlop, 2011) but success rates can be low, particularly with Precambrian rocks (Lloyd et al., 2021a). To overcome this and enhance the robustness of the results, a common approach in modern palaeointensity studies is to use multiple methods in the acquisition of palaeointensity data (e.g., Yamamoto et al., 2007; de Groot et al., 2013; Monster et al., 2015; Hawkins et al., 2019). We adopt this approach here, utilising three independent techniques: the thermal Thellier-Coe and IZZI methods (Coe, 1967; Tauxe & Staudigel, 2004), the Shaw double heating technique, in part, with low temperature demagnetisation (DHT-LTD; Tsunakawa & Shaw, 1994; Yamamoto et al., 2003) and the Microwave method (Biggin et al., 2007; Hill et al., 2002; Walton et al., 1992).

Thellier and Shaw-DHT measurements were performed using an automated RAPID 2G superconducting rock magnetometer (Morris et al., 2009) in a magnetically shielded cage where the residual field was less than 100 nT. Thermal Thellier experiments were carried out on a total of 57 specimens, consisting of a sequence of paired heatings in air, to a set of increasing temperatures. The IZZI+ protocol was used (Tauxe & Staudigel, 2004), which alternates the zero-field and infield steps with partial thermal remanent magnetisation (pTRM) checks after every two step pairs. The sequence of steps was repeated up to an average of 590 °C, with an infield laboratory bias field of 20 μT and bulk susceptibility measurements taken at every pTRM check. Heatings were carried out in a Magnetic Measurements Ltd MMTDSC super-cooled thermal demagnetiser within the same shielded environment, and specimens were held at temperature for a median 40 minutes.

The reliability of the Shaw LTD-DHT method has been repeatedly demonstrated using historical lava flows in Hawaii and Japan where the geomagnetic field when the lavas formed is known (Yamamoto et al., 2003; Mochizuki et al., 2004; Oishi et al., 2005; Yamamoto & Yamaoka, 2018). Most experiments in this study are undertaken without the addition of LTD; the use of which was recently found to have no systematic effect on palaeointensity results between sister specimens from Precambrian dykes (Lloyd et al., 2021a). In this study, 157 specimens were alternating field (AF) demagnetised up to 99 or 100 mT using a Rapid 2G system in a zero-field environment. Anhysteretic remanence magnetisation (ARM) was imparted using a DC bias field of between 60 and 70 μT. Laboratory TRMs were imparted by heating to 610 °C in a vacuum and maintained at that temperature for various durations ranging from 15 to 35 minutes (TRM_1) and 15 to 45 minutes (TRM_2). Samples were subjected to a DC field of 20 μT throughout the heating and cooling cycle. By varying the hold durations, it helps to ensure that palaeointensities and the validation of the ARM alteration corrections are robust. Twenty-six specimens from the BMS sites were subjected to low temperature demagnetisation (LTD) treatment, which is known to preferentially target remanence carried by multidomain grains (Yamamoto et al., 2003). These specimens were soaked in liquid nitrogen in a plastic dewar for 10 minutes and then removed and allowed to warm to room temperature in a zero field for 60 minutes. This procedure was carried out prior to the demagnetisation of each of the thermal and anhysteretic remanent magnetisations imparted during the Shaw DHT-LTD method (Yamamoto et al., 2003).

A further 80 experiments were carried out on a 14.2 GHz microwave palaeointensity system with low-temperature SQUID magnetometer (Suttie et al., 2010). Small cylindrical cores (5 mm diameter) are centred in the resonant cavity, where the microwave field couples with the magnetic system within the sample, producing magnons (quasi-particles associated with spin waves) which demagnetise the sample as the energy is increased. The mechanism of microwave/

magnon is analogous to heat/ phonon but without significantly heating the bulk specimen. The previously mentioned IZZI+ protocol was used in combination with the quasi-perpendicular method (ChRM makes an angle of at least 45 ° with the lab field); this achieves a compromise between minimising any non-ideal behaviour arising from multi-domain effects while also being able to detect its presence (Yu & Tauxe, 2005; Hawkins et al., 2019). The technique has been demonstrated to produce equivalent results to thermal Thellier-style experiments (e.g. Biggin et al., 2007) and has been successfully used in previous studies (Grappone et al., 2019; Hawkins et al., 2019). Various laboratory fields were used in order to test for any non-linear TRM effects. The Coe version of the Thellier method (Coe, 1967) incorporating pTRM tail checks (Riisager & Riisager, 2001) was also applied to a very small number of specimens. The tails are a consequence of non-reciprocal thermal blocking and unblocking and their detection might indicate that multi-domain remanence biases the palaeointensity estimate.

TH & MW	*n*	*α* (^{o})	*MAD* (^{o})	*FRAC* (%)	*f* (%)	N_{pTRM}	$\lvert k' \rvert$	*b*	*DRAT* (%)	*CDRAT* (%)
	≥ 4	≤ 15	≤ 10	≥ 35	≥ 35	≥ 2	≤ 0.25	≤ 0.11	≤ 12	≤ 15

SH	*class*	*α* (^{o})	*MAD (a&f)* (^{o})	*FRAC* (%)	*rN*	$\lvert k' \rvert$	f_{RESID}	*sT* 1 (+/-)	*rT*	*sA1* 1 (+/-)
	A	≤ 10	≤ 10	≥ 45	≥ 0.990	≤ 0.2	≤ 0.2	0.05	≥ 0.990	≤ 0.4
	B	≤ 10	≤ 10	≥ 45	≥ 0.990	≤ 0.2	≤ 0.2	0.10	≥ 0.990	≤ 0.3

Table 5.1. Thermal Thellier (TH), Microwave (MW) and Shaw-DHT (SH) selection criteria; used and defined, where possible, according to the standard palaeointensity definitions (Paterson et al., 2014). n, number points used in best-fit line; α, angular difference between the anchored and unanchored best-fit directions on the orthogonal diagram; MAD, maximum angular deviation of the (anchored and free) best-fit to the directional data used in an orthogonal diagram (Kirschvink, 1980); FRAC, fraction of NRM used for the best-fit on an Arai diagram (Shaar & Tauxe, 2013); f, fraction of NRM used for the best-fit on an Arai diagram by vector difference sum (Coe et al., 1978); NpTRM, number of pTRM checks; q, quality of palaeointensity; |k'|, curvature of the Arai plot as determined by the best-fit circle to the selected best-fit Arai plot segment (Paterson, 2011); β, a measure of the relative scatter around the best-fit line (standard error of the slope/ absolute value of the slope (Coe et al., 1978); DRAT, maximum absolute difference produced by a pTRM check, normalized by the length of the line (Selkin et al., 2000); CDRAT, Cumulative DRAT (Kissel & Laj, 2004). Shaw-DHT selection criteria parameters are as TH and MW except: rN, R^2 correlation of the palaeointensity slope($_N$); f_{RESID}, defined in the text below; sT, slope$_T$ (TRM$_1$/

TRM_2 (Yamamoto et al., 2003); rT, R^2 correlation of the $slope_T$; sA1, slope (ARM_0/ ARM_1).*

Our selection criteria are a modified combination of PICTRIT03 (Kissel & Laj, 2004) and MC-CRIT.A1 (Paterson et al., 2015), including, for example, both parameters f and FRAC (Table 5.1). Due to the large overprints associated with these ancient rocks (e.g., Figures 5.4a & e), the *f* criterion is considered appropriate to quantify the required minimum fraction of NRM; however, we maintain that a minimum FRAC must also be present. Three specimens with high *f* values are accepted with FRAC ≥ 25 % (Supplementary Tables C2.2 and C2.5). DRAT and CDRAT are relaxed slightly, but remain strict for use in analysing ancient rocks (e.g., Kodama et al., 2019). Strict linearity is adhered to in all results (|k'| ≤ 0.25) with the exception of two MDS specimen results (|k'| ≤ 0.35) which produced palaeointensities concordant with others and met the other criteria easily.

We expand the typical selection criteria used in analysing Shaw-DHT data (Yamamoto et al., 2003) to include three additional criteria; these place stricter emphasis on linear, origin-trending palaeointensity slopes with limited ARM alteration.

1) $f_{\mathrm{RESID}} = \frac{|Y\ int|}{\Delta Y'}$ (Paterson et al., 2016)

This is an analogy of the NRM fraction (f) of Coe et al. (1978) where *Yint* is the y-intercept of the palaeointensity $slope_{(N)}$ and ΔY' is the change in the NRM lost over the selected segment. The criterion quantifies the residual difference between the y-intercept and the origin of the plot. A non-origin trending slope is brought about when NRM and TRM_1* are not unblocking equally and their demagnetisation spectra can be fundamentally different shapes (something which is often not determined by the R^2 criterion).

2) |k'| (Paterson, 2011; Paterson et al., 2016)

Defined in Table 5.1 caption and used in addition to the R^2 correlation, which is not as strict a measure of linearity; this is particularly important in Shaw-DHT pseudo-Arai plots because the palaeointensity slope is insensitive to alteration (Tanaka & Komuro, 2009). We apply a strict minimum of |k'| ≤ 0.2 to all Shaw results (e.g., Lloyd et al., 2021b).

3) slope A_1 (ARM_0/ ARM_1) is limited to 1 ± 0.4 thereby limiting the amount of ARM alteration correction accepted and any associated uncertainty, including influences from remanence anisotropy and changes in magnetostatic interactions.

5.4 Rock magnetic and SEM results

5.4.1 SEM

Backscattered electron images (BEI) obtained from MDS (Figures 5.2a – d) and BMS (Figures 5.2e – j) show opaque grains of varying sizes, textures and oxidation stages. MDS BEI obtained from site MD6 (Figures 5.2a – c) show an area of cross-cutting fine, elongate, low-Ti lamellae (Figure 5.2a; bottom left); these well-developed lenses are mottled indicating oxidation to stage C4 or C5 (Haggerty, 1991). There is evidence of cracking, potentially related to low temperature oxidation (Figure 5.2b); however, κ (T) curves do not show notable evidence of maghemite.

At higher resolutions, fine sub-micron trellis intergrowths of two Ti phases are observed (Figure 5.2c); these are interpreted to be low-Ti titanomagnetite and ilmenite, although EDS analysis could not confirm this. A notably similar pattern is reported in other Precambrian dykes (Hodych, 1996; Smirnov & Tarduno, 2005). These very fine intergrowths suggest oxy-exsolution occurred above or close to the Curie temperature (Haggerty, 1991; Wilson & Watkins, 1967). Perpendicular sets of elongate lamellae, very fine in width, are also observed in site MD3 (Figure 5.2d) and suggest oxidation to stage C2 – 3.

BMS BEI of a specimen from site BM7 show large (~100 μm) ilmenite grains (Figures 5.2e - j) to very fine sub-micron intergrowths of two Ti-phases which are present throughout (Figures 5.2g - i) and are likely responsible for higher coercivity remanence. There are also lathe-like lamellae present, which vary in thickness, including some that are submicron in width and appear pristine (Figure 5.2j; top left). Most grains appear unaltered by low temperature processes and only show evidence of high-temperature deuteric oxidation which may have progressed to stage C7 in parts (e.g., the decomposition of the large ilmenite grain in figure 5.2j).

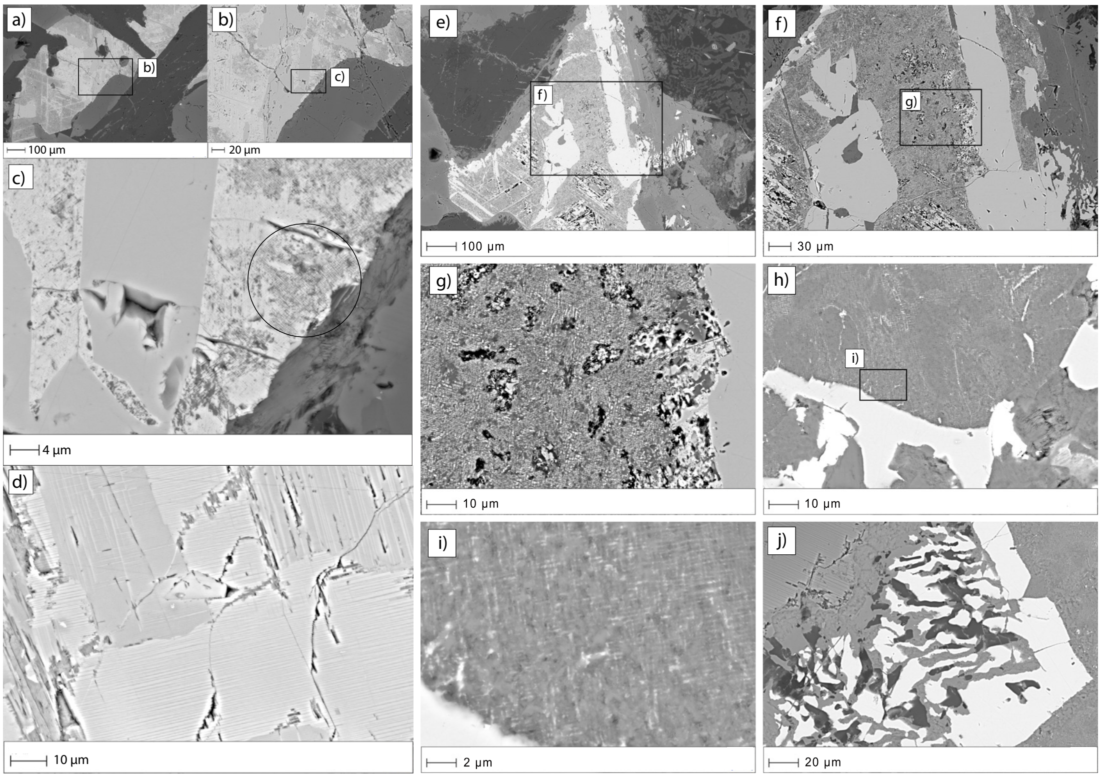

Figure 5.2. Backscattered SEM images of typical grain assemblages from MDS sites MD6 and MD3 (a – c, specimen MD6-4C; d, specimen MD3-4D), and BMS site BM7 (e – j, specimen BM7-4B). a) 100 µm scale image shows a large cluster of opaque grains which contain sub-sets of smaller assemblages. Textures indicate oxidation has occurred to stage C4. b) 20 µm scale showing cross-cutting elongate lamellae, composed of low and high-Ti phases (left). Textures indicate oxidation has occurred to stage C5. c) Submicron intergrowths of two phases, interpreted to be low-Ti titanomagnetite and ilmenite, are visible (highlighted). d) Elongate lamellae are submicron in width are interpreted to consist of low and high-Ti phases. e - i) Various magnifications show three types of opaque grain; very large (>100 µm) ilmenite, much thinner lathe-like lamellae and very fine intergrowths of two Ti-phases. j) Large oxy-exsolved ilmenite grain (stage C7) and an area of pristine lamellae which are sub-micron in width (top left).

5.4.2 Rock magnetic results - MDS

The acquired κ (T) curves are grouped according to quality (Figures 5.3a & b). Site MD5 produces highly non-reversible curves and is omitted from the reported analysis. Large increases and decreases in susceptibility occur in sites MD1, 7, and 8 between ~300 and 350 °C which we attribute to the presence of titanomaghemite (Figure 5.3a). Site MD4 does not produce this feature but is included in the same diagram due its non-reversible results; defined here as >20 % difference between heating and cooling at T_0. Sites MD2, 3, and 6 produce the most reversible curves typical of lower alteration and low-Ti titanomagnetite (Figure 5.3b). A small susceptibility tail extending beyond 600 °C indicates the presence of a small amount of hematite in several specimens, although this is not detected in sIRM results. Most IRM curves saturate in fields less than 300 mT; saturation magnitudes are consistent across sites MD2, 3 and 6, and close to zero in sites MD5, 7 and 8 consistent (Figure 5.3c).

In the thermomagnetic analysis, Curie temperatures for the main ferrimagnetic phase are found between 560 and 575 °C, suggesting that low Ti-titanomagnetite is the magnetic remanence-bearing mineral (Dunlop et al., 1998). The more reversible curves are limited to sites MD2, 3 and 6 with a mean difference between heating and cooling curves of ~20 % at T_0 (Figures 5.3d & e); these also produce pronounced Hopkinson peaks indicative of SD grain size distributions (Dunlop, 2014).

Bulk domain stability (BDS) values for sites MD2 – 6 narrowly exceed the threshold value (0.1) at which reliable palaeointensity results are more likely (Paterson et al., 2017). All specimens follow the BDS trend, lying parallel and above it, with specimens from sites 7 and 8 giving uniquely low domain stability values (Figure 5.3f). Although site MD5 shows a high BDS value, hysteresis curves (Supplementary Figure C1.1) show that these specimens are dominated by a paramagnetic component. The BDS values of the main cluster (sites MD2 – 4, 6) represent bulk grain distributions in the vortex state range. Nevertheless, pronounced Hopkinson peaks and thermal demagnetisation observations (section 5.5.1) suggest that some population of SD grains are present.

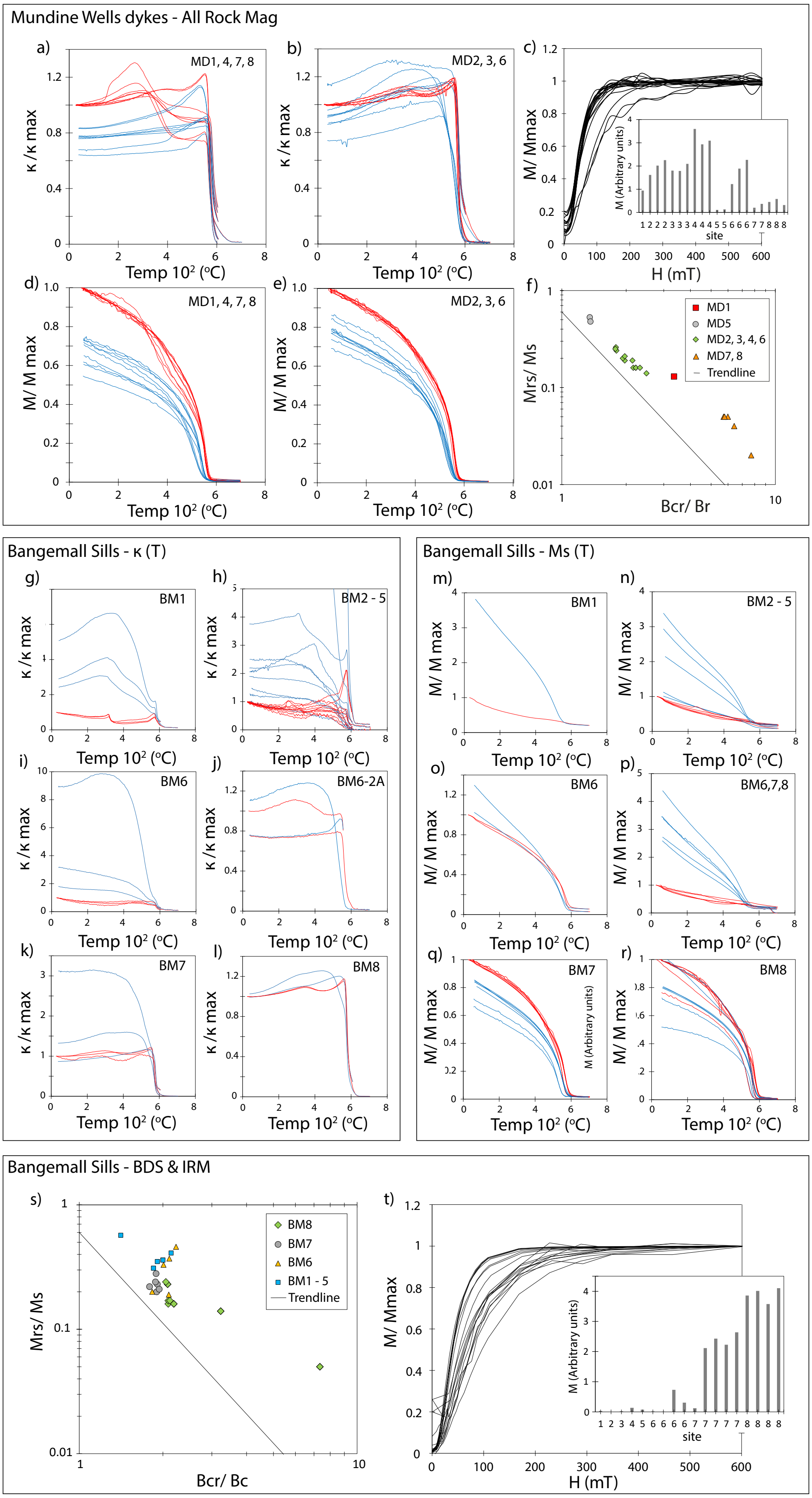

Mundine Wells dykes - All Rock Mag
a) MD1, 4, 7, 8
b) MD2, 3, 6
c)
d) MD1, 4, 7, 8
e) MD2, 3, 6
f)
MD1
MD5
MD2, 3, 4, 6
MD7, 8
Trendline
κ /κ max
M/ Mmax
M/ M max
Mrs/ Ms
M (Arbitrary units)
site
Temp 10² (°C)
H (mT)
Bcr/ Br
Bangemall Sills - κ (T)
g) BM1
h) BM2 - 5
i) BM6
j) BM6-2A
k) BM7
l) BM8
Bangemall Sills - Ms (T)
m) BM1
n) BM2 - 5
o) BM6
p) BM6,7,8
q) BM7
r) BM8
Bangemall Sills - BDS & IRM
s)
t)
BM8
BM7
BM6
BM1 - 5
Trendline
Bcr/ Bc

Figure 5.3. a – f) MDS. g – t) BMS. a & b) Normalised κ (T) diagrams with specimens from several sites grouped together. Red lines, heating curves; blue lines, cooling curves. c) Normalised IRM curves, with inset plot showing the values of saturation magnetisation (M_s) for each specimen. d & e) Normalised M_s (T) diagrams with specimens from several sites grouped together. Red lines, heating curves; blue lines, cooling curves. f) BDS diagram with logarithmic scale. M_{rs}/ M_s, remanent saturation magnetisation/ saturation magnetisation; B_{cr}/ B_c, coercivity of remanence/ coercivity. BDS = (M_{rs}/ M_s)/ (B_{cr}/ B_c). g – l) Normalised κ (T) diagrams. j) Single κ (T) diagram for a specimen from site BM6 which was heated to 550 °C, cooled and heated to 700 °C. m – r) Normalised M_s (T) diagrams. p) Diagram groups non-reversible curves together, from sites BM6, 7 and 8. s) BDS diagram with logarithmic scale (see Figure 5.3f). t) Normalised IRM curves with insert showing magnitude of saturation of individual specimens within the site shown on the x-axis.

5.4.3 Rock magnetic results - BMS

Measurements of NRM and bulk susceptibility reveal that specimens from sites BM2 – 5 are weakly magnetised (~10 mAm^{-1}) with very low bulk susceptibility values (Supplementary Figure C1.2). κ (T) curves are highly non-reversible in sites BM1 – 5, with some strong inflections in susceptibility observed at ~300 °C; this is particularly apparent in site BM1 (Figures 5.3g & h) and is interpreted to be caused by the presence of titanomaghemite.

Specimens from site BM6 exhibit a mixture of highly non-reversing κ (T) curves and some with less alteration observed; however, most of the alteration appears to occur at high temperature, between 550 °C and 700 °C (Figures 3i and j). We do not see the same low-temperature inflections associated with titanomaghemite here, although Wingate et al. (2002) report type-A and B magnetisation present in this site. Sites BM7 and BM8 produce more reversible κ (T) curves of varying quality (Figures 5.3k & l); many exhibiting changes in the heating-cooling cycle of less than 10 %.

M_s (T) curves produce similar results. Sites BM1 – 5 are highly non-reversible (Figures 5.3m & n). Non-reversible curves are also obtained from sites BM6, 7 and 8 (Figure 5.3p shows one or two from each site); however, these sites tend to produce more reversible M_s (T) curves (most exhibiting a difference of less than 25 % at T_0; Figures 5.3o, q & r), demonstrating heterogeneity in the samples sets. Curie temperatures for sites BM1 – 4 range between 590 and 650 °C whereas that for BM5 is ~360 °C. Site BM6 TC's range between 570 and 580 °C and some, but not all, specimens produce a small step in the curves with an associated TC of 670 °C. Site BM7 TC's range between 570 and 580 °C and site BM8 between 580 and 600 °C. The primary TC's from sites BM6 – 8 are indicative of magnetite.

Mean BDS values for sites BM6 and 7 are 0.15 and 0.12 respectively, while site BM8 mean is 0.07 with some specimens above 0.1 (Figure 5.3s). IRM curves all saturate in fields less than 300 mT (Figure 5.3t); saturation magnitudes are close to zero in sites BM1 – 5 and much higher in sites BM7 and 8, with site BM6 showing variability consistent with other rock magnetic results (Figures 5.3i, j, o & p; Supplementary Figure C1.2). Hysteresis loops reveal that many specimens from site BM6 are dominated by a paramagnetic signal, which once removed, reveals properties indicative of a small distribution of SD grains (Supplementary Figure C1.1).

5.5 Palaeointensity results

Extracting palaeointensity data from Precambrian rocks is extremely challenging. To ensure that the results are robust and reliable, we apply a relatively strict set of selection criteria to all data (Table 5.1). Largely as a result of laboratory induced alteration, the overall success rate for both rock units were low: just 34 successful results out of 293 specimens.

5.5.1 Palaeointensity results - MDS

A summary of palaeointensity results is found in Table 5.2, and specimen level results in Supplementary Tables C2.1 – C2.3. Site-mean palaeointensity estimates were determined from the unweighted average of successful results from all methods from a given site. All specimens from sites MD1, 5, 7 and 8 were rejected after failure of a small number of pilot Shaw-DHT experiments confirmed the poor-quality rock magnetic results. Specimens from these sites suffer from alteration and multi-domain effects (Figures 3a, d and f; Supplementary Table C2.2). Site MD4 produces slightly scattered palaeomagnetic directions (Supplementary Figure C1.3) and no successful palaeointensity results.

The only successful results are from sites MD2, 3 and 6 (sites EMBC, G and B respectively;

Wingate & Giddings, 2000); these were difficult to obtain, and success rates for MD2 and 3 are low. AF and thermally demagnetised palaeomagnetic directions obtained from this study are found in Supplementary Figure C1.3. Sites MD2 and MD3 are scattered but their means, using a 45 ° cut-off, are within an angular distance of 20 ° from those obtained in the original study (Wingate & Giddings, 2000). The MD6 site mean is within 5 ° of the original and is associated with more precise palaeomagnetic directions (D=12.6 °, I = 32.6 °, k = 64.4); twelve successful palaeointensities are produced from this site (Table 5.2; Supplementary Tables C2.1 – C2.3; Figure 5.4; Supplementary Figure C1.3).

Results obtained from these three sites are consistently high and in good agreement between and within sites; site mean palaeointensity results are within 1 μT of each other (Table 5.2). All three methods also produced consistent results: Microwave results were obtained from three sites (30.7 ± 4.3 μT; N = 11), thermal Thellier results from sites MD3 and MD6 (26.3 ± 1.0 μT; N = 2), and Shaw-DHT results from site MD6 only (24.3 ± 1.6 μT; N = 5). The highest success rate (35 %) was achieved by the Microwave method, compared to 7 % from both the thermal Thellier and Shaw-DHT methods.

Successful palaeointensities from the thermal Thellier method show that ChRM is unblocked between 560 – 580 °C, which could support the presence of a narrow distribution of SD Magnetite grains. This is particularly apparent in the high-quality result (q = 20.2) from site MD6 (Figure 5.4b; Supplementary Table C2.1). Although a limited number of results are obtained for sites MD2 and MD3, they pass strict selection criteria and are considered robust; they are also equivalent to the high-quality results from site MD6 (Table 5.2, Figure 5.4).

Arai diagrams from site MD3 display two-slope behaviour; these account for four specimen results (Figure 5.4 and Supplementary Figure C1.4 show three of these). The thermal Thellier result (MD3-6C; Figure 5.4a) suffers severe NRM loss up until ~560 °C without acquiring a TRM; after which a notably linear and stable palaeointensity slope is obtained. This may be related to its large overprint; similar overprints are observed in many Shaw-DHT specimens, and are generally removed using AF demagnetisation by 15 mT (Figures 5.4e & f). It may be possible that they are related to the recently identified 'fragile' curvature (Tauxe et al., 2021), however, we think this is unlikely since the palaeointensity results are remarkably consistent with all other results, including highly-linear, single-slope Arai slopes and across multiple methods (Figures 5.4b & 5.d). For the same reason, we think it unlikely that the grains that unblock at low temperatures are biasing palaeointensity results; although they will still contribute to the laboratory-induced remanence. Once the remanence carried by higher coercivity magnetite grains are unblocked, linear palaeointensity slopes with values of ~30 μT are observed. These high-power sections of the respective Arai diagrams are associated with origin trending directional data and are interpreted as the ChRM.

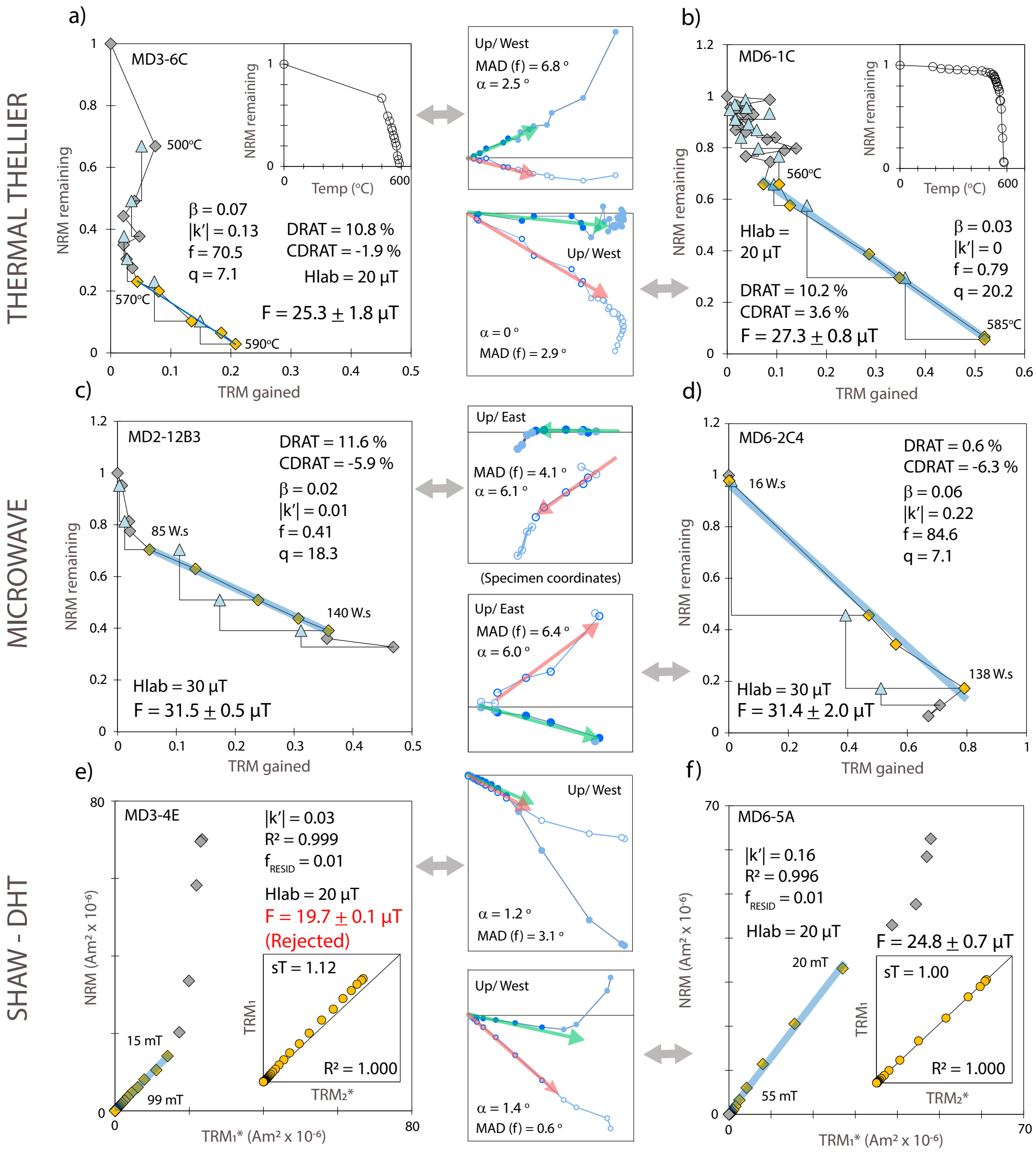

Figure 5.4. Example Arai/ Shaw plots with associated orthogonal plots in geographic coordinates unless otherwise stated (two from each method). a & b) Thermal Thellier specimens MD3-6C and MD6-1C. c & d) Microwave specimens MD2-12B3 and MD6-2C4. e & f) Shaw-DHT specimens MD3-4E and MD6-5A respectively. Thermal Thellier plots include the thermal demagnetisation

insert. Orange markers, steps used; grey markers, steps not used; light blue triangles, pTRM checks; thick blue lines, best-fit line used in palaeointensity estimate; red and green lines, best-fit lines determined from principal component analysis of the directional data; q, quality factor (Coe et al., 1978). All selection criteria used here are listed in Table 5.1.

A Thellier-Coe experiment with both pTRM and pTRM tail checks was used to determine the extent to which pTRM tails may be influencing the estimates from site MD3. We use the $DRAT_{TAIL}$ criterion (Biggin et al., 2007) to quantify the extent of pTRM tails; the result ($DRAT_{TAIL}$ = 6.1; Supplementary Figure C1.4b) suggests that pTRM tails are not a significant cause of the two-slope behaviour.

The data were tested against a relaxed set of selection criteria (Supplementary Table C2.8) to determine whether those applied are reasonable; this allowed 16 additional successful results from Shaw-DHT (11), thermal Thellier (4) and Microwave methods (1). These additional results (Supplementary Figure C1.5) are distinct from those obtained using the stricter criteria. Their inclusion into the overall accepted set of results reduces the site-means for MD2 and MD3 by 20 % and 12 % respectively, while MD6 would increase by 9 %. We maintain that the strict selection criteria are justified and that the results falling outside these criteria should be rejected on the basis that they bias the results slightly. It is worth noting, however, that the number of results would increase by ~50 % and that all site-mean palaeointensities remain similarly high.

5.5.2 Palaeointensity results - BMS

A summary of palaeointensity results is given in Table 5.2 and specimen level results in Supplementary Tables C2.4 – C2.6. Specimens from five sampling sites (BM1 – 5) were weakly magnetised (less than 10 mA m^{-1} on average; Supplementary Figure C1.2). In addition, highly non-reversible κ (T) curves (Figures 5.3g & h) combined with uninterpretable AF demagnetisations of the NRM of selected specimens from these sites, led to a blanket rejection.

Thermal Thellier experiments performed poorly and no results were successful for any specimens from the remaining three sites. Many specimens from site BM6 were too weakly magnetised (10 – 100 mA m^{-1}) for use on the Microwave system and only a single Shaw-

DHT palaeointensity (3.0 µT) was obtained that satisfied the selection criteria. This result is equivalent to the weak-intensity results obtained from site BM8 from both Shaw-DHT and Microwave methods (2.9 ± 0.4 µT); however, only three palaeointensity results were obtained for this site.

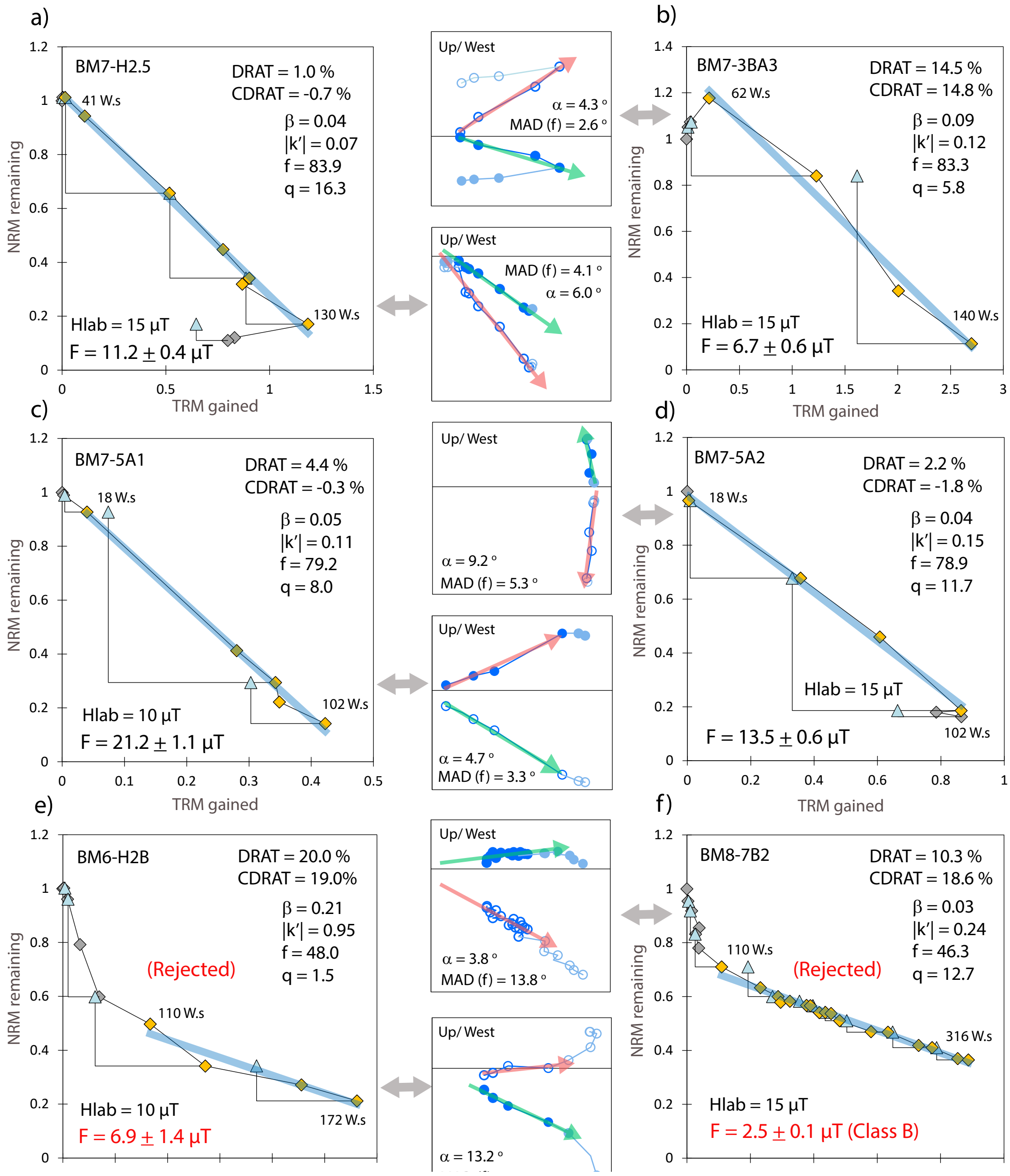

Figure 5.5. Microwave example Arai diagrams and associated orthogonal diagrams in specimen coordinates. a – d) Example results from site BM7 showing the variation seen in the Microwave results from this site. e & f) Rejected specimen results from sites BM6 and BM8 respectively. Specimens from these sites demagnetise at noticeably higher power than those in site BM7. Plot descriptions are the same as for Figure 5.4.

Causes of failure were typically related to alteration rather than MD effects with many Microwave and Shaw-DHT specimen results falling only slightly short of the selection criteria. Microwave experiments produced high DRAT or CDRAT values although these were associated with linear Arai plots; Shaw-DHT specimen results failed in the $slope_N$ correlation rather than $slope_T$ (Supplementary Tables C2.5 and C2.6).

A wide range of results were obtained for site BM7 producing a mean palaeointensity of 14.3 ± 7.6 μT (N = 12) (Figure 5.5; Table 5.2; Supplementary Tables C2.5 and C2.6). Successful Shaw-DHT specimens from site BM7 require an ARM correction that is small in absolute terms (mean 1.4 μT) as seen in the $slope_{A1}$ values (Supplementary Table C2.6). Specimens that underwent LTD treatment produced no successful results and, if we compare narrowly rejected results, we see that LTD treatment was not affecting the palaeointensity estimates (Supplementary Table C2.6).

Specimens from site BM7 produced linear palaeointensity slopes which start at low power (~50 W.s) and slightly low coercivities (10 – 15 mT; Supplementary Figure C1.6). They are typically fully demagnetised by 120 W.s and 40 mT respectively (Figures 5.5a – d). This contrasts with specimens from sites BM6 and BM8 whose characteristic components are isolated above ~100 W.s and which are not fully demagnetised by 200 – 300 W.s (Figure 5.5e & f). Separating results for site BM7 by method produces a notable difference; Shaw-DHT palaeointensities are lower and more precise (7.8 ± 0.9 μT, N = 5) compared to the higher and more dispersed Microwave results (18.8 ± 6.4 μT, N = 7).

A single, narrowly rejected thermal Thellier result from site BM7 would be in approximate agreement with the site mean result (14.3 μT; Table 5.2). An estimate of 11.4 μT is obtained, but with high values of DRAT and CDRAT of 25 % and 23 % respectively (Supplementary Figure C1.7). The alteration produces a trend in pTRM checks which, after applying a correction (Valet et al., 1996), would produces a higher estimate of 16.4 μT (Supplementary Figure C1.7); however, we note that this result is not robust.

Site	Ref	Age (Ma)	Type	Lat (°S)	Lon (°E)	Dec (°)	Inc (°)	N(n)	k	a_{95} (°)	F (μT)	σ_F (μT)	n/N_{PI}	N_{mic}	N_{Shaw}	N_{Thel}	VDM Am^2 (10^{22})	σ_{VDM}	Q_{PI}
MD2	EDMC	755	Dyke	23.96	115.61	6.2	38.6	10 (1)	64	6.1	28.9	2.6	2/36	2	-	-	6.29	0.57	7
MD3	EDMG	755	Dyke	23.88	115.64	15.8	33.3	6	205	4.3	28.2	4.7	4/38	3	-	1	6.41	1.08	7
MD6	EDMB	755	Dyke	23.91	115.56	17.2	35.1	11	51	6.6	28.5	4.7	12/33	6	5	1	6.08	1.45	9
BM6	WG1*	1070	Sill	23.52	116.58	359.8	48.7	9(3)	75	5.6	3.0	-	1/27	-	1	-	0.60	-	6
BM7	WG8	1070	Sill	23.94	116.91	343.7	42.9	6	257	3.8	14.3	7.6	12/44	7	5	-	2.98	1.53	8
BM8	WG6	1070	Sill	23.78	116.56	337.0	35.2	8(3)	41	8.2	2.9	0.4	3/43	2	1	-	0.64	0.10	8

Table 5.2. Summary of palaeomagnetic results from both localities. Ref, site reference from original study;, indicates that our site was close to, but not the exact original site; D (°), magnetic tectonic declination; I (°), magnetic tectonic inclination; N(n), total number of samples given unit weight in calculation of dyke means (number of samples included from baked contact); k , the Fisher precision parameter; α95, 95 % confidence limit on the mean direction; F, field intensity; σ_F, absolute standard deviation; NPI, number of palaeointensity results; Nmic, NShaw, NThel, number of results for each respective method; VDM, virtual dipole moment; σ_{VDM}, absolute standard deviation; Q_{PI}, quality score of palaeointensity (see Supplementary Table C2.7). Directional information taken from Wingate & Giddings (2000) and Wingate et al. (2002).*

5.5.3 Q_{PI} results

Successful site-mean results are assessed using the Q_{PI} system (Biggin & Paterson, 2014). Previous comprehensive palaeomagnetic studies combine with modern palaeointensity techniques here to produce high overall site scores of between 6 and 9 for both localities (Table 5.2; Supplementary Table C2.7). Well-defined directions are associated with primary remanent magnetisation and accurate U-Pb ages (Wingate & Giddings, 2000; Wingate et al., 2002). SEM images also suggest that the remanences are primary (Figure 5.2). Palaeointensity techniques test for, or remain clear of, alteration and MD effects. This is achieved through pTRM checks, pTRM tail checks and ARM corrections, and is supported by rock magnetic results (Figures 5.3b, e, k, l, q & r). Additionally, there is reasonable evidence that the final estimate was not significantly biased by anisotropy of TRM, cooling rate effects, or non-linear TRM effects. This is provided by low γ-values, evidence of PSV grain size distributions (Figures 5.3f & s) that are unlikely to be strongly affected by cooling rate differences (Biggin et al., 2013), and varying the applied field strength in alternate experiments respectively.

5.6 Discussion

Palaeointensity results are obtained from three cooling units for each studied rock target. MDS results are remarkably consistent, however the results for BMS are lower quality and a difference can be observed according to the method used (Supplementary Figure C1.8). Multiple lines of evidence support the presence of primary thermal remanence magnetisation in both targets (Wingate & Giddings, 2000; Wingate et al., 2002), including the new SEM evidence. Both MDS and BMS produced well-defined mean palaeopoles which have been used for plate reconstructions. It is uncertain, however, whether the associated palaeointensity results are sufficiently time-averaged and capture the true dipole strength rather than extremes of palaeosecular variation. It should be noted that BMS directions of opposite polarity (original sample site 25; Wingate et al., 2002) imply that the intrusive event spanned at least one reversal of the Earth's magnetic field, suggesting that the type-A magnetisations are adequately averaging palaeosecular variation.

5.6.1 MDS

MDS rock magnetic and palaeointensity results are consistent; sites from which we observe more reversible M_s (T) and κ (T) curves (Figure 5.3) also produce the successful palaeointensities (Figures 5.3 & 4; Supplementary Figure C1.4; Supplementary Tables C2.1 – C2.3). Backscatter SEM images show submicron intergrowths of magnetite (Figure 5.2c), which are attributed to the thermal demagnetisation of a narrow distribution of SD remanence in sites MD3 and MD6. Evidence of occasional alteration cracking in some larger grains from samples in sites MD2 and 3 may be the cause of the lower overall success rates in these sites. The palaeointensity results obtained from MD2, 3 and 6 are high and in excellent agreement within and between site (and method). Application of strict selection criteria improves the results, by avoiding what appear to be slightly biased results (Supplementary Figure C1.5). Palaeomagnetic directions from these sites are consistent with other MDS sites and those from the Northampton block (Embleton & Schmidt, 1985; Wingate & Giddings, 2000). The consistent directions combined with positive baked contact tests rule out IRM as the source of the high palaeointensities (Wingate & Giddings, 2000).

Two-slope (rather than sagging) Arai diagrams seen in some specimens from site MD3 (Figure 5.4a; Supplementary Figure C1.4) are a common phenomenon in Thellier palaeointensity results which is not well-understood (Kosterov & Prévot, 1998; Sprain et al., 2018; Tauxe et al., 2021). The slope values associated with the low-power/ temperature section of the Arai plot can be attributed to overprint if the values are Earth-like. These sections do correspond to overprint regions in the orthogonal diagrams (e.g., Figure 5.4a), however, the intensity values associated would be too high. This would be true of any high intensities with two-slope behaviour, and although this may be related to MD remanence or some form of annealing (Kosterov & Prévot, 1998), it is more likely to be a moderate IRM overprint.

VDMs from all three sites range between 5.3 and 6.7 $Am^2 \times 10^{22}$ with standard deviations of less than 1.5 $Am^2 \times 10^{22}$ (Table 5.2), similar in strength to the uniquely high MCR results from ~325 Myr earlier. Results which provide evidence of a strong geomagnetic field in the mid-Neoproterozoic are not expected if ICN has yet to occur, as suggested by recent models (Bono et al., 2019; Driscoll, 2016). At this time, the available thermal energy is estimated to have decreased to a level which could only sustain a weakly powered geodynamo.

5.6.2 BMS

Despite carrying out experiments on 165 individual specimens, the number of results from the BMS is less than ideal, particularly since we must rely on just three out of eight sites for palaeointensity. Intensity estimates from site BM8 are very weak and site BM6 produces just a single result (also weak). In contrast, site BM7 produces many more results with a notably higher mean and large within-site dispersion.

Site BM7 was originally interpreted to be of higher quality with only type-A magnetisation reported (Wingate et al., 2002). Rock magnetic results suggest that there is localised heterogeneity within-site (Figures 5.3k, p & q). Furthermore, SEM results show that specimens contain a mixture of grain assemblages (Figure 5.2) which may be responsible for the high within-site scatter seen in palaeointensity results. In agreement, high and low microwave palaeointensities are obtained from the same mother samples (core 5, samples A and C and core H2; Supplementary Table C2.5). No specific correlation can therefore be made, between rock magnetic results and particular palaeointensity values.

With such few results from sites BM6 and BM8, and high dispersion in site BM7, we examine results with certain selection criteria relaxed to determine if any qualitative value can be obtained. We note that site BM6 includes a further five Shaw-DHT results which were rejected due to failure of the $slope_T$ criterion alone. These specimens produced well-correlated ($R^2 \geq 0.990$) and linear ($|k'| \leq 0.2$) palaeointensity slopes. They are also associated with accurate palaeomagnetic directions (Supplementary Table C2.6) obtained from type-A (primary, thermally stable magnetisation; Wingate et al., 2002) and SD-type hysteresis loops (Supplementary Figure C1.1). We can quantify the errors associated with specimens that only fail the $slope_T$ criterion.

A non-unit $slope_T$ places a potential lower or upper bound on the palaeointensity estimate; e.g., a $slope_T$ of 0.70 suggests that the associated palaeointensity may under-estimate the field by up to 30 %. For weak palaeointensity estimates, the equivalent absolute error value is small; the five rejected results would produce a mean palaeointensity of 6.6 ± 1.6 μT, however, their low $slope_T$ values suggest an upper bound of 8.9 μT ± 1.8 μT (Supplementary Table C2.6). These narrowly rejected, consistent results suggest that site BM6 was recording a weak palaeofield at this time. While we do not determine this site robust enough to report a VDM, these results are remarkably similar to Shaw-DHT results from site BM7 (7.8 ± 0.9 μT, N = 5), and relatively close, in absolute terms, to the results from site BM8 (2.9 ± 0.4 μT, N = 3). It may be possible that the large scatter associated with site BM7 microwave data is due to the much smaller specimens containing heterogeneous abundances of particular magnetic minerals.

Site BM8 produces consistently more reversible κ (T) curves, with specimens demagnetising at high power and coercivities; these are likely to be associated with the fine, pristine opaque grains observed in the backscatter SEM images. The palaeointensity results, obtained from two methods, are precise and very weak. The evidence, therefore, suggests that the results from this site are robust.

We arrive at the conclusion that reasonable site mean palaeointensities are obtained for sites BM7 and BM8, which produce VDM's of 3.0 and 0.6 Am^2 x 10^{22} respectively (Table 5.2). Site BM6 produces a single specimen result and is therefore rejected. We tentatively suggest that a conservative estimate for this site is would be 1.8 ± 0.4 Am^2 x 10^{22} (based on a 9 μT upper bound mean) and note that this would support a mean VDM from the accepted sites (1.8 ± 1.2 Am^2 x 10^{22}). This reenforces our interpretation that these sills are recording a moderately weak field at this time. At 1070 ± 6 Ma, the BDS results are concordant with a long-term decreasing trend associated with a decaying thermal regime in a fully liquid core (Figure 5.6a; Bono et al., 2019). They are, however, at odds with the considerably higher dipole moment values obtained at a similar time (~1087 Ma) from the Mid-Continent Rift.

5.6.3 Implications for the Precambrian geodynamo

Little is known about Precambrian dipole moment variability on any time scale. While we cannot rule out the possibility that our results are biased by short-term deviations from the time-averaged field, these new combined results suggest that the variability of the field on timescales tens of millions of years may have been similar in the Precambrian to that observed in the Phanerozoic.

We compare VDM results (Figure 5.6a) from MDS at ~755 Ma (6.3 ± 0.1 Am^2 x 10^{22}) with those from the Franklin LIP at ~720 Ma (1.0 ± 0.5 Am^2 x 10^{22}; Lloyd et al., 2021a). These two datasets are from the spatially distinct palaeocontinents of Australia and Laurentia. We also compare the weak VDM results from BMS at 1070 ± 6 Ma (1.8 ± 1.2 $Am^2 \times 10^{22}$) which are at odds with those from the MCR at 1087 ± 2 Ma (5.4 ± 1.2 $Am^2 \times 10^{22}$; N > 3; Kulakov et al., 2013; Sprain et al., 2018). The data in these two comparisons are separated temporally by ~35 Ma and ~17 Ma respectively, and would require significant changes in field intensity or dipole behaviour to explain the extreme contrast.

These Precambrian variations are similar to, or greater than, those seen for much younger time periods populated by larger data sets; for example, two ~5 Ma (0.05 – 5 Ma and 10 – 15 Ma) average VDM values (6.9 ± 2.8 $Am^2 \times 10^{22}$ and 3.6 ± 1.7 $Am^2 \times 10^{22}$) were compared by Smirnov (2017).

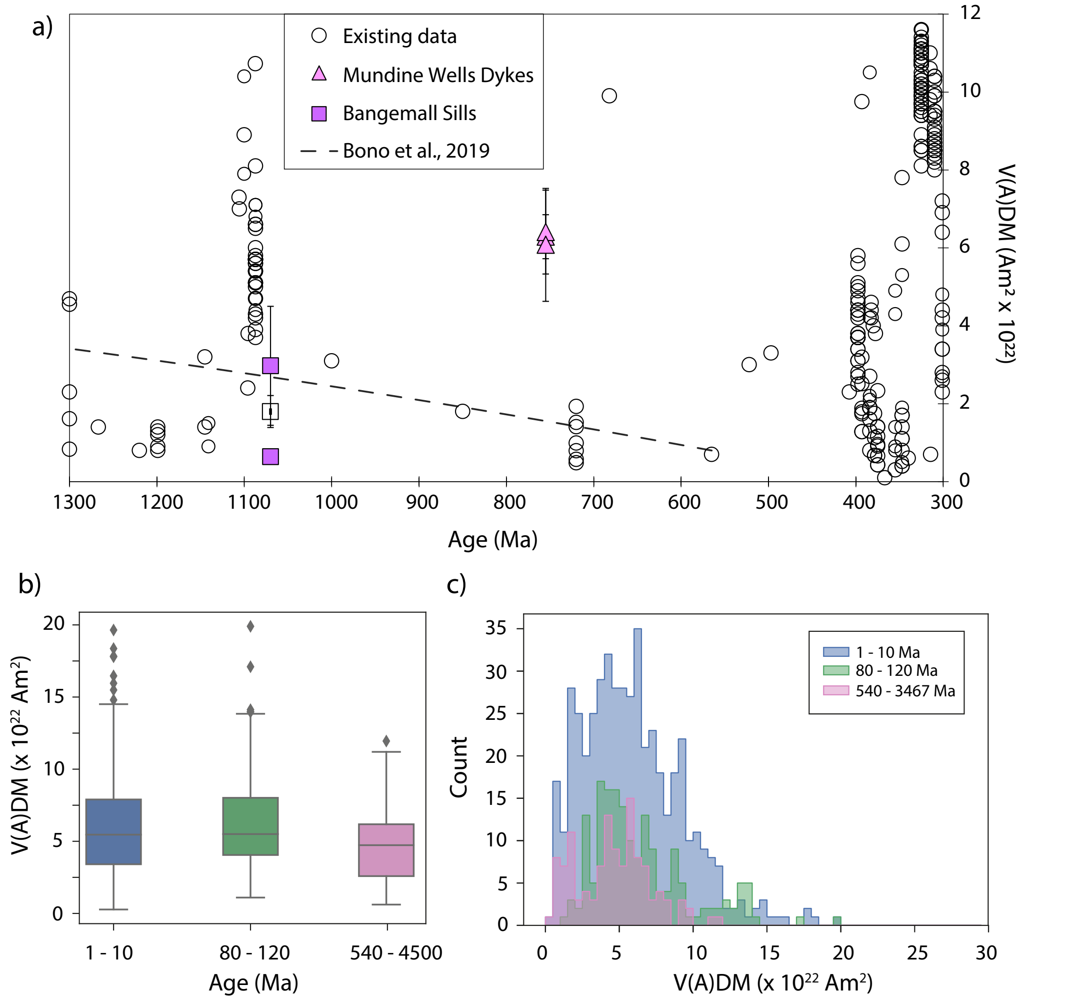

Figure 5.6. a) Plot showing global data of virtual (Axial) dipole moments taken from the PINT database (v.2015.05; http://earth.liv.ac.uk/pint/; Biggin et al., 2015) for the period 300 – 1300 Ma. All existing data prior to 500 Ma is filtered so that each cooling unit has N ≥ 3. All data ≥ 500 Ma

is also filtered by QPI ≥ 3 (Biggin et al., 2015). Second order polynomial best-fit line from Bono et al. (2019), dashed line. BDS site BM6 is depicted (square outline) for context only. b) Box and whisker plot of virtual (Axial) dipole moments taken from the PINT database (v.2015.05; http://earth.liv.ac.uk/pint/; Biggin et al. 2015) separated into three time periods (N ≥ 3). c) Distribution of virtual (Axial) dipole moments over similar time periods (labelled).

A Precambrian study of PSV (which include BMS; Smirnov et al., 2011) of the time period 1.0 – 2.2 Ga produces the Model G (McFadden et al., 1988) parameters a = 11.1 ± 1.5 ° and b = 0.21 ± 0.09, where a and b are constants that quantify the scatter of virtual geomagnetic poles at the equator and its rate of increase with palaeolatitude respectively. When we compare these with recently calculated parameters for the last 10 Ma (a = 11.3 ± 1.3 ° and b = 0.27 ± 0.08; Cromwell et al., 2018; Doubrovine et al., 2019) we see that the 'a' parameter values are indistinguishable. This supports that, on average, the axial dipole was similarly dominant over higher-order fields (Biggin et al., 2020) in the Precambrian as it was in the last 10 Ma.

Analysis of current PINT data indicate that the field was slightly less variable in the Precambrian compared with younger periods (Figure 5.6b); however, the data is so sparsely populated that it is likely that variability is not fully captured. The distribution of dipole moments is also remarkably similar but the amount of data for the last 10 Ma is almost five times greater than for the entire Precambrian (Figure 5.6c).

We therefore identify multiple similarities between the Precambrian field and that of the last 10 Ma: distribution of dipole moments, average variability in PINT, dipole dominance inferred from PSV data, and from this study, large changes in dipole moment apparent on timescales of tens of Myrs. Observational parameters such as palaeointensity act as a constraint on numerical dynamo simulations which aim to solve many deep earth problems in the ancient past, including events such as ICN (Biggin et al., 2015; Bono et al., 2019). However, it appears that the data coverage in the Precambrian may be insufficient to accurately average the field in order to use with an acceptable level of uncertainty.

5.7 Conclusions

We have obtained new palaeointensity measurements from two important periods in the

Precambrian era. Weak site-mean intensities (3 and 14 μT) are obtained from two Bangemall Sills at 1070 ± 6 Ma with VDMs of 0.6 and 3 Am^2 x 10^{22}. An additional sill provides a single weak intensity (3 μT) with evidence to suggest the true value may be closer to 9 μT; an amended VDM from this sill would be equivalent to the mean of the two accepted VDMs. These new weak-field results are in stark contrast with the strong field reported at 1087 Ma, suggesting that the field was highly variable at this time. The higher of these new results are also concordant with a long-term decaying dipole trend.

At 755 ± 3 Ma, three MDS sites produce a high-fidelity palaeointensity results of 28.5 ± 0.3 μT and equally precise VDMs of 6.3 ± 0.1 Am^2 x 10^{22}. Results are consistent within and between-site, and from three independent techniques; they are also associated with high Q_{PI} scores between 7 and 9. A strong field at this time, at face value, does not support recent predictions of a young inner core and is highly distinct to recently reported mid-Neoproterozoic weak intensities from the Franklin Large Igneous Province (Lloyd et al., 2021a).

These combined new data allow for comparisons with existing data that are from rocks differing in age by 17 and 35 Myr. They suggest that Precambrian field variability is similar to that observed in more recent times. With severe paucity in global records, particularly for the Neoproterozoic era, it is therefore likely that palaeointensities may capture only part of a highly variable field. Using spatial or temporal anomalies as a proxy for events such as ICN may not be robust until many further data is obtained.

5.8 References cited

Biggin, A. J., & Böhnel, H. N. (2003). A method to reduce the curvature of Arai plots produced during Thellier palaeointensity experiments performed on multidomain grains. *Geophysical Journal International*, *155*(3). https://doi.org/10.1111/j.1365-246X.2003.02089.x

Biggin, A. J., Badejo, S., Muxworthy, A. R., & Dekkers, M. J. (2013). The effect of cooling rate on the intensity of thermoremanent magnetisation (TRM) acquired by assemblages of pseudo-single domain, multidomain and interacting single-domain grains. *Geophysical Journal International*, *193*(3), 1239–1249. https://doi.org/10.1093/gji/ggt078

Biggin, A. J., Piispa, E. J., Pesonen, L. J., Holme, R., Paterson, G. A., Veikkolainen, T., & Tauxe, L. (2015). Palaeomagnetic field intensity variations suggest Mesoproterozoic inner-core nucleation. *Nature*, *526*(7572), 245–248. https://doi.org/10.1038/nature15523

Biggin, A. J., & Paterson, G. A. (2014). A new set of qualitative reliability criteria to aid inferences on palaeomagnetic dipole moment variations through geological time. *Frontiers in Earth Science*, *2*(October), 1–9. https://doi.org/10.3389/feart.2014.00024

Biggin, A. J., Perrin, M., & Shaw, J. (2007). A comparison of a quasi-perpendicular method of absolute palaeointensity determination with other thermal and microwave techniques. *Earth and Planetary Science Letters*, *257*(3–4), 564–581. https://doi.org/10.1016/j.epsl.2007.03.016

Biggin, A. J., Perrin, M., & Dekkers, M. J. (2007). A reliable absolute palaeointensity determination obtained from a non-ideal recorder. *Earth and Planetary Science Letters*, *257*(3–4), 545–563. https://doi.org/10.1016/j.epsl.2007.03.017

Biggin, A. J., de Wit, M. J., Langereis, C. G., Zegers, T. E., Voûte, S., Dekkers, M. J., & Drost, K. (2011). Palaeomagnetism of Archaean rocks of the Onverwacht Group, Barberton Greenstone Belt (southern Africa): Evidence for a stable and potentially reversing geomagnetic field at ca. 3.5Ga. *Earth and Planetary Science Letters*, *302*(3–4), 314–328. https://doi.org/10.1016/j.epsl.2010.12.024

Bono, R. K., Tarduno, J. A., Nimmo, F., & Cottrell, R. D. (2019). Young inner core inferred from Ediacaran ultra-low geomagnetic field intensity. *Nature Geoscience*, *12*(2), 143–147. https://doi.org/10.1038/s41561-018-0288-0

Coe, R. S. (1967). The Determination of Palaeo-Intensities of the Earth's Magnetic Field with Emphasis on Mechanisms Which Could Cause Non-Ideal Behavior in Thellier's Method. *Journal of Geomagnetism and Geoelectricity*, *19*(3), 157–179. https://doi.org/10.5636/jgg.19.157

Coe, R. S., Grommé, S., & Mankinen, E. A. (1978). Geomagnetic palaeointensities from radiocarbon-dated lava flows on Hawaii and the question of the Pacific nondipole low. *Journal of Geophysical Research: Solid Earth*, *83*(B4), 1740–1756. https://doi.org/10.1029/jb083ib04p01740

Cromwell, G., Johnson, C. L., Tauxe, L., Constable, C. G., & Jarboe, N. A. (2018). PSV10: A Global Data Set for 0–10 Ma Time-Averaged Field and Palaeosecular Variation Studies. *Geochemistry, Geophysics, Geosystems*, *19*(5), 1533–1558. https://doi.org/10.1002/2017GC007318

Doubrovine, P. V., Veikkolainen, T., Pesonen, L. J., Piispa, E., Ots, S., Smirnov, A. V., et al. (2019). Latitude Dependence of Geomagnetic Palaeosecular Variation and its Relation to the Frequency of Magnetic Reversals: Observations From the Cretaceous and Jurassic. *Geochemistry, Geophysics, Geosystems*, *20*(3), 1240–1279. https://doi.org/10.1029/2018GC007863

Driscoll, P. E. (2016). Simulating 2 Ga of geodynamo history. *Geophysical Research Letters*, *43*(11), 5680–5687. https://doi.org/10.1002/2016GL068858

Dunlop, D., Özdemir, Ö., & Fuller, M. D. (1998). Rock Magnetism: Fundamentals and Frontiers. *Physics Today*. https://doi.org/10.1063/1.882466

Dunlop, D. J. (2011). Physical basis of the Thellier-Thellier and related palaeointensity methods. *Physics of the Earth and Planetary Interiors*, *187*(3–4), 118–138. https://doi.org/10.1016/j.pepi.2011.03.006

Dunlop, D. J. (2014). High-temperature susceptibility of magnetite: A new pseudo-single-domain effect. *Geophysical Journal International*, *199*(2), 707–716. https://doi.org/10.1093/gji/ggu247

Embleton, B. J. J., & Schmidt, P. W. (1985). Age and significance of magnetisations in dolerite dykes from the northampton block, western australia. *Australian Journal of Earth Sciences*, *32*(3), 279–286. https://doi.org/10.1080/08120098508729330

Grappone, J. M., Biggin, A. J., & Hill, M. J. (2019). Solving the mystery of the 1960 Hawaiian lava flow: Implications for estimating Earth's magnetic field. *Geophysical Journal International*, *218*(3), 1796–1806. https://doi.org/10.1093/gji/ggz252

de Groot, L. V., Mullender, T. A. T., & Dekkers, M. J. (2013). An evaluation of the influence of the experimental cooling rate along with other thermomagnetic effects to explain anomalously low palaeointensities obtained for historic lavas of Mt Etna (Italy). *Geophysical Journal International*, *193*(3), 1198–1215. https://doi.org/10.1093/gji/ggt065

Haggerty, S. E. (1991). Chapter 5.Oxide Textures - A Mini-Atlas. In *Oxide Minerals* (pp. 129–220). https://doi.org/10.1515/9781501508684-008

Hawkins, L. M. A., Anwar, T., Shcherbakova, V. V., Biggin, A. J., Kravchinsky, V. A., Shatsillo, A. V., & Pavlov, V. E. (2019). An exceptionally weak Devonian geomagnetic field recorded by the Viluy Traps, Siberia. *Earth and Planetary Science Letters*, *506*, 134–145. https://doi.org/10.1016/j.epsl.2018.10.035

Hill, M. J., Gratton, M. N., & Shaw, J. (2002). A comparison of thermal and microwave palaeomagnetic techniques using lava containing laboratory induced remanence. *Geophysical Journal International*, *151*(1), 157–163. https://doi.org/10.1046/j.1365-246X.2002.01745.x

Hodych, J. P. (1996). Inferring domain state from magnetic hysteresis in high coercivity dolerites bearing magnetite with ilmenite lamellae, *142*, 523–533.

Kirschvink, J. L. (1980). The least-squares line and plane and the analysis of palaeomagnetic data. *Geophysical Journal of the Royal Astronomical Society*. https://doi.org/10.1111/j.1365-246X.1980.tb02601.x

Kissel, C., & Laj, C. (2004). Improvements in procedure and palaeointensity selection criteria (PICRIT-03) for Thellier and Thellier determinations: Application to Hawaiian basaltic long cores. *Physics of the Earth and Planetary Interiors*, *147*(2-3 SPEC.ISS.), 155–169.

https://doi.org/10.1016/j.pepi.2004.06.010

Kodama, K. P., Carnes, L. K., Tarduno, J. A., & Berti, C. (2019). Palaeointensity of the 1.3 billion-yr-old Gardar basalts, southern Greenland revisited: No evidence for onset of inner core growth. *Geophysical Journal International*, *217*(3), 1974–1987. https://doi.org/10.1093/gji/ggz126

Kosterov, A. A., & Prévot, M. (1998). Possible mechanisms causing failure of Thellier palaeointensity experiments in some basalts. *Geophysical Journal International*, *134*(2), 554–572. https://doi.org/10.1046/j.1365-246X.1998.00581.x

Kulakov, E. V., Sprain, C. J., Doubrovine, P. V., Smirnov, A. V., Paterson, G. A., Hawkins, L., et al. (2019). Analysis of an Updated Palaeointensity Database (QPI-PINT) for 65–200 Ma: Implications for the Long-Term History of Dipole Moment Through the Mesozoic. *Journal of Geophysical Research: Solid Earth*, *124*(10), 9999–10022. https://doi.org/10.1029/2018JB017287

Kulakov, Evgeniy V., Smirnov, A. V., & Diehl, J. F. (2013). Absolute geomagnetic palaeointensity as recorded by ~1.09 Ga Lake Shore Traps (Keweenaw Peninsula, Michigan). *Studia Geophysica et Geodaetica*, *57*(4), 565–584. https://doi.org/10.1007/s11200-013-0606-3

Li, Z. X., Bogdanova, S. V., Collins, A. S., Davidson, A., De Waele, B., Ernst, R. E., et al. (2008). Assembly, configuration, and break-up history of Rodinia: A synthesis. *Precambrian Research*, *160*(1–2), 179–210. https://doi.org/10.1016/j.precamres.2007.04.021

Lloyd, S. J., Biggin, A. J., Halls, H., & Hill, M. J. (2021a). First Palaeointensity Data from the Cryogenian and their potential implications for Inner Core Nucleation Age. *Geophysical Journal International*. https://doi.org/10.1093/gji/ggab090

Lloyd, S. J., Paterson, G. A., Thallner, D., & Biggin, A. J. (2021b). Improvements to the Shaw-Type Absolute Palaeointensity Method. *Frontiers in Earth Science*, *9*(July), 1–11. https://doi.org/10.3389/feart.2021.701863

McFadden, P. L., Merrill, R. T., & Mcelhinny, M. W. (1988). Dipole / Quadrupole Family Modeling of Palaeosecular Variation. *Journal of Geophysical Research*, *93*(7), 11,583-11,588.

Meert, J. G., & Torsvik, T. H. (2003). The making and unmaking of a supercontinent: Rodinia revisited. *Tectonophysics*, *375*(1–4), 261–288. https://doi.org/10.1016/S0040-1951(03)00342-1

Mochizuki, N., Tsunakawa, H., Oishi, Y., Wakai, S., Wakabayashi, K. ichi, & Yamamoto, Y. (2004). Palaeointensity study of the Oshima 1986 lava in Japan: Implications for the reliability of the Thellier and LTD-DHT Shaw methods. *Physics of the Earth and Planetary Interiors*, *146*(3–4), 395–416. https://doi.org/10.1016/j.pepi.2004.02.007

Monster, M. W. L., Groot, L. V. De, Biggin, A. J., & Dekkers, M. J. (2015). The performance of various palaeointensity techniques as a function of rock magnetic behaviour – A case study for La Palma. *PHYSICS OF THE EARTH AND PLANETARY INTERIORS*, *242*, 36–49. https://doi.org/10.1016/j.pepi.2015.03.004

Morris, E. R., Schillinger, W., Coe, R. S., Pluhar, C. J., & Jarboe, N. A. (2009). Automating the 2G superconducting rock magnetometer for single-solenoid alternating field demagnetisation. *Geochemistry, Geophysics, Geosystems*, *10*(5). https://doi.org/10.1029/2008GC002289

Muhling, P.C., Brakel, A.T. (1985). Geology of the Bangemall Group – the evolution of an intracratonic Proterozoic basin. In: Geological Survey Western Australia Bulletin 128, 1–219.

Oishi, Y., Tsunakawa, H., Mochizuki, N., Yamamoto, Y., Wakabayashi, K. I., & Shibuya, H. (2005). Validity of the LTD-DHT Shaw and Thellier palaeointensity methods: A case study of the Kilauea 1970 lava. *Physics of the Earth and Planetary Interiors*, *149*(3–4), 243–257. https://doi.org/10.1016/j.pepi.2004.10.009

Paterson, G. A. (2011). A simple test for the presence of multidomain behavior during palaeointensity experiments. *Journal of Geophysical Research: Solid Earth*, *116*(10), 1–12.

https://doi.org/10.1029/2011JB008369

Paterson, G. A., Tauxe, L., Biggin, A. J., Shaar, R., & Jonestrask, L. C. (2014). Standard Palaeointensity Definitions v1.1, 0–43. Retrieved from http://www.palaeomag.net/SPD/spdweb.html

Paterson, G. A., Biggin, A. J., Hodgson, E., & Hill, M. J. (2015). Thellier-type palaeointensity data from multidomain specimens. *Physics of the Earth and Planetary Interiors*, *245*, 117–133. https://doi.org/10.1016/j.pepi.2015.06.003

Paterson, G. A., Heslop, D., & Pan, Y. (2016). The pseudo-Thellier palaeointensity method: New calibration and uncertainty estimates. *Geophysical Journal International*, *207*(3), 1596–1608. https://doi.org/10.1093/gji/ggw349

Paterson, G. A., Muxworthy, A. R., Yamamoto, Y., & Pan, Y. (2017). Bulk magnetic domain stability controls palaeointensity fidelity. *Proceedings of the National Academy of Sciences of the United States of America*, *114*(50), 13120–13125. https://doi.org/10.1073/pnas.1714047114

Riisager, P., & Riisager, J. (2001). Detecting multidomain magnetic grains in Thellier palaeointensity experiments. *Physics of the Earth and Planetary Interiors*, *125*(1–4), 111–117. https://doi.org/10.1016/S0031-9201(01)00236-9

Schmidt, P. W. (1993). Palaeomagnetic cleaning strategies. *Physics of the Earth and Planetary Interiors*, *76*(1–2), 169–178. https://doi.org/10.1016/0031-9201(93)90066-I

Selkin, P. A., Gee, J. S., Tauxe, L., Meurer, W. P., & Newell, A. J. (2000). The effect of remanence anisotropy on palaeointensity estimates: A case study from the Archean Stillwater Complex. *Earth and Planetary Science Letters*, *183*(3–4), 403–416. https://doi.org/10.1016/S0012-821X(00)00292-2

Shaar, R., & Tauxe, L. (2013). Thellier GUI: An integrated tool for analyzing palaeointensity data from Thellier-type experiments. *Geochemistry, Geophysics, Geosystems*. https://doi.

org/10.1002/ggge.20062

Shaar, R., & Tauxe, L. (2015). Instability of thermoremanence and the problem of estimating the ancient geomagnetic field strength from non-single-domain recorders. *Proceedings of the National Academy of Sciences of the United States of America*, *112*(36), 11187–11192. https://doi.org/10.1073/pnas.1507986112

Shcherbakov, V. P., Gribov, S. K., Lhuillier, F., Aphinogenova, N. A., & Tsel'movich, V. A. (2019). On the Reliability of Absolute Palaeointensity Determinations on Vasaltic Rocks Bearing a Thermochemical Remanence. *Journal of Geophysical Research: Solid Earth*, *124*(8), 7616–7632. https://doi.org/10.1029/2019JB017873

Smirnov, A. V. (2017). Intensity of geomagnetic field in the Precambrian and evolution of the Earth's deep interior. *Izvestiya, Physics of the Solid Earth*, *53*(5), 760–768. https://doi.org/10.1134/S1069351317050123

Smirnov, A. V., Tarduno, J. A., & Evans, D. A. D. (2011). Evolving core conditions ca. 2 billion years ago detected by palaeosecular variation. *Physics of the Earth and Planetary Interiors*, *187*(3–4), 225–231. https://doi.org/10.1016/j.pepi.2011.05.003

Smirnov, A. V., Kulakov, E. V., Foucher, M. S., & Bristol, K. E. (2017). Intrinsic palaeointensity bias and the long-term history of the geodynamo. *Science Advances*, *3*(2), 1–8. https://doi.org/10.1126/sciadv.1602306

Smirnov, A. V., & Tarduno, J. A. (2005). Thermochemical remanent magnetisation in Precambrian rocks: Are we sure the geomagnetic field was weak? *Journal of Geophysical Research: Solid Earth*, *110*(6), 1–12. https://doi.org/10.1029/2004JB003445

Sprain, C. J., Swanson-Hysell, N. L., Fairchild, L. M., & Gaastra, K. (2018). A field like today's? The strength of the geomagnetic field 1.1 billion years ago. *Geophysical Journal International*, *213*(3), 1969–1983. https://doi.org/10.1093/gji/ggy074

Suttie, N., Shaw, J., & Hill, M. J. (2010). Direct demonstration of microwave demagnetisation of a whole rock sample with minimal heating. *Earth and Planetary Science Letters*. https://doi.org/10.1016/j.epsl.2010.02.002

Tanaka, H., & Komuro, N. (2009). The Shaw palaeointensity method: Can the ARM simulate the TRM alteration? *Physics of the Earth and Planetary Interiors*, *173*(3–4), 269–278. https://doi.org/10.1016/j.pepi.2009.01.003

Tarduno, J. A., Cottrell, R. D., Bono, R. K., Oda, H., Davis, W. J., Fayek, M., et al. (2020). Palaeomagnetism indicates that primary magnetite in zircon records a strong Hadean geodynamo. *Proceedings of the National Academy of Sciences of the United States of America*, *117*(5), 2309–2318. https://doi.org/10.1073/pnas.1916553117

Tauxe, L., Santos, C. N., Cych, B., Zhao, X., Roberts, A. P., Nagy, L., & Williams, W. (2021). Understanding Nonideal Palaeointensity Recording in Igneous Rocks: Insights From Aging Experiments on Lava Samples and the Causes and Consequences of "Fragile" Curvature in Arai Plots. *Geochemistry, Geophysics, Geosystems*, *22*(1), 1–24. https://doi.org/10.1029/2020GC009423

Tauxe, L., & Staudigel, H. (2004). Strength of the geomagnetic field in the cretaceous normal superchron: New data from submarine basaltic glass of the troodos ophiolite. *Geochemistry, Geophysics, Geosystems*, *5*(2). https://doi.org/10.1029/2003GC000635

Tsunakawa, H., & Shaw, J. (1994). The Shaw method of palaeointensity determinations and its application to recent volcanic rocks. *Geophysical Journal International*, *118*(3), 781–787. https://doi.org/10.1111/j.1365-246X.1994.tb03999.x

Walton, D., Shaw, J., Share, J., & Hakes, J. (1992). Microwave demagnetisation. *Journal of Applied Physics*, *71*(3), 1549–1551. https://doi.org/10.1063/1.351230

Wilson, R. L., & Watkins, N. D. (1967). Correlation of Petrology and Natural Magnetic Polarity in Columbia Plateau Basalts. *Geophysical Journal of the Royal Astronomical Society*, *12*(4), 405–424. https://doi.org/10.1111/j.1365-246X.1967.tb03150.x

Wingate, M. T. D., & Giddings, J. W. (2000). Age and palaeomagnetism of the Mundine Well dyke swarm, Western Australia: Implications for an Australia-Laurentia connection at 755 Ma. *Precambrian Research*, *100*(1–3), 335–357. https://doi.org/10.1016/S0301-9268(99)00080-7

Wingate, M. T. D., Pisarevsky, S. A., & Evans, D. A. D. (2002). Rodinia connections between Australia and Laurentia: No SWEAT, no AUSWUS? *Terra Nova*, *14*(2), 121–128. https://doi.org/10.1046/j.1365-3121.2002.00401.x

Yamamoto, Y., Tsunakawa, H., & Shibuya, H. (2003). Palaeointensity study of the Hawaiian 1960 lava: Implications for possible causes of erroneously high intensities. *Geophysical Journal International*, *153*(1), 263–276. https://doi.org/10.1046/j.1365-246X.2003.01909.x

Yamamoto, Y., Tsunakawa, H., Shaw, J., & Kono, M. (2007). Palaeomagnetism of the Datong monogenetic volcanoes in China: Palaeodirection and palaeointensity during the middle to early Brunhes Chron. *Earth, Planets and Space*, *59*(7), 727–746. https://doi.org/10.1186/BF03352736

Yamamoto, Y. & Yamaoka, R. (2018). Palaeointensity study on the holocene surface lavas on the island of Hawaii using the Tsunakawa–Shaw method. *Frontiers in Earth Science*, *6*(May), 1–10. https://doi.org/10.3389/feart.2018.00048

Yu, Y., & Tauxe, L. (2005). Testing the IZZI protocol of geomagnetic field intensity determination. *Geochemistry, Geophysics, Geosystems*, *6*(5). https://doi.org/10.1029/2004GC000840

Chapter 6

Conclusions

6.1 Summary of results

The primary aim of this project was to provide additional constraints for numerical geodynamo and statistical field models that are purposed with determining the nucleation age of Earth's Inner Core (ICN). This requires laying the foundation for the acquisition of new, high-quality palaeointensity data for key periods of the Proterozoic eon, which, by its very nature, is inherently difficult. However, I have successfully populated three important periods spanning 720 Ma to 1070 Ma with reliable new data from cooling units located in High Arctic Canada, Greenland and Western Australia.

Throughout the project, emphasis has been on producing reliable absolute palaeointensity (API) results. This involved and necessitated the use of multiple API techniques, which were supported by extensive rock magnetic experiments and scanning electron microscopy. One API method that is becoming increasingly popular in the study of ancient rocks is the Tsunakawa-Shaw method. As part of this research, I have identified several areas of improvement in the method, demonstrating how analytical changes could improve the accuracy and precision of results, while potentially reducing experimental time (Chapter 3).

I have presented new data from the Franklin Large Igneous Province (721 ± 4 Ma; Denyszyn et al., 2009). These mafic dykes provide the first palaeointensity data in a 300 Mry gap in global records, close in time to where recent models, which use updated thermal conductivity values, predict the onset of ICN (see Chapter 2). From this study, reliable virtual dipole moments (VDMs) are accepted from seven widespread dykes, ranging from 0.5 to 1.9 Am^2 x 10^{22}. The results are consistent within and between sites, using three palaeointensity methods (Chapter 4).

An analysis of the original directions from the Franklin LIP (Denyszyn et al., 2009) produce a typical value for the dispersion of virtual geomagnetic poles when compared to the last 10 Myrs. This suggests that emplacement occurred during a time period where the average axial dipole dominance was similar to recent times, despite a substantially reduced average dipole moment (Biggin et al., 2020). Therefore, the VDM results are likely representative of the average dipole moment rather than capturing secular variation; the results also include a reversal of the Earth's magnetic field at one site, and capture what is understood to be a transitional field in another site, where VDM is lowest recorded (0.5 Am^2 x 10^{22}) of all the sites. These new data fit well on the second-order polynomial long-term trend determined by Bono et al. (2019), who predict an average decaying field until ICN at ~565 Ma. I note however, that the data selection used in this trend-line excluded many data, where only slow-cooled units were given any weighting.

I additionally carried out palaeomagnetic sampling in Western Australia, taking advantage of the reliable palaeomagnetic directions, and primary TRM, reported from rocks emplaced during two further periods of interest; these include the Mundine Wells dyke swarm (MDS; 755 ± 3 Ma; Wingate & Giddings, 2000) and the Bangemall Sills (BMS; 1070 + 6 Ma; Wingate et al., 2002). Studying rocks from these periods allowed for a comparison of the recently acquired Franklin LIP data and the anomalously high data from the Mid-continent ridge (MCR; 1087 ± 2 Ma; Kulakov et al., 2013; Sprain et al., 2018).

After extensive rock magnetic and palaeointensity (293) experiments, only three sites from each location produced successful palaeointensity results. The Mundine Wells dyke swarm produced high-quality results which were consistently high between and within site, and from three separate palaeointensity methods with reported VDMs are between 6.1 and 6.4 Am^2 x 10^{22}. The Bangemall Sills results are less consistent with low overall success rates, with one site (BM6) producing only a single result according to the selection criteria used; this site is not used to determine a VDM. However, I note that five specimen results, using slightly relaxed selection criteria, from the same site suggest it recorded a weak field and would produce a VDM of 1.8 ± 1.2 Am^2 x 10^{22}. API results from the other two sites are not in good agreement producing VDMs of 0.6 and 3.0 Am^2 x 10^{22}. The site with the higher value is associated with high scatter in microwave API result but is consistent in Shaw-DHT API results. The mean from VDM from these two sites is supported by the evidence from site BM6. I therefore reasonably conclude that a moderately weak field existed during this time (Chapter 5).

In addition to the results reported in Chapters 4 and 5, palaeomagnetic work was carried out on the ~532 Ma Chatham Grenville and Mont Rigaud stocks. The original palaeomagnetic study (McCausland et al., 2007) revealed consistent primary directions, however, I was unable to reproduce these, likely in part, due to being unable to resample at the same locations. One of the original dykes from Chatham Grenville was in agreement with the original directions and produced consistent palaeointensity results (Appendix D). A VDM from this site is calculated as 0.96 ± 0.18 $Am^2 \times 10^{22}$; this is almost an order of magnitude lower than the present-day field and suggests that the period of extremely weak Ediacaran field extends into the Cambrian era.

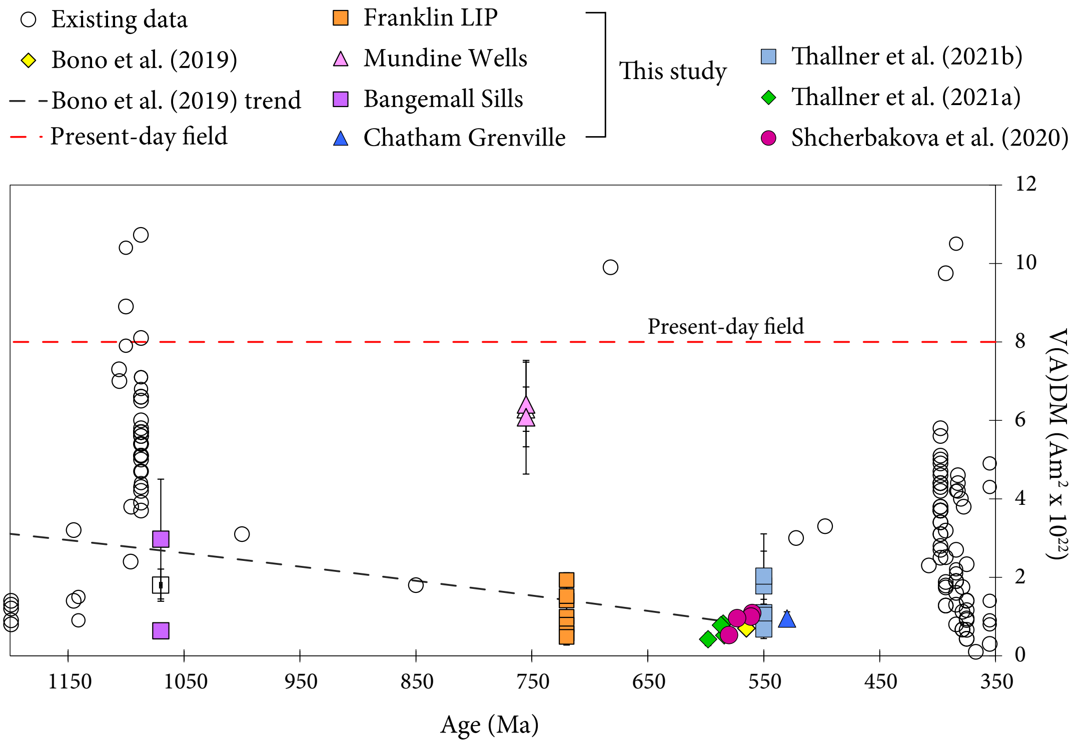

Figure 6.1. Current PINT data for the period 350 - 1200 Ma, with recent data highlighted. See Figure 5.6 for detailed description.

6.2 Implications for the Proterozoic palaeomagnetic field

These new palaeointensity data are somewhat conflicting when compared to themself and the existing palaeointensity (PINT) database (v.2015.05; http://earth.liv.ac.uk/ pint/; Biggin et al., 2015); presenting a Proterozoic palaeofield that is highly variable (Section 5.6; Figure 5.6). The high MDS VDM values are in stark contrast to the results from the Franklin LIP, which are separated by ~35 Myrs. Such a high field strength is not expected at a time leading up to the latest predictions for ICN. Just prior to the onset of a young ICN, the geodynamo may have relied predominantly on thermal energy alone, which will have been substantially depleted over the course of Earth history. The BMS results are concordant, for the time period, with a long-term decaying palaeomagnetic field; and in this respect, are less surprising than the MDS results. However, they differ considerably from the MCR data, separated by ~17 Myrs.

PSV studies suggest that the palaeomagnetic field in the Precambrian was more stable than in the Phanerozoic (Veikkolainen & Pesonen, 2014). Additionally, PINT data seems to suggest that Precambrian intervals with high median fields are less variable than equivalent intervals in the Phanerozoic (alluded to in Figure 5.6). However, based on the assumption that they average out palaeosecular variation, the two datasets in our comparisons (Chapter 5) suggest that long-term variability of field strength (> 10s Myrs) in the Proterozoic is similar to values from the highly variable Phanerozoic. Variability on these timescales is indicative of mantle forcing of the geodynamo through changes in the core–mantle heat flux (Biggin et al., 2012). This mantle control is likely why dipole dominance of the field has also remained fairly consistent throughout much of Earth history despite substantial changes to core regime (Biggin et al., 2020); e.g., before and after ICN.

It is necessary to distinguish any signature of ICN and growth from a higher-frequency, 200 Myr quasi-periodicity in dipole strength. This potential feature has been identified in the Phanerozoic by periods of weak dipole moment 10 – 100 Myrs prior to the onset of three superchrons, where dipole strength is unequivocally high. Recent evidence for a Mid-Proterozoic dipole low adds further support for such a feature (Hawkins et al., 2021). If this were to extend back to the Proterozoic, it may help explain anomalously high MCR and MDS data.

Recent hypotheses based on statistical field models have been based on relatively small datasets to hypothesise ICN age; as a result, estimates vary considerably from ~1.3 to 0.6 Ga (Biggin et al., 2015; Bono et al., 2019). The most recent estimates for ICN are detailed in Chapter 2 (Figure 2.1). The majority of estimates fall between 0.4 and 0.8 Ga, coinciding with weak-field API results recently reported in the Ediacaran (Bono et al., 2019; Shcherbakova et al., 2020; Thallner et al., 2021a, 2021b). This age range is also consistent with many of these new data (Franklin LIP and BMS) which are supportive of a long-term decaying dipole that culminates at its weakest point sometime during or after the Ediacaran. However, the anomalously high data (MDS and MCR) complicate this hypothesis; the huge gaps and general sparsity of Precambrian palaeointensity data suggest that long-term variability in the palaeomagnetic field during this time is not accurately represented in the records.

This is a substantial problem considering that significant bias may be introduced when using these sparse data to constrain models which solve for significant deep Earth events linked to the geodynamo, or when determining long-term trends in the palaeomagnetic field. The Precambrian requires similar data coverage to the Phanerozoic in order to fully resolve the changing geomorphology, to identify signals in the ancient palaeomagnetic field, and to relate these to deep Earth processes. Obtaining reliable palaeointensity data for ancient periods is intrinsically difficult; despite this, many data are beginning to fill key gaps in the records; however, the results presented here highlight that there is still a vital need for more data.

6.3 Future work

As previously mentioned, a severe lack of data currently restricts our ability to accurately represent the Precambrian or even the Proterozoic palaeomagnetic field; this includes periods that have been linked to ICN (Figure 2.1). Therefore, future work must include a continued focus on acquiring high-resolution palaeointensity data for key periods of Earth history. The consistently weak palaeointensity results recently reported to spanning much of the Ediacaran are a prime example of how a focussed (~50 Myrs) drive for new data can substantially improve our understanding of that particular period of time.

The previously discussed palaeointensity results gathered in recent years coupled with latest numerical geodynamo models suggest a young inner core, with some models suggesting that it may be as young as 400 Ma (Pozzo et al., 2012; Davies et al., 2015; Davies et al., 2021). In light of this, attention is drawn to the early to mid-Palaeozoic (~540 – 420 Ma) for which almost no palaeointensity data exists (Figure 6.1). The Cambrian period not only signifies a marked explosion of life on Earth, but palaeomagnetically, it follows on from a period of very low dipole strength and anomalous palaeomagnetic direction records. A key area of research would be to determine how long this behaviour continued, whether there is a signal of ICN, and whether data would further support the hypothesis of a 200 Myr cycle in dipole strength.

The Neoproterozoic era is also of particular interest; not only because it remains one of the least populated periods of Earth history, but new palaeointensity data may provide further understanding of deep earth conditions potentially leading up to ICN. Furthermore, this elusive time includes anomalously high dipole moments (Figure 6.1) that need to be further understood.

6.4 References cited

Biggin, Bono, Meduri, Sprain, Davies, Holme, Doubrovine, P. . (2020). Quantitative estimates of average geomagnetic axial dipole dominance in deep geological time. *Nature Communications*.

Biggin, A. J., Steinberger, B., Aubert, J., Suttie, N., Holme, R., Torsvik, T. H., et al. (2012). Possible links between long-term geomagnetic variations and whole-mantle convection processes. *Nature Geoscience*, *5*(8), 526–533. https://doi.org/10.1038/ngeo1521

Biggin, A. J., Piispa, E. J., Pesonen, L. J., Holme, R., Paterson, G. A., Veikkolainen, T., & Tauxe, L. (2015). Palaeomagnetic field intensity variations suggest Mesoproterozoic inner-core nucleation. *Nature*, *526*(7572), 245–248. https://doi.org/10.1038/nature15523

Bono, R. K., Tarduno, J. A., Nimmo, F., & Cottrell, R. D. (2019). Young inner core inferred from Ediacaran ultra-low geomagnetic field intensity. *Nature Geoscience*, *12*(2), 143–147. https://doi.org/10.1038/s41561-018-0288-0

Davies, C. J., Pozzo, M., Gubbins, D., & Alfè, D. (2015). Constraints from material properties on the dynamics and evolution of Earth's core. *Nature Geoscience*, *8*(9), 678–685. https://doi.org/10.1038/ngeo2492

Davies, C. J., Bono, R. K., Meduri, D. G., Aubert, J., Greenwood, S., & Biggin, A. J. (2021). Dynamo constraints on the long-term evolution of Earth's magnetic field strength. *Geophysical Journal International*, *228*(1), 316–336. https://doi.org/10.1093/gji/ggab342

Denyszyn, S. W., Halls, H. C., Davis, D. W., & Evans, D. A. D. (2009). Paleomagnetism and U-Pb geochronology of Franklin dykes in high arctic Canada and Greenland: A revised age and paleomagnetic pole constraining block rotations in the Nares Strait region. *Canadian Journal of Earth Sciences*, *46*(9), 689–705. https://doi.org/10.1139/E09-042

Hawkins, L. M. A., Grappone, J. M., Sprain, C. J., Saengduean, P., Sage, E. J., Thomas-Cunningham, S., et al. (2021). Intensity of the Earth's magnetic field: Evidence for a Mid-Paleozoic dipole low. *Proceedings of the National Academy of Sciences of the United States of America*, *118*(34). https://doi.org/10.1073/pnas.2017342118

Kulakov, E. V., Smirnov, A. V., & Diehl, J. F. (2013). Absolute geomagnetic paleointensity as recorded by ~1.09 Ga Lake Shore Traps (Keweenaw Peninsula, Michigan). *Studia Geophysica et Geodaetica*, *57*(4), 565–584. https://doi.org/10.1007/s11200-013-0606-3

McCausland, P. J. A., Van der Voo, R., & Hall, C. M. (2007). Circum-Iapetus paleogeography of the Precambrian-Cambrian transition with a new paleomagnetic constraint from Laurentia. *Precambrian Research*, *156*(3–4), 125–152. https://doi.org/10.1016/j.precamres.2007.03.004

Pozzo, M., Davies, C., Gubbins, D., & Alfè, D. (2012). Thermal and electrical conductivity of iron at Earth's core conditions. *Nature*, *485*(7398), 355–358. https://doi.org/10.1038/nature11031

Shcherbakova, V. V., Bakhmutov, V. G., Thallner, D., Shcherbakov, V. P., Zhidkov, G. V., & Biggin, A. J. (2020). Ultra-low palaeointensities from East European Craton, Ukraine support a globally anomalous palaeomagnetic field in the Ediacaran. *Geophysical Journal International*, *220*(3), 1920–1946. https://doi.org/10.1093/gji/ggz566

Sprain, C. J., Swanson-Hysell, N. L., Fairchild, L. M., & Gaastra, K. (2018). A field like today's? The strength of the geomagnetic field 1.1 billion years ago. *Geophysical Journal International*, *213*(3), 1969–1983. https://doi.org/10.1093/gji/ggy074

Thallner, D., Biggin, A. J., & Halls, H. C. (2021). An extended period of extremely weak geomagnetic field suggested by palaeointensities from the Ediacaran Grenville dykes (SE Canada). *Earth and Planetary Science Letters*, *568*, 117025. https://doi.org/10.1016/j.

epsl.2021.117025

Thallner, D., Biggin, A. J., McCausland, P. J. A., & Fu, R. R. (2021). New Paleointensities From the Skinner Cove Formation, Newfoundland, Suggest a Changing State of the Geomagnetic Field at the Ediacaran-Cambrian Transition. *Journal of Geophysical Research: Solid Earth*, *126*(9). https://doi.org/10.1029/2021JB022292

Veikkolainen, T., & Pesonen, L. J. (2014). geodynamo in the Precambrian, 1515–1526. https://doi.org/10.1093/gji/ggu348

Wingate, M. T. D., & Giddings, J. W. (2000). Age and palaeomagnetism of the Mundine Well dyke swarm, Western Australia: Implications for an Australia-Laurentia connection at 755 Ma. *Precambrian Research*, *100*(1–3), 335–357. https://doi.org/10.1016/S0301-9268(99)00080-7

Wingate, M. T. D., Pisarevsky, S. A., & Evans, D. A. D. (2002). Rodinia connections between Australia and Laurentia: No SWEAT, no AUSWUS? *Terra Nova*, *14*(2), 121–128. https://doi.org/10.1046/j.1365-3121.2002.00401.x

Appendix A

Supplementary Material for Chapter 3

The data provided in Appendix A supplements Chapter 3. Raw measurement data is available on the MagIC database under:

Simon J. Lloyd, Greig A. Paterson, Daniele Thallner, Andrew J. Biggin; Improvements to the Shaw-type absolute palaeointensity method; Magic Information Consortium (MagIC), doi: 10.7288/V4/MAGIC/17121.

A1 Supplementary Figures

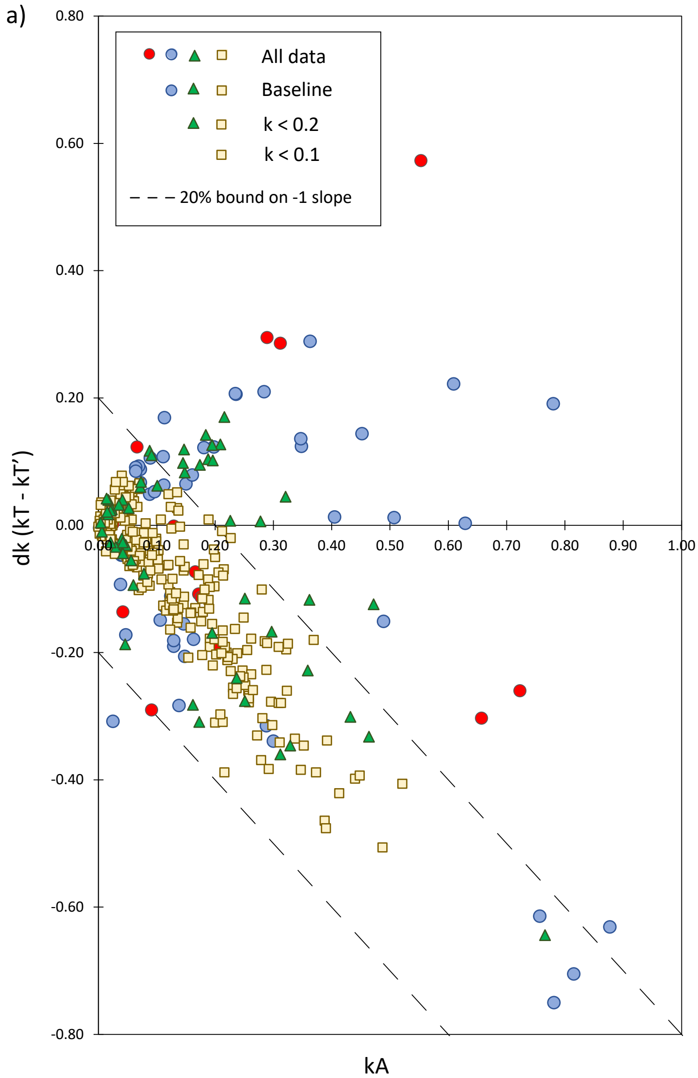

Supplementary Figure A1.1. Slope$_A$ curvature (kA) plotted against the difference in curvature (δk) between the corrected palaeointensity slope (kT) and the uncorrected (kT') palaeointensity slope. The data (426 specimens from this study) is iteratively reduced according to the selection criteria used until only results with $|k'| \leq 0.1$ remain. It shows that as the selection criteria is reduced, the data fit to the observed relationship between ka and δk improves.

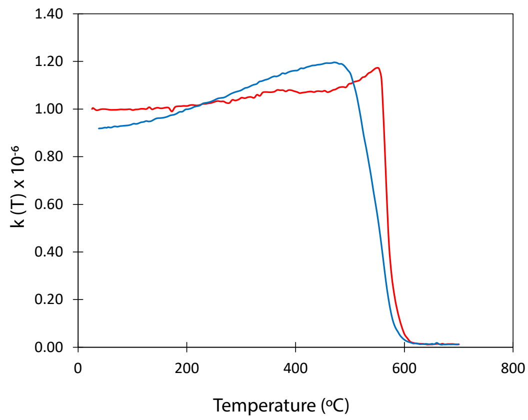

Supplementary Figure A1.2. High-temperature susceptibility (κ-T) plot for specimen MD6.4.

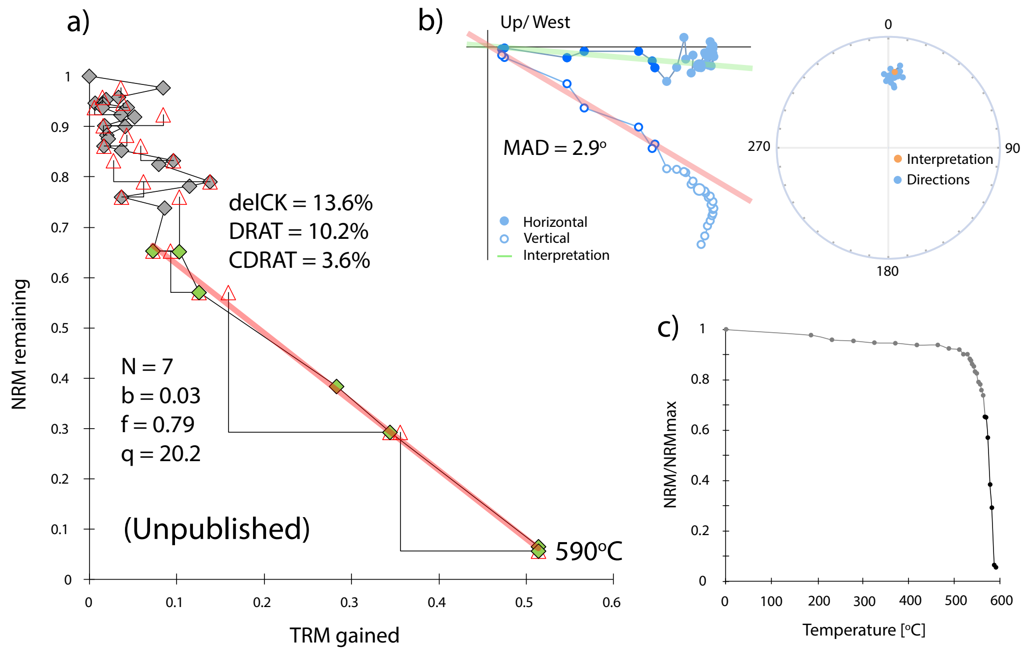

Supplementary Figure A1.3. Example Aria and orthogonal plot for specimen MD6-1C from a Thellier IZZI experiment. The palaeointensity result is near equivalent to that of specimen MD6-2A used in Figure 3.4 and sister specimen MD6-1A.. This is despite the Shaw specimen slopeT values of 2.55 and 2.16, respectively.

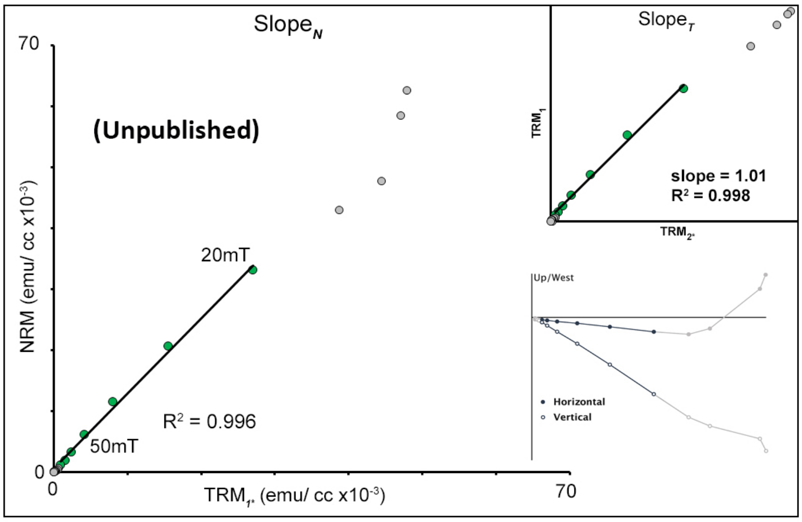

Supplementary Figure A1.4. Pseudo-Arai and slope$_T$ plots for Specimen MD6-5A, from the same site (MD6) as specimen MD6-2A. This was part of a separate Shaw-DHT experiment with hold durations of 25 and 55 minutes for TRM$_1$ and TRM$_2$ acquisitions respectively. Here, a near unit slope$_T$ is achieved due to the difference in hold durations.

A2 Supplementary Tables

Supplementary Table A2.1. List of specimens included in the single DHT experiment referred to in section 3.3.2 and Figure 3.5.

Bangemall Sills (1070 Ma)	Mundine Wells Dyke (755 Ma)	Northampton Dykes (755 Ma)
BM6.1CA	MD2.4C	NH5.2CB
BM6.3D	MD2.10A	NH5.2ED
BM6.4BB	MD2.11C	NH5.3AD
BM6.5BD	MD3.1C	NH5.3CB
BM7.1AA	MD3.3E	
BM7.1BC	MD3.4A	
BM7.4BA	MD4.5C	
	MD4.6C	
	MD6.1A	
	MD6.2A	
	MD6.3C	
	MD6.5C	

Supplementary Table A2.2. List of specimens and their selection criteria values fused in the simulated palaeointensity experiment.

		Base selcrit								Linear selcrit		used for Supp. Fig 1		
Sample	File	Alpha_t	DANG_t	MAD a_t	MAD f_t	sA2	sT	beta_t	fRESID	kT	rT	kA2	kT'	kT-kT'
B1BM1.1C	BANG1	0.42	0.40	0.14	0.49	0.66	0.86	0.00	0.04	0.11	1.00	0.03	0.15	-0.03
B1BM1.7D	BANG1	0.58	0.60	0.28	0.64	0.72	0.94	0.01	0.06	0.22	0.99	0.06	0.28	-0.06
B1BM5.3E	BANG1	0.87	0.90	0.19	0.51	0.49	0.81	0.01	0.05	0.19	1.00	0.09	0.07	0.12
B1BM6.1AB	BANG1	0.74	0.80	0.35	0.72	0.66	1.13	0.01	0.09	0.32	0.99	0.15	0.47	-0.16
B1BM6.4AD	BANG1	0.40	0.50	0.29	0.78	0.01	92.24	0.08	0.64	1.35	0.27	0.75	0.34	1.01
B1BM6.4BC	BANG1	0.81	0.90	0.35	0.73	0.49	0.89	0.01	0.05	0.21	0.99	0.01	0.21	0.00
B1BM7.3BB	BANG1	0.25	0.70	0.52	0.51	1.01	0.96	0.00	0.00	0.03	1.00	0.08	0.06	-0.02
B1BM7.4AB	BANG1	0.48	1.00	0.59	0.37	0.97	0.98	0.00	0.00	0.01	1.00	0.06	0.07	-0.06
B1BM7.5B	BANG1	0.58	1.60	0.86	0.47	0.99	0.97	0.00	0.00	0.02	1.00	0.06	0.08	-0.06
B1BM8.12E	BANG1	1.56	1.70	0.80	2.76	0.89	0.80	0.02	0.03	0.32	0.98	0.04	0.37	-0.05
B1BM8.3C	BANG1	0.19	0.60	0.56	0.60	0.98	0.98	0.00	0.00	0.03	1.00	0.07	0.04	-0.01
B1BM8.4E	BANG1	0.10	0.30	0.30	0.32	0.97	0.99	0.00	0.00	0.03	1.00	0.09	0.06	-0.04
B1BM8.6D	BANG1	0.16	0.40	0.31	0.28	0.97	1.02	0.01	0.01	0.08	1.00	0.12	0.03	0.05
B1BM8.8D	BANG1	0.12	0.30	0.32	0.35	0.97	1.03	0.00	0.00	0.03	1.00	0.12	0.09	-0.06
BABM6.1BA	BANG3	0.35	179.50	0.34	0.47	0.37	0.78	0.03	0.05	0.30	0.99	0.04	0.35	-0.05
BABM6.4BE	BANG3	0.17	179.80	0.56	1.00	0.23	0.95	0.03	0.06	0.34	0.98	0.00	0.35	0.00
BABM6.5AA	BANG3	0.91	178.70	0.78	0.83	0.36	1.11	0.01	0.01	0.10	1.00	0.23	0.35	-0.26
BABM6.5BB	BANG3	0.19	179.70	0.35	0.54	0.33	1.08	0.01	0.03	0.16	1.00	0.25	0.43	-0.28
BABM7.1AC	BANG3	0.05	179.90	0.20	0.27	0.68	1.11	0.00	0.00	0.01	1.00	0.34	0.35	-0.34
BABM7.1BB	BANG3	0.36	179.40	0.40	0.40	0.52	1.29	0.01	0.01	0.03	1.00	0.31	0.37	-0.34
BABM8.1A	BANG3	0.24	179.30	0.62	0.64	0.82	1.01	0.00	0.00	0.02	1.00	0.30	0.29	-0.28
BABM8.4F	BANG3	0.06	179.80	0.54	0.66	0.81	1.07	0.00	0.00	0.01	1.00	0.35	0.35	-0.35
BABM8.7E	BANG3	0.05	179.90	0.55	0.69	0.82	1.06	0.00	0.00	0.01	1.00	0.37	0.40	-0.39
BZBM6.1AC	BANG4	0.67	179.10	0.73	1.27	0.26	0.68	0.01	0.05	0.25	0.99	0.09	0.14	0.11
BZBM6.1AE	BANG4	0.91	178.80	0.69	0.89	0.27	0.71	0.02	0.03	0.33	0.99	0.07	0.24	0.09
BZBM6.1BB	BANG4	0.52	179.30	0.62	1.02	0.31	0.79	0.02	0.05	0.34	0.99	0.02	0.36	-0.02
BZBM6.1BC	BANG4	1.05	178.60	0.81	1.20	0.24	0.71	0.02	0.05	0.27	0.99	0.07	0.17	0.09
BZBM6.3B	BANG4	1.09	178.50	0.82	0.87	0.29	1.08	0.01	0.02	0.22	0.99	0.16	0.40	-0.18
BZBM6.4AE	BANG4	0.45	179.40	0.89	1.71	0.21	0.80	0.01	0.03	0.21	0.99	0.06	0.12	0.09
BZBM6.4BG	BANG4	0.49	179.20	0.82	1.21	0.36	1.07	0.01	0.02	0.20	0.99	0.29	0.52	-0.32
BZBM6.5AB	BANG4	1.90	177.40	1.44	1.53	0.25	0.77	0.01	0.04	0.21	0.99	0.06	0.12	0.09
BZBM6.5AD	BANG4	1.03	178.20	1.10	1.01	0.38	1.03	0.01	0.02	0.15	1.00	0.31	0.51	-0.36
BZBM6.5BA	BANG4	1.26	178.20	1.23	1.57	0.30	0.94	0.02	0.04	0.25	0.99	0.11	0.38	-0.13
BZBM8.1C	BANG4	0.51	178.30	0.99	0.70	0.91	1.07	0.00	0.00	0.03	1.00	0.26	0.29	-0.26
BZBM8.1E	BANG4	0.33	178.80	0.90	0.86	0.92	1.09	0.01	0.00	0.02	1.00	0.25	0.27	-0.25
BZBM8.2A	BANG4	1.10	178.40	0.79	0.55	0.28	0.72	0.01	0.02	0.13	1.00	0.15	0.05	0.08
BZBM8.2C	BANG4	0.50	179.20	0.52	0.56	0.22	0.83	0.02	0.03	0.20	1.00	0.02	0.16	0.04
BZBM8.2E	BANG4	0.37	179.40	0.39	0.43	0.22	0.86	0.01	0.03	0.14	1.00	0.04	0.17	-0.03
BZBM8.4A	BANG4	0.47	178.80	0.72	0.51	0.89	1.04	0.01	0.01	0.12	1.00	0.24	0.36	-0.24
BZBM8.5C	BANG4	0.28	179.20	0.44	0.30	0.84	1.04	0.00	0.00	0.02	1.00	0.35	0.41	-0.38
BZBM8.6B	BANG4	0.33	179.20	0.53	0.45	0.91	1.06	0.01	0.01	0.06	1.00	0.30	0.37	-0.31
MP1C4	DTBB40	1.64	177.50	1.62	1.98	1.03	1.01	0.01	0.00	0.00	1.00	0.01	0.01	-0.01
MP1F3	DTBB40	0.98	178.30	1.26	1.43	1.01	1.01	0.01	0.00	0.01	1.00	0.04	0.05	-0.04
MP2B4	DTBB40	0.91	178.90	0.54	0.64	1.03	1.04	0.03	0.02	0.24	0.98	0.11	0.14	0.11
MP2C4	DTBB40	1.04	178.70	0.62	0.76	1.02	1.00	0.00	0.00	0.01	1.00	0.02	0.01	0.00
MP5A3	DTBB40	1.02	178.80	0.48	0.86	0.98	1.02	0.01	0.01	0.04	1.00	0.04	0.00	0.04
MP5B1	DTBB40	1.06	178.70	0.60	0.72	1.01	1.00	0.01	0.00	0.01	1.00	0.01	0.02	-0.01
MP6D2	DTBB40	0.63	178.80	0.68	0.43	1.01	0.82	0.00	0.00	0.03	1.00	0.03	0.00	0.03
MP6D5	DTBB40	0.51	179.00	0.52	0.31	1.01	0.94	0.00	0.00	0.00	1.00	0.05	0.05	-0.05
MP7A2	DTBB40	1.05	178.60	0.75	0.91	1.02	0.97	0.01	0.01	0.03	1.00	0.02	0.01	0.03
MP8A1	DTBB40	0.58	179.30	0.24	0.24	0.99	1.03	0.00	0.01	0.02	1.00	0.02	0.01	0.01
MP8A4	DTBB40	0.39	179.50	0.33	0.67	1.02	1.00	0.00	0.01	0.01	1.00	0.02	0.02	-0.01
MP9B1	DTBB40	0.35	179.60	0.22	0.34	1.03	1.02	0.00	0.00	0.01	1.00	0.02	0.02	-0.01
MP1D5	DTBB60	1.37	177.90	1.42	1.76	1.02	0.99	0.01	0.01	0.06	1.00	0.02	0.04	0.02
MP1F2	DTBB60	0.35	179.40	0.55	0.69	1.02	1.03	0.01	0.01	0.09	1.00	0.03	0.06	0.03
MP2A2	DTBB60	0.27	179.50	0.57	0.71	1.00	1.06	0.01	0.01	0.11	1.00	0.02	0.09	0.03
MP2C3	DTBB60	0.80	179.00	0.44	0.60	1.05	0.96	0.01	0.01	0.05	1.00	0.02	0.04	0.01
MP4A2	DTBB60	12.39	167.30	2.11	0.35	1.00	1.02	0.00	0.00	0.02	1.00	0.01	0.01	0.01
MP5B3	DTBB60	0.55	179.40	0.31	0.52	1.00	1.02	0.01	0.01	0.08	1.00	0.01	0.07	0.01
MP5D1	DTBB60	0.50	179.40	0.33	0.67	1.00	1.01	0.01	0.00	0.01	1.00	0.01	0.02	-0.01
MP6D3	DTBB60	0.65	178.70	0.74	0.55	1.01	1.02	0.00	0.00	0.03	1.00	0.02	0.05	-0.02
MP7A3	DTBB60	2.17	176.60	1.86	1.40	1.01	1.00	0.01	0.00	0.00	1.00	0.01	0.01	-0.01
MP7C3	DTBB60	0.25	179.60	0.24	0.31	1.02	0.97	0.01	0.00	0.01	1.00	0.00	0.01	0.00
MP8B2	DTBB60	0.42	179.50	0.20	0.27	1.00	1.02	0.00	0.01	0.03	1.00	0.01	0.01	0.02
MP9C2	DTBB60	0.58	179.20	0.33	0.10	1.00	1.00	0.00	0.00	0.02	1.00	0.01	0.02	0.00
10202A	DTGD	1.27	177.60	1.26	0.59	0.96	1.06	0.00	0.00	0.01	1.00	0.06	0.05	-0.04
1083A	DTGD	3.79	174.70	2.64	2.26	0.90	1.04	0.02	0.01	0.14	0.99	0.05	0.11	0.03
14103A	DTGD	0.63	179.10	0.88	1.37	0.93	0.94	0.01	0.02	0.05	1.00	0.23	0.21	-0.16
1452A	DTGD	1.19	178.10	1.20	1.24	0.93	0.90	0.02	0.01	0.02	1.00	0.31	0.30	-0.28
1541A	DTGD	3.47	173.80	3.33	1.92	0.92	0.99	0.01	0.00	0.00	1.00	0.07	0.11	-0.10
1661A	DTGD	1.25	177.70	2.51	3.28	0.95	1.02	0.01	0.02	0.02	1.00	0.19	0.20	-0.18
1662A	DTGD	1.00	178.20	1.56	1.96	0.97	0.97	0.01	0.01	0.02	1.00	0.23	0.25	-0.23
1943A	DTGD	0.88	178.90	0.72	1.14	0.74	1.01	0.01	0.02	0.03	1.00	0.09	0.12	-0.10
211A	DTGD	0.40	179.00	1.05	1.19	0.97	1.09	0.01	0.00	0.03	1.00	0.05	0.02	0.01
2321A	DTGD	0.79	179.00	0.56	0.88	0.90	0.98	0.01	0.03	0.09	1.00	0.15	0.30	-0.21
2582A	DTGD	1.41	177.60	1.31	0.78	0.95	1.07	0.01	0.01	0.01	1.00	0.14	0.16	-0.15
2592A	DTGD	0.82	178.80	0.71	0.70	0.89	1.03	0.01	0.01	0.04	1.00	0.05	0.10	-0.05
2652A	DTGD	0.75	178.90	0.67	0.84	0.90	0.99	0.01	0.01	0.16	1.00	0.06	0.26	-0.09
2662A	DTGD	0.63	179.00	0.67	0.75	0.93	1.00	0.01	0.00	0.01	1.00	0.19	0.20	-0.19

2911B	DTGD	0.24	179.60	0.51	0.74	1.01	0.98	0.01	0.00	0.04	1.00	0.06	0.03	0.01
29141	DTGD	0.52	179.30	0.59	0.94	0.90	0.90	0.01	0.01	0.01	1.00	0.11	0.13	-0.13
3384B	DTGD	2.58	176.50	1.72	1.42	0.90	0.89	0.01	0.02	0.06	1.00	0.03	0.05	0.01
3785A	DTGD	0.43	179.40	0.46	0.59	0.93	0.94	0.01	0.01	0.01	1.00	0.23	0.28	-0.27
37H44	DTGD	1.55	178.00	1.09	1.43	0.99	1.11	0.01	0.01	0.07	1.00	0.04	0.04	0.03
37H53	DTGD	5.57	172.90	3.51	4.28	1.01	1.06	0.01	0.01	0.09	1.00	0.00	0.10	-0.01
1942A	DTGD_Shaw1	10.02	167.50	5.50	4.98	0.65	1.09	0.05	0.11	0.41	0.97	0.29	0.11	0.30
2911A	DTGD_Shaw1	7.49	169.20	6.67	8.01	1.01	0.90	0.03	0.09	0.09	0.99	0.04	0.08	0.01
2944A	DTGD_Shaw1	2.74	173.50	4.74	4.58	0.98	0.80	0.05	0.04	0.32	0.96	0.36	0.03	0.29
3381A	DTGD_Shaw1	6.30	171.20	4.93	5.54	1.00	0.99	0.04	0.00	0.16	0.98	0.15	0.04	0.12
1073A	DTGD_SHaw2	0.41	0.70	0.46	0.52	1.01	1.03	0.01	0.00	0.03	1.00	0.10	0.07	-0.04
2341	DTGD_SHaw2	0.96	1.20	0.54	0.50	0.74	0.93	0.00	0.00	0.03	1.00	0.27	0.36	-0.33
2572	DTGD_SHaw2	0.16	0.20	0.26	0.47	1.02	1.01	0.01	0.01	0.04	1.00	0.12	0.21	-0.16
291B9	DTGD_SHaw2	0.82	1.90	1.83	2.11	1.00	1.01	0.00	0.00	0.00	1.00	0.06	0.04	-0.04
2961	DTGD_SHaw2	0.15	0.30	0.27	0.39	0.90	0.93	0.01	0.01	0.07	1.00	0.14	0.22	-0.15
2991	DTGD_SHaw2	0.29	0.50	0.31	0.34	0.96	0.93	0.00	0.01	0.02	1.00	0.13	0.15	-0.13
29H43	DTGD_SHaw2	40.53	11.30	1.35	6.09	0.81	0.62	0.15	0.17	0.25	0.72	0.07	0.13	0.12
782A	DTGD_Shaw2	0.12	0.20	0.32	0.47	1.01	1.06	0.01	0.01	0.10	1.00	0.07	0.03	0.07
H2A4	DTGD_Shaw2	0.09	0.10	0.21	0.38	1.01	1.06	0.02	0.03	0.18	1.00	0.21	0.05	0.13
101A	DTSC_Shaw1	1.11	175.10	4.51	4.55	1.09	1.14	0.05	0.08	0.38	0.97	0.78	0.19	0.19
3122	DTSC_Shaw1	19.04	159.30	7.72	16.93	0.96	0.35	0.03	0.08	0.21	0.99	0.72	0.47	-0.26
516A	DTSC_Shaw1	28.57	134.80	24.25	17.36	1.01	1.15	0.01	0.01	0.06	1.00	0.09	0.35	-0.29
622A	DTSC_Shaw1	10.73	167.80	4.10	3.17	0.41	1.28	0.03	0.06	0.22	0.99	0.09	0.17	0.05
103A	DTSC_Shaw2	0.11	0.30	0.34	0.40	1.18	0.83	0.01	0.00	0.05	1.00	0.06	0.00	0.05
104A	DTSC_Shaw2	0.25	0.60	0.91	1.09	0.88	1.08	0.01	0.00	0.00	1.00	0.15	0.13	-0.12
1112A	DTSC_Shaw2	0.43	0.50	0.31	0.64	0.72	1.03	0.01	0.02	0.06	1.00	0.03	0.09	-0.03
1404A	DTSC_Shaw2	0.21	0.30	0.51	1.03	0.79	1.06	0.01	0.02	0.13	1.00	0.06	0.19	-0.06
1413A	DTSC_Shaw2	0.81	0.90	0.35	0.43	0.85	1.02	0.00	0.00	0.02	1.00	0.07	0.08	-0.07
1413B	DTSC_Shaw2	1.50	1.70	0.57	0.36	0.87	1.00	0.00	0.01	0.02	1.00	0.00	0.01	0.01
1504A	DTSC_Shaw2	0.63	0.90	0.88	1.33	0.91	0.94	0.02	0.01	0.12	1.00	0.25	0.24	-0.12
1505A	DTSC_Shaw2	0.06	0.10	0.46	0.71	0.91	1.13	0.01	0.01	0.04	1.00	0.17	0.17	-0.13
308A	DTSC_Shaw2	0.30	0.50	0.59	0.90	1.01	1.06	0.00	0.01	0.04	1.00	0.16	0.18	-0.14
309A	DTSC_Shaw2	1.50	1.80	0.91	1.42	0.91	0.99	0.01	0.01	0.03	1.00	0.05	0.04	-0.02
312A	DTSC_Shaw2	0.60	0.80	0.40	0.57	0.94	1.00	0.00	0.00	0.02	1.00	0.06	0.07	-0.05
515A	DTSC_Shaw2	2.18	3.40	1.80	1.39	1.03	1.11	0.01	0.01	0.06	1.00	0.20	0.22	-0.16
517B	DTSC_Shaw2	1.29	2.20	1.15	0.58	1.01	0.98	0.00	0.00	0.02	1.00	0.21	0.33	-0.31
625A	DTSC_Shaw2	0.66	0.80	0.30	0.26	0.83	1.01	0.00	0.01	0.04	1.00	0.04	0.01	0.03
626A	DTSC_Shaw2	1.20	1.40	0.53	0.49	0.83	1.02	0.00	0.01	0.03	1.00	0.03	0.08	-0.05
TS02A	DTSC_Shaw2	4.38	7.00	4.19	3.99	1.03	0.98	0.01	0.01	0.08	1.00	0.12	0.22	-0.13
TS04A	DTSC_Shaw2	0.32	0.60	0.96	1.38	0.99	1.02	0.01	0.00	0.07	1.00	0.04	0.02	0.05
TS04B	DTSC_Shaw2	0.38	0.60	0.58	0.81	1.00	0.99	0.01	0.01	0.05	1.00	0.06	0.02	0.04
TS05B	DTSC_Shaw2	1.76	177.70	1.32	1.74	0.99	0.99	0.02	0.02	0.16	1.00	0.04	0.12	0.04
C4602A	DTV1_PTSD1	12.82	164.00	6.64	4.06	1.01	0.08	0.08	0.18	0.58	0.91	0.31	0.29	0.29
C4605A	DTV1_PTSD1	8.65	152.30	13.83	6.23	0.94	0.13	0.07	0.03	0.35	0.94	0.20	0.54	-0.19
C4611A	DTV1_PTSD1	21.21	158.70	1.34	3.86	1.25	0.37	0.07	0.10	0.62	0.93	0.01	0.60	0.02
C4615A	DTV1_PTSD1	0.40	178.30	1.90	2.03	0.88	0.64	0.06	0.02	0.33	0.96	0.11	0.16	0.17
C4616A	DTV1_PTSD1	0.82	170.20	4.60	3.89	0.97	0.96	0.02	0.02	0.16	1.00	0.07	0.10	0.06
C4617A	DTV1_PTSD1	3.00	171.20	7.59	7.82	0.97	0.81	0.05	0.06	0.47	0.97	0.01	0.49	-0.01
C4618A	DTV1_PTSD1	0.23	170.40	6.10	5.99	0.94	0.35	0.08	0.03	0.36	0.91	0.03	0.67	-0.31
C4620A	DTV1_PTSD1	6.29	159.50	10.12	4.30	1.02	0.17	0.06	0.02	0.45	0.96	0.17	0.56	-0.11
C4621A	DTV1_PTSD1	1.19	176.60	2.19	1.83	0.95	0.35	0.03	0.03	0.22	0.98	0.12	0.33	-0.11
C4622A	DTV1_PTSD1	30.08	76.00	12.59	4.21	1.01	0.95	0.03	0.01	0.14	0.99	0.03	0.14	0.00
C4624A	DTV1_PTSD1	0.21	179.20	1.03	1.12	1.00	0.85	0.02	0.02	0.18	1.00	0.05	0.21	-0.03
C4625A	DTV1_PTSD1	0.64	177.00	2.21	2.07	0.87	0.46	0.05	0.09	0.55	0.96	0.76	1.16	-0.61
C8201A	DTV1_PTSD1	1.13	178.20	1.06	0.95	1.16	0.47	0.01	0.01	0.09	1.00	0.12	0.21	-0.12
CK306A	DTV1_PTSD1	48.63	53.60	29.56	18.98	4900.33	0.43	0.32	0.18	2.32	0.07	0.17	2.40	-0.07
CK308A	DTV1_PTSD1	6.57	140.80	15.89	5.32	0.97	0.18	0.03	0.04	0.25	0.99	0.18	0.36	-0.11
CK310A	DTV1_PTSD1	1.69	173.70	3.38	2.26	0.59	0.44	0.05	0.08	0.49	0.97	1.18	1.40	-0.91
CK311A	DTV1_PTSD1	6.55	55.80	17.12	2.72	0.77	0.22	0.10	0.12	1.03	0.86	0.66	1.33	-0.30
CK313A	DTV1_PTSD1	1.01	174.90	3.36	2.98	0.67	0.19	0.05	0.05	0.62	0.96	0.88	1.25	-0.63
CK320A	DTV1_PTSD1	11.20	168.80	0.67	2.34	1.28	0.98	0.02	0.00	0.12	0.99	0.04	0.08	0.03
CK321A	DTV1_PTSD1	14.15	165.80	0.70	2.42	1.12	0.88	0.02	0.04	0.08	0.99	0.02	0.07	0.01
CK328A	DTV1_PTSD1	0.30	179.20	0.85	0.97	0.69	0.77	0.04	0.08	0.34	0.98	0.78	1.09	-0.75
CK331A	DTV1_PTSD1	0.54	178.90	0.76	0.74	1.34	0.63	0.02	0.03	0.20	1.00	0.20	0.37	-0.17
BAZ01A	DTV1_PTSD2	0.22	179.70	0.15	0.17	1.21	0.81	0.02	0.03	0.16	1.00	0.17	0.06	0.10
BAZ02A	DTV1_PTSD2	0.78	179.10	0.37	0.23	1.15	0.82	0.02	0.02	0.19	1.00	0.28	0.19	0.01
BAZ03A	DTV1_PTSD2	0.76	179.10	0.31	0.43	0.90	1.02	0.01	0.02	0.11	1.00	0.30	0.28	-0.17
BAZ05A	DTV1_PTSD2	0.43	179.50	0.29	0.37	0.94	0.96	0.02	0.02	0.19	0.99	0.47	0.31	-0.12
BAZ06A	DTV1_PTSD2	0.47	179.40	0.35	0.39	0.99	0.95	0.01	0.02	0.04	1.00	0.19	0.16	-0.12
BAZ08A	DTV1_PTSD2	0.34	179.70	0.05	0.55	0.92	0.65	0.02	0.02	0.14	0.99	0.36	0.26	-0.12
BAZ09A	DTV1_PTSD2	0.41	179.60	0.10	0.37	0.91	0.68	0.01	0.02	0.02	1.00	0.22	0.40	-0.39
BAZ10A	DTV1_PTSD2	0.69	179.30	0.11	0.52	1.00	0.76	0.03	0.03	0.24	0.98	0.41	0.23	0.01
BAZ11A	DTV1_PTSD2	0.70	179.30	0.10	0.72	0.97	0.71	0.03	0.03	0.19	0.99	0.32	0.15	0.05
BAZ12A	DTV1_PTSD2	1.25	178.70	0.24	0.34	0.74	0.90	0.02	0.05	0.22	0.99	0.14	0.51	-0.28
BM01A	DTV1_PTSD2	0.16	179.70	0.19	0.22	1.11	0.91	0.00	0.00	0.01	1.00	0.02	0.01	0.00
BM02A	DTV1_PTSD2	0.19	179.70	0.24	0.31	1.23	0.83	0.01	0.01	0.04	1.00	0.03	0.01	0.03
BM04A	DTV1_PTSD2	1.11	178.50	0.72	0.58	1.22	0.75	0.00	0.01	0.02	1.00	0.07	0.05	-0.03
BM05A	DTV1_PTSD2	0.61	179.10	0.47	0.37	1.11	0.88	0.01	0.01	0.06	1.00	0.01	0.08	-0.02
BM06A	DTV1_PTSD2	0.08	179.90	0.25	0.45	1.19	0.81	0.01	0.01	0.01	1.00	0.04	0.04	-0.03
BR01A	DTV1_PTSD2	0.60	179.30	0.28	0.45	1.00	0.83	0.02	0.01	0.11	1.00	0.04	0.14	-0.02
BR02A	DTV1_PTSD2	0.49	179.50	0.11	0.42	0.74	0.86	0.02	0.05	0.22	0.99	0.13	0.41	-0.19

BR03A	DTV1_PTSD2	0.82	179.00	0.43	0.39	1.31	0.85	0.01	0.00	0.03	1.00	0.20	0.25	-0.22
BR04A	DTV1_PTSD2	0.55	179.40	0.24	0.36	0.88	0.80	0.05	0.06	0.43	0.97	0.11	0.58	-0.15
BR05A	DTV1_PTSD2	0.52	179.40	0.28	0.50	1.17	0.82	0.03	0.04	0.28	0.99	0.10	0.23	0.05
BR06A	DTV1_PTSD2	0.21	179.80	0.21	0.57	0.80	0.78	0.03	0.02	0.16	0.99	0.16	0.44	-0.28
BR07A	DTV1_PTSD2	0.89	178.90	0.52	0.60	1.35	0.74	0.01	0.02	0.09	1.00	0.26	0.36	-0.27
BR08A	DTV1_PTSD2	0.45	179.50	0.24	0.71	0.72	0.91	0.03	0.05	0.26	0.99	0.30	0.60	-0.34
BR09A	DTV1_PTSD2	0.01	180.00	0.17	0.47	1.28	0.78	0.02	0.02	0.21	0.99	0.49	0.36	-0.15
BR11A	DTV1_PTSD2	0.52	179.40	0.33	0.61	0.78	1.03	0.02	0.00	0.10	1.00	0.43	0.41	-0.30
BR12A	DTV1_PTSD2	0.72	179.10	0.40	0.51	1.30	0.95	0.02	0.00	0.11	0.99	0.77	0.75	-0.64
BR13A	DTV1_PTSD2	0.36	179.50	0.31	0.47	0.85	0.93	0.01	0.02	0.00	1.00	0.49	0.51	-0.51
BZ01A	DTV1_PTSD2	1.58	178.30	0.38	0.68	0.84	0.81	0.01	0.02	0.05	1.00	0.28	0.42	-0.37
BZ02A	DTV1_PTSD2	0.49	179.50	0.16	0.56	0.61	0.93	0.03	0.09	0.25	0.99	0.82	0.96	-0.71
BZ04A	DTV1_PTSD2	0.77	179.20	0.21	0.27	0.69	1.01	0.01	0.01	0.05	1.00	0.39	0.52	-0.46
BZ05A	DTV1_PTSD2	1.30	178.70	0.15	0.69	0.80	0.59	0.03	0.06	0.23	0.99	0.15	0.16	0.07
BZ06A	DTV1_PTSD2	0.39	179.60	0.05	0.52	0.73	0.61	0.03	0.08	0.20	0.99	0.20	0.08	0.12
BZ07A	DTV1_PTSD2	0.93	179.00	0.19	0.47	0.79	0.76	0.03	0.07	0.27	0.99	0.15	0.48	-0.21
BZ08A	DTV1_PTSD2	1.44	178.50	0.16	0.83	0.75	0.56	0.03	0.09	0.25	0.99	0.04	0.34	-0.09
BZ09A	DTV1_PTSD2	0.72	179.30	0.09	0.66	0.68	0.59	0.04	0.12	0.36	0.98	0.04	0.49	-0.14
BZ10A	DTV1_PTSD2	1.53	178.50	0.18	0.92	0.63	0.74	0.02	0.04	0.12	1.00	0.05	0.31	-0.19
BZ11A	DTV1_PTSD2	0.35	179.60	0.07	0.63	0.62	0.74	0.03	0.07	0.26	0.99	0.05	0.43	-0.17
BZ12A	DTV1_PTSD2	1.00	179.00	0.25	0.67	0.68	0.96	0.01	0.01	0.07	1.00	0.20	0.38	-0.31
BZ13A	DTV1_PTSD2	0.05	179.90	0.09	0.35	0.74	0.93	0.02	0.03	0.16	1.00	0.33	0.51	-0.35
BZ14A	DTV1_PTSD2	1.19	178.80	0.22	0.31	0.69	0.90	0.02	0.03	0.13	1.00	0.17	0.44	-0.31
BZ15A	DTV1_PTSD2	0.47	179.50	0.16	0.23	0.82	0.87	0.01	0.02	0.07	1.00	0.44	0.47	-0.40
BZ16A	DTV1_PTSD2	0.37	179.60	0.12	0.25	0.78	0.95	0.02	0.05	0.17	0.99	0.36	0.40	-0.23
BZ17A	DTV1_PTSD2	0.33	179.60	0.24	0.65	0.85	0.84	0.01	0.01	0.09	1.00	0.52	0.50	-0.41
BZ18A	DTV1_PTSD2	0.55	179.40	0.21	0.36	0.84	0.92	0.02	0.03	0.16	1.00	0.46	0.49	-0.33
BZ19A	DTV1_PTSD2	0.69	179.30	0.21	0.34	0.90	0.89	0.01	0.02	0.01	1.00	0.21	0.31	-0.30
BZ20A	DTV1_PTSD2	0.73	179.20	0.26	0.37	0.90	0.89	0.01	0.01	0.08	1.00	0.45	0.47	-0.39
PA102A	DTV1_PTSD2	0.27	179.60	0.26	0.33	1.04	0.89	0.01	0.01	0.03	1.00	0.39	0.37	-0.34
PA104A	DTV1_PTSD2	0.57	179.10	0.48	0.45	1.05	0.90	0.01	0.01	0.01	1.00	0.29	0.24	-0.23
PA105A	DTV1_PTSD2	0.77	178.80	0.60	0.37	1.18	0.83	0.01	0.00	0.07	1.00	0.24	0.27	-0.20
PA107A	DTV1_PTSD2	0.23	179.60	0.42	0.62	1.17	0.82	0.01	0.01	0.04	1.00	0.09	0.09	-0.05
PA108A	DTV1_PTSD3	0.25	179.60	0.21	0.21	0.99	0.91	0.01	0.01	0.01	1.00	0.22	0.21	-0.20
PA109A	DTV1_PTSD3	0.52	179.20	0.39	0.29	1.02	0.89	0.01	0.02	0.09	1.00	0.12	0.22	-0.13
PA110A	DTV1_PTSD3	0.19	179.70	0.36	0.58	1.02	0.89	0.01	0.02	0.12	1.00	0.02	0.15	-0.03
PA111A	DTV1_PTSD3	0.41	179.40	0.32	0.25	1.01	0.91	0.02	0.01	0.10	1.00	0.01	0.11	-0.01
PA112A	DTV1_PTSD3	0.30	179.60	0.27	0.39	1.00	0.92	0.04	0.06	0.40	0.98	0.28	0.19	0.21
PA114A	DTV1_PTSD3	0.25	179.70	0.21	0.27	1.00	1.03	0.01	0.00	0.00	1.00	0.01	0.01	-0.01
PA115A	DTV1_PTSD3	0.42	179.40	0.33	0.33	1.04	0.90	0.02	0.04	0.22	0.99	0.24	0.01	0.21
PA116A	DTV1_PTSD3	0.33	179.50	0.28	0.31	1.00	0.89	0.03	0.04	0.28	0.99	0.45	0.13	0.14
PA117A	DTV1_PTSD3	0.24	179.60	0.25	0.27	1.04	0.93	0.01	0.02	0.08	1.00	0.14	0.05	0.03
PA118A	DTV1_PTSD3	0.30	179.60	0.38	0.59	0.89	1.00	0.03	0.04	0.29	0.99	0.63	0.29	0.00
PA119A	DTV1_PTSD3	0.13	179.80	0.12	0.15	1.03	0.98	0.01	0.01	0.11	1.00	0.07	0.04	0.07
PA120A	DTV1_PTSD3	0.24	179.60	0.22	0.25	1.07	0.92	0.02	0.04	0.19	1.00	0.22	0.02	0.17
PA121A	DTV1_PTSD3	0.23	179.70	0.22	0.29	1.01	0.97	0.02	0.04	0.22	0.99	0.35	0.10	0.12
PA123A	DTV1_PTSD3	0.05	179.90	0.15	0.25	1.04	0.99	0.03	0.04	0.25	0.99	0.51	0.23	0.01
PA124A	DTV1_PTSD3	0.22	179.70	0.19	0.20	1.06	1.00	0.02	0.03	0.16	1.00	0.20	0.04	0.13
PA125A	DTV1_PTSD3	0.22	179.70	0.21	0.32	1.03	0.97	0.04	0.04	0.38	0.98	0.61	0.16	0.22
PA126A	DTV1_PTSD3	0.32	179.50	0.27	0.30	1.11	0.93	0.01	0.00	0.02	1.00	0.05	0.02	0.01
PA127A	DTV1_PTSD3	0.19	179.70	0.20	0.29	1.05	0.96	0.02	0.04	0.22	0.99	0.24	0.01	0.21
PA128A	DTV1_PTSD3	0.28	179.60	0.20	0.15	1.45	0.73	0.02	0.04	0.15	0.99	0.09	0.04	0.11
PL03A	DTV1_PTSD3	0.65	179.10	0.66	1.00	1.11	0.90	0.01	0.02	0.11	1.00	0.02	0.09	0.02
PL09A	DTV1_PTSD3	0.53	177.50	2.47	2.53	0.68	0.30	0.06	0.00	0.60	0.95	1.46	1.44	-0.84
PL10A	DTV1_PTSD3	0.26	179.60	0.24	0.28	1.05	0.84	0.01	0.02	0.08	1.00	0.26	0.27	-0.20
PL13A	DTV1_PTSD3	0.26	179.60	0.40	0.72	1.00	0.86	0.01	0.03	0.09	1.00	0.32	0.35	-0.26
PL16A	DTV1_PTSD3	0.18	179.70	0.19	0.26	1.05	0.92	0.01	0.03	0.07	1.00	0.12	0.18	-0.11
PL17A	DTV1_PTSD3	0.35	179.50	0.25	0.31	1.05	0.99	0.01	0.02	0.06	1.00	0.07	0.12	-0.06
PL18A	DTV1_PTSD3	0.28	179.60	0.19	0.18	1.13	0.95	0.01	0.01	0.09	1.00	0.04	0.06	0.03
PL19A	DTV1_PTSD3	0.16	179.80	0.24	0.42	1.04	0.95	0.00	0.00	0.00	1.00	0.08	0.08	-0.08
PL21A	DTV1_PTSD3	0.53	179.20	0.39	0.16	1.09	0.93	0.01	0.01	0.03	1.00	0.07	0.13	-0.10
PL22A	DTV1_PTSD3	0.21	179.70	0.20	0.27	1.12	0.98	0.01	0.02	0.09	1.00	0.06	0.04	0.05
PL24A	DTV1_PTSD3	0.72	178.90	0.54	0.31	1.14	0.92	0.01	0.02	0.12	1.00	0.23	0.11	0.01
PL25A	DTV1_PTSD3	0.37	179.50	0.28	0.24	1.08	0.95	0.00	0.01	0.03	1.00	0.09	0.07	-0.04
PL27A	DTV1_PTSD3	0.67	179.10	1.38	2.47	1.08	0.91	0.01	0.02	0.08	1.00	0.01	0.08	0.00
PL28A	DTV1_PTSD3	0.22	179.70	0.33	0.58	1.27	0.75	0.07	0.31	0.60	0.93	0.55	0.03	0.57
PL30A	DTV1_PTSD3	0.43	179.50	0.28	0.40	1.06	1.11	0.01	0.02	0.08	1.00	0.06	0.13	-0.05
PL32A	DTV1_PTSD3	0.36	179.50	0.30	0.32	1.02	1.06	0.00	0.01	0.02	1.00	0.01	0.03	-0.01
PL40A	DTV1_PTSD3	0.33	179.50	0.38	0.64	1.05	1.03	0.03	0.00	0.16	0.99	0.19	0.06	0.10
PL41A	DTV1_PTSD3	0.55	179.10	0.50	0.42	0.97	1.03	0.01	0.01	0.04	1.00	0.08	0.04	0.00
P1502A	DTVT_PTSD	8.66	168.90	5.36	5.71	0.58	1.20	0.02	0.00	0.08	1.00	0.14	0.21	-0.13
P2400A	DTVT_PTSD	4.25	174.30	2.91	2.93	1.04	1.09	0.03	0.06	0.19	0.99	0.08	0.27	-0.08
P4000A	DTVT_PTSD	11.11	164.60	8.94	10.53	0.85	0.45	0.19	0.04	1.85	0.54	0.53	0.65	1.20
FRBB5.1A	FRK1_PTSD	0.19	0.30	0.26	0.33	0.98	0.90	0.01	0.00	0.04	1.00	0.18	0.24	-0.20
FRCG2.3A	FRK1_PTSD	3.04	4.90	2.55	1.57	0.98	0.92	0.01	0.00	0.03	1.00	0.18	0.18	-0.15
FRCH2.4A	FRK1_PTSD	0.54	1.10	0.97	1.12	0.97	1.00	0.00	0.00	0.01	1.00	0.09	0.09	-0.08
FRLG4.4A	FRK1_PTSD	1.23	2.00	1.22	1.13	0.99	0.95	0.01	0.01	0.00	1.00	0.06	0.05	-0.05
FRSG2.4.1A	FRK1_PTSD	0.95	1.90	1.24	1.09	0.96	1.04	0.00	0.00	0.01	1.00	0.09	0.07	-0.06
FRSG3.5.3A	FRK1_PTSD	0.09	0.10	0.26	0.39	0.99	1.01	0.01	0.01	0.04	1.00	0.19	0.13	-0.10
FRTB7.1A	FRK1_PTSD	0.49	0.80	0.47	0.46	0.91	1.07	0.01	0.00	0.04	1.00	0.13	0.05	-0.01
F2BB5.1B	FRK2_PTSD	0.08	0.20	0.21	0.28	0.97	0.98	0.01	0.00	0.05	1.00	0.15	0.12	-0.07

F2CG2.3B	FRK2_PTSD	3.31	5.60	2.94	1.71	0.98	0.90	0.01	0.00	0.08	1.00	0.22	0.14	-0.07
F2CH2.4B	FRK2_PTSD	0.37	0.70	0.83	1.05	0.96	1.00	0.01	0.00	0.02	1.00	0.12	0.08	-0.06
F2GR3.7B	FRK2_PTSD	0.81	1.10	0.63	0.70	0.77	0.91	0.02	0.03	0.05	0.99	0.28	0.36	-0.30
F2LG4.4B	FRK2_PTSD	1.03	1.80	1.05	0.91	0.98	0.90	0.01	0.00	0.02	1.00	0.18	0.15	-0.14
F2SG2.4.1B	FRK2_PTSD	1.15	2.20	1.29	0.96	0.92	1.02	0.00	0.00	0.02	1.00	0.13	0.15	-0.13
F2SG3.5.3B	FRK2_PTSD	0.10	0.20	0.24	0.37	0.98	0.95	0.01	0.01	0.08	1.00	0.20	0.13	-0.05
F2TB7.1B	FRK2_PTSD	0.49	0.80	0.44	0.37	0.89	1.01	0.01	0.01	0.01	1.00	0.13	0.12	-0.12
P1CA7-6A	FRK3_PTSD	0.42	0.70	0.86	1.26	0.99	1.02	0.00	0.00	0.01	1.00	0.04	0.03	-0.03
P1PW4-2B	FRK3_PTSD	0.14	0.20	0.21	0.27	1.00	0.99	0.00	0.00	0.02	1.00	0.10	0.04	-0.02
P1QA4-1B	FRK3_PTSD	0.30	0.50	0.35	0.43	0.96	0.95	0.00	0.00	0.00	1.00	0.06	0.06	-0.06
P1SG3.61A	FRK3_PTSD	0.45	0.60	0.32	0.28	1.00	1.04	0.01	0.01	0.06	1.00	0.21	0.13	-0.07
P1TB3-1B	FRK3_PTSD	0.18	0.40	0.47	0.58	0.97	1.05	0.01	0.01	0.07	1.00	0.32	0.26	-0.20
P1TB9.10B	FRK3_PTSD	0.09	0.20	0.38	0.47	0.98	1.07	0.00	0.00	0.01	1.00	0.12	0.10	-0.09
S1BG1.3A	FRK3_PTSD	0.23	0.50	0.48	0.60	0.94	1.00	0.01	0.02	0.02	1.00	0.15	0.13	-0.11
S1BP4.3B	FRK3_PTSD	0.47	0.90	0.49	0.34	0.98	1.04	0.00	0.00	0.02	1.00	0.13	0.16	-0.13
S1CA2.2B	FRK3_PTSD	0.18	0.30	0.39	0.69	0.97	1.00	0.01	0.01	0.09	1.00	0.14	0.04	0.05
S1KL18.2A	FRK3_PTSD	0.60	1.00	0.65	0.61	0.99	0.97	0.01	0.01	0.07	1.00	0.14	0.07	0.00
S1NU21.1B	FRK3_PTSD	0.63	1.00	0.56	0.45	1.00	1.00	0.01	0.00	0.01	1.00	0.10	0.06	-0.04
S1PW2.1A	FRK3_PTSD	0.41	0.70	0.41	0.42	1.00	0.92	0.00	0.00	0.01	1.00	0.09	0.07	-0.06
S1QA4.3A	FRK3_PTSD	0.31	0.40	0.32	0.48	0.95	0.94	0.01	0.00	0.02	1.00	0.05	0.03	-0.01
T1BG2.1A	FRK3_PTSD	0.15	0.20	0.27	0.39	-582.79	0.00	0.07	0.12	0.60	0.93	1.99	0.14	0.46
T1BP6.1A	FRK3_PTSD	0.22	0.40	0.30	0.29	0.99	1.04	0.00	0.00	0.02	1.00	0.06	0.05	-0.03
T1PW10.1B	FRK3_PTSD	0.15	0.20	0.43	0.66	0.99	0.92	0.00	0.00	0.00	1.00	0.13	0.11	-0.11
T1QA2.1A	FRK3_PTSD	0.78	1.00	0.51	0.67	0.74	0.99	0.01	0.00	0.07	1.00	0.20	0.27	-0.20
T1SG34.1A	FRK3_PTSD	0.23	0.30	0.20	0.23	0.98	1.01	0.01	0.01	0.04	1.00	0.15	0.07	-0.03
T1TB7.4B	FRK3_PTSD	0.15	0.40	0.22	0.18	0.99	0.99	0.00	0.01	0.03	1.00	0.10	0.10	-0.07
BP6.2B	FRK4_PTSD	0.04	0.10	0.25	0.37	0.95	1.15	0.01	0.00	0.01	1.00	0.08	0.10	-0.09
BP9.6A	FRK4_PTSD	0.17	0.30	0.32	0.44	0.83	0.41	0.09	0.07	0.77	0.91	0.11	0.71	0.06
GR4.4B	FRK4_PTSD	0.25	0.40	0.21	0.22	1.02	0.01	0.31	0.40	1.42	0.16	0.13	1.42	0.00
LG3.3A	FRK4_PTSD	0.41	0.70	0.48	0.47	0.93	1.08	0.01	0.01	0.05	1.00	0.06	0.08	-0.03
NU152B	FRK4_PTSD	0.35	0.60	0.33	0.28	0.92	1.09	0.01	0.01	0.06	1.00	0.20	0.16	-0.10
PW101A	FRK4_PTSD	0.42	0.70	0.65	0.96	0.88	1.00	0.02	0.01	0.02	0.99	0.19	0.15	-0.13
PW3.1B	FRK4_PTSD	0.19	0.40	0.38	0.47	0.86	1.05	0.02	0.00	0.07	0.99	0.33	0.26	-0.19
PW6-3A	FRK4_PTSD	0.58	0.90	0.73	0.92	0.88	1.03	0.02	0.02	0.06	1.00	0.11	0.15	-0.09
QA4.3B	FRK4_PTSD	0.62	1.00	0.78	1.04	0.75	0.93	0.02	0.01	0.04	0.99	0.29	0.42	-0.38
M24.1D	M2_PTSD	0.12	0.30	0.31	0.38	1.00	1.02	0.00	0.00	0.00	1.00	0.04	0.03	-0.03
M24.4B	M2_PTSD	0.57	1.30	0.71	0.42	1.01	1.02	0.00	0.01	0.05	1.00	0.03	0.01	0.04
M24.9E	M2_PTSD	0.19	0.40	0.24	0.12	1.00	1.03	0.00	0.00	0.03	1.00	0.04	0.02	0.01
M25.10B	M2_PTSD	0.76	1.00	0.52	0.64	0.54	1.14	0.01	0.01	0.05	1.00	0.39	0.53	-0.48
M25.4B	M2_PTSD	1.97	2.10	0.49	0.63	0.87	1.12	0.00	0.00	0.01	1.00	0.07	0.06	-0.04
M25.6D	M2_PTSD	0.85	1.00	0.43	0.64	0.96	1.23	0.01	0.02	0.06	1.00	0.00	0.06	0.00
M26.1E	M2_PTSD	0.22	0.60	0.32	0.22	0.96	1.07	0.00	0.00	0.01	1.00	0.06	0.05	-0.04
M26.4A	M2_PTSD	0.26	0.70	0.55	0.55	0.95	1.08	0.01	0.00	0.07	1.00	0.12	0.04	0.03
M26.5D	M2_PTSD	0.62	1.80	1.08	0.80	0.96	1.10	0.00	0.00	0.02	1.00	0.10	0.07	-0.05
M27.3A	M2_PTSD	0.16	0.40	0.53	0.62	0.86	1.35	0.02	0.01	0.25	0.99	0.35	0.12	0.14
M27.5B	M2_PTSD	0.12	0.20	0.67	0.96	0.00	-244.99	-0.37	0.71	2.48	0.08	2.37	0.28	2.20
M28.7A	M2_PTSD	0.92	1.20	0.73	1.02	0.78	0.97	0.01	0.00	0.06	1.00	0.07	0.10	-0.05
MD1.2C	MD_PTSD	0.11	0.20	0.35	0.47	0.89	1.02	0.00	0.01	0.05	1.00	0.09	0.12	-0.07
MD2.11D	MD_PTSD	0.11	0.30	0.42	0.48	0.96	1.96	0.02	0.02	0.42	0.98	0.18	0.30	0.12
MD2.3D	MD_PTSD	2.77	5.80	3.13	1.57	0.84	0.22	0.04	0.07	0.64	0.96	0.16	0.56	0.08
MD2.8B	MD_PTSD	0.05	0.10	0.50	0.60	0.96	2.46	0.05	0.08	0.86	0.91	0.13	1.04	-0.18
MD3.1E	MD_PTSD	0.19	0.60	0.51	0.54	0.94	1.09	0.00	0.00	0.05	1.00	0.17	0.13	-0.08
MD3.4E	MD_PTSD	0.17	0.50	0.52	0.58	0.94	1.12	0.00	0.00	0.04	1.00	0.18	0.14	-0.10
MD3.7C	MD_PTSD	0.11	0.30	0.23	0.21	0.91	1.15	0.00	0.00	0.05	1.00	0.29	0.23	-0.18
MZM6H1.1B	MZ_PTSD	0.22	179.40	0.34	0.26	0.88	1.32	0.01	0.01	0.05	1.00	0.26	0.33	-0.28
MZM6H2A.1B	MZ_PTSD	0.11	179.70	0.19	0.17	0.90	1.35	0.01	0.01	0.05	1.00	0.26	0.33	-0.27
MZM6H2A.1D	MZ_PTSD	0.10	179.80	0.27	0.31	0.90	1.37	0.01	0.01	0.08	1.00	0.24	0.34	-0.26
MZMD2.11A	MZ_PTSD	0.13	179.60	0.28	0.27	0.94	1.22	0.00	0.00	0.02	1.00	0.25	0.25	-0.23
MZMD2.12A	MZ_PTSD	0.11	179.70	0.37	0.41	0.95	1.22	0.00	0.00	0.02	1.00	0.26	0.25	-0.23
MZMD2.12E	MZ_PTSD	0.13	179.60	0.45	0.51	0.94	1.19	0.00	0.00	0.01	1.00	0.31	0.29	-0.28
MZMD2.4A	MZ_PTSD	0.21	179.30	0.64	0.66	0.95	1.02	0.00	0.00	0.01	1.00	0.20	0.19	-0.18
MZMD2.4D	MZ_PTSD	0.15	179.50	0.67	0.75	0.94	1.04	0.00	0.00	0.00	1.00	0.22	0.19	-0.19
MZMD2.5D	MZ_PTSD	0.17	179.40	0.59	0.64	0.94	1.06	0.00	0.00	0.02	1.00	0.21	0.18	-0.17
MZMD2.6C	MZ_PTSD	0.05	179.80	0.15	0.15	0.91	1.12	0.00	0.00	0.03	1.00	0.26	0.21	-0.18
MZMD2.7E	MZ_PTSD	0.15	179.50	0.27	0.19	0.92	1.04	0.01	0.01	0.07	1.00	0.21	0.25	-0.18
MZMD3.1A	MZ_PTSD	0.06	179.80	0.35	0.41	0.91	1.20	0.01	0.00	0.06	1.00	0.29	0.24	-0.19
MZMD3.2A	MZ_PTSD	0.10	179.70	0.55	0.65	0.90	1.11	0.00	0.00	0.03	1.00	0.23	0.24	-0.21
MZMD3.2C	MZ_PTSD	0.14	179.60	0.55	0.62	0.89	1.13	0.01	0.00	0.08	1.00	0.31	0.27	-0.19
MZMD3.3A	MZ_PTSD	0.13	0.40	0.41	0.44	0.01	164.80	0.32	1.08	1.68	0.00	1.36	0.27	1.42
MZMD3.3D	MZ_PTSD	0.11	179.70	0.35	0.38	0.00	256.32	0.21	0.59	1.60	0.32	1.35	0.26	1.34
MZMD3.8A	MZ_PTSD	0.04	179.90	0.25	0.30	0.87	1.10	0.00	0.00	0.01	1.00	0.41	0.43	-0.42
MZMD6.2D	MZ_PTSD	0.44	178.80	0.74	0.57	0.94	1.31	0.00	0.01	0.02	1.00	0.25	0.26	-0.24
OTMD2.10C	OT_PTSD	0.17	179.60	0.30	0.29	0.98	1.07	0.00	0.00	0.01	1.00	0.22	0.22	-0.21
OTMD2.13B	OT_PTSD	0.21	179.60	0.23	0.25	0.91	0.94	0.01	0.01	0.08	1.00	0.27	0.34	-0.26
OTMD2.5A	OT_PTSD	0.11	179.80	0.33	0.42	0.93	0.98	0.01	0.01	0.07	1.00	0.24	0.30	-0.24
OTMD2.6A	OT_PTSD	0.03	179.90	0.13	0.17	0.94	1.01	0.01	0.00	0.04	1.00	0.22	0.25	-0.21
OTMD2.9B	OT_PTSD	0.08	179.80	0.40	0.48	0.94	1.06	0.00	0.00	0.01	1.00	0.21	0.21	-0.20
OTMD3.2D	OT_PTSD	0.12	179.60	0.49	0.56	0.92	1.02	0.01	0.00	0.10	1.00	0.37	0.28	-0.18
OTMD3.6A	OT_PTSD	0.08	179.80	0.31	0.36	0.96	1.11	0.00	0.00	0.05	1.00	0.25	0.20	-0.15
OTMD3.8E	OT_PTSD	0.32	179.20	0.50	0.36	0.92	1.04	0.01	0.01	0.05	1.00	0.16	0.21	-0.16
OTMD4.2C	OT_PTSD	0.08	179.80	0.16	0.17	1.00	1.00	0.00	0.01	0.04	1.00	0.10	0.07	-0.03

OTMD4.7E	OT_PTSD	0.54	178.70	0.96	0.92	0.99	1.00	0.00	0.01	0.03	1.00	0.09	0.08	-0.05
OTMD6.1B	OT_PTSD	0.47	178.70	0.73	0.45	0.98	1.01	0.00	0.00	0.03	1.00	0.18	0.14	-0.12
OTMD6.3B	OT_PTSD	0.28	179.20	0.50	0.39	0.97	1.03	0.00	0.00	0.00	1.00	0.16	0.14	-0.14
OTMD6.5A	OT_PTSD	0.94	177.20	1.53	0.92	0.98	1.00	0.00	0.00	0.05	1.00	0.19	0.13	-0.09
OTNH53BC	OT_PTSD	0.84	178.70	1.00	1.36	0.96	0.97	0.01	0.01	0.06	1.00	0.06	0.01	0.05
OTNH53CA	OT_PTSD	1.16	178.10	1.17	1.21	0.95	0.97	0.01	0.00	0.07	1.00	0.07	0.01	0.06
OTNH53CC	OT_PTSD	0.70	178.90	0.89	1.26	0.94	0.97	0.01	0.01	0.07	1.00	0.05	0.03	0.05
OZBM6.1CA	OZ_PTSD	0.37	179.60	0.23	0.77	0.01	91.03	0.24	0.89	1.41	0.20	1.22	0.17	1.23
OZBM6.3D	OZ_PTSD	0.31	179.70	0.21	0.53	0.81	1.00	0.01	0.02	0.08	1.00	0.13	0.21	-0.13
OZBM6.4BB	OZ_PTSD	0.17	179.70	0.29	0.37	0.92	1.07	0.00	0.00	0.05	1.00	0.15	0.11	-0.07
OZBM6.5BD	OZ_PTSD	0.45	179.50	0.22	0.47	0.66	0.96	0.01	0.02	0.06	1.00	0.05	0.13	-0.06
OZBM7.1AA	OZ_PTSD	0.04	179.90	0.16	0.23	0.97	1.01	0.00	0.00	0.02	1.00	0.05	0.04	-0.02
OZBM7.1BC	OZ_PTSD	0.10	179.80	0.16	0.16	0.98	0.99	0.00	0.00	0.01	1.00	0.05	0.05	-0.03
OZBM7.4BA	OZ_PTSD	0.36	179.10	0.52	0.37	0.97	1.00	0.00	0.00	0.04	1.00	0.06	0.10	-0.06
OZMD2.10A	OZ_PTSD	0.16	179.60	0.32	0.30	1.00	1.08	0.00	0.00	0.02	1.00	0.06	0.04	-0.01
OZMD2.11C	OZ_PTSD	0.05	179.90	0.15	0.16	0.98	1.14	0.00	0.00	0.06	1.00	0.06	0.00	0.06
OZMD2.4C	OZ_PTSD	0.15	179.50	0.50	0.53	0.99	1.07	0.00	0.00	0.00	1.00	0.01	0.01	-0.01
OZMD3.1C	OZ_PTSD	0.05	179.80	0.34	0.40	0.98	1.58	0.02	0.01	0.22	1.00	0.07	0.15	0.07
OZMD3.3E	OZ_PTSD	0.13	179.60	0.45	0.48	0.99	1.81	0.02	0.01	0.23	0.99	0.02	0.21	0.02
OZMD3.4A	OZ_PTSD	0.12	179.60	0.38	0.40	0.99	1.59	0.02	0.01	0.27	0.99	0.02	0.25	0.02
OZMD4.5C	OZ_PTSD	0.17	179.60	0.34	0.34	0.99	1.20	0.01	0.02	0.16	1.00	0.02	0.14	0.02
OZMD4.6C	OZ_PTSD	0.16	179.60	0.40	0.45	1.00	1.23	0.01	0.01	0.15	1.00	0.00	0.15	0.00
OZMD6.1A	OZ_PTSD	0.45	178.70	0.70	0.36	1.00	1.72	0.02	0.02	0.31	0.99	0.03	0.29	0.02
OZMD6.2A	OZ_PTSD	0.40	178.80	0.81	0.70	0.99	1.95	0.02	0.02	0.31	0.99	0.04	0.28	0.03
OZMD6.3C	OZ_PTSD	0.24	179.30	0.57	0.57	0.99	1.80	0.01	0.01	0.22	1.00	0.02	0.20	0.02
OZMD6.5C	OZ_PTSD	0.85	177.30	1.45	0.90	0.99	2.18	0.02	0.02	0.34	0.99	0.00	0.35	0.00
OZNH5.2CB	OZ_PTSD	13.62	160.60	9.01	2.17	0.98	1.70	0.02	0.01	0.12	0.99	0.02	0.10	0.02
OZNH5.2ED	OZ_PTSD	14.16	159.40	9.66	1.75	0.97	1.65	0.02	0.02	0.15	1.00	0.02	0.17	-0.02
OZNH5.3AD	OZ_PTSD	2.58	176.10	2.10	1.75	0.96	1.57	0.02	0.03	0.18	0.99	0.04	0.21	-0.03
OZNH5.3CB	OZ_PTSD	4.12	173.90	3.06	1.92	0.96	1.46	0.02	0.02	0.14	0.99	0.04	0.18	-0.04
SC12.10A1	SC_PTSD	3.16	4.90	2.55	1.63	0.96	1.07	0.00	0.00	0.03	1.00	0.18	0.09	-0.06
SC12.10A2	SC_PTSD	3.84	6.10	3.18	2.03	0.94	1.01	0.01	0.01	0.07	1.00	0.19	0.06	0.01
SC12.11A2	SC_PTSD	3.15	4.60	2.51	2.23	0.93	1.06	0.01	0.01	0.01	1.00	0.13	0.09	-0.08
SC12.11C2	SC_PTSD	3.59	4.80	2.32	2.18	0.95	1.11	0.01	0.01	0.04	1.00	0.06	0.10	-0.06
SC12.1A1	SC_PTSD	0.68	1.40	1.13	1.27	0.91	1.09	0.01	0.01	0.14	1.00	0.18	0.00	0.14
SC12.3B1	SC_PTSD	2.24	4.20	2.27	1.29	0.95	1.06	0.01	0.01	0.13	1.00	0.15	0.03	0.10
SC12.3B2	SC_PTSD	2.11	4.00	2.27	1.53	0.95	1.06	0.01	0.01	0.11	1.00	0.10	0.04	0.06
SC12.4C1	SC_PTSD	0.11	0.20	0.35	0.58	0.94	1.04	0.01	0.01	0.04	1.00	0.11	0.03	0.01
SC12.4C2	SC_PTSD	1.72	2.70	1.49	1.13	0.94	1.07	0.00	0.00	0.02	1.00	0.08	0.03	-0.01
SC12.5A2	SC_PTSD	2.29	3.30	1.73	1.57	0.94	1.00	0.01	0.01	0.11	1.00	0.20	0.01	0.10
SC12.5B2	SC_PTSD	3.52	5.10	2.65	2.23	0.94	1.06	0.00	0.00	0.03	1.00	0.07	0.05	-0.02
SC12.7C2	SC_PTSD	3.26	4.60	2.33	1.79	0.95	1.01	0.00	0.01	0.04	1.00	0.20	0.08	-0.04
SC12.7D1	SC_PTSD	3.53	4.70	2.22	1.83	0.94	1.04	0.01	0.01	0.07	1.00	0.21	0.07	-0.01
SC12.8C1	SC_PTSD	1.32	2.60	1.54	1.22	0.95	1.03	0.00	0.00	0.01	1.00	0.14	0.07	-0.06
SC12.9B1	SC_PTSD	2.95	4.50	2.41	1.90	0.93	1.06	0.00	0.01	0.03	1.00	0.21	0.11	-0.08
SCG2.10B	SCG_PTSD	2.55	4.10	2.23	1.57	0.94	1.07	0.01	0.01	0.04	1.00	0.23	0.06	-0.02
SCG2.11B	SCG_PTSD	3.05	5.00	2.84	2.43	0.98	1.05	0.01	0.01	0.00	1.00	0.28	0.10	-0.10
SCG2.1B	SCG_PTSD	1.30	2.70	1.53	1.05	1.06	0.98	0.00	0.01	0.01	1.00	0.08	0.04	-0.03
SCG2.2A	SCG_PTSD	1.40	2.70	1.55	1.08	1.04	0.95	0.01	0.00	0.01	1.00	0.06	0.02	-0.01
SCG2.3A	SCG_PTSD	2.01	3.60	1.98	1.22	1.00	0.91	0.01	0.01	0.06	1.00	0.05	0.03	0.03
SCG2.6A	SCG_PTSD	1.16	1.80	1.06	1.09	0.99	0.90	0.01	0.01	0.09	1.00	0.07	0.06	0.03
SCG2.6B	SCG_PTSD	1.93	3.10	1.73	1.39	1.01	0.89	0.01	0.01	0.01	1.00	0.09	0.02	-0.01
SCG2.7B	SCG_PTSD	2.50	3.60	1.85	1.42	1.00	0.98	0.01	0.01	0.04	1.00	0.14	0.02	0.02
SW01-01A-1	SAK	0.50	1.00	0.94	1.14	1.00	1.03	0.00	0.00	0.00	1.00	0.01	0.00	0.00
SW01-02A-1	SAK	0.14	0.20	0.48	0.76	1.01	1.00	0.00	0.00	0.03	1.00	0.01	0.02	0.01
SW01-04A-1	SAK	0.38	0.50	0.50	0.87	0.99	0.98	0.01	0.01	0.03	1.00	0.00	0.02	0.01
SW01-05A-1	SAK	0.27	0.40	0.43	0.77	1.02	0.98	0.01	0.00	0.07	1.00	0.04	0.01	0.06
SW01-06A-1	SAK	0.17	0.20	0.41	0.79	1.02	0.96	0.01	0.01	0.07	1.00	0.04	0.02	0.05
SW01-08A-1	SAK	0.08	0.10	0.27	0.55	0.99	1.00	0.01	0.01	0.07	1.00	0.03	0.01	0.06
SW01-09A-1	SAK	0.06	0.10	0.19	0.41	0.99	0.99	0.01	0.02	0.05	1.00	0.02	0.01	0.04
SW01-10A-1	SAK	0.20	0.30	0.31	0.60	1.00	0.97	0.00	0.00	0.01	1.00	0.01	0.03	-0.02
SW01-11A-1	SAK	0.06	0.10	0.28	0.57	0.98	0.96	0.00	0.01	0.01	1.00	0.02	0.01	0.00
SW01-13A-1	SAK	0.12	0.20	1.81	2.50	0.99	0.97	0.01	0.00	0.01	1.00	0.01	0.02	-0.01
SW01-14A-1	SAK	0.22	0.30	0.40	0.65	1.00	0.98	0.00	0.01	0.03	1.00	0.02	0.03	-0.01
SW01-15A-1	SAK	1.30	1.90	2.21	3.62	1.02	0.97	0.01	0.01	0.07	0.99	0.05	0.01	0.06
SW01-16A-1	SAK	1.80	2.60	4.38	7.51	1.02	0.99	0.01	0.01	0.01	0.99	0.02	0.01	0.00
SW01-18A-1	SAK	0.11	0.10	0.21	0.43	1.01	0.96	0.01	0.02	0.00	1.00	0.00	0.00	0.00
TS01-01A-1	SAK	0.10	0.20	0.76	1.31	1.00	1.00	0.00	0.01	0.02	1.00	0.00	0.03	0.00
TS01-03A-2	SAK	0.43	0.70	0.78	1.21	1.04	0.93	0.01	0.01	0.07	0.99	0.06	0.03	0.03
TS01-04A-2	SAK	0.32	0.40	0.68	1.29	0.99	0.98	0.00	0.00	0.01	1.00	0.01	0.02	-0.01
TS01-05A-1	SAK	0.15	0.20	0.22	0.40	1.02	0.96	0.00	0.01	0.01	1.00	0.01	0.02	-0.01
TS01-06C-1	SAK	0.07	0.10	0.79	1.61	1.00	0.99	0.01	0.00	0.02	1.00	0.01	0.04	-0.02
TS01-08A-1	SAK	0.06	0.10	0.33	0.63	0.99	0.98	0.01	0.00	0.02	1.00	0.02	0.01	0.01
TS01-10A-1	SAK	0.10	0.20	0.81	1.25	1.00	0.98	0.01	0.00	0.08	1.00	0.05	0.03	0.04
TS01-11C-1	SAK	0.12	0.20	0.76	1.21	1.02	1.00	0.00	0.01	0.00	1.00	0.01	0.01	0.00
TS01-12A-1	SAK	0.19	0.40	3.16	4.31	1.01	1.09	0.01	0.00	0.11	0.99	0.02	0.09	0.02
TS01-14A-1	SAK	0.08	0.10	0.73	1.22	1.05	0.95	0.01	0.02	0.00	1.00	0.01	0.05	-0.04
TS01-17A-1	SAK	0.23	0.30	0.67	1.28	1.01	0.94	0.01	0.00	0.02	1.00	0.02	0.01	0.00
TS01-18A-1	SAK	0.12	0.20	0.58	1.09	1.03	0.95	0.01	0.01	0.01	1.00	0.01	0.01	-0.01
TS01-19A-1	SAK	0.27	0.40	1.01	1.74	1.02	0.97	0.01	0.01	0.02	1.00	0.03	0.06	-0.04
TS01-20A-1	SAK	0.04	0.10	0.61	1.23	1.04	0.92	0.01	0.01	0.00	1.00	0.01	0.00	0.00

TS01-22A-1	SAK	0.03	0.00	0.50	1.10	1.02	0.97	0.01	0.00	0.03	1.00	0.01	0.02	0.01
TS01-23A-1	SAK	0.06	0.10	0.30	0.64	1.02	0.97	0.01	0.01	0.04	0.99	0.01	0.00	0.04
TS01-25A-1	SAK	0.12	0.10	0.43	1.04	1.00	1.02	0.01	0.00	0.04	0.99	0.02	0.02	0.01
TS01-26A-1	SAK	0.27	0.40	0.84	1.56	1.02	0.94	0.01	0.02	0.01	0.99	0.00	0.03	-0.01
TS02-01A-1	SAK	0.06	0.10	0.61	1.01	1.02	0.96	0.01	0.00	0.08	0.99	0.04	0.00	0.08
TS02-03A-1	SAK	0.09	0.10	0.60	1.01	1.01	0.96	0.00	0.02	0.02	1.00	0.01	0.01	0.01
TS02-05A-1	SAK	0.16	0.30	0.44	0.70	0.99	0.99	0.01	0.02	0.03	1.00	0.03	0.01	0.02
TS02-06A-1	SAK	0.13	0.20	0.64	1.13	0.98	0.98	0.01	0.01	0.04	1.00	0.01	0.02	0.02
TS02-11A-1	SAK	0.31	0.50	0.65	1.03	0.99	1.04	0.02	0.03	0.07	0.98	0.03	0.01	0.07
TS02-12A-1	SAK	0.11	0.20	0.56	1.00	0.99	1.04	0.01	0.01	0.07	1.00	0.02	0.09	-0.02
TS02-13A-1	SAK	0.24	0.30	0.66	1.18	0.99	1.07	0.01	0.01	0.11	1.00	0.01	0.07	0.04
TS02-14A-1	SAK	0.31	0.40	0.46	0.75	0.99	1.03	0.01	0.02	0.06	1.00	0.02	0.04	0.02
TS02-15A-1	SAK	0.20	0.30	0.82	1.33	0.99	1.01	0.00	0.01	0.01	1.00	0.02	0.01	0.00
TS02-16A-1	SAK	0.60	0.80	0.72	1.19	0.96	1.02	0.01	0.03	0.07	0.99	0.04	0.00	0.07
TS02-18A-1	SAK	0.07	0.10	0.66	1.08	1.00	1.02	0.01	0.00	0.07	1.00	0.02	0.06	0.01
TS02-19A-1	SAK	0.40	0.60	0.88	1.52	1.01	0.98	0.01	0.00	0.05	0.99	0.01	0.04	0.00
TS02-20A-1	SAK	0.30	0.50	0.93	1.47	0.98	0.99	0.01	0.01	0.02	1.00	0.01	0.03	-0.02
TS02-21A-1	SAK	0.40	0.60	0.94	1.55	0.99	1.03	0.01	0.02	0.00	0.99	0.02	0.02	-0.02
TS02-22A-1	SAK	0.39	0.60	0.98	1.60	1.01	1.01	0.01	0.02	0.03	0.99	0.00	0.00	0.03
TS02-23A-1	SAK	0.02	0.00	0.47	0.76	1.03	0.98	0.01	0.00	0.01	1.00	0.00	0.01	0.00
TS02-24A-1	SAK	0.04	0.10	0.47	0.76	1.01	1.02	0.01	0.00	0.03	0.99	0.02	0.05	-0.02
TS02-25A-1	SAK	0.27	0.40	0.99	1.55	0.99	1.01	0.01	0.02	0.01	1.00	0.00	0.01	0.00
TS02-26A-1	SAK	0.21	0.40	1.00	1.57	1.00	1.03	0.01	0.04	0.02	0.99	0.01	0.01	0.02

Appendix B

Supplementary Material for Chapter 4

The data provided in Appendix B supplements Chapter 4. Raw measurement data is available on the MagIC database under:

S. Lloyd, A. Biggin, H. Halls, M. Hill; First palaeointensity data from the cryogenian and their potential implications for inner core nucleation age; Magic Information Consortium (MagIC), doi: 10.7288/V4/MAGIC/17065.

B1 Supplementary Figures

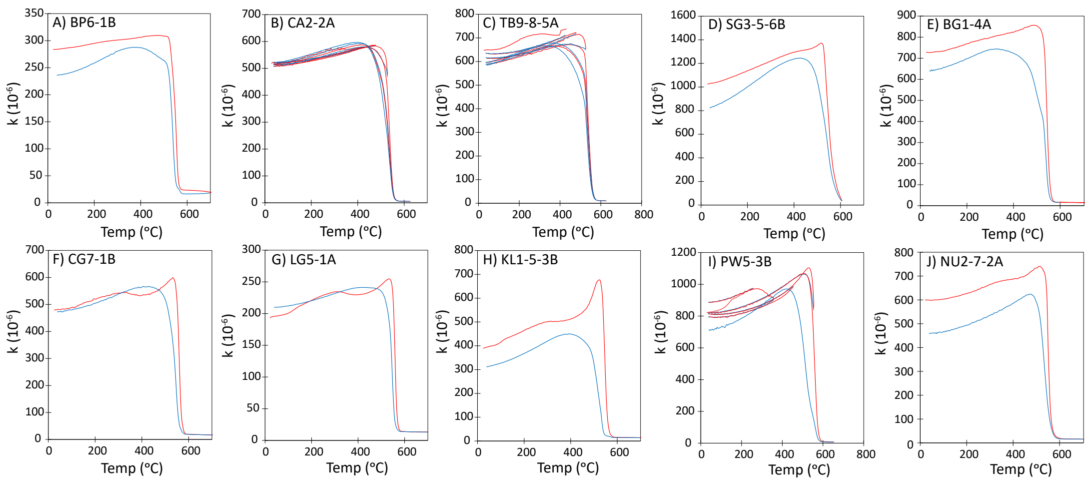

Supplementary Figure B1.1: κ-T curves. Red lines, heating curve; blue lines, cooling curve; κ, susceptibility; T, temperature.

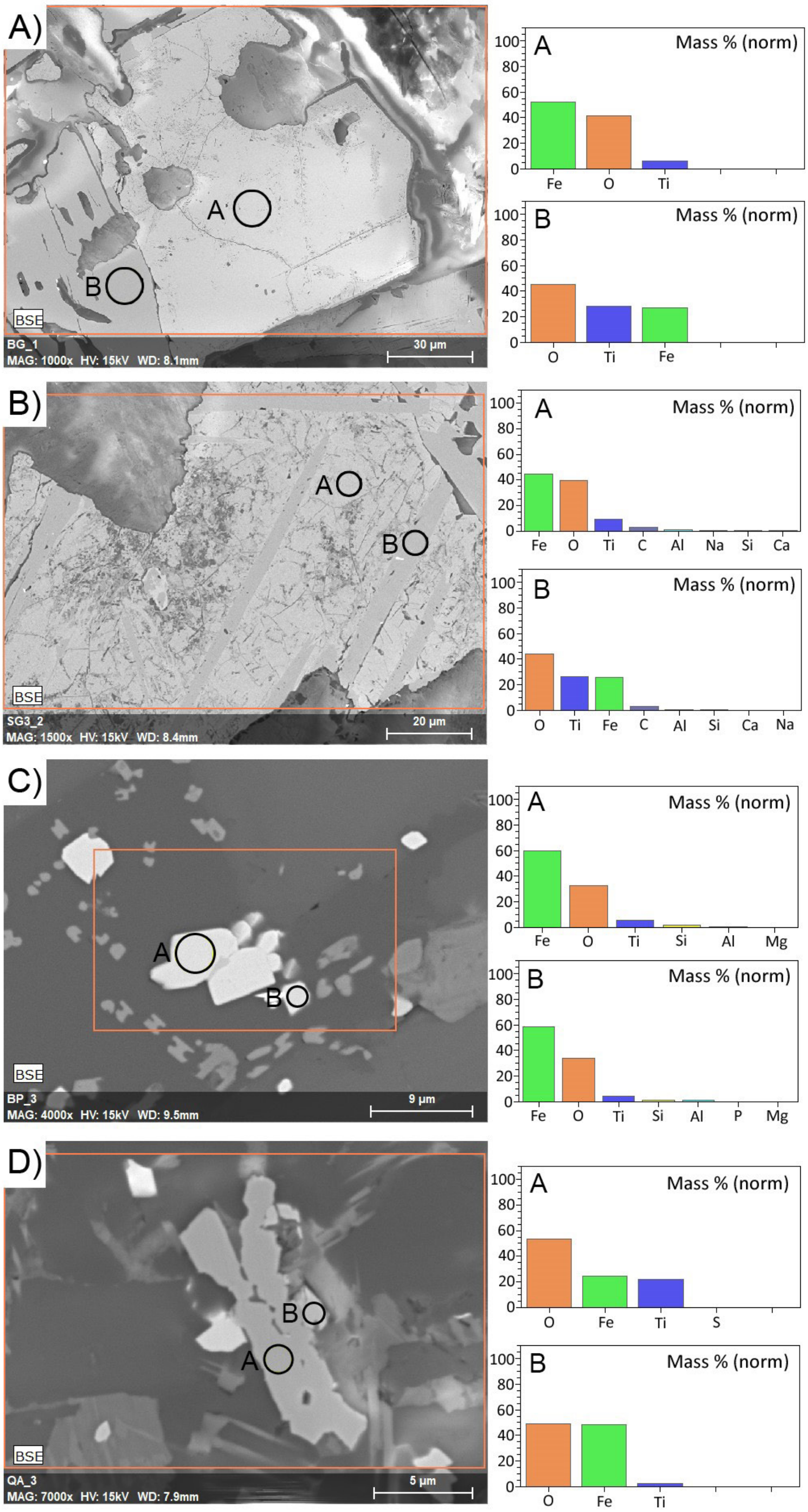

Supplementary Figure B1.2: Electron-dispersive X-ray spectroscopy (EDS) results for four thin sections: A) BG2-3A; B) SG3-3-B; C) BP9-6B; D) QA2-1B.

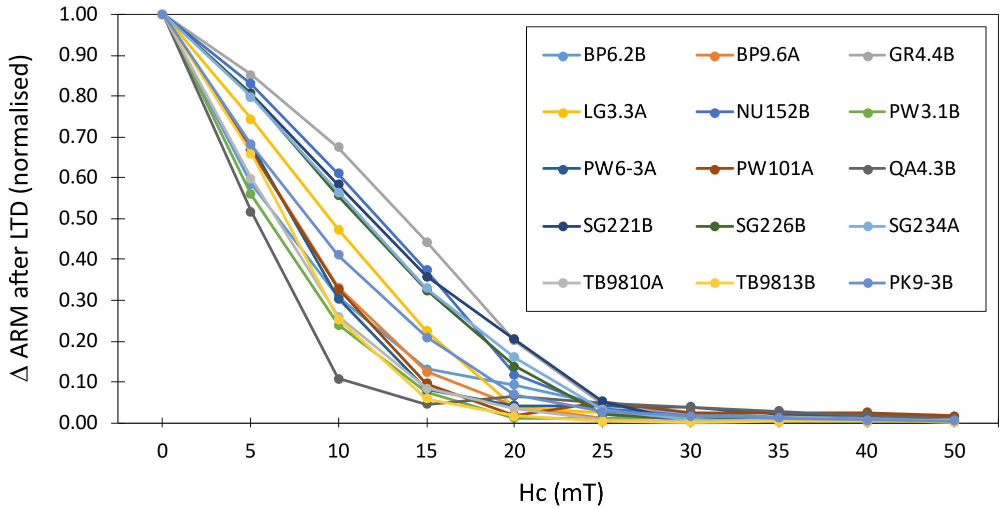

Supplementary Figure B1.3. Plot showing the difference in ARM after LTD treatment normalised by maximum difference and where zero equals identical ARM in LTD and non-LTD sister specimens (17 samples across 10 sites); hence, the maximum difference is one at 0 mT. Specimen SG3-5-3B lost no remanence after LTD treatment and is not included in this plot, while specimen QA12-2A had no magnetisation to lose and is also excluded.

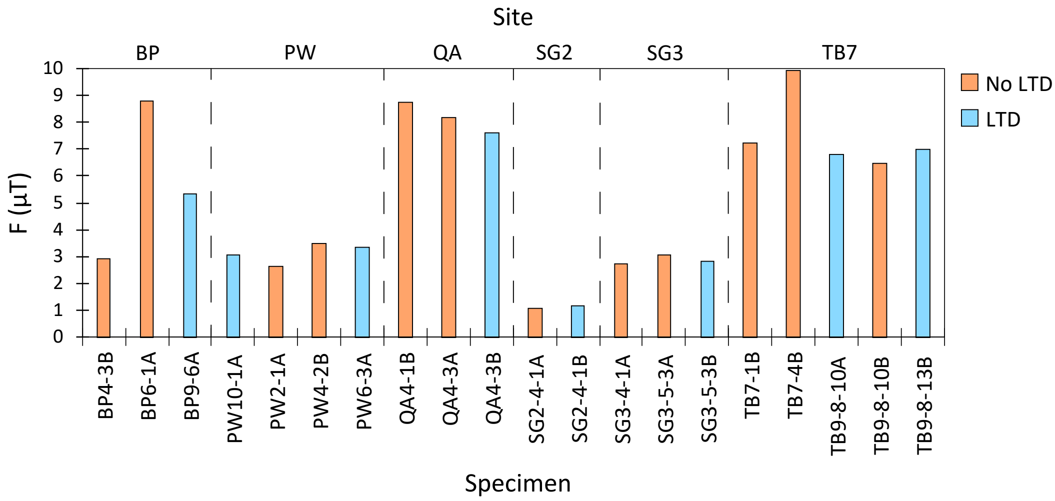

Supplementary Figure B1.4. Comparison of the effect of LTD treatment on successful paleointensity results from Shaw (LTD) DHT experiments, consisting of 20 specimens across six sites.

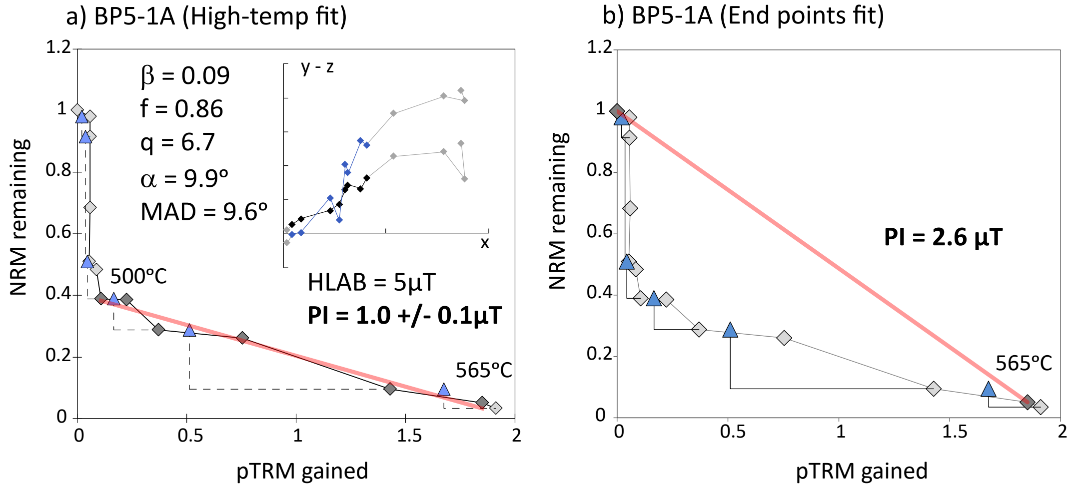

Supplementary Figure B1.5. a) Specimen BP5-1A slope is fitted from 500 to 565 °C producing a palaeointensity of 1.0 μT. b) The same specimen slope fitted from the initial step to 565 °C produces a palaeointensity of 2.6 μT. The low temperature section of the Arai diagram corresponds to an overprint direction and could not be taken as the ChRM. The figure illustrates that the potential error from under-estimation associated with selecting the high-temperature section of this two-slope Arai diagram is small.

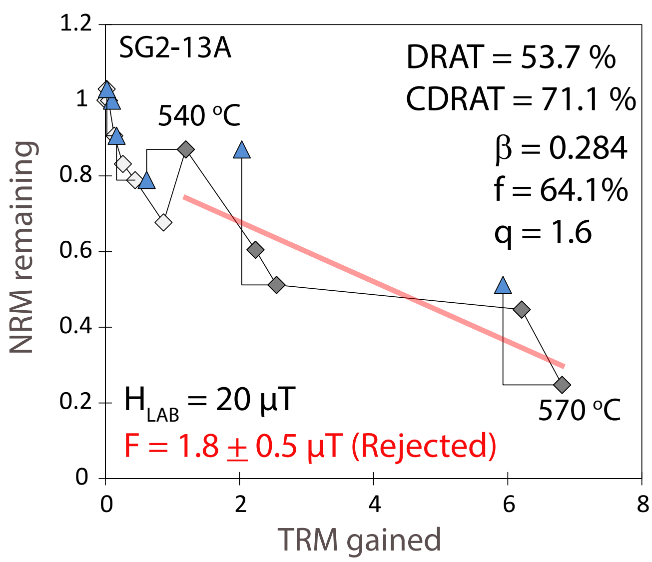

Supplementary Figure B1.6. Example Arai plot showing excessive 'zigzagging' in specimen SG2-13A; quantified by the β parameter.

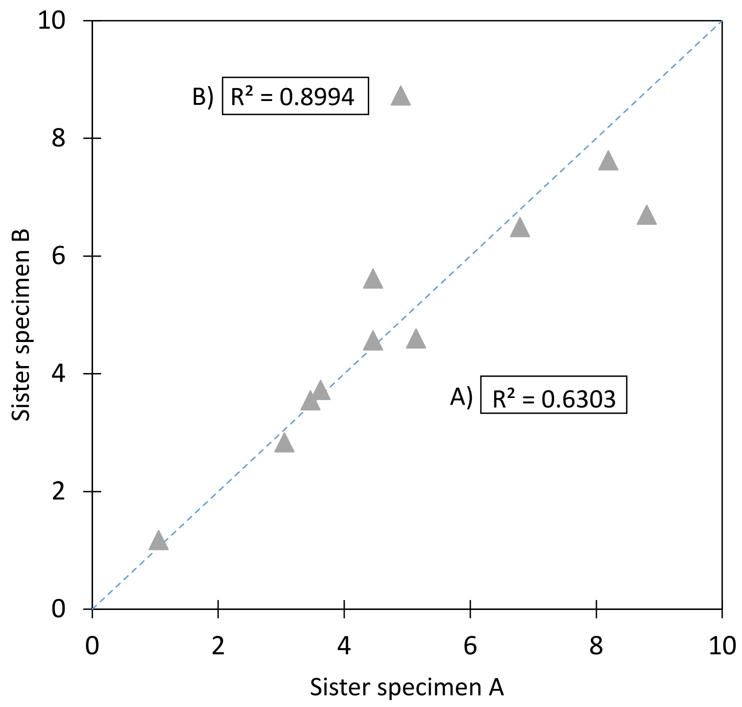

Supplementary Figure B1.7. Plot of direct sister specimen comparison from Shaw-DHT and Microwave methods. R^2 correlation A, full specimen correlation; R^2 correlation B, after removal of single adjacent outlier.

B2 Supplementary Tables

Supplementary Table B2.1: Specimen level Shaw-DHT results. D, declination; I, inclination; N, number of measurement steps used; H_L, lowest coercivity step used; fN, fraction of NRM used for the best-fit on an Arai diagram by vector difference sum; α, angular difference between the anchored and unanchored best-fit directions on the orthogonal diagram (alpha criteria); MAD, maximum angular deviation of the (free) best-fit to the directional data used in an orthogonal diagram; LTD, low-temperature demagnetisation; γ, gamma value; sA_1 and sA_2, slopesA_1 and A_2; sN, $slope_N$; rN, R^2 correlation coefficient for $slope_N$; sT, $slope_T$; rT, R^2 correlation of $slope_T$; F, field intensity estimate; Class, results classification based on the selection criteria used. Specimens with no data produced uninterpretable directions from the AF demagnetisation of the NRM and were removed from the experiment. Missing Dec and Inc information was determined to be unreliable. See Table 5.1 for further details of parameters listed.

Specimen	D (°)	I (°)	N	H_L (mT)	*f*N	α (°)	MAD (°)	LTD	γ	sA_1	sN	rN	sA_2	sT	rT	F (μT)	Class
BB5-1A	286.4	-16.6	9	25	*0.15*	9.1	13.9	-	-	0.35	0.10	*0.927*	0.81	0.912	0.999	-	-
BB5-1B	-	-	9	25	0.29	*22.9*	25.4	-	-	0.53	0.12	*0.691*	0.83	1.000	1.000	-	-
BG1-3A	-	-	8	30	0.21	13.5	11.0	-	-	0.58	0.35	*0.941*	0.76	*0.853*	0.995	-	-
BG2-1A	-	-	8	25	*0.13*	13.9	6.8	-	-	0.41	0.23	*0.980*	-	*0.003*	*0.754*	-	-
BP4-3B	268.0	-11.9	6	20	0.57	4.6	2.7	-	5.8	0.80	0.15	0.999	0.96	1.040	1.000	2.9	A
BP5-1B	-	-	-	-	-	-	-	-	-	-	-	-	-	-	-	-	-
BP6-1A	284.3	-1.8	6	25	0.26	0.3	0.5	-	6.4	0.31	0.44	0.995	0.91	1.029	0.999	8.8	A
BP6-2B	283.3	-9.9	6	20	0.53	0.4	0.4	Yes	3.8	0.67	0.36	0.995	0.98	*1.131*	0.999	-	-
BP9-6A	269.5	5.0	10	15	0.51	1.5	1.3	Yes	3.2	0.75	0.27	0.997	0.84	1.024	0.995	5.3	A
CA2-2B	no orientation		11	20	0.23	8.7	6.4	-	2.8	0.56	0.28	0.996	0.89	1.052	0.999	5.6	B
CA7-6A	no orientation		7	10	0.45	9.6	3.8	-	-	1.11	0.04	0.995	1.00	1.026	1.000	0.8	A
CG2-3A	-	-	5	25	0.41	*28.2*	3.3	-	-	0.67	0.20	*0.918*	0.92	0.945	0.999	-	-
CG2-3B	262.3	-3.4	5	25	0.53	*30.9*	3.9	Yes	-	0.71	0.22	*0.932*	0.93	0.940	1.000	-	-
GR21-3A	-	-	-	-	-	-	-	-	-	-	-	-	-	-	-	-	-
GR21-3B	-	-	-	-	-	-	-	-	-	-	-	-	-	-	-	-	-
GR3-7A	280.7	34.8	5	50	0.38	*22.7*	3.9	-	-	0.78	0.28	*0.946*	0.89	*0.853*	0.998	-	-
GR3-7B	279.3	10.7	5	50	0.45	5.1	3.8	Yes	9.0	0.67	0.41	*0.958*	0.65	*0.846*	0.994	-	-
GR4-4B	278.9	46.3	6	20	0.57	6.5	7.2	Yes	3.4	0.81	0.12	0.999	1.08	1.056	0.999	2.3	B
KL1-8-2A	262.8	-1.5	5	40	*0.17*	10.0	2.0	-	-	0.63	0.26	*0.984*	0.90	0.983	1.000	-	-
LG3-3A	242.5	20.3	5	30	0.35	2.4	2.7	Yes	3.0	0.49	0.25	*0.955*	0.96	1.027	0.999	-	-
LG4-4A	-	-	5	25	0.35	6.5	6.8	-	3.3	0.71	0.18	*0.978*	0.96	0.996	0.999	-	-
LG4-4B	-	-	5	25	0.45	6.6	7.2	-	3.0	0.68	0.19	*0.973*	0.93	0.955	0.999	-	-
NU1-5-2B	103.9	55.0	6	20	0.45	5.3	7.9	Yes	4.5	0.78	0.09	*0.978*	0.92	1.105	0.998	-	-
NU2-1-1B	-	-	5	20	0.42	2.1	1.3	-	2.6	0.74	0.22	0.993	0.96	1.015	0.999	4.4	A
PK8-2A	-	-	-	-	-	-	-	-	-	-	-	-	-	-	-	-	-
PK9-3A	-	-	-	-	-	-	-	-	-	-	-	-	-	-	-	-	-
PK9-3B	-	-	-	-	-	-	-	-	-	-	-	-	-	-	-	-	-
PW10-1A	294.1	18.9	6	50	0.37	13.6	3.5	Yes	3.2	1.32	0.15	0.999	0.68	0.926	1.000	3.1	B
PW10-1B	302.9	25.3	6	40	0.27	*21.8*	6.2	-	-	0.75	0.16	0.994	0.91	0.925	1.000	-	
PW2-1A	290.5	32.3	10	35	0.58	13.0	4.7	-	7.0	0.73	0.13	0.994	1.00	0.911	1.000	2.6	B
PW3-1B	-	-	6	20	*0.16*	14.8	10.2	Yes	-	0.70	0.05	*0.977*	0.73	1.101	0.999	-	
PW4-2B	286.0	21.2	6	50	0.37	14.8	6.5	-	1.6	0.72	0.18	0.990	0.93	1.012	1.000	3.5	A
PW6-3A	297.6	14.8	6	50	0.33	13.1	8.2	Yes	10.1	1.40	0.17	0.997	0.66	0.901	1.000	3.3	B
QA11-3A	-	-	-	-	-	-	-	-	-	-	-	-	-	-	-	-	-
QA12-2A	-	-	6	25	0.64	9.5	5.0	Yes	-	0.41	0.02	*0.982*	0.19	*0.837*	*???*	-	-
QA1-2A	-	-	-	-	-	-	-	-	-	-	-	-	-	-	-	-	-
QA1-2B	-	-	-	-	-	-	-	-	-	-	-	-	-	-	-	-	-
QA2-1A	295.3	12.6	6	20	*0.19*	2.6	2.1	-	-	0.37	0.22	*0.990*	0.70	0.931	1.000	-	-
QA4-1B	295.7	17.6	7	25	0.20	4.4	4.4	-	3.0	0.27	0.44	0.995	0.88	0.946	1.000	8.7	B
QA4-3A	295.0	17.2	8	30	0.20	1.5	6.6	-	4.0	0.14	0.41	0.991	0.91	0.952	1.000	8.2	B
QA4-3B	305.4	30.2	10	10	0.66	6.2	2.9	Yes	3.0	0.60	0.38	0.999	0.71	0.910	0.997	7.6	B
SG2-1-3B	-	-	-	-	-	-	-	-	-	-	-	-	-	-	-	-	-
SG2-2-1B	111.6	-15.6	5	10	0.91	4.5	2.5	Yes	2.6	0.86	0.05	0.997	0.99	*1.124*	0.998	-	-
SG2-2-6B	124.1	-14.4	5	10	0.98	6.8	6.2	Yes	2.6	0.86	0.05	0.998	0.99	*1.123*	0.999	-	-
SG2-3-4A	125.0	-14.2	*4*	20	0.41	6.5	6.0	Yes	-	0.86	0.02	*0.963*	0.94	1.064	1.000	-	-
SG2-4-1A	105.5	-21.7	7	10	0.86	1.3	3.9	-	8.5	0.90	0.05	0.993	0.98	1.037	1.000	1.1	A
SG2-4-1B	106.7	-22.8	7	10	0.98	2.4	2.8	Yes	5.4	0.83	0.06	0.997	0.96	1.035	1.000	1.2	A
SG3-4-1A	70.3	48.2	5	25	0.37	6.1	2.8	-	2.9	0.61	0.14	0.990	1.02	0.957	0.993	2.7	A
SG3-4-1B	67.2	57.6	7	10	0.56	11.4	3.5	Yes	-	1.21	0.08	*0.975*	1.26	0.927	0.983	-	-
SG3-5-3A	85.9	61.3	7	15	0.30	4.0	4.6	-	2.7	0.44	0.15	0.997	0.91	1.060	0.996	3.1	B
SG3-5-3B	77.6	57.5	6	20	0.51	1.1	2.1	Yes	2.2	0.43	0.14	0.997	0.96	0.955	0.999	2.8	A
SG3-6-1A	66.4	63.1	6	20	0.44	4.2	2.5	-	-	0.57	0.08	*0.930*	1.02	0.995	0.996	-	-
TB3-1B	293.8	25.6	5	25	*0.06*	3.6	3.0	-	-	0.70	0.11	0.997	0.83	0.970	0.998	-	-
TB7-1A	290.7	24.4	8	35	*0.12*	1.3	1.6	-	-	0.38	0.46	0.995	0.82	1.053	1.000	-	-
TB7-1B	287.0	23.1	11	20	0.32	0.7	1.9	-	4.9	0.56	0.36	0.992	0.82	0.994	0.998	7.2	A
TB7-4B	295.4	33.2	8	10	0.47	0.3	1.5	-	1.4	0.78	0.50	0.997	0.98	0.971	1.000	9.9	A
TB9-8-10A	no orientation		8	15	0.48	7.0	1.6	Yes	3.3	0.80	0.34	0.996	0.87	1.027	0.999	6.8	A
TB9-8-10B	no orientation		7	15	0.28	5.8	2.4	-	3.6	0.81	0.32	0.999	0.94	1.064	0.999	6.5	B
TB9-8-13B	no orientation		9	15	0.37	5.4	2.9	Yes	2.3	0.74	0.35	0.998	0.88	0.981	0.998	7.0	A

Supplementary Table B2.2. Specimen-level thermal Thellier results. γ, gamma value; AF, 5 mT cleanse before each measurement step; T_L, lowest temperature used; T_H, highest temperature used; H_{LAB}, laboratory bias field used; N, number of measurement steps used; k', curvature of the Arai slope; β, relative scatter around the best-fit line; FRAC, fraction of NRM used; g, gap factor; q, quality factor; delCK, maximum absolute difference produced by a pTRM check normalized by total TRM; MAD, maximum angular deviation of the best-fit to the directional data used in an orthogonal diagram; DRAT, maximum absolute difference produced by a pTRM check, normalized by the length of the line; CDRAT, Cumulative DRAT; α, angular difference between the anchored and unanchored best-fit directions on the orthogonal diagram. For a more detailed description of parameters, see Table 5.1 and Standard paleointensity definitions v1.1 (Paterson et al., 2014). Specimens with no results were uninterpretable.

Sample	γ (°)	AF (mT)	T_L (°C)	T_H (°C)	H_{LAB} (μT)	N	k'	β	*FRAC*	g	q	delCK (%)	DRAT (%)	CDRAT (%)	α (°)	MAD (°)	F (μT)	Class
BG1-3B	-	5	300	540	5	6	-	0.087	0.59	0.56	6.1	*30.4*	*30.7*	*31.4*	1.3	4.1	-	-
BG1-4B	2.3	5	400	550	5	6	0.10	0.073	0.55	0.67	7.7	13.0	14.7	11.8	4.6	4.0	1.6	B
BG2-3B	-	5	500	560	5	5	-	0.078	*0.32*	0.67	5.7	*30.4*	*45.3*	*62.5*	*22.8*	-	-	-
BP4-3A	-	5	500	560	5	5	-	0.070	0.57	0.71	8.7	17.1	*18.0*	*21.5*	4.0	4.6	-	-
BP5-1A	5.6	5	500	565	5	6	0.34	0.091	0.36	0.72	6.7	7.1	8.1	8.0	9.9	9.6	1.0	A
BP6-2A	-	5	540	570	5	5	-	0.089	0.55	0.68	6.3	*21.4*	*20.2*	*23.8*	1.9	5.1	-	-
BP7-1B	0.7	5	450	565	5	7	0.17	0.073	0.55	0.75	7.1	9.0	8.1	14.4	2.2	4.1	6.2	A
BP8-3A	3.8	5	400	570	5	9	0.01	0.029	0.70	0.84	25.6	10.1	6.3	17.4	2.8	2.6	7.4	A
BP9-6B	-	-	-	-	-	-	-	-	-	-	-	-	-	-	-	-	-	-
CA1-1A	-	5	540	570	5	5	-	0.100	0.32	0.66	4.1	14.8	*23.7*	17.5	3.8	4.1	-	-
CA1-1B	-	5	500	570	5	7	-	0.098	0.41	0.73	4.0	8.3	*15.4*	7.3	*23.3*	8.7	-	-
CA7-6B	-	-	-	-	-	-	-	-	-	-	-	-	-	-	-	-	-	-
CG2-11A	-	-	-	-	-	-	-	-	-	-	-	-	-	-	-	-	-	-
CG2-5B1	-	-	-	-	-	-	-	-	-	-	-	-	-	-	-	-	-	-
CG2-6C1	-	-	-	-	-	-	-	-	-	-	-	-	-	-	-	-	-	-
CG2-7C1	-	-	-	-	-	-	-	-	-	-	-	-	-	-	-	-	-	-
CG2-8C2	-	-	-	-	-	-	-	-	-	-	-	-	-	-	-	-	-	-
CG2-9B2	-	-	-	-	-	-	-	-	-	-	-	-	-	-	-	-	-	-
NU2-72B	-	-	-	-	-	-	-	-	-	-	-	-	-	-	-	-	-	-
PW3-1A	-	5	450	550	5	5	-	*0.222*	*0.15*	0.50	1.7	*45.7*	*61.2*	*105.3*	5.1	*15.0*	-	-
PW5-2A	-	5	500	550	5	4	-	*0.193*	*0.20*	0.58	2.4	6.3	8.0	-2.9	12.4	9.6	-	-
PW5-2B	-	5	400	550	5	6	-	*0.172*	*0.24*	0.66	2.9	2.0	2.7	2.5	*20.6*	8.4	-	-
PW6-3B	-	5	400	550	5	6	-	*0.158*	*0.22*	0.66	2.5	6.1	9.8	-10.3	14.8	5.6	-	-
PW8-3A	-	-	-	-	-	-	-	-	-	-	-	-	-	-	-	-	-	-
QA1-3B	-	5	500	570	5	7	-	0.093	*0.34*	0.81	4.8	*26.3*	*44.4*	*62.3*	2.7	4.3	-	-
QA2-1B	-	-	-	-	-	-	-	-	-	-	-	-	-	-	-	-	-	-
QA3-1A	-	5	500	560	5	5	-	0.071	0.52	0.72	7.3	*27.4*	*24.1*	*23.7*	4.0	4.2	-	-
QA3-1B	1.1	5	500	570	5	7	0.21	0.080	0.60	0.77	7.9	16.2	11.6	-12.6	2.3	2.9	6.8	A
SG2-1-3A	-	5	540	570	5	5	-	*0.284*	0.36	0.71	1.6	*34.6*	*53.7*	*71.1*	*40.3*	*19.5*	-	-
SG2-2-1A	-	5	540	570	5	5	-	*0.240*	0.35	0.74	1.7	*24.0*	*42.2*	*57.1*	*38.4*	*16.2*	-	-
SG2-26A	-		-	-	-	-	-	-	-	-	-	-	-	-	-	-	-	-
SG2-3-1A	-	5	540	565	5	4	-	*0.462*	*0.14*	0.64	*0.6*	6.3	13.3	8.7	*17.9*	5.2	-	-
SG2-3-1B	-	5	540	565	5	4	-	*0.460*	*0.08*	0.65	*0.4*	4.8	*15.7*	*29.5*	10.8	3.7	-	-
SG2-42B	-	-	-	-	-	-	-	-	-	-	-	-	-	-	-	-	-	-
SG3-3-3B	-	-	-	-	-	-	-	-	-	-	-	-	-	-	-	-	-	-
TB3-1A	-	-	-	-	-	-	-	-	-	-	-	-	-	-	-	-	-	-

Supplementary Table B2.3. Specimen-level Microwave results. P_L, lowest power used; P_H, highest power used. See Supplementary Table B2.1 for description of all other parameters.

Sample	γ (°)	P_L (W.s)	P_H (W.s)	H_{LAB} (μT)	N	k'	β	*FRAC*	g	q	delCK (%)	DRAT (%)	CDRAT (%)	α (°)	MAD (°)	F (μT)	Class
BP6-1B3	7.4	120	185	10	5	0.23	0.04	0.53	0.604	10	8.2	10.3	11.6	13.5	9.3	6.7	A
BR1-3A	2.4	97	200	30	6	0.06	0.038	0.37	0.74	11.52	7.8	12.9	19.6	6.3	3.6	5.1	A
BR1-3B	4.5	148	373	8	11	0.35	0.056	0.35	0.86	9.10	10.2	14.8	-7.1	1.2	1.3	4.6	A
CA2-2A	1.4	82	195	10	9	0.42	0.067	0.35	0.79	8.95	6.5	7.9	-9.0	5.8	4.0	4.5	A
CA2-2A2	3.2	81	194	5	8	0.16	0.044	0.35	0.77	13.64	5.8	5.5	-4.4	1.8	3.9	4.6	A
GR11-4B	-	55	105	10	4	-	*0.163*	0.45	0.63	2.80	*33.1*	*38.9*	*38.6*	3.1	3.4	-	-
GR4-2A1	-	86	135	10	4	-	*0.222*	*0.28*	0.55	0.88	2.6	6.8	7.4	13.9	3.4	-	-
LG4-3A	-	95	133	10	4	-	*0.214*	*0.08*	0.63	0.61	1.3	4.9	-2.7	*16.4*	2.4	-	-
LG4-3A2	-	82	185	10	8	-	0.057	*0.34*	0.68	5.42	10.7	*22.1*	*47.6*	*48.3*	*12.2*	-	-
PK8-1A1	-	82	124	10	4	-	*0.222*	*0.23*	0.61	1.51	4.8	7.0	-2.3	4.1	1.5	-	-
PW2-1B1		90	173	10	6	-	0.062	*0.31*	0.79	7.82	4.1	5.1	-7.4	5.9	4.0	-	-
PW2-1B2	-	96	158	10	5	-	*0.184*	*0.22*	0.64	1.07	3.0	7.0	-8.8	*29.7*	6.2	-	-
PW2-1B3	-	91	165	10	6	-	*0.117*	*0.22*	0.71	2.03	4.9	12.9	14.5	8.8	4.5	-	-
PW2-1B4	-	100	175	10	6	-	0.042	*0.25*	0.71	8.79	6.1	9.1	-4.1	*15.4*	6.4	-	-
QA4-1A	-	77	138	10	5	-	*0.101*	*0.22*	0.72	4.17	10.2	*15.9*	*28.4*	*33.0*	*16.4*	-	-
QA4-1A2	1.2	96	162	10	6	0.14	0.037	0.23	0.74	8.20	4.3	9.3	-3.2	6.2	2.7	4.9	B
QA4-1A3	-	112	154	10	4	-	*0.143*	*0.16*	0.53	1.41	5.6	13.5	-5.5	6.6	3.2	-	-
QA4-1A4	-	91	135	10	4	-	0.047	*0.25*	0.65	5.70	4.0	6.6	0.7	*21.2*	6.3	-	-
SG2-4-2A1	5.4	103	181	10	6	0.43	0.088	0.37	0.75	5.06	3.0	4.7	-0.5	1.7	2.0	3.6	A
SG2-4-2A2	8.4	78	186	10	9	0.45	0.082	0.39	0.86	5.95	2.6	4.3	3.0	5.5	2.2	3.7	A
SG3-5-6B1	-	78	152	10	6	-	*0.111*	0.36	0.75	4.79	5.7	4.0	-2.3	5.7	3.6	-	-
SG3-5-6B2	-	104	141	10	4	-	*0.155*	*0.26*	0.57	2.20	7.8	12.5	14.3	*21.7*	*22.2*	-	-
SG3-5-6B3	-	85	149	10	5	-	0.072	*0.26*	0.56	2.86	15.6	*24.5*	*46.9*	*16.1*	4.9	-	-
TB9-5A2	1	65	169	10	6	0.27	0.074	0.36	0.62	6.34	1.6	2.0	-0.1	3.2	6.0	3.5	A
TB9-5A3	2.9	55	118	10	5	0.19	0.046	0.40	0.62	10.67	10.7	12.7	7.7	8.3	5.9	3.5	A
TB9-85A	-	100	290	10	8	-	0.098	*0.20*	0.77	2.61	6.6	*17.9*	-11.1	*16.0*	3.9	-	-

Supplementary Table B2.4. Data used to determine the VGP scatter. Dec, declination; Inc, inclination; Ndir, number used for direction; kdir, k statistic; Slat, site latitude; Slon, site longitude; Plat, unrotated VGP palaeolatitude; Plon, unrotated VGP palaelongitude; PlatR, rotated VGP palaeolatitude; PlonR, rotated VGP palaeolongitude. DecR, declination recalculated from pole rotations for Canada and Greenland (see Supplementary text B3). Slat, Slon, Plat and Plon taken from Denyszyn et al., 2009. Plat and Plon for sies SG2 and NU1 are antipoles.

Site	Dec (°)	Inc (°)	Ndir	kdir	Slat (°N)	Slon (°W)	Plat (°N)	Plon (°E)	PlatR (°N)	PlonR (°E)	DecR (°)
BB	286.0	-18.0	9	91	75.72	82.99	-5.1	169.3	0.5	150.3	306.0
GR	272.9	23.3	8	190	76.43	83.02	12.5	187.1	18.6	167.9	292.8
BG	271.3	34.5	7	24	75.60	80.20	18.7	193.4	24.9	174.3	291.3
BP	279.2	-7.5	9	57	75.77	81.32	-1.4	178.8	4.6	159.7	299.2
BR	282.6	–7.5	7	226	75.47	81.55	-0.5	175.3	5.3	156.2	302.6
EG	280.1	24.8	7	134	75.82	82.07	15.1	181.4	21.1	161.9	300.1
LG	243.1	13.7	7	91	78.73	75.68	1.8	222.0	7.2	203.2	262.7
CG	251.9	1.8	7	46	78.29	77.11	-2.7	210.8	3.2	191.8	271.7
CM	282.5	1.7	7	55	74.63	80.47	4.2	177.7	10.1	158.4	302.5
EA	273.4	31.5	11	79	75.82	82.08	17.3	188.9	23.4	169.7	293.3
HM	244.2	-4.7	4	240	74.64	80.21	-8.9	214.2	-3.1	194.9	264.3
SG2 (R)	101.2	-26.4	6	103	75.70	84.00	16.3	178.6	22.2	159.0	301.3
KL	283.0	10.9	8	74	78.68	70.67	7.9	187.6	12.5	175.3	295.9
TB	296.5	26.4	9	37	76.46	69.24	19.6	178.0	24.5	166.0	308.8
NU2	289.3	16.3	8	123	77.38	71.48	12.3	181.4	17.1	169.2	302.0
PK	288.7	-18.5	7	132	77.94	72.21	-5.5	177.6	-0.5	164.8	302.3
KC	290.6	15.7	4	327	77.57	70.26	12.2	181.2	17.0	169.0	303.3
PW	293.6	15.9	7	144	77.20	70.84	13.0	177.8	17.9	165.5	306.3
QA	298.8	26.1	6	106	77.49	68.87	19.5	175.7	24.5	163.6	311.2
KA	307.8	-1.6	2	435	77.21	70.78	7.0	162.0	12.3	149.3	321.0
CA	295.4	9.3	5	234	76.74	73.22	10.2	173.0	15.3	160.6	308.3
GF	295.6	17.3	6	68	76.86	69.93	14.4	177.0	19.4	164.8	308.2
NU1 (R)	108.8	37.7	8	59	77.41	71.56	-16.6	175.6	-16.6	175.6	288.8

Supplementary Table B2.5. Potentially rejected specimens due to application of stricter selection criteria and their effect on the site mean. These original results would be rejected as a consequence of applying a stricter DRAT and CDRAT minima of 13 % and 15 % respectively to thermal Thellier and Microwave data, and a slightly stricter $slope_T$ of 1 ± 0.6 in Shaw-DHT data. The effect of removing these results is negligible. TH, Thellier, MW, Microwave, SH, Shaw-DHT; $CRIT_{REJECT}$, reason for rejection; B_{ANC}, palaeointensity result.

Sample	Method	$CRIT_{REJECT}$	B_{ANC} (μT)	Effect on site mean
BG1-4B	TH	DRAT	1.6	no VDM determined for this site
BP8-3A	TH	CDRAT	7.4	decreases from 5.5 μT to 5.2 μT
BR1-3A	MW	CDRAT	5.1	no VDM determined for this site
BR1-3B	MW	DRAT	4.6	no VDM determined for this site
PW10-1A	SH	$slope_T$	3.1	no notable effect - site mean 3.1 μT
PW2-1A	SH	$slope_T$	2.6	no notable effect - site mean 3.1 μT
PW6-3A	SH	$slope_T$	3.3	no notable effect - site mean 3.1 μT
QA4-3B	SH	$slope_T$	7.6	decreases from 8.1 μT to 7.2 μT

Supplementary Table B2.6. Q_{PI} breakdown per site.

Site	AGE	STAT	TRM	ALT	MD	ACN	TECH	LITH	MAG	DIR	Q_{PI}
BG	1	0	0	1	1	1	0	0	1	0	5
BP	1	0	1	1	1	1	1	0	1	1	8
BR	1	0	0	1	1	1	0	0	1	1	6
CA	1	0	0	1	1	1	1	0	1	0	6
GR	1	0	0	1	1	1	0	0	1	1	6
NU2	1	0	0	1	1	1	0	0	1	1	6
PW	1	0	0	1	1	1	0	0	1	1	6
QA	1	1	1	1	1	1	1	0	1	1	9
SG2	1	0	0	1	1	1	1	0	1	0	6
SG3	1	0	0	1	1	1	0	0	1	0	5
TB	1	0	0	1	1	1	1	0	1	0	6

B3 Supplementary Text

Canada and Greenland data were combined by rotating the Ellesmere microplate 20 ° counterclockwise about an Euler pole of 72 °N, 274 °E and Greenland by 14 ° counter clockwise about a pole of 67.5 °N, 118.48 °W (Denyszyn et al., 2009). An analysis of virtual geomagnetic pole (VGP) dispersion, corrected for within-site scatter (Mcfadden, 1991), used a Vandamme (1994) cut-off (25 °) to produce an angular dispersion (SB) of 11.6 ° with 95 % lower and upper confidence bounds (calculated using 10,000 bootstraps) of 8.6 ° and 14.4 ° respectively. This VGP dispersion is normal compared to Phanerozoic rocks from similar inferred paleolatitudes of ~5 °N (Cromwell et al., 2018; Doubrovine et al., 2019). Data used to determine the VGP scatter is found in Supplementary Table B2.4.

B4 References cited

Cromwell, G., Johnson, C.L., Tauxe, L., Constable, C.G., and Jarboe, N.A., 2018, PSV10: A Global Data Set for 0–10 Ma Time-Averaged Field and Paleosecular Variation Studies: Geochemistry, Geophysics, Geosystems, v. 19, p. 1533–1558, doi:10.1002/2017GC007318.

Denyszyn, S.W., Halls, H.C., Davis, D.W., and Evans, D.A.D., 2009, Paleomagnetism and U-Pb geochronology of Franklin dykes in high arctic Canada and Greenland: A revised age and paleomagnetic pole constraining block rotations in the Nares Strait region: Canadian Journal of Earth Sciences, v. 46, p. 689–705, doi:10.1139/E09-042.

Doubrovine, P. V., Veikkolainen, T., Pesonen, L.J., Piispa, E., Ots, S., Smirnov, A. V., Kulakov, E. V., and Biggin, A.J., 2019, Latitude Dependence of Geomagnetic Paleosecular Variation and its Relation to the Frequency of Magnetic Reversals: Observations From the Cretaceous and Jurassic: Geochemistry, Geophysics, Geosystems, v. 20, p. 1240–1279, doi:10.1029/2018GC007863.

Mcfadden, P.L., 1991, Reversals of the Earth ' s Magnetic Field and Temporal Variations of the Dynamo Families: Journal of Geophysical Research: Solid Earth, v. 96, p. 3923–3933.

Paterson, G. A., Tauxe, L., Biggin, A. J., Shaar, R., & Jonestrask, L. C. (2014). Standard Paleointensity Definitions v1.1, 0–43. Retrieved from http://www.paleomag.net/SPD/spdweb.html

Appendix C

Supplementary Material for Chapter 3

The data provided in Appendix C supplements Chapter 5. Raw measurement data is available on the MagIC database under:

S. Lloyd, A. Biggin, Zheng-Xiang Li (2021); New paleointensity data suggest possible Phanerozoic-type geomagnetic variations in the Precambrian; Magic Information Consortium (MagIC), doi: 10.7288/V4/MAGIC/17452

C1 Supplementary Figures

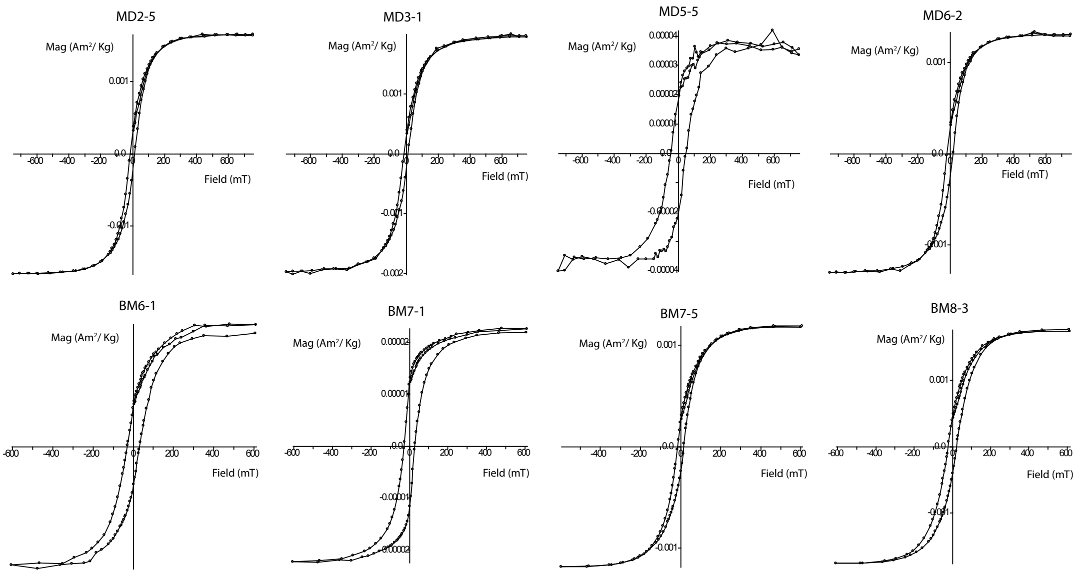

Supplementary Figure C1.1. A selection of hysteresis loops from Mundine Wells dykes (top row) and Bangemall Sills (bottom row). All with paramagnetic component removed.

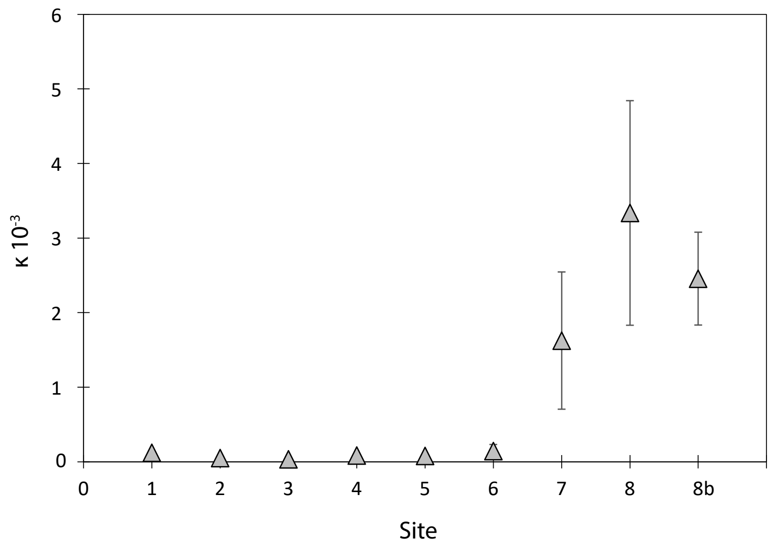

Supplementary Figure C1.2. Mean bulk susceptibility and standard deviation for Bangemall Sills. ~35 samples per site measured. Site 8b is the baked contact for site 8.

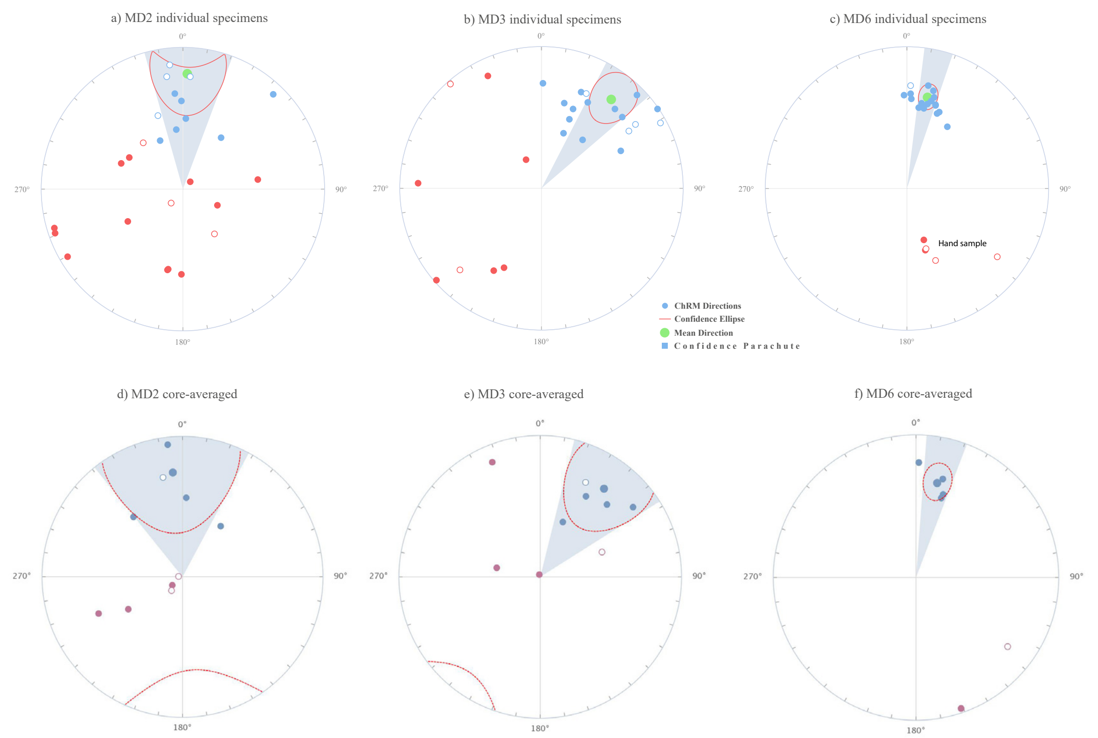

Supplementary Figure C1.3. ChRM directions for sites MD2, MD3 and MD6. a – c) Individual specimen-level directions. d – f) Directions averaged by core. All figures have had a 45 ° cut off applied; directions outside this are shown in red.

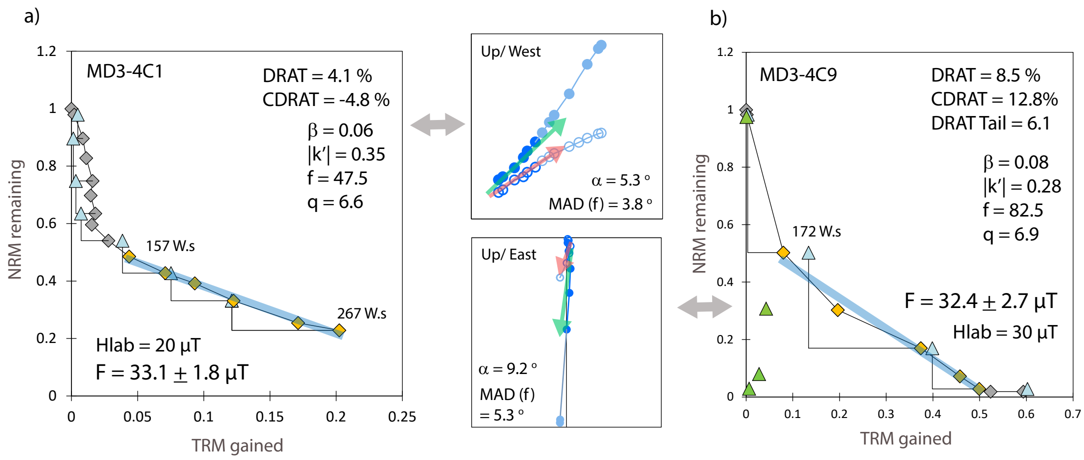

Supplementary Figure C1.4. Additional Microwave Arai diagrams from site MD3. a) Two-slope behavior b) Thellier-Coe experiment showing DRAT$_{TAILS}$.

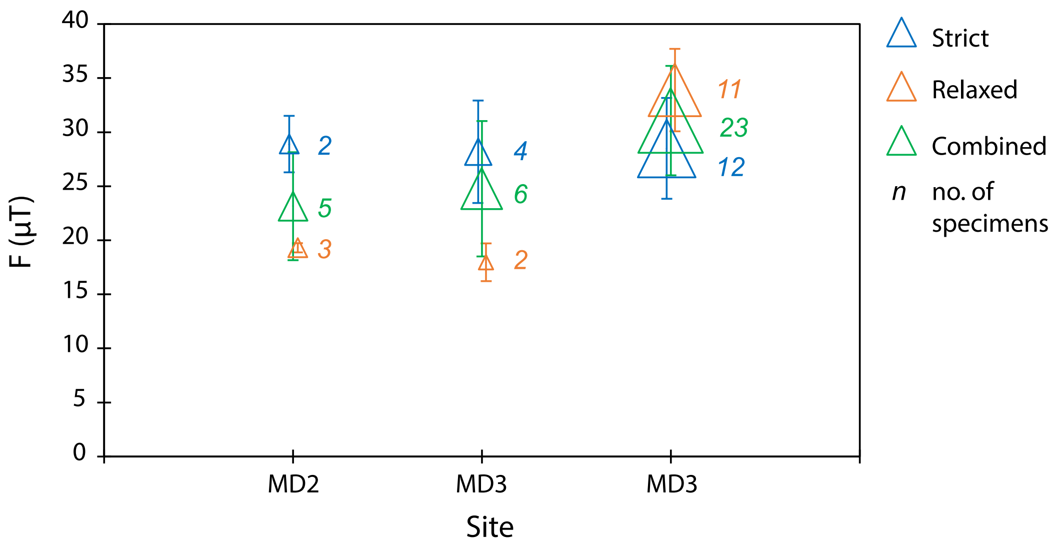

Supplementary Figure C1.5 Comparison of site-mean using strict and relaxed selection criteria. Blue triangles, site-mean palaeointensity results obtained from the strict selection criteria (Tables 5.1, 5.2 & 5.3); Orange triangles, mean palaeointensity results using only the additional specimens that would pass the relaxed selection criteria (Supplementary Tables C2.1, C2.2 & C2.8); Green triangles, combined site-mean results from all data that passes the relaxed selection criteria. The size of the data points is a qualitative representation of the number of data used to calculate the mean, with the number of specimens also listed.

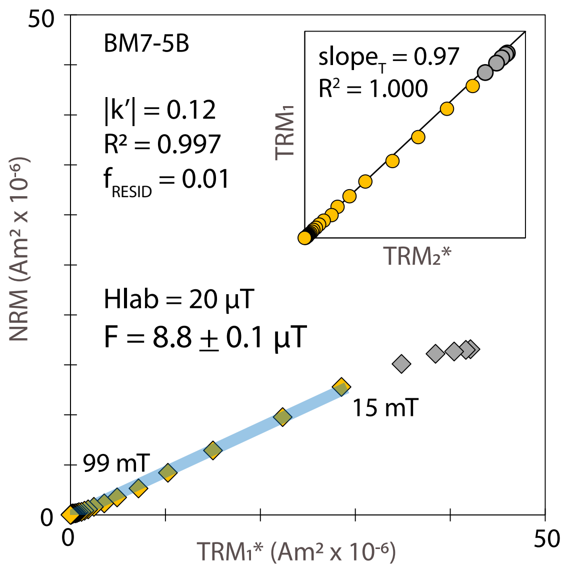

Supplementary Figure C1.6. Typical Shaw-DHT diagram from site BM7. For description of items in this figure, refer to Figure 5.4.

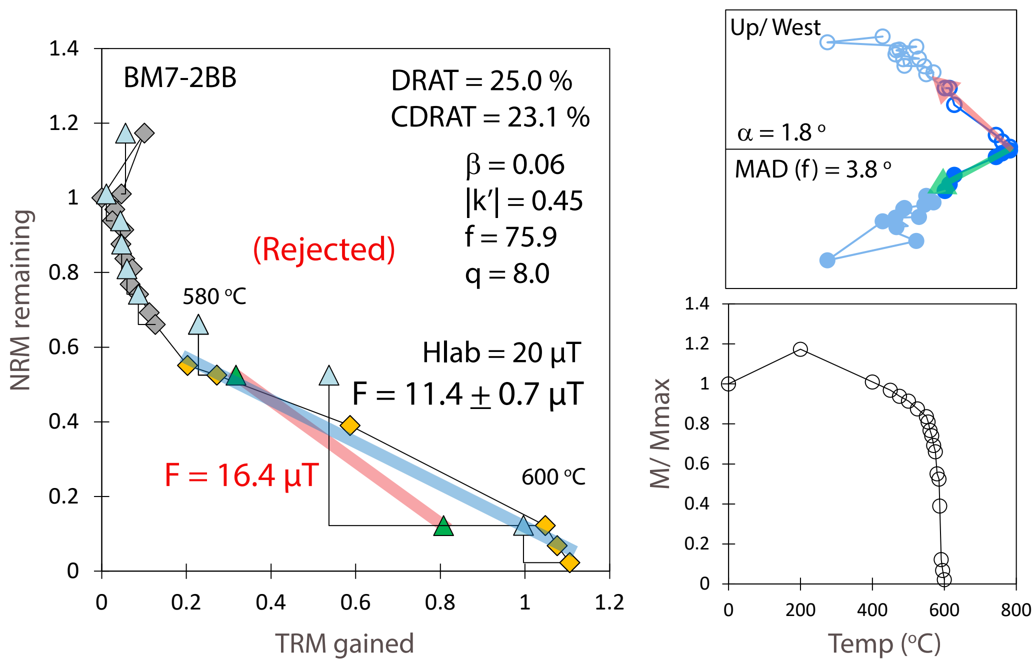

Supplementary Figure C1.7. Thermal Thellier Arai, demagnetization spectra and orthogonal diagram for specimen BM7-5A2. The result from this specimen is rejected (black) and for qualitative analysis, a result corrected according to Valet et al. (1996) is also shown (red). The thermal demagnetization is characteristic of primary, type-A magnetisation.

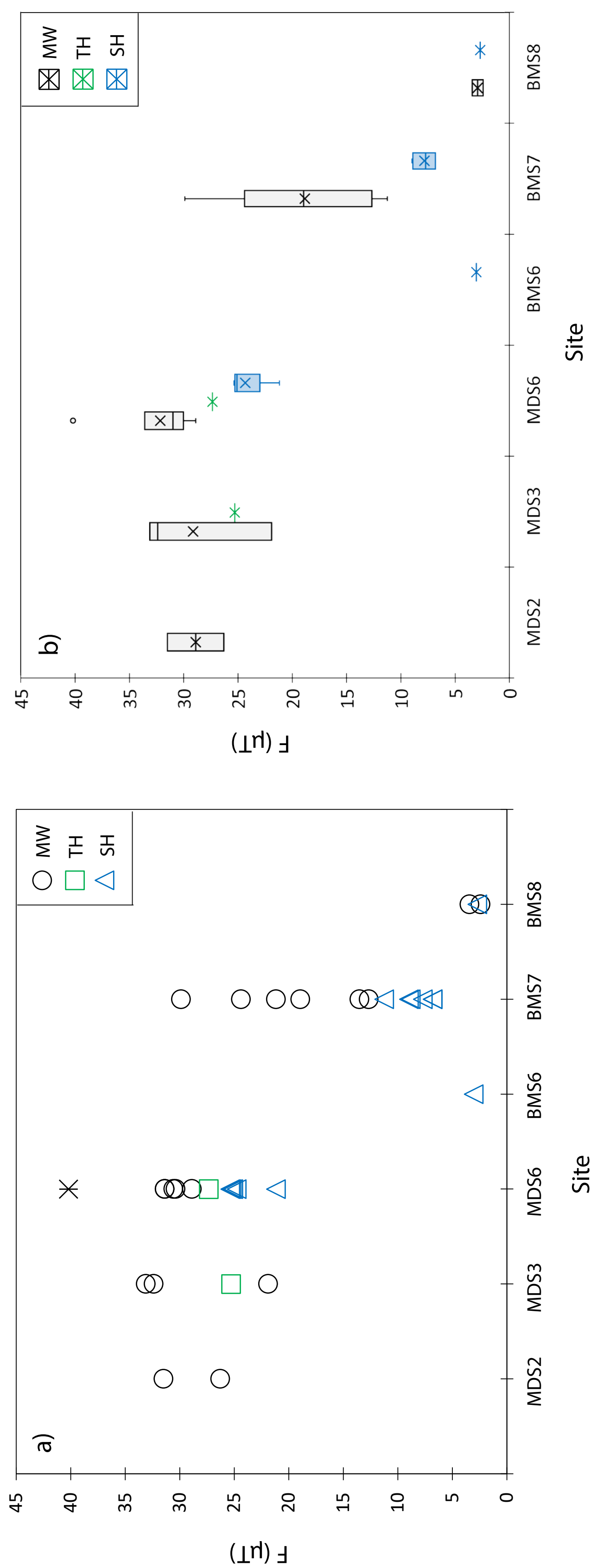

Supplementary Figure 5.8. All specimen-level palaeointensity results plotted according to site and method (a) and represented in a box and whisker plot (b).

C2 Supplementary Tables

Supplementary Table C2.1. Specimen-level thermal Thellier results for Mundine Wells dykes. See Supplementary Table B2.2 (appendix B) for description of parameters. Additional parameters: f, fraction of NRM used for the best-fit on an Arai diagram by vector difference sum; B_{ANC}, palaeointensity estimate; StdErr, standard error. Temperatures from experiment 1 (those treated with AF 5 mT) have been adjusted by 9% after oven calibration. It only affects one specimen. Results in italics are rejected but retained in the table for comparison using a relaxed set of selection criteria.

Sample	AF (mT)	H_{LAB} (μT)	T_L (°C)	T_H (°C)	N	β	|k'|	*FRAC* (%)	*f* (%)	g	q	DRAT (%)	CDRAT (%)	α (°)	MAD_a (°)	B_{ANC} (μT)	StdErr (μT)
2.10B	5	20	556	580	7	*0.29*	-	*9.6*	*25.9*	-	0.5	*107.5*	*-73.6*	0.0	3.2	-	-
2.12C	5	20	556	577	6	*0.31*	-	*8.5*	*27.5*	-	0.6	*22.8*	*29.3*	0.0	2.2	-	-
2.12D	10	20	585	590	*2*	-	-	-	-	-	-	-	-	-	-	-	-
2.1A	5	20	560	564	*2*	-	-	-	-	-	-	-	-	-	-	-	-
2.3C	10	20	555	590	8	0.08	-	*2.4*	40.0	-	4.4	*26.0*	*27.5*	10.4	3.0	-	-
2.8A	10	20	585	590	*2*	-	-	-	-	-	-	-	-	-	-	-	-
2.8D	10	20	585	590	*2*	-	-	-	-	-	-	-	-	-	-	-	-
2.8E	5	20	572	577	*2*	-	-	-	-	-	-	-	-	-	-	-	-
3.1B	5	20	564	588	6	0.06	-	*8.9*	49.2	-	4.8	*34.2*	*-37.6*	0.0	2.6	-	-
3.1D	10	20	570	590	5	0.09	*0.53*	*18.9*	37.2	-	2.9	*19.3*	10.3	*17.0*	4.9	-	-
3.3C	10	20	550	575	7	*0.14*	-	*34.4*	37.4	-	2.1	*16.2*	*30.8*	*22.1*	5.0	-	-
3.4B	5	20	564	577	4	*0.24*	-	*7.4*	*21.7*	-	0.4	*55.5*	*-30.9*	0.0	3.8	-	-
3.5B	10	20	550	580	7	*0.16*	-	37.3	41.9	-	2.0	*18.3*	*33.0*	*23.8*	5.9	-	-
3.5C	10	20	530	580	9	*0.13*	*0.63*	44.6	58.1	-	3.7	10.7	7.6	*17.6*	5.6	-	-
3.5D	5	20	550	572	7	*0.17*		*10.2*	*22.4*	-	1.1	*47.8*	*51.2*	0.0	3.9	-	-
3.6C	10	20	570	590	5	0.07	0.13	*19.2*	70.5	*1.4*	7.1	10.8	-1.9	2.5	3.9	25.3	1.8
3.6E	10	20	580	590	*3*	0.06	-	*13.1*	39.3	-	3.1	*22.2*	*-19.5*	4.8	3.3	-	-
3.9C	5	20	560	577	5	0.35	-	*4.7*	*29.6*	-	0.5	*167.4*	*-189.9*	0.0	2.5	-	-
4.7D	5	20	543	572	9	*0.17*	-	*17.5*	87.5	-	4.0	*17.5*	12.6	0.5	4.4	-	-
6.1C	5	20	556	580	7	0.03	0.00	37.2	78.5	*2.1*	20.2	10.2	3.6	0.0	2.9	27.3	0.8
6.2E	10	20	560	590	7	*0.12*	*0.43*	51.5	83.2	-	5.3	*18.4*	*24.1*	1.2	1.9	*26.2*	*3.2*
6.3A	10	20	550	590	9	0.08	0.24	79.4	89.2	-	9.6	11.8	*15.4*	0.7	2.3	*35.5*	*2.7*
6.3D	5	20	556	580	7	0.05	-	*32.0*	72.7	-	11.9	*16.6*	*45.6*	0.0	3.4	-	-
6.3E	10	20	550	590	9	0.07	-	49.8	90.8	-	11.1	9.9	*27.4*	1.5	3.7	-	-
6.5B	10	20	530	590	11	0.07	*0.49*	74.4	88.9	-	8.8	*15.1*	9.2	0.6	2.7	*37.7*	*2.8*
6.5E	5	20	535	580	13	0.03	0.02	41.6	90.8	-	25.2	*13.7*	*23.7*	0.3	2.4	*37.7*	*1.1*
7.3B	5	20	524	550	9	0.07	-	*1.3*	37.7	-	4.7	*250.0*	*-645.8*	*16.2*	4.9	-	-
7.7E	5	20	511	550	11	0.10	-	*6.7*	63.5	-	5.4	*86.1*	*22.8*	11.5	4.5	-	-
8.1D	5	20	479	524	5	0.08	-	*6.7*	36.8	-	3.3	*44.6*	*-103.1*	13.4	3.8	-	-
8.5C	5	20	527	546	7	0.07	-	*5.6*	61.4	-	6.8	*59.0*	*-64.0*	4.0	2.9	-	-

*Supplementary Table C2.2. Specimen-level Microwave results for Mundine Wells dykes. See Supplementary Table B2.2 (appendix B) and Supplementary Table C2.1 for description of parameters. P_L, lowest power used; P_H, highest power; -, specimens were either too strongly magnetised for the Microwave system or the Arai-diagram was uninterpretable; italics, rejected specimen used in the comparison of selection criteria; *, Coe experiment; #, lower accepted selection criterion.*

Sample	P_L (W.s)	P_H (W.s)	Hlab (μT)	N	β	|k'|	*FRAC* (%)	*f* (%)	g	q	DRAT (%)	CDRAT (%)	α (°)	MAD_a (°)	B_{ANC} (μT)	StdErr (μT)
2-11E1	-	-	-	-	-	-	-	-	-	-	-	-	-	-	-	-
2-11E2	-	-	-	-	-	-	-	-	-	-	-	-	-	-	-	-
2-11E3	-	-	-	-	-	-	-	-	-	-	-	-	-	-	-	-
2-12B1	55	109	30	*3*	0.07	-	51.8	79.4	-	4.9	10.6	10.8	3.4	3.8	-	-
2-12B2	58	103	25	4	0.04	0.10	36.0	53.0	*7.0*	6.5	0.2	-0.9	6.5	2.3	26.3	1.1
2-12B3	85	140	30	5	0.02	0.01	30.0	41.4	*7.3*	18.3	11.6	-5.9	6.1	1.6	31.5	0.5
2-6D	-	-	-	-	-	-	-	-	-	-	-	-	-	-	-	-
3-2B	-	-	-	-	-	-	-	-	-	-	-	-	-	-	-	-
3-4C0	123	200	30	4	0.07		17.0	*31.5*	-	2.8	*15.5*	12.5	2.2	0.7	-	-
3-4C1	157	267	20	6	0.06	$0.35^{\#}$	25.9	47.5	*5.5*	6.6	4.1	-4.8	5.3	1.7	33.1	1.8
3-4C3	122	189	20	4	0.10	*0.46*	27.1	42.3	-	2.7	3.6	0.4	7.8	2.5	-	-
3-4C4	163	281	30	6	0.05	*0.26*	19.3	*29.5*	-	4.7	8.9	-0.5	4.4	0.9	-	-
3-4C9*	107	250	30	5	0.08	0.28	47.2	82.5	*1.6*	6.9	8.5	12.8	2.2	2.2	32.4	2.7
3-5A1	115	210	30	5	0.02	0.07	39.6	64.9	-	18.1	*12.9*	0.5	3.1	2.4	*16.2*	*0.3*
3-5A2	145	185	30	4	0.11	0.10	32.4	50.4	*4.2*	3.1	12.0	10.5	0.5	1.2	21.9	2.4
3-6D1	-	-	-	-	-	-	-	-	-	-	-	-	-	-	-	-
3-7A1	-	-	-	-	-	-	-	-	-	-	-	-	-	-	-	-
3-8C1	-	-	-	-	-	-	-	-	-	-	-	-	-	-	-	-
6-1D1	40	119	15	5	0.03	0.04	45.9	46.2	*17.0*	11.1	5.5	6.0	14.2	3.5	28.9	0.8
6-1D2	127	160	25	4	0.05	0.14	18.4	*18.3*	-	3.1	*22.2*	*21.7*	14.1	1.3	-	-
6-1D4	19	140	30	6	0.08	0.20	48.2	47.1	-	4.6	*21.6*	*23.9*	4.0	1.3	-	-
6-1D6	19	89	20	4	0.07	0.19	34.0	$34.1^{\#}$	*6.2*	3.1	3.2	3.4	5.7	1.0	31.4	2.3
6-1D7	40	273	30	10	0.06	0.15	83.8	86.9	-	11.6	11.6	*22.8*	4.9	3.1	-	-
6-1D8	100	257	30	8	0.08	0.11	50.2	70.0	*15.2*	4.8	3.2	-11.1	8.3	2.4	30.6	2.4
6-2C1	20	338	30	12	0.07	*0.44*	84.0	86.0	-	10.0	6.7	10.3	8.2	4.4	-	-
6-2C2	0	170	30	5	0.07	$0.34^{\#}$	74.0	71.2	*4.7*	4.6	1.1	-7.4	4.4	2.9	30.4	2.2
6-2C3	109	257	20	7	0.03	0.11	67.6	72.7	*1.3*	17.8	7.0	4.3	1.5	2.1	40.2	1.0
6-2C4	16	138	30	4	0.06	0.22	72.6	84.6	*8.9*	7.1	0.6	-6.3	6	5.1	31.4	2.0

Supplementary Table C2.3. Specimen level Shaw-DHT results for Mundine Wells dykes. Description of parameters as detailed in Supplementary Table B2.1 with the following additional criteria: MAD_a and MAD_f, anchored and free maximum angular deviations; f_{RESID}, residual difference between the y-axis intercept of the palaeointensity slope and the origin in a pseudo-Arai plot (Paterson et al., 2016); kN, |k′| curvature of the Arai plot as determined by the best-fit circle to the selected best-fit Arai plot segment (Paterson, 2011); H_{Lb} and H_{Mb}, denotes subsequent column values calculated using the full coercivity range; sA_{2b}, sT_b and rT_b are defined the same as sA_2, sT and rT but are calculated using the full coercivity range; B_{ANC}, palaeointensity estimate; StdErr, standard error. Italics denote rejected results, retained only for comparison using the set of relaxed selection criteria.

Sample	D (°)	I (°)	H_L (mT)	H_M (mT)	N	H_{LAB} (μT)	α (°)	MAD_a (°)	MAD_f (°)	*FRAC* (%)	*f*N	f_{RESID}	sN	rN	kN	sA_1	sA_2	sT	rT	kT	H_{Lb} (mT)	H_{Mb} (mT)	sA_{2b}	sT_b	rT_b	B_{ANC} (μT)	StdErr (μT)	Class
1.2C	246.0	43.8	30	99	24	20	0.7	0.3	0.7	0.45	0.41	0.15	2.96	*0.881*	0.85	0.87	0.83	0.96	0.998	0.10	0	99	0.89	1.02	1.00	-	-	-
2.10A	352.0	-21.1	30	100	15	20	4.6	4.6	1.8	*0.07*	0.21	0.02	1.00	0.998	0.11	0.55	0.95	*1.14*	0.999	0.06	0	100	1.00	1.08	1.00	-	-	-
2.10C	355.7	33.4	35	70	8	20	5.0	3.6	1.5	*0.03*	0.12	0.02	0.83	0.999	0.02	0.49	0.78	1.09	0.999	0.06	0	100	0.98	1.07	1.00	-	-	-
2.11A	180.9	39.5	20	100	17	20	0.5	2.7	3.1	*0.19*	0.51	0.00	0.99	1.000	0.01	0.82	0.84	*1.20*	0.999	0.04	0	100	0.94	*1.22*	1.00	*19.8*	*0.1*	-
2.11C	4.0	-21.4	40	70	7	20	9.2	5.0	2.5	*0.02*	0.06	0.08	1.05	0.996	0.12	0.60	0.89	*1.30*	1.000	0.01	0	100	0.98	*1.14*	1.00	-	-	-
2.11D	359.7	38.6	27	63	13	20	1.5	1.5	1.0	*0.09*	0.24	0.01	0.76	*0.988*	0.20	0.70	0.84	*2.83*	0.997	0.04	0	99	0.96	*1.96*	*0.98*	-	-	-
2.12A	190.8	41.5	15	100	18	20	0.7	3.2	3.5	*0.32*	0.69	0.00	0.94	0.999	0.02	0.84	0.89	*1.21*	1.000	0.02	0	100	0.95	*1.22*	1.00	*18.8*	*0.1*	-
2.12E	193.0	37.2	15	100	18	20	0.9	3.6	3.9	*0.32*	0.67	0.01	0.97	0.996	0.01	0.85	0.86	*1.17*	1.000	0.03	0	100	0.94	*1.19*	1.00	*19.4*	*0.2*	-
2.13B	218.8	-79.9	35	100	14	20	1.3	1.5	1.7	*0.14*	0.40	0.02	0.66	0.999	0.04	0.45	1.09	0.99	1.000	0.03	0	100	0.91	0.94	1.00	-	-	-
2.3D	352.9	-14.4	60	99	14	20	*21.4*	4.0	1.7	0.68	0.28	0.13	16.18	*0.957*	0.48	*1.82*	0.76	*0.60*	*0.982*	0.16	0	99	0.84	*0.22*	*0.96*	-	-	-
2.4A	253.1	6.0	20	100	17	20	1.8	6.2	5.2	*0.06*	0.29	0.02	1.97	*0.971*	0.44	0.83	0.79	1.02	1.000	0.01	0	100	0.95	1.02	1.00	-	-	-
2.4C	82.4	48.2	40	70	7	20	3.4	6.8	3.9	*0.00*	0.04	0.05	1.05	0.999	0.04	0.67	0.87	1.07	0.998	0.12	0	100	0.99	1.07	1.00	-	-	-
2.4D	250.9	5.7	20	100	17	20	3.7	6.7	6.2	*0.09*	0.33	0.01	2.19	0.990	0.16	0.81	0.79	1.06	0.999	0.03	0	100	0.94	1.04	1.00	-	-	-
2.5A	43.9	8.7	20	50	7	20	0.5	0.6	0.3	*0.21*	0.92	*3.05*	-680.27	*0.709*	0.89	*0.00*	0.88	0.92	0.997	0.13	0	100	0.93	0.98	1.00	-	-	-
2.5D	239.5	6.7	20	100	17	20	0.4	1.4	1.2	*0.21*	0.30	0.04	7.91	*0.939*	0.62	0.83	0.78	1.08	1.000	0.02	0	100	0.94	1.06	1.00	-	-	-
2.6A	144.6	-58.1	25	60	8	20	0.1	0.4	0.5	*0.26*	0.17	0.19	14.47	*0.955*	0.57	0.50	0.80	1.02	0.999	0.07	0	100	0.94	1.01	1.00	-	-	-
2.6C	319.7	-54.9	20	100	17	20	0.4	3.2	3.3	0.52	0.35	0.04	15.98	*0.977*	0.29	0.85	0.74	*1.17*	0.999	0.04	0	100	0.91	*1.12*	1.00	-	-	-
2.7E	37.0	52.8	20	100	17	20	2.0	3.8	3.6	0.96	0.26	0.07	47.41	*0.755*	1.02	0.58	0.79	0.99	0.999	0.05	0	100	0.92	1.04	1.00	-	-	-
2.8B	335.0	59.2	51	96	16	20	3.4	4.5	6.8	*0.00*	0.02	0.07	1.04	*0.947*	0.53	0.93	0.49	*0.67*	*0.988*	0.14	0	99	0.96	*2.46*	*0.91*	-	-	-
2.9B	293.1	51.4	60	100	9	20	*21.7*	7.5	5.9	*0.00*	0.02	0.13	1.22	*0.917*	0.57	0.45	0.52	*1.13*	0.991	0.13	0	100	0.94	1.06	1.00	-	-	-
3.1A	228.8	2.4	15	100	18	20	0.2	1.0	1.1	*0.12*	0.51	0.01	0.83	0.994	0.19	0.80	0.79	*1.24*	1.000	0.00	0	100	0.91	*1.20*	1.00	-	-	-
3.1C	40.1	52.7	20	75	12	20	0.3	0.9	1.0	*0.07*	0.34	0.00	0.82	0.998	0.09	0.66	0.93	*1.88*	0.996	0.15	0	100	0.98	*1.58*	1.00	-	-	-
3.1E	55.3	0.1	24	69	16	20	2.0	2.0	1.2	*0.06*	0.23	0.02	0.69	0.999	0.03	0.73	0.83	*1.12*	1.000	0.01	0	99	0.94	1.09	1.00	-	-	-
3.2A	56.0	-20.6	25	100	16	20	0.3	1.0	0.8	*0.44*	0.27	0.06	15.79	*0.915*	0.73	0.79	0.72	*1.10*	0.999	0.03	0	100	0.90	*1.11*	1.00	-	-	-
3.2C	56.8	-22.0	30	100	15	20	0.2	0.4	0.1	*0.28*	0.13	0.07	22.93	*0.933*	0.63	0.75	0.56	*1.16*	1.000	0.01	0	100	0.89	*1.13*	1.00	-	-	-
3.2D	225.1	-20.0	35	65	7	20	0.7	0.9	0.2	*0.14*	0.07	*0.21*	20.05	*0.968*	0.47	0.68	0.65	*1.11*	1.000	0.03	0	100	0.92	1.02	1.00	-	-	-
3.3A	205.0	38.1	15	100	18	20	1.3	2.6	2.2	*0.39*	0.29	0.05	0.01	*0.929*	0.64	*63.96*	0.01	*78.3*	*0.003*	*1.78*	0	100	0.01	*164.80*	*0.00*	-	-	-
3.3D	272.5	14.1	15	100	18	20	-	*14.6*	*10.7*	*0.40*	0.48	*0.27*	0.01	*0.156*	2.07	*0.00*	0.01	*128.0*	*0.31*	*1.57*	0	100	0.00	*256.32*	*0.32*	-	-	-
3.3E	331.9	71.0	25	60	8	20	0.8	1.1	1.5	*0.15*	0.17	0.02	0.78	0.997	0.12	0.66	0.99	*2.38*	0.998	0.12	0	100	0.99	*1.81*	0.99	-	-	-
3.4A	65.2	37.9	20	60	9	20	0.5	0.7	0.7	*0.13*	0.38	0.02	1.13	0.995	0.18	0.69	0.96	*1.99*	0.996	0.17	0	100	0.99	*1.59*	0.99	-	-	-
3.4E	22.8	27.4	15	99	29	20	1.2	3.3	3.1	*0.20*	0.60	0.01	0.99	0.999	0.03	0.77	0.89	*1.14*	1.000	0.04	0	99	0.94	*1.12*	1.00	*19.7*	*0.1*	-
3.6A	1.0	26.9	30	60	7	20	4.0	3.0	1.6	*0.03*	0.14	0.04	0.96	0.999	0.05	0.74	0.78	*1.15*	1.000	0.01	0	100	0.96	*1.11*	1.00	-	-	-
3.7C	25.7	-27.4	24	48	9	20	2.3	3.0	1.8	*0.20*	0.20	0.16	8.32	*0.955*	0.54	0.71	0.76	*1.22*	1.000	0.01	0	99	0.91	*1.15*	1.00	-	-	-
3.8A	210.1	33.5	15	100	18	20	0.2	2.0	2.1	0.51	0.54	0.04	11.84	*0.957*	0.51	0.75	0.73	*1.11*	1.000	0.02	0	100	0.87	*1.10*	1.00	-	-	-
3.8E	28.7	31.7	20	100	17	20	0.4	1.0	1.6	0.52	0.32	0.04	18.77	*0.942*	0.58	0.54	0.85	1.00	0.998	0.08	0	100	0.92	1.04	1.00	-	-	-
4.1D	329.0	7.0	30	100	15	20	8.3	*10.9*	7.7	*0.05*	0.31	0.00	0.29	*0.986*	0.27	0.64	0.96	1.03	0.999	0.04	0	100	1.00	1.02	1.00	-	-	-
4.2C	33.7	16.2	30	100	15	20	*13.2*	*17.6*	8.6	*0.02*	0.37	0.00	0.12	*0.986*	0.28	0.88	0.91	1.05	1.000	0.01	0	100	1.00	1.00	1.00	-	-	-
4.4B	19.8	24.8	25	100	16	20	4.0	4.3	3.3	*0.23*	0.48	0.02	0.13	*0.979*	0.35	0.78	0.98	1.05	0.999	0.06	0	100	1.01	1.02	1.00	-	-	-
4.5C	353.2	32.6	20	65	10	20	2.2	2.5	1.5	*0.25*	0.62	0.00	0.20	0.997	0.12	0.74	0.98	*1.25*	0.997	0.15	0	100	0.99	*1.20*	1.00	-	-	-
4.6C	9.0	-2.3	30	65	8	20	6.1	5.3	3.2	*0.03*	0.33	0.02	0.18	0.998	0.07	0.72	0.99	*1.40*	0.999	0.00	0	100	1.00	*1.23*	1.00	-	-	-
4.7E	18.6	0.9	30	100	15	20	*14.7*	*30.0*	6.4	*0.04*	0.40	0.01	0.16	1.000	0.02	0.86	0.91	1.04	0.999	0.06	0	100	0.99	1.00	1.00	-	-	-
4.9E	11.9	3.5	30	100	15	20	6.1	7.5	3.3	*0.12*	0.31	0.04	0.13	*0.976*	0.37	0.75	0.96	1.06	1.000	0.02	0	100	1.00	1.03	1.00	-	-	-
5.10B	271.4	-24.1	60	100	9	20	*13.2*	4.0	*18.5*	*0.02*	0.35	0.06	1.12	*0.652*	0.46	*0.03*	0.87	*1.25*	0.999	0.01	0	100	0.54	*1.14*	1.00	-	-	-
5.4B	56.9	11.5	30	100	15	20	7.6	4.2	*13.4*	*0.24*	0.83	0.02	0.25	*0.981*	0.22	*0.15*	0.90	*1.11*	1.000	0.02	0	100	0.87	*1.12*	1.00	-	-	-
5.6D	78.4	-18.1	25	100	16	20	0.8	1.2	1.8	*0.23*	0.57	0.08	9.68	*0.923*	0.65	1.41	0.96	*1.21*	0.999	0.06	0	100	0.96	*1.23*	1.00	-	-	-
6.1A	2.2	-28.4	25	60	8	20	1.3	1.4	0.4	*0.40*	0.31	0.02	1.70	0.997	0.15	0.63	1.00	*2.16*	0.993	0.20	0	100	1.00	*1.72*	0.99	*34.0*	*0.8*	-
6.1B	2.4	33.7	15	55	9	20	1.0	1.3	1.2	0.85	0.79	0.02	1.06	0.995	0.20	0.92	0.96	1.00	1.000	0.04	0	100	0.98	1.01	1.00	21.2	0.6	A
6.1E	358.3	34.4	20	100	17	20	0.9	1.2	0.8	0.75	0.63	0.03	1.27	0.995	0.17	0.79	0.94	1.07	1.000	0.02	0	100	0.96	1.07	1.00	25.4	0.5	B
6.2A	11.8	26.7	25	60	8	20	0.4	0.7	0.7	0.51	0.31	0.01	1.76	0.995	0.19	0.65	0.96	*2.55*	0.998	0.11	0	100	0.99	*1.95*	0.99	*35.3*	*1.0*	-
6.2D	196.6	34.9	20	100	17	20	0.1	1.2	1.3	0.77	0.55	0.01	1.65	0.994	0.20	0.75	0.86	*1.29*	1.000	0.00	0	100	0.94	*1.31*	1.00	*33.1*	*0.4*	-
6.3B	16.7	33.4	25	65	9	20	0.9	1.4	1.0	0.65	0.35	0.02	1.25	1.000	0.01	0.80	0.88	1.04	1.000	0.05	0	100	0.97	1.03	1.00	25.1	0.2	A
6.3C	9.7	38.8	25	55	7	20	0.6	0.8	0.9	0.61	0.35	0.00	1.83	0.997	0.15	0.66	0.98	*2.11*	0.997	0.15	0	100	0.99	*1.80*	1.00	*36.5*	*0.9*	-
6.4A	15.2	29.2	25	100	16	20	0.4	1.3	1.3	*0.14*	0.38	0.01	1.60	0.999	0.04	0.67	0.86	*1.15*	1.000	0.02	0	100	0.95	1.08	1.00	-	-	-
6.5A	8.9	42.9	20	50	7	20	1.4	1.4	0.6	0.52	0.54	0.01	1.24	0.996	0.16	0.88	0.93	1.01	0.998	0.10	0	100	0.98	1.00	1.00	24.8	0.7	A
6.5C	33.6	47.1	25	65	9	20	2.4	2.8	0.5	*0.28*	0.28	0.01	1.61	1.000	0.03	0.64	0.99	*3.06*	0.990	*0.27*	0	100	0.99	*2.18*	0.99	-	-	-
6.5D	19.5	38.0	20	100	17	20	1.1	1.9	0.7	0.46	0.53	0.00	1.26	0.995	0.18	0.80	0.91	*1.11*	1.000	0.04	0	100	0.96	1.10	1.00	25.2	0.5	B
6H1.1B	127.0	-20.7	15	100	18	20	0.3	1.7	1.9	0.69	0.81	0.00	1.33	0.999	0.08	0.81	0.84	*1.30*	0.999	0.04	0	100	0.88	*1.32*	1.00	*26.6*	*0.2*	-
6H2A.1B	163.0	52.3	30	100	15	20	0.9	1.9	1.2	*0.10*	0.56	*0.33*	154.43	*0.281*	1.71	*0.01*	0.68	*1.32*	0.997	0.12	0	100	0.90	*1.35*	1.00	-	-	-
6H2A.1D	161.4	58.8	25	100	16	20	0.7	2.2	2.0	*0.20*	0.32	0.01	1.82	0.999	0.05	0.57	0.77	*1.32*	0.997	0.12	0	100	0.90	*1.37*	1.00	*36.4*	*0.2*	-
6H2B.1B	160.5	-47.4	20	100	17	20	0.4	4.0	4.5	*0.24*	0.53	0.00	1.69	0.998	0.11	0.69	0.82	*1.36*	0.999	0.06	0	100	-	-	-	*33.8*	*0.3*	-
6H2B.1D	157.9	-40.8	20	100	17	20	1.3	3.3	3.8	*0.33*	0.54	0.03	1.45	*0.988*	0.26	0.68	0.86	*1.17*	0.995	0.17	0	100	-	-	-	-	-	-
7.3A	195.3	17.0	0	60	13	20	0.3	0.5	0.3	1.00	1.10	0.13	22.66	*0.897*	0.87	0.67	0.91	*1.32*	0.990	*0.28*	0	100	0.86	*1.35*	0.99	-	-	-
7.5B	352.4	34.3	60	100	9	20	9.1	1.3	4.5	*0.01*	0.00	*0.32*	0.04	*0.484*	1.29	*12.17*	0.04	*14.84*	*0.009*	*2.12*	0	100	0.00	*-244.99*	*0.08*	-	-	-
7.7D	204.0	37.9	-	-	-	-	-	-	-	-	-	-	-	-	-	-	-	-	-	-	0	100	-	-	-	-	-	-
8.1B	312.2	-43.0	-	-	-	-	-	-	-	-	-	-	-	-	-	-	-	-	-	-	0	100	-	-	-	-	-	-
8.5D	348.6	-54.3	-	-	-	-	-	-	-	-	-	-	-	-	-	-	-	-	-	-	0	100	-	-	-	-	-	-
8.7A	4.9	-20.0	40	100	13	20	3.4	4.2	3.1	*0.06*	0.12	0.05	3.89	*0.983*	0.31	*0.11*	0.80	0.93	0.999	0.02	0	100	0.78	0.97	1.00	-	-	-

Supplementary Table C2.4. Specimen-level thermal Thellier results for Bangemall Sills. See Supplementary Table B2.2 (appendix B) and Supplementary Table C2.1 for description of parameters. -, Arai-diagram was uninterpretable.

Sample	AF (mT)	H_{LAB} (μT)	T_L (°C)	T_H (°C)	N	β	|k'|	*FRAC*	*f* (%)	g	q	delCK (%)	DRAT (%)	CDRAT (%)	α (°)	MAD_a (°)	B_{ANC} (μT)	StdErr (μT)
1.1D	5	20	-	-	-	-	-	-	-	-	-	-	-	-	-	-	-	-
1.8E	5	20	-	-	-	-	-	-	-	-	-	-	-	-	-	-	-	-
2.10E	5	20	350	500	4	0.10	0.31	17.7	-	0.5	1.8	4.7	9.3	0.6	33.2	7.3	-	-
2.4D	5	20	-	-	-	-	-	-	-	-	-	-	-	-	-	-	-	-
3.3BD	5	20	-	-	-	-	-	-	-	-	-	-	-	-	-	-	-	-
4.3E	5	20	500	590	8	0.13	0.87	6.3	-	0.8	2.9	26.3	55.3	25.0	12.5	9.1	-	-
4.8C	5	20	-	-	-	-	-	-	-	-	-	-	-	-	-	-	-	-
5.2E	5	20	-	-	-	-	-	-	-	-	-	-	-	-	-	-	-	-
5.9D	5	20	560	600	5	0.29	1.11	29.0	-	0.7	0.8	13.6	18.3	-12.2	1.6	1.1	-	-
6.1CC	5	20	550	600	6	0.09	0.42	15.0	-	0.7	2.0	19.2	81.2	110.5	2.4	1.7	-	-
6.1DA	5	20	575	595	6	0.18	0.58	16.3	-	0.8	2.7	137.9	205.9	310.6	3.4	1.5	-	-
6.4BF	5	20	-	-	-	-	-	-	-	-	-	-	-	-	-	-	-	-
7.2AA	5	20	555	591	9	0.14	0.64	31.9	-	0.8	3.9	19.5	19.9	59.1	5.3	2.3	-	-
7.2AB	5	20	575	595	6	0.18	0.30	18.5	-	0.8	2.6	16.5	21.3	25.9	5.2	2.5	-	-
7.2BA	5	20	575	591	5	0.16	0.13	37.0	-	0.6	2.3	20.9	8.3	8.3	1.0	1.2	-	-
7.2BB	5	20	580	600	6	0.06	-	31.6	75.9	0.6	8.0	22.0	25.0	23.1	1.8	2.6	11.4	0.7
7.3AB	5	20	575	595	6	0.16	0.14	24.9	-	0.8	4.3	169.2	153.8	198.4	4.2	4.0	-	-
7.3AC	5	20	570	600	4	0.18	0.75	14.9	-	0.4	0.5	4.7	21.5	-56.7	14.8	1.7	-	-
7.4AA	5	20	570	595	7	0.31	1.74	23.6	-	0.6	1.3	717.4	304.7	335.1	0.7	1.0	-	-
8.10A	5	20	575	600	7	0.19	1.32	16.4	-	0.7	0.7	5.1	26.8	65.6	54.9	7.4	-	-
8.10B	5	20	400	540	5	0.03	0.25	13.5	-	0.7	5.7	12.5	41.9	-6.1	17.4	2.8	-	-
8.11E	5	20	565	587	6	0.32	1.21	14.3	-	0.8	1.1	1068.6	1900.8	1975.0	34.1	18.6	-	-
8.2B	5	20	350	500	4	0.24	0.81	11.7	-	0.5	0.6	14.8	31.2	-32.3	13.5	2.5	-	-
8.3B	5	20	585	600	5	0.11	0.53	9.5	-	0.6	3.9	21.3	31.6	50.8	11.3	13.2	-	-
8.4C	5	20	0	565	11	0.16	0.95	52.5	-	0.8	4.3	14.2	11.6	9.2	16.8	11.6	-	-
8.5E	5	20	200	560	9	0.16	0.68	36.9	-	0.8	3.0	8.9	13.1	1.2	39.0	14.9	-	-
8.8C	5	20	560	600	5	0.34	1.63	30.1	-	0.6	0.8	7.9	16.2	14.0	6.4	2.4	-	-

Supplementary Table C2.5. Specimen-level Microwave results for Bangemall Sills. See Supplementary Table B2.2 (appendix B) and Supplementary Table C2.1 and C2.2 for description of parameters.

Sample	P_L (W.s)	P_H (W.s)	Hlab	N	β	$\lvert k' \rvert$	*FRAC* (%)	*f* (%)	g	delCK (%)	DRAT (%)	CDRAT (%)	α (°)	MAD_a (°)	B_{ANC} (μT)	StdErr (μT)
6-H2A	74	220	10	5	0.10	0.21	70.7	81.9	-	7.4	6.4	5.5	*20.0*	*14.0*	-	-
6-H2B	110	172	10	4	*0.21*		*0.3*	48.0	-	11.6	*20.0*	*19.0*	13.2	5.5	-	-
6-H2C	117	181	10	*3*	0.06	*0.41*	52.6	58.2	-	7.3	6.3	6.5	*24.2*	*11.5*	-	-
7-3BA1	58	80	15	*3*	*0.22*	*0.85*	*18.2*	*24.6*	-	4.6	*14.8*	-14.8	*23.0*	3.4	-	-
7-3BA2	18	145	15	4	0.08	0.13	81.9	86.3	6.0	0.4	0.3	0.1	3.8	2.6	18.9	1.6
7-3BA3	62	114	15	4	0.09	0.12	65.5	83.3	-	13.3	*14.5*	14.8	4.3	3.3	-	-
7-3BA4	73	101	15	*3*	*0.14*	*0.50*	39.7	56.0	-	14.1	*20.6*	*21.1*	2.1	2.4	-	-
7-3BA5	41	82	15	4	0.09	*0.38*	59.7	62.8	-	4.4	5.9	-4.7	5.8	3.1	-	-
7-5A1	52	118	10	5	0.05	0.11	76.5	79.2	6.6	8.3	4.4	-0.3	4.6	3.8	21.2	1.1
7-5A2	18	102	15	4	0.04	0.15	78.6	78.9	2.1	2.4	2.2	-1.8	9.2	5.4	13.5	0.6
7-5A3	21	100	10	5	0.09	*0.52*	95.9	100.0	-	6.4	2.7	2.7	3.9	3.8	-	-
7-5A4	18	107	15	4	0.11	*0.52*	46.5	46.8	-	15.9	*17.9*	-18.4	6.1	3.8	-	-
7-5C1	42	80	10	3	*0.19*	*2.29*	*25.7*	*26.8*	-	4.4	6.0	-6.0	8.7	1.7	-	-
7-5C2	56	101	20	5	0.03	0.06	63.9	76.6	8.6	8.0	5.8	8.3	4.8	2.6	29.9	0.8
7-5C5	80	94	10	*3*	*0.28*	*1.02*	*22.0*	*28.8*	-	0.5	1.4	-2.5	6.0	1.0	-	-
7-5C8	46	95	15	4	0.06	*0.29*	55.9	58.5	-	11.6	*15.8*	*16.4*	11.4	4.5	-	-
7-5C9	37	96	15	5	0.06	0.04	63.0	65.6	12.5	6.0	7.0	-2.6	9.3	5.0	12.7	0.7
7-6A1	73	190	15	11	0.03	0.06	*34.2*	55.8	-	4.4	6.8	-0.5	*25.3*	8.3	-	-
7-6A2	140	153	15	*2*	-	-	-	-	-	-	-	-	-	-	-	-
7-H210	-	-	-	-	-	-	-	-	-	-	-	-	-	-	-	-
7-H211	36	105	15	7	0.03	0.15	50.9	52.2	-	8.4	*14.1*	*19.0*	5.8	1.7	-	-
7-H212	-	-	-	-	-	-	-	-	-	-	-	-	-	-	-	-
7-H213	59	94	15	4	0.06	0.17	56.9	60.7	-	17.2	*20.8*	*21.1*	3.1	1.9	-	-
7-H214	85	142	15	6	0.02	0.10	76.6	79.6	10.3	7.5	4.9	7.6	8.3	4.9	24.4	0.6
7-H215	64	108	15	4	0.09	*0.41*	82.8	93.3	-	11.5	9.0	7.3	3.1	3.1	-	-
7-H216	-	-	-	-	-	-	-	-	-	-	-	-	-	-	-	-
7-H217	40	95	15	4	*0.13*	*0.64*	68.0	77.2	-	0.1	0.1	0.1	5.9	3.2	-	-
7-H25	41	130	15	7	0.04	0.07	79.4	83.9	7.9	1.0	1.0	-0.7	6.0	3.9	11.3	0.4
7-H26	55	113	15	4	0.05	0.13	57.3	60.1	-	20.6	*29.0*	*28.9*	*15.2*	5.5	-	-
7-H27	-	-	-	-	-	-	-	-	-	-	-	-	-	-	-	-
7-H28	-	-	-	-	-	-	-	-	-	-	-	-	-	-	-	-
7-H29	-	-	-	-	-	-	-	-	-	-	-	-	-	-	-	-
8-1F1	129	215	10	5	0.07	*0.42*	*27.4*	49.4	-	8.3	*15.8*	*25.0*	12.0	4.2	-	-
8-2D1	-	-	-	-	-	-	-	-	-	-	-	-	-	-	-	-
8-3A1	122	166	5	4	0.11	*0.42*	*19.8*	38.9	-	3.0	6.4	0.2	*20.6*	4.5	-	-
8-3A1b	122	175	15	5	0.11	*0.36*	*12.8*	*22.1*	-	1.8	7.9	4.1	*26.0*	3.3	-	-
8-3A2	96	116	20	*2*	-	-	-	-	-	-	-	-	-	-	-	-
8-4B1	72	140	10	4	*0.12*	*0.38*	45.7	57.5	-	12.4	*19.6*	*19.7*	14.1	5.0	-	-
8-4B3	117	183	10	5	0.06	0.20	45.7	65.1	-	16.4	*23.5*	*40.2*	8.4	3.6	-	-
8-5B1	149	260	10	5	0.07	*0.37*	53.7	77.5	-	22.2	*27.4*	*42.9*	12.8	8.5	-	-
8-5B2	119	215	10	6	0.02	0.03	49.4	68.6	-	11.3	*15.4*	9.5	10.5	5.4	-	-
8-5B3	126	180	10	4	0.05	0.09	28.9$^{\#}$	35.7	2.1	1.0	2.7	-2.9	11.6	2.7	3.4	0.2
8-5B4	142	193	5	5	0.07	*0.35*	47.0	61.3	-	12.5	*16.5*	*23.0*	12.1	4.8	-	-
8-5B5	112	171	5	5	0.05	*0.25*	39.9	51.8	-	8.6	*13.8*	*18.0*	8.8	2.6	-	-
8-6A1	55	111	10	4	*0.21*	*1.88*	37.6	*32.4*	-	7.4	4.3	-0.5	15.0	4.0	-	-
8-7B1	75	131	15	6	0.08	0.20	*22.4*	*20.0*	-	2.1	10.2	*16.7*	7.1	1.6	-	-
8-7B2	110	316	15	16	0.03	0.24	49.9	46.3	-	4.8	10.3	*18.6*	3.8	3.0	-	-
8-8A1	137	236	10	4	0.07	*0.26*	29.0$^{\#}$	58.8	2.7	7.3	*12.0*	9.3	*15.2*	6.2	2.4	0.2
8-8A2	136	203	10	5	0.09	*0.53*	*11.7*	38.7	-	5.4	*13.3*	*16.8*	*25.9*	7.8	-	-

Supplementary Table C2.6. Specimen level Shaw-DHT results for Bangemall sills. For parameter descriptions, see Supplementary Tables B2.1 and C2.3. Italics denote specimens which produced uninterpretable demagnetisation of NRM and some failed due to problems with the compressor and/ or oven. Failed results (italics) left in to show consistent weak estimates.

Sample	H_L (mT)	H_M (mT)	N	H_{LAB} (µT)	MAD_a (°)	MAD_f (°)	LTD	α (°)	FRAC (%)	ƒN	f_{RESID}	sN	rN	kN	sA_1	sA_2	sT	rT	H_{Lb} (mT)	H_{Mb} (mT)	sA_{2b}	sT_b (full Hc used)	rT_b	B_{ANC} (µT)	StdErr (µT)	Class
1.1B	-	-	-	-	-	-	-	-	-	-	-	-	-	-	-	-	-	-	-	-	-	-	-	-	-	-
1.1C	21	99	28	20	5.2	11.5	no	1.3	1.29	0.63	0.03	1.05	0.963	0.03	0.68	0.65	0.840	0.998	0	99	0.66	0.86	0.998	-	-	-
1.4C	-	-	-	-	-	-	-	-	-	-	-	-	-	-	-	-	-	-	-	-	-	-	-	-	-	-
1.6C	-	-	-	-	-	-	-	-	-	-	-	-	-	-	-	-	-	-	-	-	-	-	-	-	-	-
1.7D	21	99	28	20	6.6	11.9	no	3.1	0.08	0.46	0.02	1.11	0.904	0.04	1.04	0.71	0.89	0.994	0	99	0.72	0.94	0.993	-	-	-
1.8C	-	-	-	-	-	-	-	-	-	-	-	-	-	-	-	-	-	-	-	-	-	-	-	-	-	-
2.3B	-	-	-	-	-	-	-	-	-	-	-	-	-	-	-	-	-	-	-	-	-	-	-	-	-	-
2.3E	-	-	-	-	-	-	-	-	-	-	-	-	-	-	-	-	-	-	-	-	-	-	-	-	-	-
2.6D	-	-	-	-	-	-	-	-	-	-	-	-	-	-	-	-	-	-	-	-	-	-	-	-	-	-
3.1BC	-	-	-	-	-	-	-	-	-	-	-	-	-	-	-	-	-	-	-	-	-	-	-	-	-	-
3.3AE	-	-	-	-	-	-	-	-	-	-	-	-	-	-	-	-	-	-	-	-	-	-	-	-	-	-
3.4AA	-	-	-	-	-	-	-	-	-	-	-	-	-	-	-	-	-	-	-	-	-	-	-	-	-	-
4.1B	-	-	-	-	-	-	-	-	-	-	-	-	-	-	-	-	-	-	-	-	-	-	-	-	-	-
4.1D	-	-	-	-	-	-	-	-	-	-	-	-	-	-	-	-	-	-	-	-	-	-	-	-	-	-
4.2C	-	-	-	-	-	-	-	-	-	-	-	-	-	-	-	-	-	-	-	-	-	-	-	-	-	-
4.5E	-	-	-	-	-	-	-	-	-	-	-	-	-	-	-	-	-	-	-	-	-	-	-	-	-	-
4.7C	-	-	-	-	-	-	-	-	-	-	-	-	-	-	-	-	-	-	-	-	-	-	-	-	-	-
4.7F	-	-	-	-	-	-	-	-	-	-	-	-	-	-	-	-	-	-	-	-	-	-	-	-	-	-
4.8F	-	-	-	-	-	-	-	-	-	-	-	-	-	-	-	-	-	-	-	-	-	-	-	-	-	-
5.1D	-	-	-	-	-	-	-	-	-	-	-	-	-	-	-	-	-	-	-	-	-	-	-	-	-	-
5.1E	-	-	-	-	-	-	-	-	-	-	-	-	-	-	-	-	-	-	-	-	-	-	-	-	-	-
5.3C	-	-	-	-	-	-	-	-	-	-	-	-	-	-	-	-	-	-	-	-	-	-	-	-	-	-
5.3E	51	99	18	20	2.8	9.2	no	18.0	0.10	0.73	0.10	1.15	0.932	0.59	0.61	0.52	0.740	0.997	0	99	0.49	0.81	0.995	-	-	-
5.5C	-	-	-	-	-	-	-	-	-	-	-	-	-	-	-	-	-	-	-	-	-	-	-	-	-	-
5.7A	-	-	-	-	-	-	-	-	-	-	-	-	-	-	-	-	-	-	-	-	-	-	-	-	-	-
5.7C	-	-	-	-	-	-	-	-	-	-	-	-	-	-	-	-	-	-	-	-	-	-	-	-	-	-
5.8D	-	-	-	-	-	-	-	-	-	-	-	-	-	-	-	-	-	-	-	-	-	-	-	-	-	-
6.1AB	30	99	25	20	1.3	4.3	no	6.0	0.63	0.68	0.00	0.15	0.991	0.16	0.31	0.62	0.980	0.990	0	99	0.66	1.13	0.985	3.0	0.0	B
6.1AC	35	75	9	10	0.9	7.7	no	2.6	0.42	0.52	0.12	0.51	0.992	0.09	0.55	0.27	0.610	0.996	0	100	0.26	0.68	0.992	5.1	0.1	-
6.1AD	-	-	-	-	-	-	-	-	-	-	-	-	-	-	-	-	-	-	-	-	-	-	-	-	-	-
6.1AE	30	75	10	10	0.8	3.4	no	4.0	0.39	0.57	0.07	0.62	0.996	0.05	0.53	0.27	0.620	0.992	0	100	0.27	0.71	0.985	6.2	0.1	-
6.1BA	30	80	11	20	3.3	3.3	yes	13.4	0.55	0.49	0.17	0.49	0.993	0.16	0.42	0.37	0.690	0.996	0	100	0.37	0.78	0.989	9.8	0.3	-
6.1BB	30	75	10	10	1.6	4.6	no	11.6	0.38	0.47	0.21	0.62	0.997	0.08	0.42	0.30	0.680	0.997	0	100	0.31	0.79	0.985	6.2	0.1	-
6.1BC	30	100	15	10	1.5	6.2	no	7.7	0.62	0.77	0.02	0.55	0.992	0.02	0.47	0.25	0.620	0.996	0	100	0.24	0.71	0.991	5.5	0.1	-
6.1BD	-	-	-	-	-	-	-	-	-	-	-	-	-	-	-	-	-	-	-	-	-	-	-	-	-	-
6.1CA	20	100	17	20	2.5	5.0	no	5.6	0.36	0.58	0.06	0.00	0.989	0.13	18.22	0.01	-	0.248	0	100	0.01	-	-	-	-	-
6.3B	30	100	15	10	9.3	23.7	no	27.4	0.07	0.42	0.10	0.34	0.747	0.08	0.54	0.26	0.920	0.992	0	100	0.29	1.08	0.993	-	-	-
6.3C	-	-	-	-	-	-	-	-	-	-	-	-	-	-	-	-	-	-	-	-	-	-	-	-	-	-
6.3D	30	100	15	20	13.1	31.9	no	42.9	0.04	0.30	0.10	0.16	0.840	0.23	0.25	0.76	0.950	0.999	0	100	0.81	1.00	0.999	-	-	-
6.4AB	-	-	-	-	-	-	-	-	-	-	-	-	-	-	-	-	-	-	-	-	-	-	-	-	-	-
6.4AD	30	99	25	20	4.5	23.0	no	15.2	0.43	0.51	0.11	0.00	0.879	0.08	32.63	0.01	-	-	0	99	0.01	-	-	-	-	-
6.4AE	30	100	15	10	6.7	23.1	no	31.5	0.35	0.72	0.06	0.47	0.848	0.20	0.42	0.21	0.730	0.995	0	100	0.21	0.80	0.994	-	-	-
6.4BB	20	100	17	20	7.6	9.5	no	7.1	0.10	0.44	0.01	0.15	0.965	0.36	0.61	0.85	1.100	0.999	0	100	0.92	1.07	1.000	-	-	-
6.4BC	30	99	25	20	2.3	27.6	no	7.9	0.33	0.68	0.13	0.12	0.853	0.05	0.47	0.49	0.830	0.998	0	99	0.49	0.89	0.993	-	-	-
6.4BE	20	100	17	20	7.4	16.2	yes	20.3	0.33	0.64	0.16	0.24	0.907	0.29	0.57	0.22	0.830	0.987	0	100	0.23	0.95	0.984	-	-	-
6.4BG	30	100	15	10	10.0	31.0	no	19.7	0.05	0.27	0.15	0.35	0.658	0.22	0.51	0.29	0.880	0.994	0	100	0.36	1.07	0.994	-	-	-
6.5AA	20	100	17	20	4.6	6.8	yes	5.5	0.19	0.68	0.02	0.86	0.969	0.28	0.88	0.32	1.070	0.997	0	100	0.36	1.11	0.999	-	-	-
6.5AB	30	100	15	10	9.6	38.8	no	57.6	0.06	0.66	0.41	0.42	0.025	2.42	0.45	0.26	0.690	0.993	0	100	0.25	0.77	0.994	-	-	-
6.5AC	-	-	-	-	-	-	-	-	-	-	-	-	-	-	-	-	-	-	-	-	-	-	-	-	-	-
6.5AD	30	100	15	10	14.7	31.4	no	18.3	0.02	0.34	0.16	0.51	0.655	0.63	0.73	0.30	0.880	0.994	0	100	0.38	1.03	0.996	-	-	-
6.5BA	30	100	15	10	6.4	24.7	no	14.3	0.06	0.36	0.10	0.62	0.774	0.13	0.41	0.28	0.790	0.993	0	100	0.30	0.94	0.991	-	-	-
6.5BB	20	100	17	20	10.8	18.5	yes	18.9	0.18	1.24	0.15	4.61	0.198	1.56	0.04	0.29	1.020	0.994	0	100	0.33	1.08	0.997	-	-	-
6.5BD	20	100	17	20	2.7	16.7	no	10.5	0.51	0.78	0.16	0.22	0.912	0.04	0.48	0.65	0.940	1.000	0	100	0.66	0.96	0.999	-	-	-
7.1AA	10	40	7	20	2.4	2.9	no	2.0	0.83	0.86	0.12	0.39	0.991	0.14	1.15	0.99	0.990	0.999	0	100	0.97	1.01	1.000	6.8	0.3	A
7.1AB	-	-	-	-	-	-	-	-	-	-	-	-	-	-	-	-	-	-	-	-	-	-	-	-	-	-
7.1AC	25	100	16	20	4.7	6.4	yes	6.1	0.31	0.37	0.07	0.32	0.986	0.14	0.65	0.53	1.130	1.000	0	100	0.68	1.11	1.000	-	-	-
7.1BB	10	40	7	20	3.9	5.5	yes	2.8	0.88	0.91	0.14	0.25	0.998	0.05	1.20	0.62	1.310	0.999	0	100	0.52	1.29	0.999	-	-	-
7.1BC	10	40	7	20	1.4	1.7	no	0.8	0.89	0.87	0.12	0.39	0.995	0.16	1.12	1.00	0.970	0.999	0	100	0.98	0.99	1.000	6.8	0.3	A
7.3AA	-	-	-	-	-	-	-	-	-	-	-	-	-	-	-	-	-	-	-	-	-	-	-	-	-	-
7.3BB	12	99	31	20	1.9	2.0	no	0.4	0.83	0.83	0.01	0.50	0.937	0.58	0.72	1.00	0.960	0.999	0	99	1.01	0.96	1.000	-	-	-
7.4AB	15	48	12	20	0.9	1.6	no	1.5	0.80	0.61	0.19	0.45	0.999	0.05	0.76	0.96	0.980	0.999	0	99	0.97	0.98	1.000	9.0	0.1	A
7.4BA	10	40	7	20	1.8	3.9	no	0.3	0.88	0.74	0.13	0.44	0.996	0.19	0.84	0.98	1.010	0.999	0	100	0.97	1.00	1.000	7.7	0.3	A
7.5B	15	99	30	20	2.2	1.4	no	1.0	0.77	0.68	0.01	0.44	0.997	0.12	0.72	0.97	0.96	1.000	0	99	0.99	0.97	1.000	8.8	0.1	A
7.5D	-	-	-	-	-	-	-	-	-	-	-	-	-	-	-	-	-	-	-	-	-	-	-	-	-	-
7.6B	-	-	-	-	-	-	-	-	-	-	-	-	-	-	-	-	-	-	-	-	-	-	-	-	-	-
8.11A	-	-	-	-	-	-	-	-	-	-	-	-	-	-	-	-	-	-	-	-	-	-	-	-	-	-
8.12E	12	99	31	20	3.0	9.4	no	14.7	0.71	0.86	0.21	0.43	0.898	0.21	2.11	0.87	0.700	0.983	0	99	0.89	0.80	0.983	-	-	-
8.1A	20	50	7	20	4.6	2.2	yes	7.6	0.13	0.39	0.20	0.20	0.995	0.14	0.80	0.76	1.03	0.999	0	100	0.82	1.01	1.000	-	-	-
8.1C	20	100	17	10	9.4	8.6	no	10.7	0.05	0.30	0.12	0.23	0.909	0.67	0.81	0.74	1.040	1.000	0	100	0.91	1.07	1.000	-	-	-
8.1D	-	-	-	-	-	-	-	-	-	-	-	-	-	-	-	-	-	-	-	-	-	-	-	-	-	-
8.1E	20	100	17	10	9.1	12.1	no	5.6	0.06	0.29	0.17	0.21	0.769	1.01	0.82	0.75	1.040	0.998	0	100	0.92	1.09	1.000	-	-	-
8.2A	20	100	17	10	11.8	14.5	no	11.9	0.41	0.85	0.04	0.67	0.859	0.62	0.10	0.30	0.690	0.998	0	100	0.28	0.72	0.997	-	-	-
8.2C	20	100	17	10	10.0	12.0	no	5.8	0.12	0.62	0.06	0.32	0.934	0.61	0.23	0.22	0.770	0.997	0	100	0.22	0.83	0.995	-	-	-
8.2E	20	100	17	10	11.4	14.9	no	5.4	0.08	0.48	0.02	0.34	0.953	0.20	0.18	0.21	0.810	0.998	0	100	0.22	0.86	0.997	-	-	-
8.3C	12	99	31	20	7.2	9.6	no	5.2	0.35	0.64	0.07	0.09	0.954	0.41	0.83	0.96	1.000	1.000	0	99	0.98	0.98	1.000	-	-	-
8.3E	-	-	-	-	-	-	-	-	-	-	-	-	-	-	-	-	-	-	-	-	-	-	-	-	-	-
8.4A	40	100	13	10	1.8	3.9	no	4.3	0.28	0.09	0.01	1.33	0.995	0.16	0.86	0.58	0.830	0.997	0	100	0.89	1.04	0.998	-	-	-
8.4D	-	-	-	-	-	-	-	-	-	-	-	-	-	-	-	-	-	-	-	-	-	-	-	-	-	-
8.4E	12	99	31	20	7.6	11.7	no	7.0	0.36	0.63	0.07	0.06	0.940	0.46	0.83	0.95	1.000	1.000	0	99	0.97	0.99	1.000	-	-	-
8.4F	20	100	17	20	8.8	16.3	yes	4.1	0.35	0.42	0.11	0.09	0.870	0.82	0.74	0.65	1.080	0.999	0	100	0.81	1.07	1.000	-	-	-
8.5C	10	100	19	10	4.0	3.3	no	3.3	0.77	0.78	0.02	0.27	0.994	0.08	0.82	0.79	1.030	1.000	0	100	0.84	1.04	1.000	2.7	0.1	A
8.5D	-	-	-	-	-	-	-	-	-	-	-	-	-	-	-	-	-	-	-	-	-	-	-	-	-	-
8.6B	50	100	11	10	2.1	6.2	no	6.1	0.12	0.03	0.01	1.48	0.947	0.22	0.43	0.63	0.770	0.985	0	100	0.91	1.06	0.999	-	-	-
8.6C	30	100	15	10	7.7	12.2	no	26.3	0.10	0.07	0.16	0.42	0.899	0.72	0.33	0.55	1.096	0.994	0	100	0.92	1.04	1.000	-	-	-
8.6D	15	99	30	20	7.7	10.1	no	14.2	0.28	0.47	0.09	0.06	0.917	0.62	0.73	0.92	1.060	0.997	0	99	0.97	1.02	0.999	-	-	-
8.7C	50	100	11	10	9.6	15.6	no	52.9	0.06	0.02	0.03	0.92	0.946	0.04	0.21	0.47	1.072	0.994	0	100	0.89	1.07	1.000	-	-	-
8.7D	-	-	-	-	-	-	-	-	-	-	-	-	-	-	-	-	-	-	-	-	-	-	-	-	-	-
8.7E	20	100	17	20	7.6	16.4	yes	4.0	0.37	0.37	0.13	0.11	0.898	0.72	0.66	0.65	1.050	1.000	0	100	0.82	1.06	1.000	-	-	-
8.8D	12	99	31	20	5.2	7.6	no	3.6	0.58	0.64	0.05	0.08	0.976	0.18	0.77	0.94	1.040	0.999	0	99	0.97	1.03	1.000	-	-	-

Supplementary Table C2.7. Individual QPI scores for each site.

Site	AGE	STAT	TRM	ALT	MD	ACN	TECH	LITH	MAG	DIR	Q_{PI}
MD2	1	0	1	1	1	1	0	0	1	1	7
MD3	1	0	1	1	1	1	0	0	1	1	7
MD6	1	1	1	1	1	1	1	0	1	1	9
BM6	1	0	1	1	1	0	0	0	1	1	6
BM7	1	0	1	1	1	1	1	0	1	1	8
BM8	1	0	1	1	1	1	1	0	1	1	8

Supplementary Table C2.8. Relaxed selection criteria used in the comparison of Mundine Wells results (Supplementary Figure C1.5). Selection criteria are defined in Table 5.1.

Shaw	a (°)	MAD (a & f) (°)	*FRAC* (%)	rN	|k'|	f_{RESID}	sA1 1 (+/-)
selcrit	≤ 10	≤ 10	≥ 45	≥ 0.990	≤ 0.2	≤ 0.2	≤ 0.4

Thellier	a (°)	MAD (a & f) (°)	*FRAC* (%)	*f* (%)	|k'|	b	DRAT (%)	CDRAT (%)
selcrit	≤ 15	≤ 10	≥ 25	≥ 35	≤ 0.35	≤ 0.11	≤ 15	≤ 25

C3 Supplementary Text

Specimen names consist of the locality identifier, the first two letters (MD or BM), followed by the site number; a dash then separates these from the core number and specimen letter (A – F indicates that five specimens are taken from that core). Microwave specimens have an additional number at the end where more than one specimen is from the same half inch core e.g., MD6-1D4 indicates that this is the fourth microwave specimen obtained from site MD6, core 1, specimen D. Hand samples collected at sites BM3, 6 and 7 are identified slightly differently using an additional letter; e.g., specimen BM7-4AB is from site BM7, hand sample 4, core A, specimen B. Microwave specimens that were drilled from hand samples are denoted by a 'H' followed by the hand sample number, and then the specimen number.

C4 References cited

Paterson, G. A. (2011). A simple test for the presence of multidomain behavior during paleointensity experiments. Journal of Geophysical Research: Solid Earth, 116(10), 1–12. https://doi.org/10.1029/2011JB008369

Paterson, G. A., Heslop, D., & Pan, Y. (2016). The pseudo-Thellier palaeointensity method: New calibration and uncertainty estimates. Geophysical Journal International, 207(3), 1596–1608. https://doi.org/10.1093/gji/ggw349

Appendix D

Results from Chatham Grenville site 2

D1 Supplementary Figures

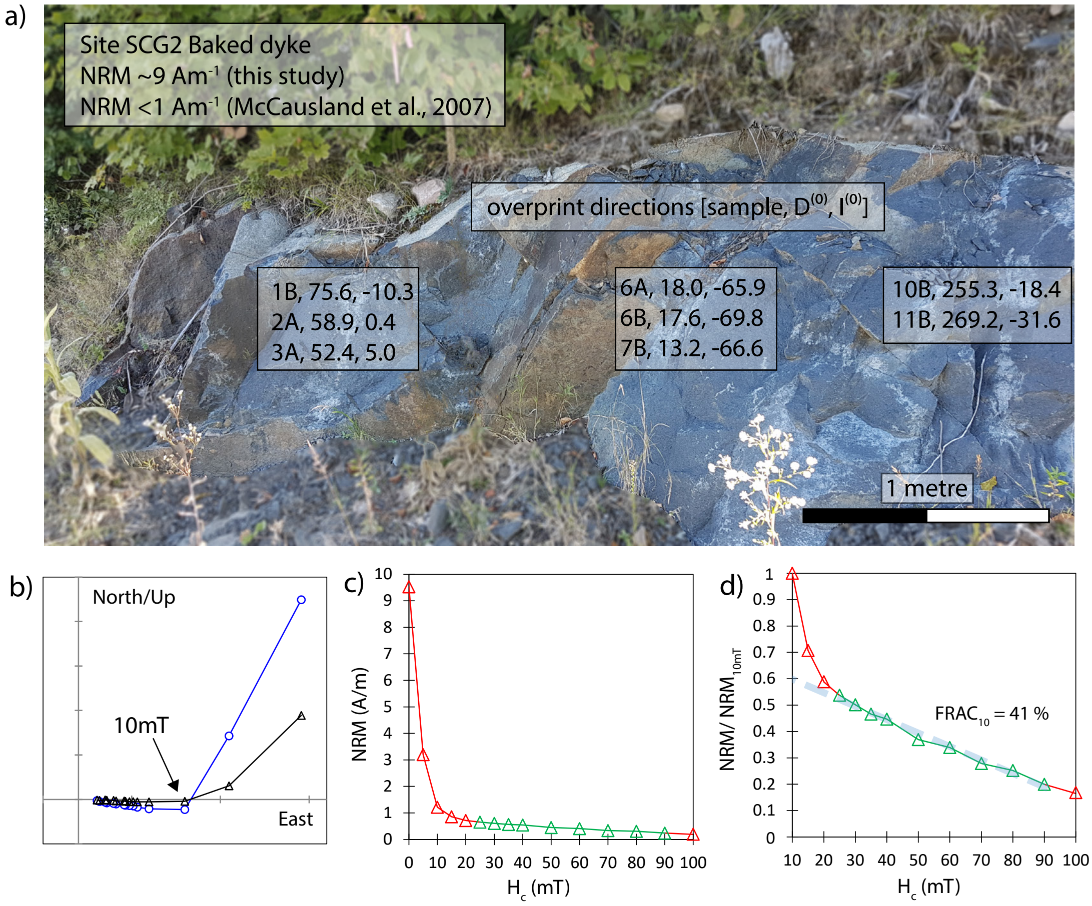

Supplementary Figure D1.1. a) Chatham Grenville results. The figure shows the difference in magnetisation between this study and the original. The grouping of overprint directions determined from principal component analysis (PCA) strongly suggests that the difference in magnetisation is due to a lightening strike induced IRM. After removal of the overprint, the magnetisation is sufficiently strong (~1 A/m) to determine a reliable palaeointensity. Consistently weak palaeointensity results (N = 12/24) are obtained using the Shaw-DHT palaeointensity method (11 results) and one result using the Microwave palaeointensity method. In each of the specimens, most of the fraction of remanence was composed of IRM overprint. . b - c) Data from specimen 2-6a used as a typical example b) Orthogonal diagram. c) NRM demagnetisation. d) NRM demagnetisation normalised by NRM at 10mT. $FRAC_{10}$, FRAC calculated accordingly.

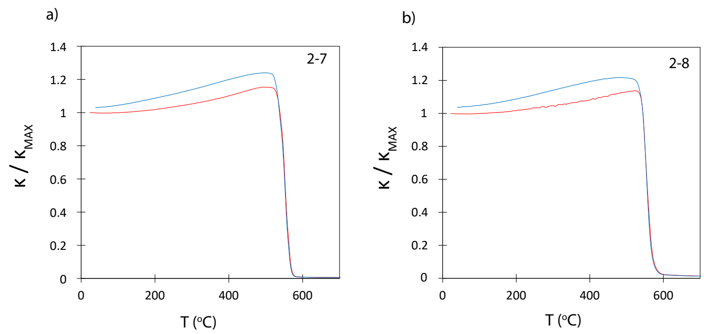

Supplementary Figure D1.2. Normalised κ-T curves for specimens 2-7 (a) and 2-8 (b). Red line, heating; blue line, cooling.

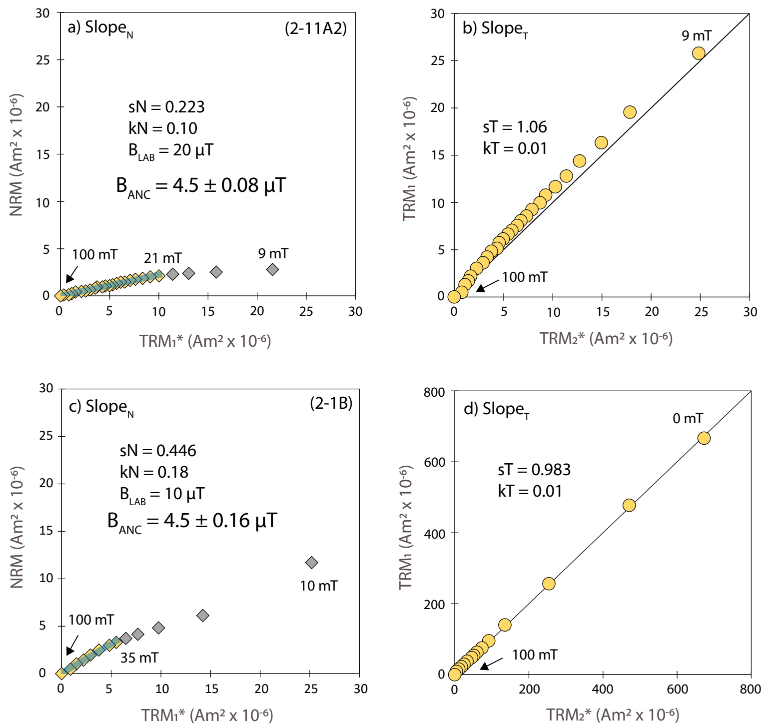

Supplementary Figure D1.3.Typical Shaw palaeointensity plot and slope$_T$. for specimens 2-11A2 (a & b) and s-1B (c & d). Note that specimen 2-11A2 slope$_T$ starts at 9mT, but 2-1B starts at 0 mT to show the difference in moment.

D2 Supplementary Tables

Supplementary Table D2.1. Selection Criteria for Shaw-DHT results for Chatham Grenville. See Table 5.1 and Supplementary Tables B2.1 and C2.3 for a detailed description of the parameters. FRAC$_{10}$, FRAC determined from NRM$_{9\ or\ 10mT}$ (9 or 10 mT depending on the steps used).

α	$MAD_{A\&F}$	kN	f_{RESID}	β	$FRAC_{10}$	sT	kT
≤ 15°	≤ 10°	≤ 0.2	≤ 0.2	≤ 0.1	0	+/- 0.08	≤ 0.2

Supplementary Table D2.2. Specimen-level Shaw-DHT results for Chatham Grenville site 2. See Supplementary Tables B2.1 and C2.3 for a detailed description of the parameters. $FRAC_{10}$, FRAC determined from $NRM_{9\ or 10mT}$; $Slope_{T(all)}$, $kT_{(all)}$ and $rT_{(all)}$ are the values produced when using the full range of coercivity steps. Italics indicate failed selection criteria.

Sample	D (°)	I (°)	α (°)	MAD_A (°)	MAD_F (°)	N	H_L (mT)	H_M (mT)	B_{LAB} (μT)	$FRAC_{10}$ (%)	sN	kN	rN	β	$Slope_{A1}$	f_{RESID}	$Slope_{A2}$	$Slope_T$	kT	rT	$Slope_{T(all)}$	$kT_{(all)}$	$rT_{(all)}$	B_{ANC} (μT)	StdErr
2.1A1	96.0	24.6	9.6	3.8	*19.0*	21	24	100	20	*19*	0.160	0.193	*0.863*	0.09	0.98	0.09	0.83	*1.202*	0.010	0.999	*1.085*	0.142	0.996	-	-
2.1B	80.6	23.1	8.5	2.4	5.5	8	35	100	10	28	0.446	0.176	0.993	0.03	1.01	0.02	0.98	1.015	0.151	0.994	0.983	0.009	1.000	4.5	0.16
2.2A	87.7	18.8	6.1	2.1	4.5	8	35	100	10	*17*	0.461	0.124	0.996	0.03	1.04	0.02	0.99	0.972	0.107	0.997	0.953	0.009	1.000	-	-
2.3A	83.6	21.5	6.5	2.3	5.9	9	30	100	10	25	0.413	0.180	0.993	0.03	1.12	0.05	0.96	0.944	0.102	0.997	*0.906*	0.060	0.999	4.1	0.13
2.3B1	95.0	18.7	9.9	2.7	10.7	20	27	100	20	*17*	0.191	*0.334*	*0.965*	0.04	1.06	0.13	0.87	*1.14*	0.018	1.000	1.055	0.127	0.997	-	-
2.3B2	87.0	20.9	4.9	1.8	7.7	20	27	100	20	*17*	0.192	*0.340*	*0.971*	0.04	1.05	0.06	0.88	*1.097*	0.028	0.999	1.060	0.105	0.997	-	-
2.4C1	87.5	18.5	5.8	1.2	6.8	19	27	95	20	*18*	0.175	*0.372*	*0.976*	0.04	1.05	0.19	0.88	*1.119*	0.054	0.999	1.039	0.040	0.999	-	-
2.4C2	88.8	16.8	4.9	1.5	9.6	19	30	100	20	*10*	0.179	*0.302*	*0.976*	0.04	1.08	0.07	0.88	*1.087*	0.061	0.999	1.069	0.017	1.000	-	-
2.5A2	92.7	18.9	5.8	1.9	4.9	21	24	100	20	50	0.225	*0.310*	*0.981*	0.03	0.87	0.05	0.85	*1.09*	0.050	0.999	1.000	0.114	0.998	-	-
2.5B2	101.8	22.6	14.5	4.4	7.2	21	24	100	20	58	0.143	0.114	0.991	0.02	1.06	0.04	0.90	1.07	0.060	0.999	1.059	0.027	1.000	2.9	0.06
2.6A	98.5	25.3	3.8	1.8	4.8	9	25	90	10	41	0.345	0.061	0.994	0.03	1.07	0.04	0.95	0.994	0.080	0.998	*0.897*	0.088	0.999	3.5	0.10
2.6B	98.8	28.2	1.3	2.9	8.5	10	25	100	10	43	0.334	0.015	0.998	0.02	1.10	0.02	0.93	1.033	0.127	0.995	*0.894*	0.007	0.999	3.3	0.06
2.7B	89.4	16.8	13.3	5.8	6.4	7	40	100	10	37	0.340	*0.244*	*0.987*	0.05	0.90	0.03	0.88	1.002	0.143	0.996	0.979	0.039	0.999	-	-
2.7C2	100.9	20.6	14.7	3.6	8.4	11	33	65	20	84	0.214	*0.244*	*0.971*	0.06	0.92	0.49	0.86	1.005	0.055	0.997	1.006	0.042	1.000	-	-
2.7D1	94.2	25.5	4.1	2.8	8.5	18	21	80	20	36	0.232	*0.303*	*0.980*	0.04	0.81	0.20	0.87	1.048	0.051	0.999	1.037	0.065	0.999	-	-
2.8C1	90.9	20.2	13.5	7.4	6.9	21	24	100	20	51	0.241	0.008	*0.987*	0.03	0.90	0.02	0.88	0.997	0.040	0.999	1.034	0.013	1.000	4.8	0.13
2.9B1	98.9	33.8	6.9	2.3	7.1	14	30	75	20	44	0.274	0.199	0.991	0.03	0.82	0.14	0.83	1.035	0.021	0.998	1.062	0.032	1.000	5.5	0.15
2.10A1	-	-	*17.5*	5.2	7.9	21	24	100	20	49	0.201	0.191	*0.987*	0.03	0.86	0.06	0.85	*1.113*	0.093	0.998	1.074	0.029	1.000	-	-
2.10A2	96.4	13.3	10.6	3.5	6.3	22	21	100	20	50	0.214	0.001	0.994	0.02	0.81	0.02	0.85	*1.117*	0.112	0.997	1.013	0.068	0.999	4.3	0.08
2.10B	97.5	23.4	6.1	2.7	7.1	10	25	100	10	80	0.323	0.051	0.993	0.03	0.99	0.02	0.79	*1.196*	0.178	0.993	1.072	0.035	0.999	3.2	0.10
2.11A2	101.1	36.4	9.4	3.6	5.2	22	21	100	20	76	0.223	0.103	0.993	0.02	0.79	0.01	0.89	*1.139*	0.127	0.996	1.058	0.009	0.999	4.5	0.08
2.11B	113.0	42.8	11.9	4.2	6.0	9	20	80	10	72	0.311	0.192	0.991	0.04	0.93	0.13	0.82	*1.132*	0.079	0.997	1.046	0.001	0.999	3.1	0.11
2.11C2	110.2	39.3	11.4	3.2	6.0	17	36	100	20	*12*	0.252	*0.311*	*0.973*	0.04	0.77	0.03	0.94	*1.148*	0.085	0.996	*1.106*	0.039	0.999	-	-